ENDOSCOPIC AND MAGNETIC ACTUATION FOR MINIATURE LIFESAVING DEVICES

By

Nicoló Garbin

Dissertation

Submitted to the Faculty of the

Graduate School of Vanderbilt University

in partial fulfillment of the requirements

for the degree of

DOCTOR OF PHILOSOPHY

in

Mechanical Engineering

February 28, 2019

Nashville, Tennessee

Approved:

Pietro Valdastri, Ph.D.

Keith L. Obstein, M.D., M.P.H.

Thomas J. Withrow, Ph.D.

Robert J. Webster III, Ph.D.

Nabil Simaan, Ph.D.

ACKNOWLEDGMENT

Many are the people and institutions who must be given credit for the achievements described in this dissertation.

First, I wish to thank my wife Stephany, and our daughter Evelyn. Stephany, thank you for joining me in this tremendous journey many miles from our homes towns. Thanks to your support, understanding, and genuine help I am able to complete this great step in our lives. Evelyn, you are the greatest gift me and your mother could ever ask for. You are a joy, a muse, and an unending source of inspiration.

Second, I greatly admire and thank my two mentors: Pietro Valdastri Ph.D., and Keith L. Obstein M.D., M.P.H. Pietro and Keith, you both are an example, and a model to seek encouragement from. Your objective help, and constructive feedback have helped me grow as a student, as a researcher, as a professional, and as a man. Thank you both for letting me leave a trace in the science and engineering world.

Third, I wish to thank Tanner Hargens, CEO of Medical Merge LLC (Brentwood, TN), and Byron Smith, Senior Engineer at Medical Merge LLC. Joining your team was one of the greatest opportunities I have ever been given, and I have enjoyed every single moment of it. Tanner, thank you for teaching me much about what goes on behind the scene of the medical device space and what are the key components for successful innovation. Byron, thank you for being such an explosion of ideas, approaches, and solutions to every problem. Working with you will never get boring.

Finally, I want to thank the National Science Foundation (NSF) for their support under grants number: IIS-1453129, GRFP-1445197; the National Institute of Health (NIH) for their support under grants number: UL1-TR000445, R01EB018992; the Engineering and Physical Sciences Research Council (EPSRC) for their support under grant number: EP/P027938/1; The Royal Society for their support under grant number: CH160052; The Higher Education Funding Council for England (HEFCE) Global Challenge Research Fund for their support under grant number: 95543290; the Gradate School of Vanderbilt University, the Vanderbilt Institute for Surgery and Engineering (VISE), the WOND'RY at Vanderbilt University, and the Mechanical Engineering Department at Vanderbilt University for their additional financial supports.

TABLE OF CONTENTS

LIST OF TABLES

LIST OF FIGURES

LIST OF ABBREVIATIONS

- AESOP - automated endoscopic system for optimal positioning;
- AGC - antrum greater curvature;
- AGC - antrum greater curvature;
- ALC - antrum lesser curvature;
- BGC - body greater curvature;
- BLC - body lesser curvature;
- CE - capsule endoscope;
- CIP - catheter-like implantable pump;
- DAQ - data acquisition board;
- DC - direct current;
- DCE - dual-continuum endoscope;
- DOF - degree of freedom;
- EAM - external anchoring magnet;
- ED - emergency department;
- EDM - external driving magnet;
- EGD - esophagogastroduodenoscopy;
- EM - electromagnetic;
- ER - emergency room;
- ET - endoscopic tip;
- EU - Europe;
- FDA - food and drugs administration;
- FE - flexible endoscope;
- FEA - finite element analysis;
- GEJ - gastroesophageal junction;
- GI - gastrointestinal;
- GP - general practitioners;
- GR - gear ratio;
- IAM - internal anchoring magnet;
- ICU - intensive care unit;
- IDM - internal driven magnet;
- IRB - institutional review board;
- IRIS - integrated real time imaging system;
- LapR-LMA - laparoscopic retractor based on local magnetic actuation;
- LED - light emitting diode;
- LESS - laparoendoscopic single site;
- LGI - lower gastrointestinal;
- LMA - local magnetic actuation;
- MAGS - magnetically anchoring and guidance system;
- MC - magnetic camera;

- MEC - magnetic external component;
- MFS - magnetic field sensor;
- MIS - minimally invasive surgery;
- NOTES - natural orice transluminal endoscopic surgery
- OCM - offset crank mechanism;
- OR - operating room;
- PBA - parallel bellows actuator;
- PG - planetary gearhead;
- PGY - postgraduate year;
- PM - permanent magnet;
- PPE - personal protective equipment;
- PS - power screw;
- PTZ - pan tilt zoom;
- REDCap - research electronic data capture;
- RL - retracting lever;
- RMSE - root mean squared error;
- SD - standard deviation;
- TEE - transesophageal echocardiography;
- TLX - task load index;
- UGI - upper gastrointestinal;
- UI - user interface;
- US - United States.

Introduction

Motivation

Two of the greatest challenges in modern medicine are the ability to increase patients' access to safe diagnostic procedures, and to treat pathological conditions in a minimally invasive fashion. Overcoming these challenges not only will provide patients with less discomfort, trauma, and pain, but it will also allow healthcare systems, both single- and multiple- payer, to save costs while offering better outcomes for the population, hence saving lives. As follows, two clinical scenarios are being described to advance medicine and improve the way mankind deals with life threatening conditions.

The first clinical scenario that this dissertation aims to improve, is the screening of the gastrointestinal tract. To date, screening procedures of both the upper and lower gastrointestinal tract are a large portion of routine exams performed in both large hospitals and smaller specialized out-patient clinics. The main disease that these procedures aim to detect early on is cancer. Colonoscopies are performed to detect colon cancer, while esophagogastroduodenoscopy to detect stomach cancer. Both procedures consist in the direct visualization of the internal anatomy via a flexible endoscope. These tools are used by gastroenterologists to treat many other conditions, but gastrointestinal cancer is the most deadly one. If this disease if detected in its early stage of development, the survival rate is extremely high. On the contrary if cancer develops to more advanced stages, the mortality rate drastically increases. The flexible endoscope is a great tool that allows diagnostic and therapeutic procedures but has many drawbacks which hinder the wide spread performance of the increasing number of gastrointestinal tract diagnostic procedures. These devices consist of a long flexible probe with an articulating section. At the tip, a camera, illumination and a series of dedicated channels for irrigation, insufflation and passing tools are present. The steerable tip is controlled by a double knobs mechanism that requires intensive training for efficient and safe use. This design solution relies on hand assembled miniaturized mechanical components, bringing the cost of a single flexible endoscope to an average of 40,000 USD and making it prone to failure due to wear and poor handling. To operate this device, a dedicated bulky endoscopic tower that averages 80,000 USD in cost, is necessary. Due to their high cost, flexible endoscopes are reprocessed for reuse, and a dedicated reprocessing facility is required. The logistic burden associated with maintaining flexible endoscopes is further increased by the need of a dedicated endoscopic suite for performing procedures, and a team of a specially trained operator (i.e. gastroenterologist), an anesthesiologist (in United States, most of the gastrointestinal screening procedure are performed under sedation), a technician, an a nurse. It must be noted that a screening procedure of the upper gastrointestinal tract requires on average 5 minutes but an incredible

amount of resources and personnel are also required. As a results patients in rural areas of developed countries may wait weeks before a procedure is scheduled and may travel many hours to reach a specialized unit. Patients in low- and middle- income countries are instead not screened at all due to the abovementioned challenges related to the performance of conventional flexible endoscopy. As an example, in Sierra Leone, a country with a population over 7 million, there is only one flexible endoscope. There is hence an urgent need of a dedicated endoscopic tool for diagnosis of the gastrointestinal tract that increases patients' access, diminishes related costs, and does not require special training for operation.

To solve these problems, the body of work presented in chapter I discusses the development, characterization, testing and evaluation toward clinical use of a novel disposable flexible endoscope specifically designed for the diagnosis of the upper gastrointestinal tract.

The second clinical scenario discussed in this dissertation is minimally invasive surgery and treatment. The introduction of minimally invasive surgical techniques has brought tremendous reduction of pain and trauma for the patients. It led to shorter hospitalization, quicker recovery time, and lower risk of infections. Laparoscopy is the use of the minimally invasive approach in abdominal surgery. During a laparoscopic procedure, surgeons access the surgical workspace (i.e. the abdominal cavity and its organs) through a series of small incisions instead of using large and invasive openings. Depending on the operation, a number of incisions that varies from 3 to 6, are used to insert different long-shaft tools that are operated from the outside of the body. The laparoscope provides surgeons with direct visualization of the target area by embedding a vision system at its tip. A surgical retractor is used to enhance visibility of hidden target areas (e.g. during a cholecystectomy the liver is retracted to expose the cholecyst). A series of surgical manipulators with various end effectors are then used to cut, cauterize, place sutures, etc. Because of the limited access to the surgical workspace via miniaturized elongated tools, the laparoscopic approach poses new technical challenges to the surgeons. In fact, the maneuverability of the instrument is constrained by the access port location, resulting in limited vision, inconvenient tool manipulation and vibration due to human hand tremor. Much research effort is being made toward simplifying surgery with the aid of robotic surgical platforms, and decreasing invasiveness further via a single or an internal incision.

The body of work of chapter II of this dissertation describes the robotic control of magnetically actuated medical devices. The development and testing of a laparoscopic retractor, a laparoscopic camera and a subcutaneously implantable pump for the treatment of refractory ascites, demonstrate the potential that magnetic actuation has toward elevating medical treatment to the next technological level.

Thesis overview

The body of work of this dissertation is organized in two main chapters.

Overview chapter I

This chapter provides the reader with the rationale that led to the implementation of a low–cost pneumatically actuated disposable flexible endoscope designed as an alternative solution to bulky, non-intuitive conventional flexible endoscopes with applications in upper gastrointestinal tract screening. The work conducted on the topic is organized as follows:

- Section I.1 - **Clinical need**. This section summarizes the disadvantages of conventional flexible endoscopy. It then presents clinical and technical requirements for the development of an upper gastrointestinal flexible endoscope (subsection I.1.1), and concludes with a literature review of continuum robots and their applications in medicine (subsection I.1.2).

- Section I.2 - **Robotic disposable upper endoscope**. This section details modeling and control strategies adopted for actuating a PBA disposable endoscope via electromechanical actuation of piston syringes. The design and description of the components of the disposable endoscope are presented in subsection I.2.1. The modeling strategy aimed to compensate for transmission losses due to compressibility of air is presented in subsection I.2.2. The results of the implemented modeling strategy toward closed-loop control are reported in subsection I.2.3.

- Section I.3 - **Dual-Continuum design approach for intuitive upper gastrointestinal endoscopy**. This section describes the development of an innovative mechanical flexible endoscope that builds on top of the robotic version presented in the previous section. A preliminary calibration (subsection I.3.4) of the endoscopic tip is necessary to identify design parameters needed to map the desired configuration input from the user into a configuration output at the tip at a tunable scale. The design (subsection I.3.5), in fact, relies on a multi backbone continuum structure as an intuitive user interface (joystick). This is mechanically coupled via a syringes and flexible multi lumen catheter to the disposable endoscopic tip previously presented. *Ex-vivo* cadaveric trials (subsection I.3.7) are reported and the need of a solution that enables single hand operation of the device is anticipated.

- Section I.4 - **Evaluation of the dual-continuum endoscope for assessment of the UGI tract**. This section

presents the latest, single hand operated, version of the manual disposable endoscope. The device is used for an evaluation carried via an IRB approved user study, described in subsection I.4.2. The efficacy and ease-of-use in visualizing six key landmarks in a stomach simulator of the novel device was benchmarked to a conventional flexible endoscope. The two devices were used by novices (people with no experience with traditional flexible endoscopes), trainees (GI fellows with less than 100 hours of operation of traditional flexible endoscopes), and attending (gastroenterologist with over 200 hours of use of traditional flexible endoscopes). Results are reported in subsection I.4.3.

Overview chapter II

The investigations conducted in the field of magnetically actuated medical devices are detailed here. Three devices that relies on robotic control of magnetic actuation are described: a laparoscopic retractor demonstrate the ability to transmit large amount of mechanical power with magnetic coupling, a laparoscopic camera demonstrates the use of magnetic coupling for fine control and large range of motion, and a subcutaneously implanted pump exploit the magnetic approach to move fluids from one compartment of the body to another without the use of embedded electronics. The work conducted on the topic is organized as follows:

- Section II.1 - **Advent of magnetically actuated surgical devices**. This section describes the recent trend in abdominal surgery to minimize surgical invasiveness. Two surgical techniques LaparoEndoscopic Single Site (LESS) surgery and Natural Orifices Tranluminal EndoSurgery (NOTES) and the more advanced robotic implementation of these are presented in subsection II.1.1 and II.1.1.1, respectively. The motivation behind the advent of magnetically actuated surgical devices is presented summarizing the classes/types of magnetically actuated devices (subsection II.1.2). The closed loop control problem of a particular magnetic actuation method, known as local magnetic actuation (LMA), is then presented in subsection II.1.3.

- Section II.2 - **Laparoscopic retractor based on LMA**. A laparoscopic retractor is proposed to demonstrate the ability of the LMA approach to transfer large amount of mechanical power across physical barriers. The principle of operation and design of each component that composes the instrument are described in subsection II.2.1. Experimental assessment consisting of quantitative, qualitative and *in-vivo* trials are discussed in subsection II.2.2.

- Section II.3 - **Laparoscopic camera based on an orthogonal magnet arrangement**. The proposed capsule laparoscope does not require a dedicated incision during MIS and evolves from the LMA approach. The

devices utilizes a magnetic arrangement that solves for magnetic singularity, enabling the control of two orientation DOFs and two positioning DOFs within the abdominal cavity. The device principle of operation (subsection II.3.1) and modeling (subsection II.3.2) are followed by its design and fabricatios (subsection II.3.3), experimental validation (subsection II.3.4), and *ex-vivo* canine trials (subsection II.3.5).

- Section II.4 - **Subcutaneously implantable pump for the treatment of refractory ascites**. To exploit the LMA approach for applications other than abdominal surgery, a subcutaneous implantable pump based on LMA is presented. The clinical need (section II.4.1), the principle of operation of the proposed alternative low-cost solution to the treatment of ascites (section II.4.2), the design - fabrication (section II.4.3), and the experimental validation (cection II.4.4) are reported. The implantable pump only embeds passive components and has a catheter-like shape which facilitates implantation. Expensive and delicate electronic components are instead embedded in an external magnetic controller which actuates and monitors the correct pump functioning. Section II.4.5 provides a summary of the results achieved during *in vivo* animal trials.

Contributions

Publications of chapter I

The innovations presented in this chapter arise from a deep understanding of a clinical need, and incremental technical improvement of a potentially disruptive technology in the field of upper gastrointestinal endoscopy. The flexible endoscopes presented in this chapter have led to the publication of two journal papers [1, 2], one conference paper [3] which was recognized with the best student paper award, and three conference abstracts [4–6]. I am lead author in all of these publications and I am lead inventor of the current patent application that describes the invention. This was submitted through the Center for Technology Transfer and Commercialization (CTTC) at Vanderbilt University.

These achievements were guided by an unparallel duo of complementary mentors: one with an outstanding engineering background and one with an innovative and objective clinical eye. The contributions of this chapter come from a series of collaborations with several institutions in the UK (University of Leeds, Imperial College of London, University College of London, and Queens Mary University of London) and within the mechanical engineering department at Vanderbilt University (ARMA Lab).

The robotic implementation of the disposable flexible endoscope disclosed in [3] was presented at the 1^{st} International Symposium of Medical Robotics (ISMR) (Atlanta, USA - March 2018). This contribution was well

received by peers and discusses the modeling and calibration toward closed loop control of a pneumatically actuated endoscopic tip. The device exploits a soft continuum endoscopic bending section composed by three rubber bellows aligned in parallel to form a parallel bellows actuator. The kinematic modeling framework is derived from multi-backbones continuum robots and considers transmission losses in the pneumatic lines to drastically reduce bending errors.

The purely mechanical flexible endoscope was published in IEEE Transaction on Biomedical Engineering [1]. This contribution represents the manual implementation of a ready-to-use, intuitive, flexible endoscope that exploits the same disposable endoscopic tip presented in [3]. The adapted kinematic model of the pneumatically actuated tip, was further developed to describe the device characterization and tunability based on design parameter. A multi-backbones continuum joystick actuating the tip, was shown to be properly designed such that the user-to-task mapping between user imposed configuration inputs at the joystick level to the distal tip resultant motion, is tunable. This purely mechanical device has low fabrication costs and is extremely intuitive to operate. A series of *in-vivo* and cadaveric trials proved the effectiveness of the device in performing diagnostic upper gastrointestinal procedures.

The same manual device was further redesigned to allow for a single hand actuation of the steerable tip, and it was compared in effectiveness and usability to a conventional flexible endoscope in performing simulated upper gastrointestinal endoscopies. The results of an IRB approved usability study are published in Endoscopy International Open [2]. A dedicated mock up phantom of the upper-gastrointestinal tract, containing relevant landmarks represented by different colored LEDs, was used as an experimental set up. Fifteen medical doctors with different level of experience using a conventional endoscope were enrolled and their performances evaluated and described.

The three conference abstracts contain preliminary results in terms of proof of concept [4], mechanical design and principle of operation [6], and *in-vivo* trials [5].

The relevant journal publications for this chapter are:

[1]: **N. Garbin**, W. Long, J.H. Chandler, K.L. Obstein, N. Simaan, and P. Valdastri, Dual-Continuum Design Approach for Intuitive and Low-Cost Upper Gastrointestinal Endoscopy, IEEE Transactions on Biomedical Engineering, in press.

[2]: **N. Garbin**, A. Mamunes, D. Sohn, R. Hawkins, P. Valdastri, and K. Obstein, "Evaluation of a novel low-cost disposable upper endoscope for assessment of the upper gastrointestinal tract," Endoscopy International Open , under revision.

The relevant conference paper is:

[3]: **N. Garbin**, L. Wang, J. H. Chandler, K. L. Obstein, N. Simaan, and P. Valdastri, A disposable continuum endoscope using piston-driven parallel bellow actuator, in Proceedings of the International Symposium on Medical Robotics (ISMR 2018). IEEE, 2018.

The relevant conference abstracts are:

[4]: **N. Garbin**, A. Stilli, A. Shiva, J. Fras, P. Slawinski, K. Obstein, K. Althoefer, H. Wurdemann, and P. Valdastri, Toward a low-cost soft robotic manipulator based on fluid-actuated bellows for gastric cancer screening, in 10th Hamlyn Symposium on Medical Robotics. Hamlyn Center, 2017, pp. 53-54.

[6]: **N. Garbin**, W. Long, S. Dennis, O. Keith, S. Nabil, and P. Valdastri, An intuitive a disposable endoscope with intrinsic pneumatic actuation, in 29th Conference of the International Society for Medical Innovation and Technology. SMIT, 2017, pp. 27-28.

[5]: **N. Garbin**, S. Sarker, D. C. Sohn, P. R. Slawinski, P. Valdastri, and K. L. Obstein, Su1180 evaluation of a novel disposable upper endoscope for unsedated bedside (non-endoscopy unit based) assessment of the upper gastrointestinal (UGI) tract, Gastrointestinal Endoscopy, vol. 85, no. 5, p. AB304, 2017.

The relevant patent application is:

N. Garbin, N. Simaan, P.R. Slawinski, K. Obstein, P. Valdastri, STEERABLE ENDOSCOPE WITH CONTINUUM MANIPULATOR, US patent application number WO2018102718A1, priority date December 02, 2016.

Publications of chapter II

The studies on magnetic devices carried in this body of work have led to six published journal papers. Five papers come from an intensive and fruitful collaboration with colleagues at Vanderbilt University, the University of Melbourne, and the University of Leeds. The sixth contribution is instead the result of an opportunity I was given while working as project lead at Medical Merge LLC (Brentwood, TN), a medical device consulting firm where I interned part time during my last year as a graduate student.

I led three of the six published papers [7–9].

The surgical retractor presented in [7] was published in American Society of Mechanical Engineering (ASME) Journal of Medical Devices. This paper discusses the development of the first ever magnetically actuated surgical device for MIS which exploits the LMA approach. I proposed and fabricated the device design, while leading magnetic and mechanical modeling for performance estimation and validation. Experimental bench top testing was instead performed in collaboration with undergraduate and graduate students from Vanderbilt University. I presented this study at the Student Mechanism & Robot Design Competition during the ASME Advanced Design and Manufacturing Conference & Expo held in Buffalo in August 2014, achieving a second place award. The *in-vivo* results highlighted the main limitation of the proposed approach for MIS, i.e. the thickness of the abdominal wall limits the exploitation of the magnetic approach to slim patients only; the need for a shielding solution to allow more

compact design; the compensation of magnetic interference to allow actuation of multiple degrees of freedom.

The two devices presented in [8] and [9], convert the understanding of magnetic actuation for medical device such that the limitations just outlined, do not apply to their clinical scenarios.

The subcutaneous pump presented in [8] is published in the ASME Journal of Medical Devices and it is an innovative low-cost solution for the treatment of refractory ascites, a condition estimated to affect over 100,000 patients by 2020 across the United States (US) and Europe (EU). The device principle of operation builds upon the LMA approach to create a positive displacement reciprocating pump, that I led in development, fabrication, and testing. While working on it I was reporting to the clinicians inventors, while coordinating with colleagues and supervising other interns. Such device, by being implanted subcutaneously, has a minimal intermagnetic distance between embedded PM and external one, and provides full exploitation of the LMA approach. The results from bench top experiments demonstrate the efficacy of the design which is modular and easy to tune. On December 11^{th} 2018, the device was also tested during *in-vivo* trials successfully. The results of these trials are not part of [8], but will be used to compile an abstract for EASL (European Association for the Study of the Liver) 2019 conference. I will be leading author for this contribution, but it will be completed after my defense and it is not added here. Nevertheless a report on the *in-vivo* experience is added in this dissertation (Section II.4.5).

The chief contribution of this chapter, the compact laparoscopic camera presented in [9], was published in IEEE Robotic and Automation Letter, and presented at IEEE International Conference on Robotics and Automation (ICRA) 2016 held in Stockholm, SWE. The device takes advantage of an innovative actuation solution (i.e. Orthogonal Magnet Arrangement - OMA) that overcomes LMA's limitations and enables the control in 4 DOF of a pill sized camera via a single, externally placed, permanent magnet. Given the device's small form factor, pediatric applications are proposed, while the use of a single external permanent magnet enables scalability to adult patients undergoing robotic and conventional abdominal and thoracic surgery. The device's external controller can either be coupled to a flexible holding arm for conventional MIS or become an alternative end-effector to a rigid laparoscope of a surgical robot. I proposed the novel magnetic actuation solution and led the development and testing of the device, while supervising Vanderbilt and visiting students.

These three publications highlight my contributions in terms of design, modeling and clinical translation to the scientific community on magnetic actuation for medical devices.

In addition, I also contributed by providing support to three additional publications [10–12] that expanded the boundary of what is known and what is possible to achieve, exploiting magnetic actuation for medical/surgical devices. The review presented by Leong in [10], published in IEEE Reviews in Biomedical Engineering summarizes

the recent advent of magnetically actuated surgical devices, providing fundamental references and guidelines to researchers that are approaching the same field. I am second author on this paper, and I helped with writing the manuscript as well as preparing images and gathering relevant references for it. The closed loop control of the LMA proposed by Di Natali in [11], published in IEEE Transaction on Robotics, is the result an internal collaboration of members of the Storm Lab. I am third author and I helped with magnetic modeling, dynamic model identification, and data post processing. Finally the cross-coupling compensation proposed by Scaglioni [12], expands from [11], to independently control multiple units of LMA for a multi-DOF single incision surgical platform. This work was led by colleagues at the University of Leeds and I am third author. I contributed by designing and fabricating an improved experimental platform, the control electronics, and replicating the Proportional Integral (PI) closed loop control algorithm of [11] to such platform within a different control software.

In summary, the relevant journal publications for this chapter are:

[7]: **N. Garbin**, C. Di Natali, J. Buzzi, E. De Momi, and P. Valdastri, Laparoscopic tissue retractor based on local magnetic actuation, Journal of Medical Devices, vol. 9, no. 1, p. 011005, 2015.

[8]: **N. Garbin**, P. Doyle, B. Smith, J.G. Taylor, M.H. Khan, Q. Khalil, P. Valdastri, "Miniature Pump for Treatment of Refractory Ascites based on Local Magnetic Actuation," Journal of Medical Devices *in press*, 2018.

[9]: **N. Garbin**, P. R. Slawinski, G. Aiello, C. Karraz, and P. Valdastri, Laparoscopic camera based on an orthogonal magnet arrangement, IEEE Robotics and Automation Letters, vol. 1, no. 2, pp. 924-929, 2016.

[10]: F. Leong, **N. Garbin**, C. Di Natali, A. Mohammadi, D. Thiruchelvam, D. Oetomo, and P. Valdastri, Magnetic surgical instruments for robotic abdominal surgery, IEEE reviews in biomedical engineering, vol. 9, pp. 66-78, 2016.

[11]: C. Di Natali, J. Buzzi, **N. Garbin**, M. Beccani, and P. Valdastri, Closed-loop control of local mag- netic actuation for robotic surgical instruments, IEEE Transactions on Robotics, vol. 31, no. 1, pp. 143-156, 2015.

[12]: B. Scaglioni, N. Fornarelli, **N. Garbin**, A. Menciassi, and P. Valdastri, Independent control of multiple degrees of freedom local magnetic actuators with magnetic cross-coupling compensation, IEEE Robotics and Automation Letters, vol. 3, no.4, pp 3622–3629, 2018.

Contributions

In summary the chief contributions of this body of work are summarized below:

Design

In this dissertation, a series of clinical and technical requirements were identified and used to drive the design of the devices to form easy to use, dexterous and low-cost solutions.

The first part this body of work, Chapter II, can be used by researchers and engineers as guidelines for the development of magnetic medical devices. The magnetic actuation based on rotating permanent magnets, i.e. the Local Magnetic Actuation (LMA), was characterized, and capitalized with the fabrication and testing of a laparoscopic retractor for MIS. The device embeds a miniaturized mechanical train that maximizes the torque available at the end effector. The experimental validation of this device identified the challenges for LMA application in MIS as a whole. The proposed actuation method was hence used to tackle a different medical need: a subcutaneous implantable pump. For such application, a device that does not require anchoring forces, and which lies under a thin layer of skin represents a great opportunity for the exploitation of wireless mechanical power provided by the LMA in a different clinical scenario. Nevertheless, to address the limitations of LMA in abdominal surgery, a novel magnetic coupling solution has been developed to actuate and anchor a miniaturized laparoscopic camera. The device takes advantage of smart placement of permanent magnets to provide a working range that avoids magnetic singularity, providing the device with 4 DOF and an autoflip feature, consisting in a 180° rotation along the device main axis at the bottom of its workspace. The camera can be reoriented in an hemispherical workspace, similar to the one that modern surveillance Pan Tilt Zoom (PTZ) cameras have. The use of a single externally placed permanent magnet for actuation, permits scalability of the device for potential use within a larger patient population (with various abdominal wall thicknesses). The compactness of the external controller can be used to decrease the number of incisions and provide better visibility of the surgical workspace for both conventional abdominal MIS and robotic MIS.

The second part of this body of work, Chapter I, was instead motivated by the urgent need for a disposable low-cost solution for the assessment of the UGI tract and aims to overcome most of conventional flexible endoscopy drawbacks. The proposed design was derived from continuum robotics which have numerous applications in medicine. A miniaturized parallel bellows actuator has been investigated as an endoscopic bending section. These bellows are actuated with standard syringes and two different coupling systems for tip motion control have been proposed. The first approach uses electromechanical actuation to form a robotic system easy to transport and which potentially could be controlled from a remote or autonomously for repetitive tasks (e.g. screening procedure). The second approach exploits instead the advantages of both rigid and flexible continuum robots to form an extremely intuitive

purely mechanical disposable endoscope. A multi-backbones continuum joystick is proposed as a novel user interface to overcome the long training required to master conventional flexible endoscope double knobs actuation. The endoscopic tip was assembled using off-the-shelf components for proof of concepts. The tip design is currently being improved to decrease its outer diameter toward human trials.

Modeling

Both main Chapters of this dissertation include modeling contributions. In Chapter II forces and torques of permanent magnets were estimated and validated via the use of both Finite Element Analysis (FEA), and analytical modeling (dipole-dipole model). The characterized magnetic coupling interactions had then been fed to quasi-static modeling aimed to predict the devices performances and functionality.

This body of work also contributes with the dynamic model formulation of the LMA that had been used to cast a linear control problem using Lagrange transformation, and a disturbance compensation control problem based on a state space formulation including a Kalman state observer.

In Chapter I we propose the adaptation of a kinematic model of rigid continuum robots (multi-backbones) to soft continuum structures (a soft endoscopic tip). The proposed framework has been successfully validated and the results suggest that, by relaxing some of the assumptions (e.g. constant curvature), the robotic implementation of the device can be controlled in closed loop. This contribution provides researchers in the field of soft continuum robots, an analytical method to build upon and take inspiration from.

In parallel, the design problem of a dual-continuum endoscopic device, with pure mechanical actuation has been cast using the same adapted model to match a desired tip configuration output in relation to an imposed user input. The modeling contribution of this device relies in the conversion of the validated adapted kinematical model in parametrical description of the coupling, toward tuning of a direct user-to-task mapping.

Clinical translation

The design and modeling contributions described above were capitalized with the fabrication of five different devices that were all successfully validated in clinically relevant scenarios. This is to be considered a major contribution since the application of innovative design had been clinically validated proving each design's efficacy.

Both a magnetically actuated laparoscopic retractor and a subcutaneous magnetic pump were tested during *in-vivo* porcine trials. The functionality of a miniaturized laparoscopic camera, was instead assessed during *ex-vivo*

canine trials that simulated a smaller surgical workspace. All of these devices exploit magnetic coupling to minimize patients trauma, help with recovery time, and lower the risk of infection. All of these devices also rely on the use of an external magnetic controller for actuation and are described in Chapter II.

A low-cost disposable endoscopic device was instead developed with two different actuation means. Either a robotic system or a novel continuum mechanical joystick connected to a pneumatically actuated endoscopic tip. Only the manual implementation of the device has been clinically tested, however the robotic version utilizes the same probe, hence it can be assumed that the validation holds for both versions of the device. The manual tool has hence been validated in both an *in-vivo* porcine model and during *ex-vivo* cadaveric trials. Furthermore, the manual device had also been tested with an Institutional Review Board (IRB) approved user study. Fifteen users with different level of experience in conventional flexible endoscopy were asked to perform visualization tasks in a mock simulator of the upper gastrointestinal tract with both the novel device and a conventional endoscope. The same device, given the promising results is currently undergoing a design freeze for human trials scheduled for 2020 in India.

Chapter I

Endoscopic actuation

I.1 Endoscopic actuation for gastrointestinal endoscopy

Flexible endoscopes (FEs) are medical instruments used for the investigation of the gastrointestinal (GI) tract in a range of procedures that include Esophagogastroduodenoscopy (EGD) (i.e. examination of the upper gastrointestinal (UGI) region). EGD is a very common procedure (>6.9 million EGDs per year in the US alone [13]), and is typically performed in a dedicated endoscopy suite due to the need for sedation, monitoring equipment, and trained personnel [14].

FE are complex, expensive, and non-intuitive medical devices that are cable actuated [15]. Most of the commercially available FEs are non-disposable and require reprocessing to avoid cross-contamination [16]. Despite reprocessing, FE related infections remain a concern and can lead to significant patient morbidity and mortality [17]. In addition, the durability of these devices is less than ideal, with breakage rates ranging from 1-10% at an average repair cost of 5,833 USD [18].

Among the indications that currently result in referral for an EGD, some may be over-served by the use of conventional FEs, and could benefit from a simpler, cheaper, and more hygienic solution. In particular, purely visual inspection (i.e. without biopsy sampling) may be appropriate for the vast majority of cases, with referral to full EGD if suspicious lesions are identified [19]. A visualization device that is easy to use and disposable has the potential to allow healthcare personnel without a formal GI training or access to reprocessing facilities to perform visual inspection of the UGI tract. In [20], endoscopy-based triage was demonstrated to improve patients outcome and reduce hospital costs. This study also highlighted the need for a device that is easy enough to use without specialistic training. Such a device would expand the availability of UGI endoscopy to general practitioners (GP), mid-level providers, emergency room (ER) clinicians, and intensive care unit (ICU) personnel. If manufacturing costs are low, then such a device would also be extremely beneficial in underdeveloped settings (e.g. low-income countries or rural areas of middle-income countries) where UGI tract pathologies have a high incidence [21], but access to healthcare facilities is scarce (e.g. Central America, rural areas of China and India) and screening programs are currently too costly to implement [22].

Commercially available disposable endoscopes include colonoscopes (SC210, Invendo Medical GmbH, now

Ambu A/S, Copenhagen, Denmark) [23], and magnetically controlled capsule endoscopes (NaviCam, Ankon Technologies Co, Ltd, Wuhan, China) [24]. However, these systems still require specialized locales to operate, and are targeted as a substitute for conventional FE, hence requiring conventionally trained operators. Conversely, a device that is supplementary in nature to conventional FE, while maintaining a lower cost, may have greater impact on the availability of UGI screening.

An example of a low-cost, disposable endoscopic platform for UGI cancer screening is the Hydrojet – a 10 mm diameter flexible catheter actuated via pressurized water jets located at the base of the distal viewing tip. The Hydrojet delivers a flexible and disposable endoscopic platform at $<$2 USD per case. However, significant challenges related to delivering intuitive and precise motion control of the viewing tip still remain to be addressed [25].

I.1.1 Clinical and technical requirements

The design of FE's have remained unchanged for over 60 years [26]. While they are used every day around the globe for the diagnosis and treatment of gastrointestinal disorders, FE's are not a perfect tool. In many cases, the design of traditional FEs limit their potential – especially in positively disrupting work-flow, improve patient access, and enhance patient care. When designing a novel FE specific for upper gastrointestinal tract exploration, many features need to be considered. These include:

1. WORKSPACE: Upper endoscopes (also known as gastroscopes) are FEs specifically designed for use in the UGI tract. The tip of the upper endoscope can be deflected with 2 degrees-of-freedom (DOF) (210° max up and 90° max down with one knob; 100° max left and 100° max right with a second knob [27]) that yields a curvature radius of approximately 40 mm. Manipulation of the endoscopes insertion tube provides two additional degrees of freedom – endoscope advancement and withdrawal and rotation of the instrument along its main axis.

2. STIFFNESS: The stiffness of the FEs insertion tube ranges within 160-240 Ncm^2, measured as a product of Young modulus and second moment of area [28], depending on the exact upper endoscope selected. Unfortunately, this stiffness can lead to unintended adverse events including perforation of the tissue that has a high mortality rate (approximately 25%) [29].

3. DIAMETER: Standard upper endoscopes are 8-9 mm in diameter. Small- (7 mm) and ultra-small (3-4 mm) diameter upper endoscopes are commercially available – although are considered specialty endoscopes and are not present in all endoscopy units. The advantage of endoscopes smaller in diameter is that the upper GI tract can be examined with administration of a topical anesthetic to mitigate the gag-reflex and without conscious sedation or monitored anesthesia care [30, 31]. In addition, these can be inserted trans-nasally and advanced down to the hypopharynx, past the upper esophageal sphincter, into the esophagus, and then to the stomach and small intestine. In this manner, examination of the GI tract can be performed solely with use of a topical anesthetic. Therefore, the major advantage of a smaller diameter endoscope is to avoid the most common cause of adverse events in upper endoscopy, i.e. sedation [32].

4. ANATOMY: The esophagus, stomach, and first part of the small intestine (duodenum) comprise the upper GI tract. The esophagus is a hollow organ that is approximately 25 cm in length and 2 cm in diameter. The stomach is a J-shaped hollow organ that is approximately

10 cm in width and 30 cm in length along its longest axis [33]. The stomach has 6 key landmarks (i.e. gastro-esophageal junction (GEJ)/cardia, antrum greater and lesser curvature (AGC and ALC), body greater and lesser curvature (BGC and BLC), and fundus) that are typically inspected during an EGD. The duodenum is a c-shaped structure between the bulb and second portion followed by a straight segment for the third and fourth portions. The duodenum is approximately 2.5 cm in diameter and 30 cm in length. The surfaces of these segments are moist and can have fluid, mucous, and debris. The hollow structures are also collapsed at rest unless air or other gas is introduced. Therefore, the upper endoscope must possess the ability to irrigate, aspirate, rinse the camera lens, and insufflate the lumen to allow for space creation and adequate mucosal visualization.

5. USABILITY: Medical providers undergo extensive training in order to be able to perform endoscopy in a competent manner. Due to the design of the endoscope, there is a steep learning curve and a real potential for adverse events if one is not well trained [29]. This learning curve and non-intuitive dual-knob controlled actuation mechanism limit the number of providers who are able to competently perform the procedure [34, 35]. Hence, there exists a true shortage of providers whom are able to perform endoscopy for an ever-expanding population of patients who need the procedure. In addition, endoscopists must be well-trained in order to be able to compensate for the 13-25° tip bending error associated with traditional FEs [27] and avoid adverse events.
6. PORTABILITY: The traditional FE tower is comprised of a box light source, image processor, monitor, computer, computer monitor, irrigation pump, and, in most current set-ups, a CO_2 insufflation system that are arranged on a large cart with wheels (range: 60-120 cm width, 115-125 cm tall, 60-65 cm deep). This system is bulky, heavy, and burdensome to transport. In addition, the system must be connected to a wall-power supply and suction mechanism. The physical size and encumbrance of the traditional FE platform alone limits its use to larger rooms/suites in the medical setting and prohibits it in patient care rooms or outpatient clinics.

   A stand-alone endoscopic device that is lightweight, portable, small in physical size, does not rely on a fixed power supply, and can be viewed on a personal device (i.e. smart phone, tablet, etc.) has the potential to provide a solution for screening in outpatient clinics, at the bedside in patient care units in medical centers, and in rural/remote locales around the globe.
7. COST: In the US, the average total cost of an upper endoscopy is 1,775 USD per procedure [13] with an average endoscope reprocessing cost of 160 USD per case [18]. The approximate upfront capital cost for an upper endoscopy tower is 80,000 USD, while for an automated endoscope reprocessing system is 40,000 USD. Therefore, these capital and recurrent costs make traditional upper endoscopy cost prohibitive outside of dedicated endoscopy units and for many low- and middle-income countries around the world.
8. DURATION OF THE PROCEDURE: An average diagnostic EGD can be completed in 4 to 12 minutes. The total time spent by a patient in an endoscopy facility can be between 60-120 minutes, as this includes the pre-procedure/sedation assessment, sedation recovery, and discharge.

I.1.2 Continuum approach in medicine

Continuum robots, defined as actuated structures whose constitutive materials form curves with continuous tangent vectors, have found numerous applications within surgical procedures [36, 37]. Examples include concentric tube robots/active cannulas [38, 39] and multi-backbone continuum robots [40, 41] for trans-oral upper airway surgery [42], single port access surgery [43, 44], minimally invasive surgery (MIS) [45], and arthroscopy [46].

The suitability, and therefore prevalence, of multi-backbone continuum medical devices may be attributed to their large range of motion, with the ability to provide high accuracy under telemanipulation guidance (e.g. [43] reported sub-millimetre motion accuracy during autonomous manipulation). However, these devices require active compliance control schemes to ensure safe insertion into human anatomy [47], thus increasing the complexity of clinical translation.

A safer implementation of the continuum approach is provided by soft, fluid driven, manipulators [48]. Examples under development for endoscopic applications are described in [49–51]. These are silicone molded devices that elongate and bend when their internal chambers are pressurized. Although these actuators can be fabricated at relatively low cost, the complexity of the material properties and internal structures provides non-linear responses, which are problematic for attaining accurate kinematic models and closed loop control. An approach that is more straightforward to model, yet maintains the benefit of having soft structures, consists in adopting expandable chambers in the form of bellows, mounted in a parallel configuration (parallel bellows actuator - PBA). A linear relationship between input pressure and bellows elongation has shown to be effective in predicting the system behaviour for closed loop control of PBA [52–54]. This approach has been extensively described in [55, 56] to control the bellows-actuated Bionic Handling Assistant (Festo, Esslingen am Neckar, Germany) while gripping and manipulating different objects.

I.2 Robotic disposable upper endoscope

The proposed device was inspired by the Bionic Handling Assistant by Festo [56] and catheter based continuum robots [52], and it takes the form of pneumatically actuated endoscope with a parallel bellow actuators (PBA) [52–54, 57] forming a steerable tip, see Figure I.1. The main advantage of this architecture is the ability to actuate the system via means of standard syringes. It is hence proposed that pressure lines and therefore bellow extensions in this work are controlled using electromechanically driven syringes.

Similar works [58–61] are relevant in that they demonstrated a potential need for models compatible for both pneumatic actuated manipulators and tendon (backbone) driven robots. This need motivates the adoption of kinematic model of multi-backbone continuum robots for pneumatic parallel bellow actuators use.

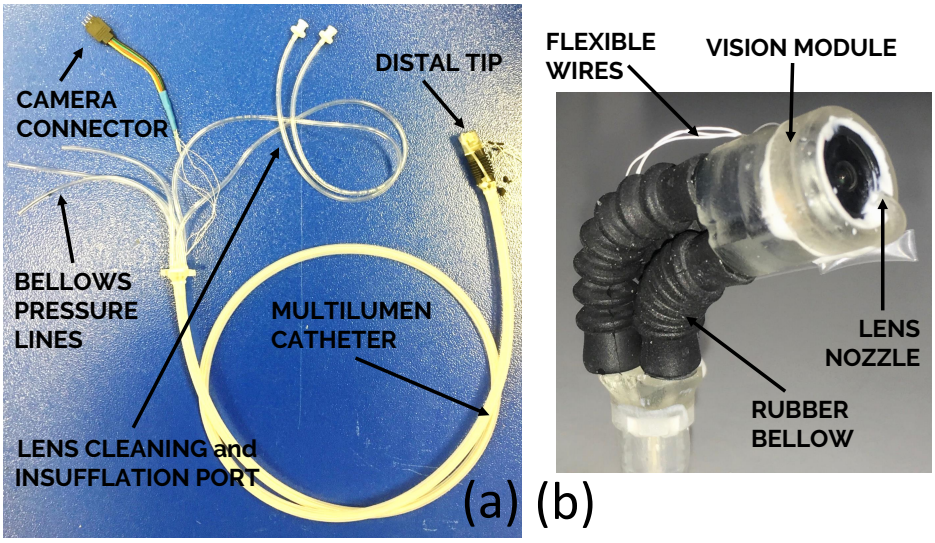

Figure I.1: Disposable flexible endoscope: (a) Overview of the endoscope; (b) Detail of the distal endoscopic viewing tip.

I.2.1 Disposable continuum endoscope

The disposable pneumatic endoscope consists of a flexible extruded catheter (Nusil MED-4880 silicone) with seven internal channels (7mm in diameter and 120 cm long). The cross-sectional profile of the catheter is shown in Fig. I.2(c). An endoscopic viewing tip is coupled to the catheter at the distal end, while independent access to each lumen is facilitated with a bespoke 3D printed adapter at the proximal end. The six peripheral lumens of the flexible catheter are used for: power, camera and lighting wires (x1); insufflation (x1); irrigation (x1); and pressure lines for tip control (x3). The central lumen is reserved for a wire rope made out of 18-8 Stainless steel with a 7x19 arrangement, and it is used to stiffen the catheter.

The endoscopic viewing tip is actuated via PBA which has 3 DOF that are controlled by changing the pressure in each of the bellows' line. By changing the bellows design, it is possible to change the manipulator range of motion as well as its overall outer diameter. The three bellows (B = 5.6mm connector $\varnothing$, 7.5mm max $\varnothing$, 14mm to 29mm variable length) at the vertexes of an equilateral triangle with side T = 7 mm, define a tip with diameter D of 13.68mm, see Fig. I.2(a).

A CMOS camera (1.3 Megapixel, 5-8cm focal length, dimensions: $9mm \times 9mm \times 9mm$) is embedded at the tip (RA78080A-60 Bangu Technology Development CO., Baoan, China). Three ultra-low power Light Emitting Diodes (LEDs) (EAHC2835WD4, Everlight Electronics, Taipei, Taiwan) surround the camera to provide bright illumination. The endoscope tip casing and connectors were 3D printed in resin (RS-F2-GPCL-02, Clear, FormLabs Somerville, MA, USA). Epoxy glue (Marine Epoxy, Loctite) was applied to the component joins to ensure a wa-

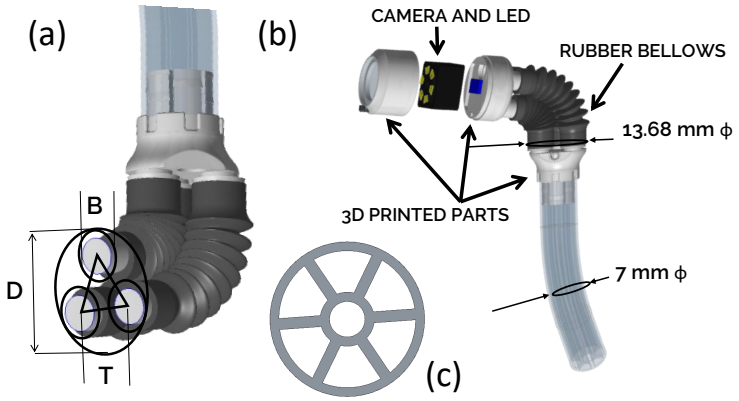

Figure I.2: CAD model of the distal steerable tip: (a) the bellows arranged in parallel having a diameter of 13.68 mm; (b) the distal tip that is connected to the multi-channel catheter and that is embedded with a camera having illumination; (c) cross sectional view of the multi-lumen catheter.

terproof seal. The irrigation conduit is extended from the multi-lumen catheter channel to the tip of the endoscope via a highly flexible single lumen catheter (6 Fr, 0.003" wall thickness Pebax-35D, Apollo Medical Extrusion, UT, USA). Power and camera communication signals connect from the multi-lumen catheter to the tip using flexible wires (Calmont, California, USA). This configuration allows these components to bypass the PBA bending section without compromising its mobility.

The proximal extremity of the multi-lumen catheter provides direct coupling to each channel. Camera wires can be connected to a frame grabber for visualization, and insufflation and lens cleaning channels have a luer lock connector for use with standard syringes or pumping systems. Finally, actuation of the distal tip can be performed through connection of external pressure lines to each independent bellows lumens.

As the device is comprised of a small number of extruded, off-the-shelf and 3D printed parts, which are integrated within simple design, it is financially feasible for the scope to be disposable. The current version was assembled with an embedded 15 USD camera which can also be disposed of. If better quality camera is required, the design may be adapted to facilitate camera retrieval for reuse.

I.2.1.1 Actuation system of the disposable continuum endoscope

The PBA range of motion depends on the pressure inside the bellows. Given the soft nature of the bellows (Nitrile, E=3MPa), the pressure rating used to actuated the PBA is low (<6 PSI). Lower pressure removes the need for pneumatic control valves and a high-pressure source such a pressurized tank.

A suitable pressure range was achieved using standard 3 ml syringes (Qosina Corporation, NY USA). By controlling the syringe's piston position, the pressure inside the bellows is varied; positive and negative pressures inducing

elongation and contraction respectively.

To precisely control the piston position, an electromechanical actuation system was assembled, as shown in Fig. I.3(c). The drive system comprises three 200 step-per-revolution Nema17 stepper motors, independently driving a 3D printed rack-and-pinion (pinion pitch diameter: 30 mm; involute teeth profile: module 1; rack: 60 mm long with the same teeth profile). The piston of each syringe are connected directly to a corresponding drive rack and the cylinder secured. Motor driver boards (Big Easy Driver, SparkFun Electronics) with improved resolution (16 micro-steps per step) were used to digitally control stepper position and therefore the piston of the syringe. Each bellow pressure line is hence controlled by actuating the stepper motor. For the specified components, the resolution of the piston position is 0.0294 mm per micro step.

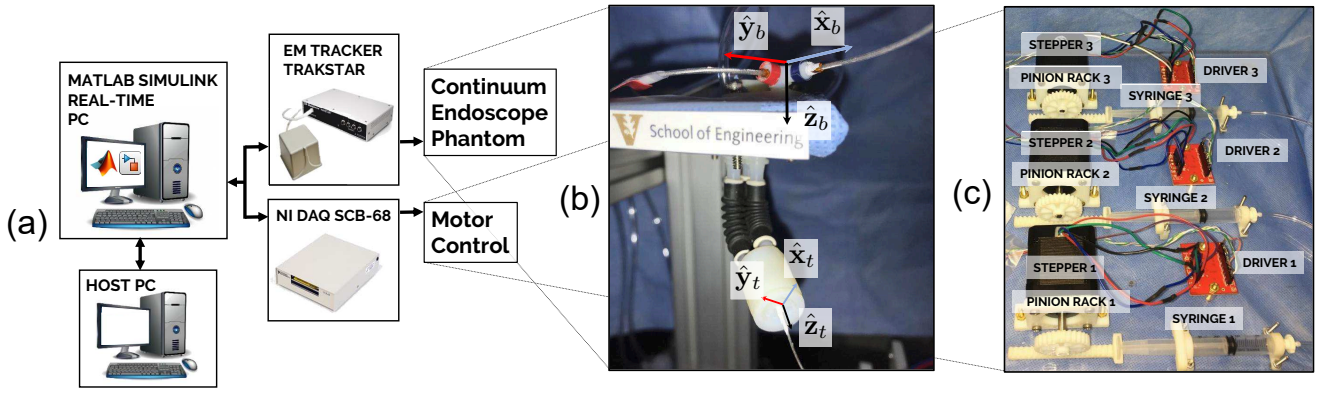

Figure I.3: Experimental setup: (a) schematic of the acquisition and control system via real-time Matlab Simulink™; (b) closed-up view of the continuum endoscope phantom used for validation. EM sensors are used to track $\hat{\mathbf{x}}_b, \hat{\mathbf{y}}_b, \hat{\mathbf{z}}_t$; (c) view of the actuation control system.

Figure I.3(a) shows a schematic of the test system developed to control the endoscopic viewing tip and validate the modeling strategies and actuation compensation method. A host machine communicates via ethernet to a Matlab Simulink™ real-time target environment. The target machine is programmed to control the stepper motors via Data Acquisition (DAQ) board (National Instrument SCB-68) at 2kHz frequency. The target machine also interfaces with an Electromagnetic (EM) Trackeing system (3D Guidance trakSTAR - Ascension, NDI, Waterloo, Canada) at 125Hz. Three 6-DOFs EM sensors (shown in Fig. I.3(b)) were used to track the end effector positions, and orientation with respect to the manipulator base frame.

A phantom end-effector was used having comparable weight to the actual camera viewing tip of the disposable device (2.58 gr). A detailed view of an inexpensive actuation system is shown in fig. I.3(c). Given the small form

factor of the actuation system, if controlled via micro controller (μC) and battery operated, it can fit a backpack facilitating system portability.

I.2.2 Kinematic modeling

Previous works [52, 56] formulated the kinematic model using internal pressure and the length of each bellow as joint space variables, respectively, both of which relied on direct pressure control. Inspired by these works, in this paper we propose to use a closed-form kinematic model for parallel bellow actuators. This model is adapted from existing multi-backbone continuum robots where the center lines of parallel bellows are used to describe the kinematic state (Fig. I.4). Constant curvature assumption is applied on all bellow center lines in this work, but it may be extended for non-circular bending as demonstrated in recent work [62].

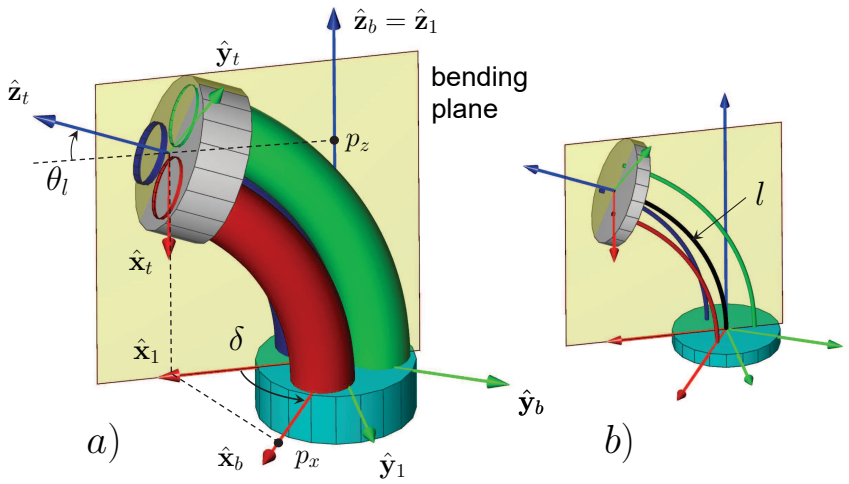

Figure I.4: Kinematic nomenclature of the parallel bellow actuator: (a) schematic representation of a PBA continuum segment; (b) illustration of the center lines of each bellow.

As illustrated in Fig. I.4, the kinematic problem of parallel bellow actuators aims to capture the relationship between the endoscope viewing tip pose (position and orientation) and the joint space variables (the electromechanically driven syringe positions). The endoscope viewing tip pose is denoted as $[\mathbf{x}, \mathbf{R}]$, termed *task space*, while the syringes actuation piston positions is denoted as $\mathbf{q}$, called the *joint space*. The task space and the joint space are

respectively defined as:

$$\mathbf{x} = [p_x, p_y, p_z]^{\mathrm{T}}, \quad \mathbf{R} = {}^{b}\mathbf{R}_{t},\ \mathbf{R} \in \mathrm{SO}(3) \tag{I.1}$$

$$\mathbf{q} = [q_1, q_2, q_3]^{\mathrm{T}} \tag{I.2}$$

To bridge the task space and the joint space of continuum robots, another kinematic space - *configuration space* - is usually defined (as [42]). In the case of the proposed continuum endoscope, the configuration space variable, $\boldsymbol{\psi}$, refers to the geometric variables that characterize the shape of the continuum segment - the bending angle at the tip θ_l, the angle of the plane in which the segment bends δ, and the imaginary central backbone length of the robot l, defined as:

$$\boldsymbol{\psi} \triangleq [\theta_l, \delta, l]^{\mathrm{T}} \tag{I.3}$$

With all three kinematic spaces defined, the goal is to derive the two kinematic mappings - the mapping from task space to configuration space, and the mapping from configuration space to joint space:

$$\mathcal{F}_{\mathrm{T}}: \quad \boldsymbol{\psi} \rightarrowtail [\mathbf{x}, \mathbf{R}] \qquad \text{config. to task space} \tag{I.4}$$

$$\mathcal{F}_{\mathrm{q}}: \quad \boldsymbol{\psi} \rightarrowtail \mathbf{q} \qquad \text{config. to joint space} \tag{I.5}$$

Further, the instantaneous kinematics can be derived after obtaining the above kinematic mappings. Using $\dot{\boldsymbol{\xi}} \in \mathbb{R}^6$ to denote the twist (velocity and angular velocity) of the endoscope viewing tip, the instantaneous kinematics aims to obtain the two Jacobian matrices as:

$$\dot{\boldsymbol{\xi}} \triangleq \mathbf{J}_{\xi\psi}\, \dot{\boldsymbol{\psi}}, \quad \mathbf{J}_{\xi\psi} \in \mathbb{R}^{6\times 3} \tag{I.6}$$

$$\dot{\mathbf{q}} \triangleq \mathbf{J}_{\mathbf{q}\psi}\, \dot{\boldsymbol{\psi}}, \quad \mathbf{J}_{\mathbf{q}\psi} \in \mathbb{R}^{3\times 3} \tag{I.7}$$

where the Jacobian $\mathbf{J}_{\xi\psi}$ propagates the configuration space speeds to the velocity and angular velocity of the viewing tip, while the Jacobian $\mathbf{J}_{\mathbf{q}\psi}$ relates the configuration space speeds to the joint velocities.

Kinematic mapping $\mathcal{F}_T$ - configuration to task

The tip position vector $\mathbf{x}$ and the rotation matrix $\mathbf{R}$ representing the tip orientation can be expressed as in (I.8-

I.10), resulting in the configuration to task space mapping $\mathcal{F}_{\mathrm{T}}$ as:

$$\mathbf{x} = e^{-\delta\,[\mathbf{z}^{\wedge}]} \int_0^l [c_{\theta(s)}, 0, s_{\theta(s)}]^{\mathrm{T}}\,\mathrm{d}s, \quad l \in [L_{\min}, L_{\max}] \tag{I.8}$$

$$\mathbf{R} = e^{-\delta\,[\mathbf{z}^{\wedge}]}\, e^{(\theta_0-\theta_l)\,[\mathbf{y}^{\wedge}]}\, e^{\delta\,[\mathbf{z}^{\wedge}]} \tag{I.9}$$

$$\theta(s) = \theta_0 + \int_0^s \kappa(\tau)\mathrm{d}\tau, \quad s \in [0, l] \tag{I.10}$$

where $c_{(\cdot)}$ and $s_{(\cdot)}$ denote the cosine and sine functions, and $[\mathbf{a}^{\wedge}]$ represents a skew symmetric matrix generated from vector $\mathbf{a}$, the variable s denotes the curve length along the imaginary primary backbone, and θ_0 is the initial bending angle ($\theta_0 = \frac{\pi}{2}$). The parameters $L_{\min}$ and $L_{\max}$ denote the maximum and minimum lengths of the imaginary central backbone of the continuum endoscope. Using the constant curvature assumption, the curvature function $\kappa(s)$ and the bending angle $\theta(s)$ become:

$$\kappa(s) = (\theta_l - \theta_0)/l, \quad \theta(s) = \theta_0 + \frac{s}{l}(\theta_l - \theta_0) = \theta(s, l) \tag{I.11}$$

To derive the configuration to task space geometric Jacobian, we partition the Jacobian matrix $\mathbf{J}_{\xi\psi}$ into column matrices as the following.

$$\begin{bmatrix} \dot{\mathbf{x}} \\ \boldsymbol{\omega} \end{bmatrix} \triangleq \underbrace{\left[\begin{array}{c:c:c} \mathbf{J}_{v\theta} & \mathbf{J}_{v\delta} & \mathbf{J}_{vl} \\ \hdashline \mathbf{J}_{\omega\theta} & \mathbf{J}_{\omega\delta} & \mathbf{J}_{\omega l} \end{array}\right]}_{\triangleq \mathbf{J}_{\xi\psi}} \begin{bmatrix} \dot{\theta}_l \\ \dot{\delta} \\ \dot{l} \end{bmatrix} \tag{I.12}$$

Then the problem becomes finding the expressions for the six column Jacobians $\mathbf{J}_{v\theta}, \mathbf{J}_{\omega\theta}, \mathbf{J}_{v\delta}, \mathbf{J}_{\omega\delta}, \mathbf{J}_{vl}, \mathbf{J}_{\omega l}$. The derivations for the first four column Jacobians can be found in [42], where the authors discussed the kinematics of a multi-segment multi-backbone continuum robot. The last two, $\mathbf{J}_{vl}$ and $\mathbf{J}_{\omega l}$, can be derived directly from (I.8) using Leibniz integral rule, which was also briefly discussed in [63]. Solving all the expressions, the configuration to task

space geometric Jacobian arrives as:

$$\mathbf{J}_{v\theta} = l \begin{bmatrix} c_\delta \chi_1 \\ -s_\delta \chi_1 \\ \chi_2 \end{bmatrix}, \mathbf{J}_{v\delta} = l \begin{bmatrix} -s_\delta \chi_3 \\ -c_\delta \chi_3 \\ 0 \end{bmatrix}, \mathbf{J}_{vl} = \begin{bmatrix} c_\delta \chi_3 \\ -s_\delta \chi_3 \\ -\frac{c_\theta}{\theta_l - \theta_0} \end{bmatrix} \tag{I.13}$$

$$\mathbf{J}_{\omega\theta} = \begin{bmatrix} -s_\delta \\ -c_\delta \\ 0 \end{bmatrix}, \mathbf{J}_{\omega\delta} = \begin{bmatrix} c_\delta \, c_{\theta_l} \\ -s_\delta \, c_{\theta_l} \\ -1 + s_{\theta_l} \end{bmatrix}, \mathbf{J}_{\omega l} = \begin{bmatrix} 0 \\ 0 \\ 0 \end{bmatrix} \tag{I.14}$$

$$\chi_1 = \frac{(\theta_l - \theta_0)c_{\theta_l} - s_{\theta_l} + 1}{(\theta_l - \theta_0)^2} \tag{I.15}$$

$$\chi_2 = \frac{(\theta_l - \theta_0)s_{\theta_l} + c_{\theta_l}}{(\theta_l - \theta_0)^2}, \quad \chi_3 = \frac{s_{\theta_l} - 1}{\theta_l - \theta_0} \tag{I.16}$$

Kinematic mapping $\mathcal{F}_q$ - configuration to joint

The configuration to joint space mapping $\mathcal{F}_\mathrm{q}$ solves the joint displacements $\mathbf{q}$, given the bending shape and length configuration ψ. This problem was solved in details in [40]: (i) by projecting the secondary backbone onto the bending plane, the problem of solving the secondary backbone length becomes solving the projected length; (ii) the projected length is obtained by calculating the radius difference - the projection of the constant apart distance, Δ_i.

$$q_i = l_i - l_0, \qquad l_i = l + \Delta_i(\theta_l - \theta_0) \tag{I.17}$$

$$\Delta_i = r\cos\sigma_i, \qquad \sigma_i = \delta + \tfrac{2\pi}{3}(i-1), \quad i \in [1,3] \tag{I.18}$$

where the parameter l_0 represents the bellow length at rest (i.e. internal pressure = atmospheric one), the variable l represents the current length of the imaginary central backbone, and the calculated expression l_i represents the length of the i^{th} bellow center line. The term r is the distance in the base plane between bellow center line and imaginary primary backbone.

The configuration to joint space Jacobian is obtained by differentiating (I.17), which was also derived in [42] in

details.

$$\mathbf{J}_{\mathbf{q}\psi} = \begin{bmatrix} rc_{\sigma_1} & -r(\theta_l - \theta_0)s_{\sigma_1} & 1 \\ rc_{\sigma_2} & -r(\theta_l - \theta_0)s_{\sigma_2} & 1 \\ rc_{\sigma_3} & -r(\theta_l - \theta_0)s_{\sigma_3} & 1 \end{bmatrix} \tag{I.19}$$

I.2.2.1 Actuation compensation

Existing works [52, 56] applied direct control on pressurization (i.e. set a pressure reference using fluid pumps). In the proposed method, a simplified and inexpensive displacement-controlled piston mechanism is used to provide the pressure change indirectly. Due to the nature of the pneumatic transmission as well as the expendability of the rubber bellow, losses occur in the transmission lines. As a result, the transmission losses (extension) need to be modeled and compensated.

Among research works on multi-backbone continuum robots, methods for modeling and compensating the extensions in the transmission lines were explored in [64, 65]. Inspired by these works, and as a preliminary investigation of the characteristic of the proposed transmission design, we discuss the actuation compensation problem in this section.

Motion transmission modeling - extension and backlash

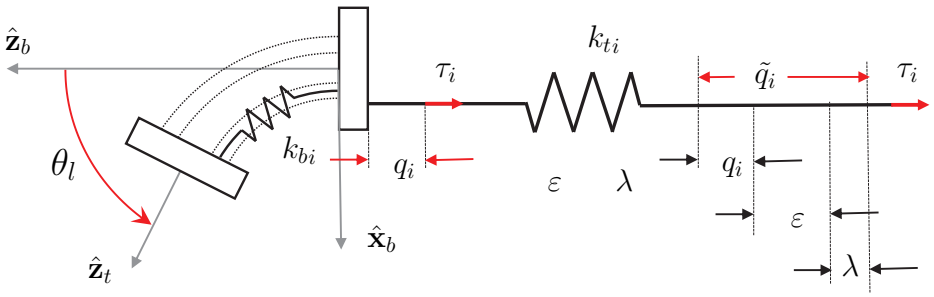

Figure I.5: The schematic of motion transmission modeling with the extension ε and the backlash λ.

The variable q_i denotes the idealized displacement provided at the base of the i^{th} bellow, which is consistent with the modeled displacement in (I.17). The variable $\widetilde{q}_i$ is then used to represent the displacement provided at the actuator, which will suffer from the transmission losses. In this work we formulate the modeling and compensation

of transmission losses to include two terms: an actuation extension ε and an backlash uncertainties λ .

$$\widetilde{\mathbf{q}} \triangleq [\widetilde{q}_1, \widetilde{q}_2, \widetilde{q}_3]^{\mathrm{T}}, \quad \widetilde{\mathbf{q}} = \mathbf{q} + \boldsymbol{\varepsilon} + \boldsymbol{\lambda}, \quad \boldsymbol{\varepsilon}, \boldsymbol{\lambda} \in \mathbb{R}^3 \tag{I.20}$$

To model the extension ε, we assume: 1) only constant longitudinal stiffness and effective cross-section area exist along each individual bellow length and its effective cross-sectional area is constant, i.e. linear relationship between bellow length variation q_i and its pressure p_i, and 2) friction is negligible through the transmission line.

Using the first assumption, with a nominal longitudinal stiffness value k_{b_i} for each bellow, the actuation forces $\boldsymbol{\tau}$ at the base of each bellow can be expressed as:

$$\boldsymbol{\tau} \triangleq [\tau_1, \tau_2, \tau_3]^{\mathrm{T}}, \quad \tau_i = p_i A = k_{bi}(l_i - l_0) \tag{I.21}$$

Considering the fluid compression as a spring having a stiffness of k_{t_i} and using the second assumption of frictionless transmission, we have $\tau_i = k_{ti}\varepsilon_i$. Equating it and (I.21), we then have:

$$\boldsymbol{\varepsilon} = [\varepsilon_1, \varepsilon_2, \varepsilon_3]^{\mathrm{T}}, \quad \varepsilon_i = k_{\varepsilon_i} q_i, \quad k_{\varepsilon_i} \triangleq (k_{b_i}/k_{t_i}) \tag{I.22}$$

where a dimensionless gain k_{ε_i} is introduced for simplicity, and defined as the ratio between the bellow and transmission stiffness.

The backlash uncertainty $\boldsymbol{\lambda}$ is modeled as directional constant biases, similar to [65]:

$$\boldsymbol{\lambda} = [\lambda_1, \lambda_2, \lambda_3]^{\mathrm{T}}, \quad \lambda_i = k_{\lambda\, i}\, \mathrm{sgn}(\dot{\mathrm{q}}_{\mathrm{i}}) \tag{I.23}$$

where, in practise, the gain k_{λ_i} may vary in positive and negative directions and the $\mathrm{sng}(\cdot)$ function may be replaced a tangent hyperbolic function.

Combining (I.22) and (I.23), the expression of compensated joint displacements can be rewritten as:

$$\widetilde{\mathbf{q}} = \mathbf{q} + \mathbf{K}_{\varepsilon}\, \mathbf{q} + \mathbf{K}_{\lambda}\, \mathrm{sgn}(\dot{\mathbf{q}}) \quad \mathbf{K}_{\varepsilon}, \mathbf{K}_{\lambda} \in \mathbb{R}^{3\times 3} \tag{I.24}$$

$$\mathbf{K}_{\varepsilon} = \mathrm{diag}\,(\mathbf{k}_{\varepsilon})\,,\ \mathbf{K}_{\lambda} = \mathrm{diag}\,(\mathbf{k}_{\lambda})\,,\ \mathbf{k}_{\varepsilon}, \mathbf{k}_{\lambda} \in \mathbb{R}^3 \tag{I.25}$$

I.2.2.2 Actuation compensation parameter estimation

Equation (I.24) can be rewritten toward the parameter estimation as:

$$\widetilde{\mathbf{q}} = \mathbf{q} + \mathrm{diag}(\mathbf{q})\,\mathbf{k}_\varepsilon + \mathrm{diag}(\mathrm{sgn}(\dot{\mathbf{q}}))\,\mathbf{k}_\lambda \tag{I.26}$$

Combining the two unknown parameter vectors as one, the estimation becomes a linear least-squared problem as:

$$\mathbf{k}_x \triangleq \left[(\mathbf{k}_\varepsilon)^{\mathrm{T}}, (\mathbf{k}_\lambda)^{\mathrm{T}}\right]^{\mathrm{T}}, \quad \mathbf{k}_x \in \mathbb{R}^{6\times 1} \tag{I.27}$$

$$\mathbf{A}\,\mathbf{k}_x \;=\; \mathbf{b}, \quad \mathbf{A} \in \mathbb{R}^{3\times 6},\, \mathbf{b} \in \mathbb{R}^{3\times 1} \tag{I.28}$$

$$\mathbf{A}(\mathbf{q}, \dot{\mathbf{q}}) = \left[\begin{array}{c:c} \mathrm{diag}(\mathbf{q}) & \mathrm{diag}\left(\mathrm{sign}(\dot{\mathbf{q}})\right) \end{array}\right], \; \mathbf{b} = \widetilde{\mathbf{q}} - \mathbf{q} \tag{I.29}$$

where $\mathbf{A}$ and $\mathbf{b}$ are the measurement matrix and vector, respectively. For the case of N measurements, we have:

$$\mathbf{\Gamma}\,\mathbf{k}_x \;=\; \mathbf{B}, \quad \mathbf{\Gamma} \in \mathbb{R}^{3N\times 6},\, \mathbf{B} \in \mathbb{R}^{3N\times 1} \tag{I.30}$$

$$\mathbf{\Gamma} \triangleq \begin{bmatrix} \mathbf{A}_1 \\ \vdots \\ \mathbf{A}_N \end{bmatrix}, \quad \mathbf{B} \triangleq \begin{bmatrix} \mathbf{b}_1 \\ \vdots \\ \mathbf{b}_N \end{bmatrix} \tag{I.31}$$

$$\mathbf{A}_j = \mathbf{A}_j(\mathbf{q}_j, \dot{\mathbf{q}}_j), \quad \mathbf{b}_j = \widetilde{\mathbf{q}}_j - \mathbf{q}_j \tag{I.32}$$

where $\mathbf{\Gamma}$ and $\mathbf{B}$ are the aggregated measurement matrix and vector, and the subscript $_j$ indicates the j^{th} measurement.

A weighted linear least-squared solution can be obtained as the following:

$$\mathbf{k}_{\mathrm{sol}} = (\mathbf{\Gamma}^{\mathrm{T}}\mathbf{W}\mathbf{\Gamma})^{-1}\,\mathbf{\Gamma}^{\mathrm{T}}\,\mathbf{W}\,\mathbf{B} \tag{I.33}$$

$$\mathbf{W} = \mathrm{diag}\left(\left[(\mathbf{w}_1)^{\mathrm{T}}, \ldots, (\mathbf{w}_{\mathrm{N}})^{\mathrm{T}}\right]^{\mathrm{T}}\right), \; \mathbf{W} \in \mathbb{R}^{3\mathrm{N}\times 3\mathrm{N}} \tag{I.34}$$

where the weight matrix $\mathbf{W}$ is given by the weight vector $\mathbf{w}_j$ of each measurement. Finally, a linear least-squared estimation is used in an iterative method.

Algorithm 1 Iterative Linear Least-squared Estimation

Require: $\mathscr{D}\{(\widetilde{\mathbf{q}}_j, \widetilde{\boldsymbol{\psi}}_j), j = 1, \ldots, N\}$; $\mathbf{k}_{x_0}$, $\beta > 0$

1: **START** Initialize: $\mathbf{k}_i \leftarrow \mathbf{k}_{x_0}$, $\mathbf{k}_0 \leftarrow 0$

2: **while** $\frac{\|\mathbf{k}_i - \mathbf{k}_{i-1}\|}{\|\mathbf{k}_{i-1}\|} \geq \beta$ **do**

3: Apply $\mathbf{k}_i$ to control, and collect new data $\mathscr{D}\{(\widetilde{\mathbf{q}}_j, \widetilde{\boldsymbol{\psi}}_j)$.

4: Update $\mathbf{k}_{i+1}$ using $\mathscr{D}\{(\widetilde{\mathbf{q}}_j, \widetilde{\boldsymbol{\psi}}_j)$:

$$\mathbf{k}_{i+1} = (\boldsymbol{\Gamma}^{\mathrm{T}} \mathbf{W} \boldsymbol{\Gamma})^{-1} \boldsymbol{\Gamma}^{\mathrm{T}} \mathbf{W} \mathbf{B}$$

Ensure: $\mathbf{k}^* \leftarrow \mathbf{k}_i$

I.2.3 Experimental validation

As previously described, the actuation compensation method is parameterized by the extension $\mathbf{k}_\varepsilon$ and the backlash $\mathbf{k}_\lambda$. In this subsection, the estimation method to identify these parameters is validated experimentally and the estimation result reported. Equation (I.33) was used in an iterative fashion, where an estimate of $\mathbf{k}$ is updated given a new experimental data set. Such input data sets were collected for each iteration, and each set consisted of 120 robot state measurements that were recorded while the robot continuum segment was commanded to bend in 12 different directions and 5 bending angles in each direction. A relative convergence criterion was used for the estimation of the compensation gain, where a threshold of 2% was applied.

The optimal estimated $\mathbf{k}^* = [\mathbf{k}_\varepsilon^{\mathrm{T}}, \mathbf{k}_\lambda^{\mathrm{T}}]^{\mathrm{T}}$ was found to be $[2.22, 2.53, 2.21, 0.87, 0.92, 0.81]^{\mathrm{T}}$. Figure I.6 shows the results and reflects the difference between the control of the endoscopic viewing tip with and without compensation. Both of Fig. I.6 (a) and (b) show significant improvements on bending angle accuracy compared to the scenario with no compensation, reducing the root mean squared errors (RMSEs) from 36.96° to 7.76° (shown in (b)). Further comparing closely (a) and (b), adding the backlash compensation helped to create a slightly smaller boundary of uncertainty and the overall RMSE was also slightly improved, from 8.04° from the case with only extension compensation, to 7.76° after backlash compensation added. Figure I.6(c) shows conversion of the $\mathbf{k}_\varepsilon$ that occurred within 7 iterations.

I.2.4 Conclusions

The modeling of the disposable endoscope has been adapted from multi-backbone continuum models. The proposed actuation compensation reduced the error between desired and actual bending angle from a root mean squared error (RMSE) of 37.0°, when no compensation is provided, to a RMSE of 7.8°. While the accuracy improvement was significant, the absolute accuracy, RMSE of 7.8°, may not be sufficient for automatic or semi-automatic endo-

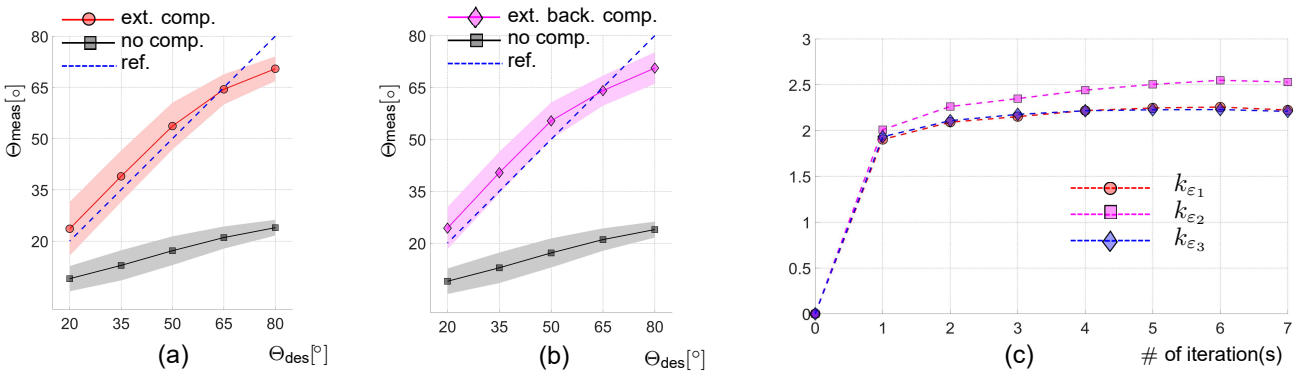

Figure I.6: Results of actuation compensation: (a) the comparison between extension compensation and no compensation; (b) the comparison between extension and backlash compensation, and no compensation; (c) convergence of the iterative compensation gain parameters estimation. In (a) and (b), the notation of angle Θ_x is used to denote the complementary angle to θ_x. The lines represent the mean values and the shading areas highlight the boundaries determined by ($\pm$ standard deviation).

scopic procedures. However, the framework put forth in this work has a big potential and through increasing the sophistication of the current model, the accuracy when compensating for extension and backlash errors is expected to improve. For example, constant curvature shape assumption can be improved through the use of a modal representation [62]. In addition, the extension compensation gains are constant and independent of the robot configuration (bending direction and bending angle). With the addition of a configuration dependent term, e.g. $\mathbf{k}_x = \mathbf{k}_x(\psi)$ or $\mathbf{k}_x = \mathbf{k}_x(\mathbf{q})$, compensation accuracy may be more accurate across the entire work space.

To facilitate closed loop control of the device, an inexpensive 9 DOFs inertial measurement unit (accelerometer, gyroscope, magnetometer) may be incorporated into the moving tip, delivering orientation information relative to an inertial reference frame. The EM trackers used in the experimental validation are too expensive for integration into a clinical version of the device.

In terms of clinical relevance, the pneumatically actuated robotic endoscope currently has a purely diagnostic use and is actuated via an inexpensive actuation system that was designed and prototyped using displacement-controlled pistons. This device aims to tackle the current limitation that endoscopic practice is facing in scars resources settings.

In fact, screening of the UGI tract is still an expensive and invasive procedure. Traditional endoscopes require trained personnel and can only be performed in dedicated unit. A robotic diagnostic disposable endoscope provide a cheaper, and easier to use solution that can help with routine operation as well as mass screening programs [66].

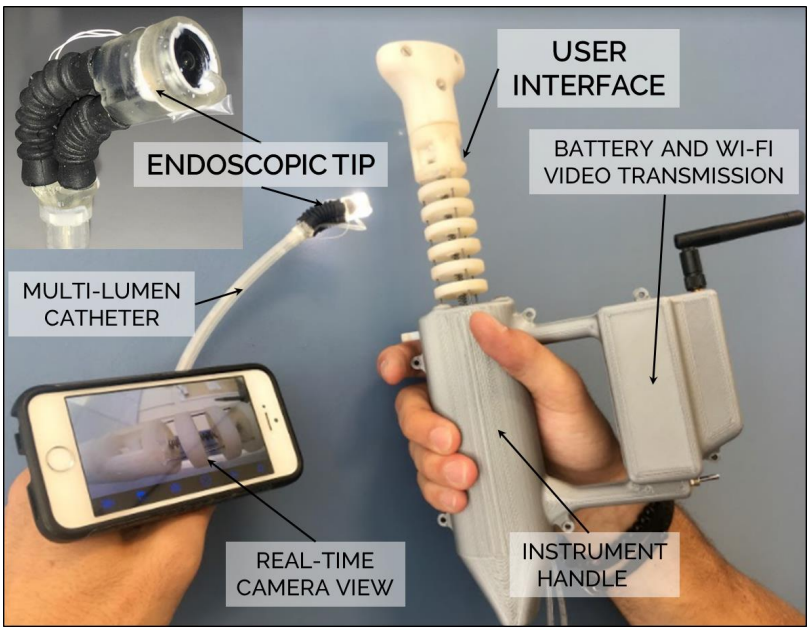

Figure I.7: The dual-continuum endoscope: Two continuum structures (i.e. a multi-backbone user interface and a pneumatically actuated endoscopic tip) are connected via syringes integrated in the instrument handle and a multi-lumen catheter.

I.3 Dual-continuum design approach for intuitive upper gastrointestinal endoscopy

In this Section a device that combines the benefits of multi-backbone continuum structures and soft robotic devices is proposed as intuitive, low-cost, and portable endoscopes for visual investigation of the UGI tract. The presented purely mechanical dual-continuum endoscope (DCE) is a stand-alone system, that possesses high intuitiveness of operation and low fabrication costs. Referring to Figure I.7, this design approach consists of a multi-backbone joystick (user interface – UI) coupled with an endoscopic tip (ET) oriented via a three-element PBA. Connection between the two units is obtained via passive pneumatic components only (i.e. syringes integrated in the instrument handle).

I.3.1 Principle of operation: dual-continuum endoscope

Referring to Figure I.8, the DCE is composed of a mechanically actuated UI and a pneumatically actuated ET that are coupled through a mechanical-pneumatic interface.

The UI is a snake-like multi-backbone continuum joystick adapted from [40, 41] to allow for extensibility in a longitudinal DOF in addition to the two DOF of bending in any direction. Superelastic Nitinol rods are used as primary and secondary backbones of the UI. The primary backbone is centrally located and surrounded by three radially equidistant secondary backbones whose extension/retraction corresponds with the three DOF of the UI. As

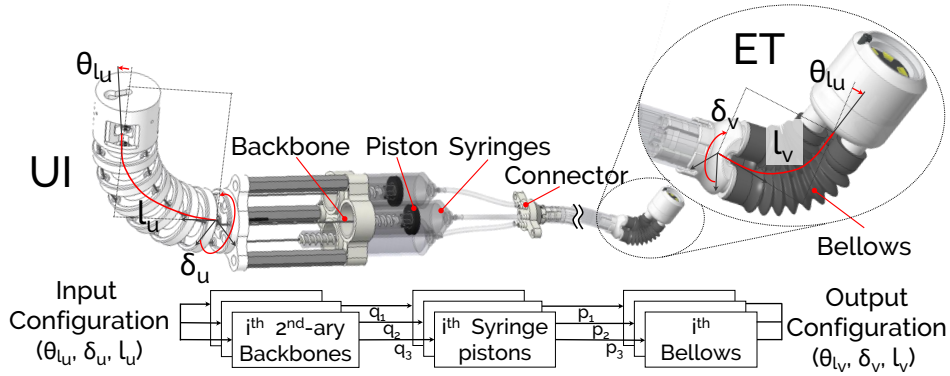

Figure I.8: Functional components of the dual-continuum endoscope implementing a direct user-to-task mapping: the user interface (UI) is mechanically coupled to the endoscopic tip (ET).

the user manipulates the UI, changing its configuration (i.e. bending angle θ_{l_u}, the angle of the plane in which the UI bends δ_u, and the nominal length l_u), the superelastic backbones extend or retract at their distal ends, which are connected directly to three syringe pistons. The motion of each syringe piston results in pressurization/depressurization of one of the three pneumatic lines coupled via a multi-lumen catheter to a corresponding bellow in the PBA. Pressure changes extend/retract the PBA bellows, resulting in a specific output configuration of the ET (i.e. θ_{l_v}, δ_v, and l_v). Coupling kinematically-similar structures in the UI and ET has the advantage of providing a direct user-to-task mapping through pure mechanical actuation, allowing for highly intuitive operation upon proper tip response tuning.

I.3.2 Kinematic modeling toward direct user-to-task mapping

As detailed in Section I.2.2.1, we adapted the modeling method from existing multi-backbone continuum robots such that the two mappings defined for describing the UI, also hold for the ET with differences only in fabrication parameters (e.g. r_v identifies distance between bellows center line and manipulator virtual main axis, and l_v is the length of the imaginary center line of the three bellows; l_{v_0} represents the length of the bellows at neutral pressure). In this Section the subscript $_u$ and $_v$ relate to the continuum user interface and the endoscopic tip, respectively.

From a fabrication standpoint, the continuum joystick joint variable $\mathbf{q_u}$ represents the mating component of the two structures, i.e. the piston displacement. This displacement, which is responsible for bellows' extension $\mathbf{q_v}$, may suffer from transmission losses due to the compressibility of air, used as transmission medium, and the compliance of the bellows.

An updated schematic representation of the actuation losses and compensation methods is shown in Figure I.9. To model the configuration mapping, the piston extension term ε is only considered such that equation I.35 reduces

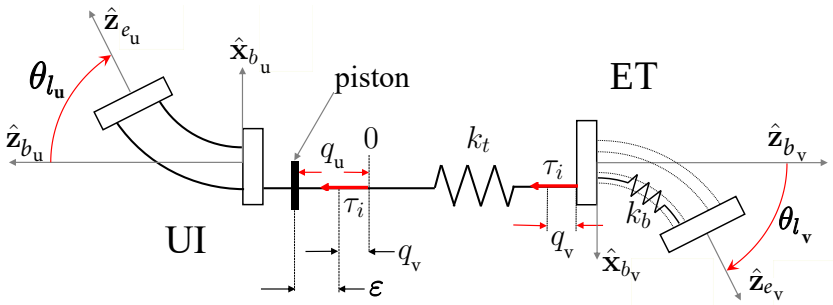

Figure I.9: Schematic representation of motion transmission modeling associated with a piston extension ε.

to:

$$\mathbf{q_u} = \varepsilon + \mathbf{q_v} \quad \varepsilon, \in \mathbb{R}^3 \tag{I.35}$$

Following the same assumption presented in Section I.2.2.1, equation I.35 can be rewritten as:

$$\mathbf{q_u} = (1 + \mathbf{K}_\varepsilon)\mathbf{q_v} \tag{I.36}$$

where $\mathbf{K}_\varepsilon$ is a 3x3 diagonal motion compensation matrix accounting for motion losses in each pneumatic line:

$$\mathbf{K}_\varepsilon, \in \mathbb{R}^{3\times3},\ \mathbf{K}_\varepsilon = \mathrm{diag}\,(\mathbf{k}_\varepsilon)\,,\ \mathbf{k}_\varepsilon \in \mathbb{R}^3 \tag{I.37}$$

The addition of a motion compensation matrix allows the description of the ET configuration as a function of the piston displacement $\mathbf{q_u}$.

I.3.3 UI-ET compensated coupling

To achieve a target mapping of 1:1 between the UI-ET coupling that includes compensation for motion loss, equation (I.36) can be reformulated to contain the tunable design parameters r_u and r_v. This involves combining equations (I.17) and (I.18), considered for both the UI and ET, with equation (I.36) under the assumption that: 1) following ET deployment in the stomach, the third DOF in elongation is not available nor necessary (i.e. $l_u = l_{u_0}$ and $l_v = l_{v_0}$); 2) the bending angles and bending directions for UI and ET are equal (i.e. $\theta_{l_u} = \theta_{l_v}$ and $\delta_u = \delta_v$). Hence, the design variables may be related as:

$$\mathbf{r_u} = (1 + \mathbf{K}_\varepsilon)\mathbf{r_v} \tag{I.38}$$

The gain $\mathbf{K}_\varepsilon$ may be experimentally determined for a given set of DCE components/design parameters. To minimize the dimension of the ET and couple the UI accordingly, we must maintain a constant kinematic radius (i.e. $\mathbf{r_u} = r_u [1\,1\,1]^{\mathrm{T}}$ and $\mathbf{r_v} = r_v [1\,1\,1]^{\mathrm{T}}$). Thus, the compensation matrix may be simplified to a single scalar gain $\bar{k}_\varepsilon$ determined by averaging elements (diag $(\mathbf{k}_{\varepsilon_i})$), therefore obtaining:

$$r_u = (1 + \bar{k}_\varepsilon) r_v \tag{I.39}$$

Equation (I.40) is fundamental for achieving a 1:1 mapping between UI and ET, while compensating for motion losses and taking into consideration the physical constraints of the target device (e.g. syringe spacing, ET maximum dimension and UI ergonomics).

I.3.4 Calibration - experimental determination of $\mathbf{K}_\varepsilon$

Our eventual design goal is to obtain a UI that comfortably fits within the user's hand while offering a direct user-to-task mapping between the UI and ET. With the bellows size fixed for the ET due to space considerations, the open design parameters included the kinematic radius r_u of the UI and the syringe sizes. Small syringes would require a larger stroke and have smaller compressible volume, while large syringes require a smaller stroke, but use more compressible volume and therefore exhibit larger motion transmission losses. However, the motion compensation gains for each syringe depend on the compressible volume and the displaced volume - therefore it is not immediately clear what syringe size should be chosen *a-priori*. With the stroke size directly related to r_u, it was important to experimentally explore different syringe sizes to discern which would correspond with a feasible design.

An improved version of the experimental platform presented in Section I.2.1.1 was used to evaluate the expected transmission motion compensation matrices $\mathbf{K}_{\varepsilon_i}, i = 1,2,3$ corresponding with syringe volumes 3 ml, 5 ml and 10 ml. The average motion compensation gain $\bar{k}_\varepsilon$ was determined and used to set the desired secondary backbone radius r_u in accordance with equation (I.40). The most appropriate syringe size was subsequently selected based on an r_u that allowed for parallel alignment of the syringes and delivered a UI size that could comfortably fit within the users hand.

The improvements of the experimental platform consist of: improved system resolution at the piston level thanks to the use of lead screw ($0.99\mu m/$step); the ability to continuously (5kHz) acquire the EVT end effector pose; addition of potentiometers that were used to define initial testing (home) positions, to improve repeatability of the experiments.

For each of the syringe sizes, $\mathbf{K}_\varepsilon$ was determined through combining ET pose and piston position data into an iterative linear least-squares problem. Bending angle data were continuously acquired ($\Theta_{des} \in [10^\circ, 70^\circ]$) on 5 equally spaced bending planes ($\delta_{des} \in [0^\circ, 120^\circ]$ - due to symmetry in the workspace). Starting from an uncompensated scenario (i.e. $\mathbf{k}_\varepsilon = [0\,0\,0]^T$), the compensation terms were calculated off-line using an iterative least squares method as previously proposed.

In Figure I.10, the measured bending angle (Θ_{meas}) as a function of desired bending angle (Θ_{des}) is shown for the three syringe sizes investigated.

As visible from the plots, all bending motions present hysteresis and a non-linear behavior once Θ_{meas} exceeds 65° (for the compensated scenario). The former is a common effect of pneumatic actuation, and is thought not to compromise the use of the device; the latter instead is a consequence of the radial expansion (ballooning) of the bellows, i.e. violation of linear relationship between pressure and elongation. Also evident in Figure I.10 are small ripples in the acquired data. These deviations were found to be random in nature for piston location and between repeats. Therefore, are assumed to be caused by friction dynamics occurring at the piston-syringe wall interface under slow linear motion, and backlash of the mechanical drive train.

Table I.1 shows the vectors of motion compensation $\mathbf{k}_\varepsilon$ as first mentioned in equation (I.37) along with the scalar gains $\bar{k}_\varepsilon$, which were defined as the mean of $\mathbf{k}_\varepsilon$ for each syringe size. The corresponding UI kinematic radii r_u predicted for direct mechanical-pneumatic mapping, determined without compensation (i.e. r_u=r_v) and with compensation (equation (I.40)), are also reported. For each syringe size assessed using motion loss compensation under robotic control, implemented according to equation (I.36), a large reduction in bending angle Root Mean Squared Errors (RMSE_{θ_l}) was evident. For example, the RMSE_{θ_l} were less than 7° for each tested syringe size after motion loss actuation compensation was implemented.

These results were used to inform the final choice of design parameters for the fabricated UI. In particular, we designed a UI using 5ml syringes and a kinematic radius $r_u = 10.25mm$ to obtain a suitable UI continuum segment dimension and feasible parallel arrangement of the syringes within a small UI body. The UI was hence fabricated and assembled with the selected syringe size to validate the direct user-to-task mapping when direct mechanical-pneumatic coupling is used.

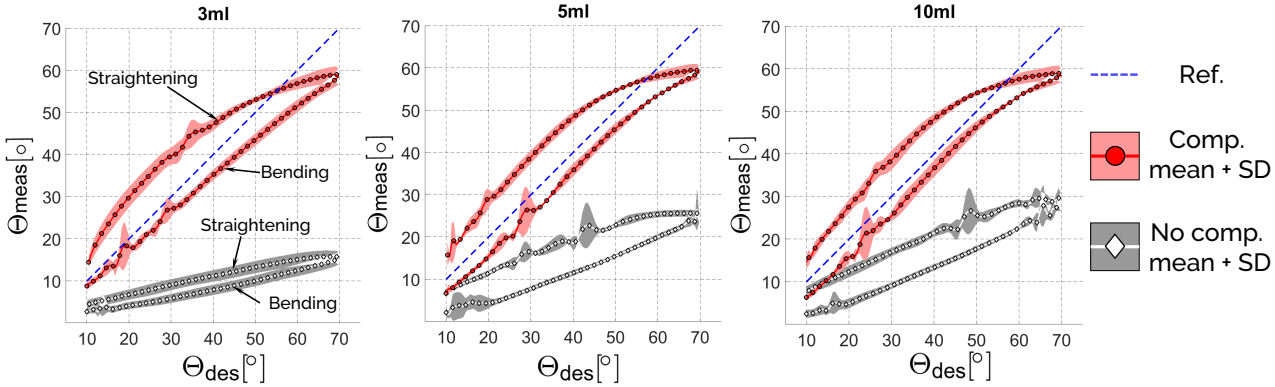

Figure I.10: Measured bending angle (Θ_{meas}) as a function of desired bending angle (Θ_{des}) before (diamonds-grey) and after (circles-red) compensation for the three syringes sizes investigated.

Table I.1: Motion loss compensation gains and required UI kinematic radius for direct coupling for three syringe sizes.

Syringe size	3 [ml]	5 [ml]	10 [ml]
Syringe diameter	8.6 [mm]	12.0 [mm]	14.6 [mm]
$\mathbf{k}_\varepsilon$	$\begin{bmatrix} 2.97 \\ 3.19 \\ 3.62 \end{bmatrix}$	$\begin{bmatrix} 1.46 \\ 1.55 \\ 1.59 \end{bmatrix}$	$\begin{bmatrix} 1.35 \\ 1.42 \\ 1.34 \end{bmatrix}$
$\bar{k}_\varepsilon$	3.26	1.53	1.37
Not Compensated coupling: $r_u = r_v, q_u = q_v$, i.e. $\mathbf{K}_\varepsilon = \mathbf{0}$			
r_u[mm]	4.04	4.04	4.04
RMSE$_{\theta_l}$[°]	33.36	27.13	25.18
Compensated coupling: $r_u > r_v$, i.e. $\mathbf{K}_\varepsilon = diag(\bar{k}_\varepsilon)$			
r_u [mm]	17.21	10.25	9.57
RMSE$_{\theta_l}$ [°]	6.97	6.40	6.30

I.3.5 Fabrication and integration of the UI with the ET

The UI syringes were connected to the PBA of the ET using a multi-lumen silicone catheter. The device was designed to facilitate detachable coupling between the two, and was therefore split into disposable and reusable assemblies.

The ET, along with the multi-lumen catheter, comes in direct contact with the patient's bodily fluid, while the syringes used for actuation may come into contact indirectly, e.g. in the case of perforation/tear in the catheter/bellows. Hence these items must be disposed of to prevent costs associated with device reprocessing.

The entire UI can instead be reused due to a modular coupling between the backbone free ends and the syringe pistons. As represented in Figure I.7, the UI is embedded in a 3D printed case that contains reusable electronics. Specifically, a rechargeable battery (Ni-MH 2A 12V 1800MAH) and Wi-Fi transmission module (WishRing Wifi, Amazon.com). The former is used to remove the need for an external power supply, and the latter to provide users with a real-time camera view on a smartphone or a tablet.

I.3.5.1 Disposable parts (ET and Catheter)

In additions to the components previously described in Section I.2.1 and represented in Figure I.2, it is worth adding other two pieces of information.

First, the flexural strength of the catheter was eastimated to be $< 34.83\ Ncm^2$ (given a material Young modulus of 7.1 MPa, and assuming a solid rod of 5 mm in diameter), which is 6 times less than a traditional FE.

Second, at the proximal end of the catheter, a second plastic adapter provides access to each catheter's lumen. The three bellows pressure lines are directly connected via PVC tubing to three syringes. The syringe centers are aligned with a 120° angular offset to the secondary backbone circumference (i.e. r_u). Access to the irrigation and insufflation channels at the proximal end is provided via tubing and standard luer-lock adapters for connection to external water and air supply.

I.3.5.2 Reusable parts (UI and Case)

The UI components, shown in Figure I.11, are:

A. 3D printed spacer discs (six in total).

B. A ⌀1.5 mm Nitinol wire as primary backbone located in the disc center.

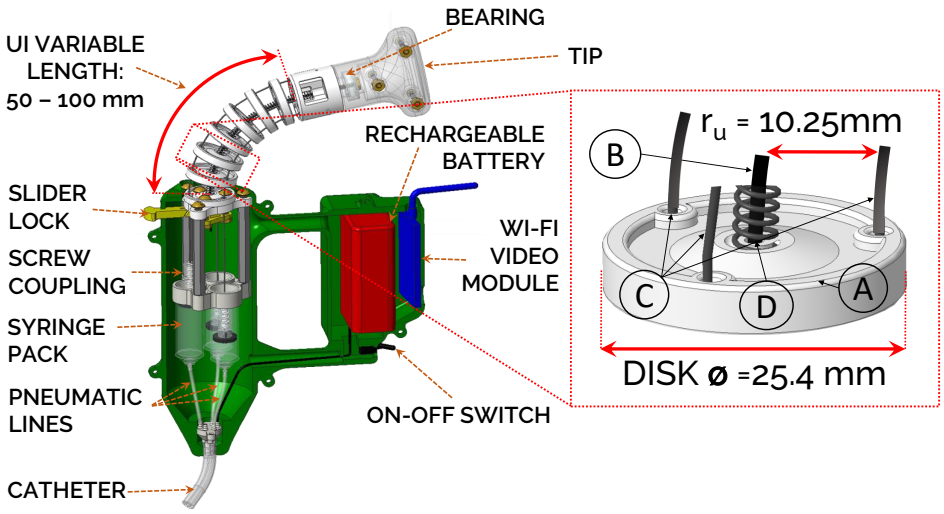

Figure I.11: The reusable user interface (UI) showing key components, and the backbones with spacer disk (inset).

C. Three ⌀1 mm Nitinol secondary backbone wires equispaced (120° offset) around the circumference of a circle of radius r_u.

D. A 3.33 lbs/in compression spring (compressed length = 48% of initial length) used as inter-discs spacer (7*mm*).

The kinematic model we used assumes no twisting of the UI. To minimize this in the physical device, we used a ball bearing (B623B1E, IGUS, Cologne, Germany) to connect the UI tip to the multi-backbone continuum structure, as shown in Figure I.11. Alternative mechanical solutions such as adding additional secondary backbones not used for actuation can be implemented to improve structural resistance to torques acting on the main axis.

A custom 3D printed screw coupling provides adjustable connection between the UI and the syringe pistons. Each screw, glued to the corresponding secondary backbone distal end, fits a nut on a custom piston, providing ease of separation between disposable and reusable parts.

A stiffer ET is useful during introduction via the esophagus and when navigating through shrinkages and complex anatomies. To lock the ET into a stiffer configuration (i.e. PBA completely depressurised), a slider lock mechanism (see Figure I.11) was integrated into the base of the UI. As the user pulls the UI to depressurise the PBA and a certain extension is reached, the slider lock mechanism can be engaged, locking the primary backbone.

I.3.5.3 Fabrication cost

Table II.5 summarizes both fabrication cost for a single functional prototype and the unit cost considering mass production (MP). MP costs were estimated by discussing the DCE design with a medical device manufacturer

Table I.2: Prototyping and estimated mass production cost of the DCE.

Disposable components		
Part	Prot. Cost [USD]	Est. MP Cost [USD]
Plastic parts	0.54	**0.25**
Multi-lumen catheter	3.71	**0.30**
Wiring and connector	2.15	**1.00**
Bellows	13.74	**3.00**
Tubing	0.33	**0.20**
Syringes and pistons	1.78	**1.00**
Camera and LEDs	17.02	**4.00**
Total cost for disposable parts	39.27	**9.75**
Reusable components		
Part	Prot. Cost [USD]	Est. MP Cost [USD]
Plastic parts	41.43	**5.00**
Screw-bolts, standoffs	9.54	**5.00**
Nitinol wires and spring	24.95	**3.00**
Bearing	2.31	**1.00**
Rechargeable batteries	32.22	**5.00**
Wi-Fi video transm.	39.96	**10.00**
Total cost for reusable parts	150.41	**29.00**

(Medical Murray, North Barrington, IL, USA). The two categories are subdivided into disposable and reusable parts. From Table II.5, it is evident that even at the prototyping stage, the cost associated with the disposable parts of the device are 76% less than of the reprocessing cost identified in [18]. With increased economy through mass production, the cost can be further reduced down to $<$30 USD for the reusable equipment and $<$10 USD for disposable.

For both the prototype and MP scenarios, the camera represents the most significant cost. Although it is economically feasible to consider this as disposable, the design may be adjusted to accommodate a reusable camera, as implemented in [25, 67], thus further cutting disposable costs to $<$6 USD.

I.3.6 Experimental validation

I.3.6.1 Experimental assessment of user-to-task mapping

To verify that we achieved the intended direct mapping through the selected design parameters, we placed the UI and ET next to each other on a dedicated bench test setup shown Figure I.12. Both end effectors of the UI and ET were magnetically tracked when the UI was moved by hand. The end effector positions and orientations ($[\mathbf{p_u}, \mathbf{R_u}]$, and $[\mathbf{p_v}, \mathbf{R_v}]$ respectively) were obtained relative to their own respective base frames $\{b_u\}$ and $\{b_v\}$. Similarly to the experimental set up used in I.3.4, a 3D printed part having comparable weight (1.25 g) to the device camera was used

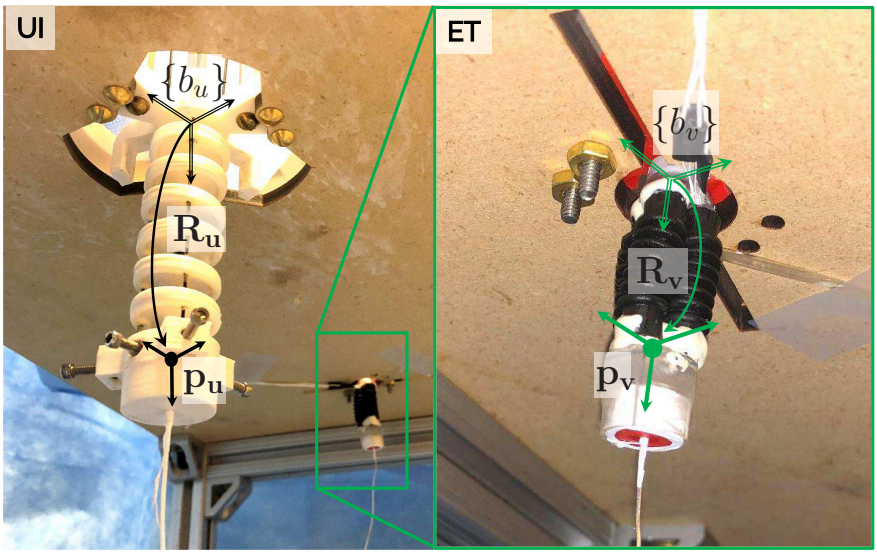

Figure I.12: Experimental set up for validation of user-to-task mapping. UI and ET were tracked while the UI was manipulated by hand within the input workspace. A zoomed view of the ET is reported on the right.

for EM sensor placement at the ET end effector. The UI and ET were initially aligned in a parallel configuration ($\{b_u\} = \{b_v\}$). Starting from an initial alignment pose, the user manually bent the UI across a range of bending angles Θ_u ($\Theta_u \in [0°, 80°]$) in different planes δ_u ($\delta_u \in [0°, 360°]$).

The imposed bending angles (Θ_u) and bending planes (δ_u) of the UI and the corresponding response of the ET (Θ_v and δ_v) are shown in Figure I.13, with the bending angles (Θ) and bending planes (δ) being shown in Figure I.13(a) and (b), respectively. The RMSE $\pm$ Standard Deviation (SD) for bending angle Θ tracking was $5.35° \pm 3.17°$ within the linear regime ($\Theta_u \in [0°, 65°]$), while the RMSE $\pm$ SD on δ tracking was $15.87° \pm 15.57°$ (values calculated once an imposed bending angle ($\theta_{l_u} > 15°$) was established, due to numerical imprecision in calculating both δ_u and δ_v when the manipulators are straight).

These errors may be attributed to a number of factors including the mechanical tolerances within the assembled device, the hysteresis within the ET pressure-bending profile, and the necessity to average the compensation parameters into a single value for the UI design.

I.3.7 Pre-clinical assessment

A feasibility *in-vivo* trial comparing the DCE with flexible endoscopy was performed by an expert gastroenterologist (>3,000 lifetime EGDs) in a 40-kg Yorkshire female pig at Vanderbilt University, with the assistance and collaboration of a specially trained medical team, in accordance with all ethical considerations and regulation related to animal experiments (IACUC Approval No. $M1700034-00$). The results were discussed in [5] and are

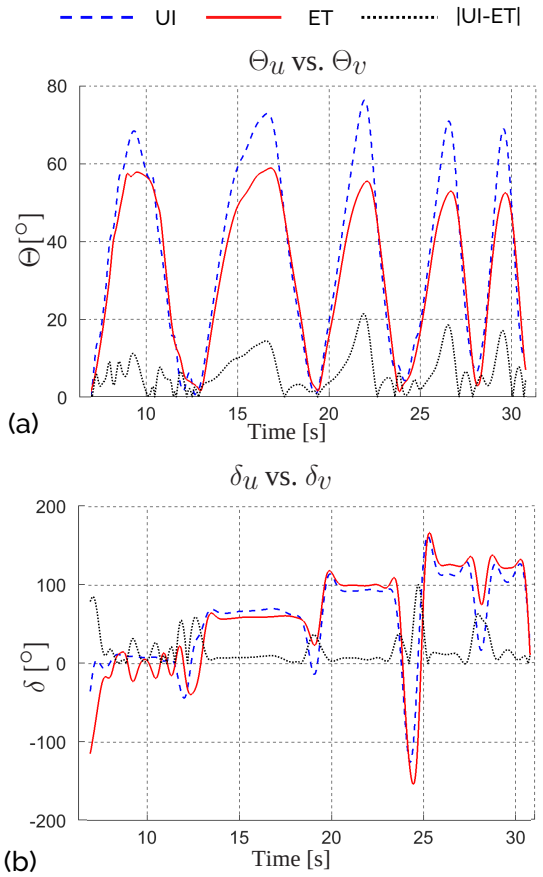

Figure I.13: Results from experimental validation of direct user-to-task mapping. Continuous (red) lines are related to the ET, dashed (blue) lines are related to the UI, dotted (black) lines represent the instantaneous error between the ET and UI motions. (a): Θ_v tracking Θ_u; (b) δ_v tracking δ_u.

briefly summarised here. The user was able to perform a diagnostic EGD, and visualize the main landmarks in 180s using conventional FE and 208s with the DCE. There were no adverse events, evidence of endoscopic or gross trauma, perforation, or histologic abnormality at necropsy. To further evaluate the efficacy and usability of the DCE

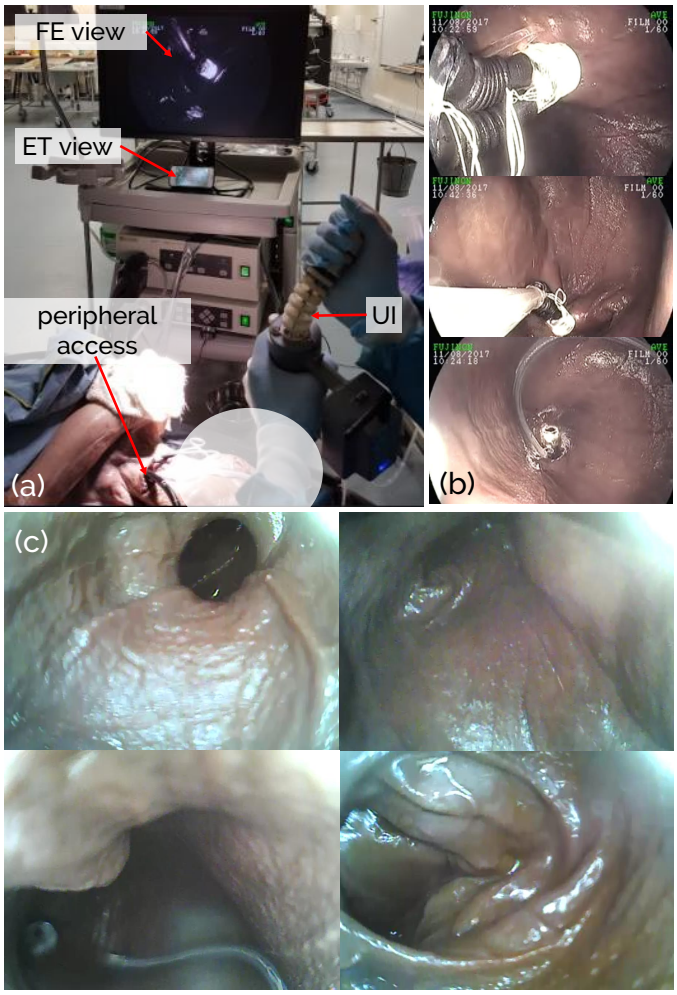

Figure I.14: Pre-clinical assessment of the DCE in a cadaver trial. (a) Experimental set up; (b) Motion of the DCE observed from the conventional FE; (c) Camera view from the DCE showing clockwise: gastro-esophageal junction, AGC and ALC, duodenum, and view during retroflexion.

in visualizing the human anatomy, an EGD procedure was performed in a soft-tissue cadaver. The procedure was executed by an expert gastroenterologist (>3,000 lifetime EGDs) in a female Thiel-embalmed cadaver (48 kg) in the facilities of the School of Medicine at the University of Leeds, with the assistance and collaboration of a specially trained medical team and in accordance with all ethical considerations and regulation related to cadaver experiments (Approval No. $AEC-2017-080617$).

First, the anatomy was explored using a conventional FE (GIF-H290, Olympus Corp., Tokyo, Japan), and then the DCE was introduced. The cadaver presented a very small anatomy of the pharynx that prevented navigation through the throat for both devices. To obviate this problem, the throat was bypassed with a peripheral access incision performed in the neck to feed both devices in the proximal section of the esophagus (Figure I.14(a)). The ET camera view was transmitted directly via WiFi to a smartphone (iPhone, Apple, USA) and a tablet (iPad, Apple, USA) located on the endoscopic tower.

The DCE successfully reached the stomach in a stiffened configuration (i.e. bellows depressurised and slider lock on, Section I.3.5.2), visualized the key landmarks, and explored the very first section of the duodenum. Retroflexion (a technique where the camera of the endoscope is turned back onto itself to view the area around the insertion tube) was then performed in the gastric body. This maneuver was accomplished with the DCE through a technique similar to that used in conventional endoscopy - the endoscope tip was maximally deflected and the insertion tube was then gently advanced to bank-it off the compliant gastric wall. Figure I.14(b) shows the ET motion inside the anatomy as visualized by the conventional FE, while Figure I.14(c) shows a view of the DCE. Illumination and image quality of the DCE were considered acceptable by the gastroenterologist. In terms of procedure duration, the visualization of the anatomical key landmarks was performed with the conventional FE in 20s, while 51s were necessary with the DCE.

The expert user highly appreciated the light weight (675 g) and the portability (on-board battery and light source, and Wi-Fi video transmission to smartphone or tablet) of the DCE. The possibility to stream the endoscopic video to any smart device was noted as a benefit for widespread adoption of this technology outside the endoscopy suite. Time to set up the DCE from taking it out of its case to starting the procedure was below 3 minutes.

I.3.8 Conclusions

An innovative UGI endoscope that is easy to set up, easy to use, extremely portable, and that can to be manufactured at an ultra-low cost has been presented.

Through coupling of a multi-backbone UI and a soft PBA-based ET, we presented a device that leverages the precision of multi-backbone continuum manipulators, with the compliance of soft robots. The adaptation of standard associated modeling techniques demonstrated a method for realizing device designs that can deliver user-to-task mapping at a tunable scale.

With respect to the requirements described in Section I.1.1, the device at the current prototyping stage: has a

linear relationship between output bending angle of the ET (Θ_v) and input bending angle of the UI (Θ_u) from 0° to 65°, on bending planes δ_v spanning from 0° to 360°; minimizes the risk of perforation thanks to an estimated flexural strength six times lower than conventional FE; has an ET 13.5 mm in diameter, and a 7 mm insertion tube; allows for the visualization of relevant anatomical landmarks within a time comparable with conventional EGD; achieves bending error ($5.35° \pm 3.17°$) lower than what has been reported for clinically used FE [27]; is extremely easy to transport and set up; is composed of a disposable endoscopic probe with material cost below 10 USD.

The main limitations of DCE compared to FE are a limited workspace, and a larger diameter. These are due to the use of off-the-shelf rubber bellows that were chosen to assess the feasibility of the design, and develop analytical models for characterizing user-to-task mappings. Future design iterations will use custom bellows with smaller diameter and larger range of motion to decrease the ET diameter, and hence enable unsedated procedures, and facilitate retroflexion. Further studies will be conducted to quantify the achievable range of the user-to-task mapping to match the steering preference of end users.

The current version of the device is solely for diagnostic procedures, i.e. it does not have a therapeutic channel. Limited stiffness of the current PBA does not allow passing a tool to the tip; however, the insufflation channel at the base of the PBA can be modified for delivering tools. Through coupling a modified version of the device with a steerable biopsy tool, such as the one proposed by [68], or with more specific tool such as a cryogenic balloon for treatment of Barrett's esophagus [69], the DCE may be enabled to perform biopsy or therapeutic procedures.

The proposed DCE has the potential to provide untrained personnel (e.g. GP, ER/ICU clinicians) with a simple to use, low-cost, and hygienic endoscopic solution for triage and diagnosis of upper GI tract pathology in non-traditional endoscopic settings. Furthermore, the analytical modeling techniques presented may facilitate adaptation of future DCE designs that could improve usability, functionality and further reduce costs.

Through adoption of DCE based platforms, the issues associated with costly, non-intuitive conventional FEs may be mitigated, and, by moving to a disposable endoscope, cross contamination may be prevented. In combination, the benefits of DCEs may allow for more widespread implementation of UGI tract screening, ultimately reducing mortality associated with disease of the UGI tract.

I.4 Evaluation of the dual-continuum endoscope for assessment of the UGI tract

The DCE presented in Section I.3 was modified to overcome some of the limitations that arose from the pre-clinical assessment (Subsection I.3.7). The device in particular has been design such that: 1) the reusable electronics

(rechargeable battery and Wi-Fi video streaming modules) could be reused and connect to the scope via an USB connector; 2) a pivoting pad as been added as end effector of the continuum joystick to provide a one hand operation. By doing so, the improved DCE is fully disposable, weighs a total of 0.56 Kg, and when produced en-masse has an inclusive cost of approximately 32 USD per endoscope.

Similar to a conventional endoscope, the device is operated using one hand to steer the tip and the other for inserting or removing the insertion tube/catheter. The device is designed for ambidextrous use (i.e. it is not hand specific) as the handle is maneuvered about the pivoting pad secured against the operators body (Figure I.15).

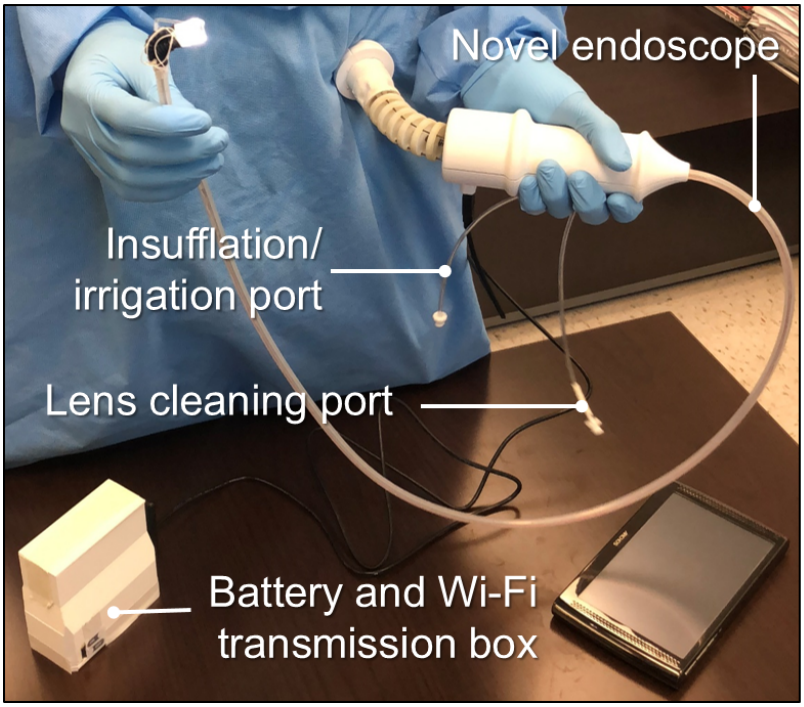

Figure I.15: Improved DCE with dedicated battery and Wi-Fi transmission box, and pivoting pad for single hand actuation of the endoscopic viewing tip.

I.4.1 Aim of the study

The aim of this study is two-fold. First, we aim to assess if our novel platform provides enough range of motion at the distal tip to allow for successful visualization key gastric landmarks. Second, we aim to quantify and compare ease of use and intuitiveness of the novel endoscope with a conventional upper endoscope.

I.4.2 Methods

I.4.2.1 Phantom

A human upper gastrointestinal tract phantom was created from the CT scan images of a 70 Kg adult male patient. The images were extracted and reconstructed to serve as a 3D printed mold (Ultimaker Inc, Geldermalsen, Netherlands). Silicone was then placed in layers to construct the phantom (EcoFlex 00-30, SmoothOn, Macungie, PA, USA) (Figure I.16). LEDs were placed at key anatomic locations within the molded stomach as it was constructed. The same six anatomic landmarks reported in Section I.1.1, were affixed: gastroesophageal (GEJ) junction, fundus, body greater curvature (BGC), body lesser curvature (BLC), antrum greater curvature (AGC), and antrum lower curvature (ALC).

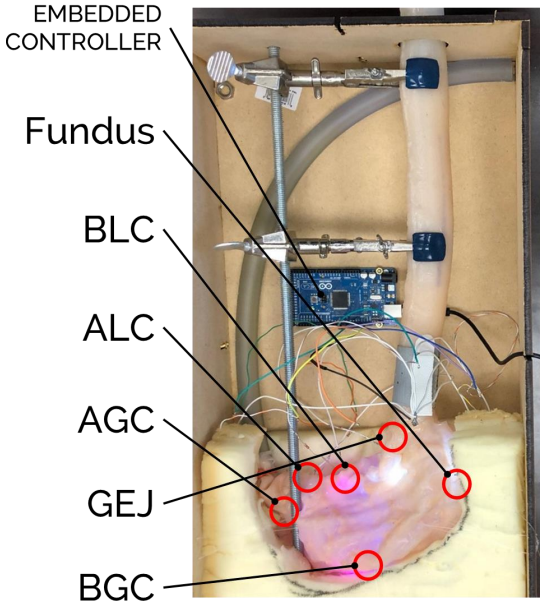

Figure I.16: The human upper gastrointestinal tract phantom with LED marked anatomic landmarks.

LED activation was controlled by an embedded micro controller (Arduino Mega 2560, Turin, Italy) connected by USB to a dedicated data-recording computer (OptiPlex 390, Dell, Round Rock, TX, USA). The phantom was encased in a wood support structure to prevent participant visualization of the landmarks or phantom externally.

I.4.2.2 Study design

A total of 15 participants were selected to perform endoscopy in the UGI tract phantom. The participants were selected from our tertiary care medical center by email and face-to-face encounters. 5 Gastroenterology attendings (>1000 lifetime conventional upper endoscopies), 5 Gastroenterology fellows (postgraduate year (PGY) 4-6), and 5 novices (PGY 1 internal medicine residents who had never handled an endoscope) were enrolled.

Each user performed endoscopic examination of the GEJ and stomach with the conventional upper endoscope (Karl Storz, Tuttlingen, Germany) and with the novel disposable endoscope. Each participant performed a total of 10 examinations using both devices in random order (conventional n=5; novel n=5; 1:1 fashion). Examination was performed in a gastroenterology outpatient clinic examination room (Figure I.17). Each user was given a 1-

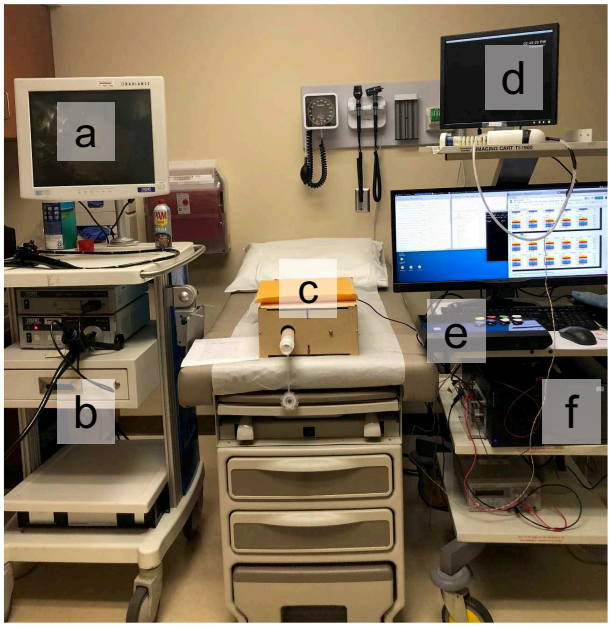

Figure I.17: Trial set-up. Conventional endoscope monitor (a) and tower (b); upper gastrointestinal tract phantom (c); novel endoscope and monitor (d); LED anatomic landmark controller (e); computer for recording of trial data (f).

minute practice period with the conventional endoscope and novel endoscope the first time it was selected. The practice period was performed outside of the phantom. After this minute, the user introduced the endoscope into the phantom and positioned the tip in the distal esophagus, 5 cm from the GE junction. The anatomic landmark LEDs were then illuminated and the user was tasked with identification of all 6 gastric landmarks (Figure I.18).

Successful identification of the landmark was denoted by en-face visualization with the endoscope and verbally

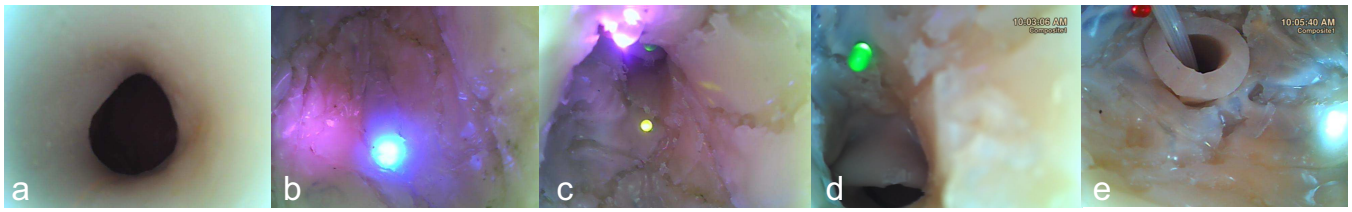

Figure I.18: Images of the upper gastrointestinal tract phantom taken with the novel disposable endoscope. The distal esophagus (a) and gastric landmarks (LED anatomic markers; (b) body greater curvature (blue); (c) antrum greater curvature (yellow) and body lesser curvature (purple); (d) antrum lesser curvature (green); (e) GE junction (red) and fundus (white)) are visualized.

communicating the color of the LED to the study staff. The time of identification was recorded and the LED was turned off. The exam was considered complete when all 6 landmarks were successfully identified or if a time >10 minutes was reached. Figure I.20 summarizes the protocol adopted for the study.

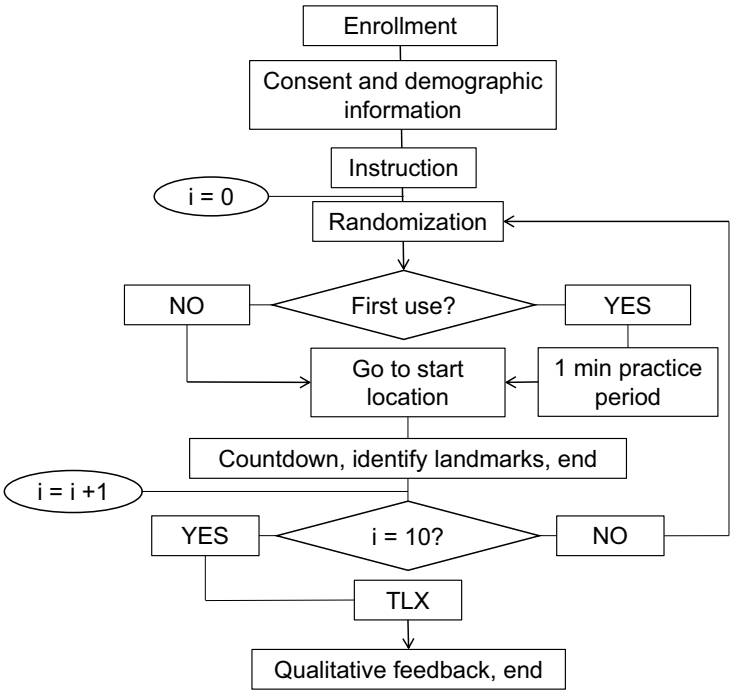

Figure I.19: Flow diagram for the trial. Each user performed a total of 10 endoscopies (conventional, n=5; novel, n=5) on the human phantom for identification of the gastric landmarks.

After all 10 exams were performed; each participant completed a validated assessment instrument for each device used (NASA Task Load Index v1.0; NASA Ames Research Center, Moffett Field, CA, USA) and assigned an overall satisfaction score [70]. The NASA Task Load Index (TLX) is composed of 6 scales: mental demand (how mentally demanding was the task), physical demand (how physically demanding was the task), temporal demand

(how hurried or rushed was the pace of the task), performance (how successful were you in accomplishing what you were asked to do), effort (how hard did you have to work to accomplish your level of performance), and frustration (how insecure, discouraged, irritated, stressed, and annoyed were you). All subscales range from 0 (very low) to 100 (very high) with the exception of performance, which ranges from 0 (perfect) to 100 (failure). Each user was then asked for non-structured qualitative feedback using open-ended questions (what are your thoughts about the endoscope (traditional; novel)?).

I.4.2.3 Study outcome and statistical analysis

The main outcome measure was successful identification of the 6 gastric landmarks. Secondary outcomes included overall time to perform gastric landmark visualization, ease of use (TLX), and user comments. The time to visualize each individual gastric landmark and the order in which they were visualized was also recorded.

To detect differences in visualization time between devices within each user group, a paired t test was used. To detect differences in visualization time for a given device between the three user groups, an ANOVA test was used. To compare the variation in total time between experienced users of conventional endoscopes when using the novel endoscope, prior data indicated a standard deviation of the difference in time of 10 seconds. With 10 experienced users (5 fellows, 5 attendings) performing 5 trials each with the novel endoscope, we had 90% power to detect a 5 second difference in time. To compare the increase in time when novices used the novel endoscope, prior data indicated a standard deviation of the difference in time of 14 seconds. With 10 experienced users and 5 novices performing 5 trials each with the novel endoscope, we had 90% power to detect a 6 second difference. All calculations assumed the probability of type I error of 5%.

Lower, median, and upper quartile ranges were calculated for continuous variables. A variable Z was utilized to assess for differences in the order of landmark visualization for each trial. Z was defined as:

$$Z = \frac{\sum_m (\sum_n (C_{mn} - \overline{C})(N_{mn} - \overline{N})}{\sqrt{(\sum_m \sum_n (C_{mn} - \overline{C})^2)(\sum_m \sum_n (N_{mn} - \overline{N})^2)}} \tag{I.40}$$

Where m and n are the rows and columns of the landmarks-order matrices, respectively; C identifies the landmarks-visualization order matrix when using the conventional endoscope; N the landmarks-visualization order matrix using the novel endoscope; and the $\overline{C}$ and $\overline{N}$ are the mean of all values of C and N, respectively.

After completion of the trial, participants completed a validated TLX assessment instrument with overall satis-

Table I.3: Participants in the study.

Participants	Women	Age	Lifetime # of endoscopic procedure	Left hand dominance
Novice (n =5)	0 (0)	29 ± 2.28	0 ± 0	0 (0)
Fellow (n = 5)	1 (20)	31 ± 0.89	900 ± 300	0 (0)
Attending (n =5)	2 (40)	41 ± 2.22	4800 ± 3000	1 (20)
All combined (n = 15)	3 (20)	33 ± 5.67	1900 ± 2700	1 (6.66)

faction score for each endoscope (conventional; novel) and provided non-structured qualitative feedback by face-to-face interview. All data was securely recorded using Research Electronic Data Capture (REDCap) (Nashville, TN, USA) [71]. This study was approved by the medical center Institutional Review Board (IRB) before initiation of data collection (IRB#171660).

I.4.3 Results

5 attendings (mean number of lifetime procedures: 4800±3000), 5 fellows (900±300), and 5 novices (0±0) completed the trial. 3 of the participants were women (20%) and 1 of the participants was left hand dominant (7%) (Table I.3).

All participants (n=15) successfully identified all 6 gastric landmarks with the conventional endoscope and with the novel endoscope for each trial (100%; n=900). The time to landmark identification for all groups combined was shorter with the conventional endoscope when compared to the novel endoscope (18.07 v. 28.16 seconds; $p<0.01$). The total time for all trials was normally distributed and there was no difference in time to landmark identification for the novice group when comparing the conventional endoscope to the novel endoscope (27.99 v. 38.09 seconds; p=0.16). For attendings and fellows, use of the conventional endoscope was quicker when compared to use of the novel endoscope (13.82 v. 26.27 seconds; $p<0.01$ and 17.7 v. 23.37 seconds; p=0.01 respectively) (Table I.4).

The maximum and minimum time to visualize all landmarks was 113.07 and 5.04 seconds with the conventional endoscope and 126.33 and 9.42 seconds with the novel endoscope. Using the conventional endoscope, attendings were quickest when compared to the other groups ($p<0.01$). When the novel endoscope was used, there was no difference in time between user groups (attending, fellow, novice) (p=0.094). Figure 7 shows the lower, median, and upper quartile of both total time and specific landmark identification time for each group of participants using both devices (conventional and novel endoscope).

Table I.4: Total time to complete the task of identifying all six gastric landmarks. Medians [Q1, Q3].

Participants	**Conventional**	**Novel**	*p-value*
Novice (n =5)	27.99 s [18.07; 43.19]	38.09 s [14.17; 64.87	p = 0.16
Fellow (n = 5)	17.7 s [11.74; 20.94]	23.37 s [18.45; 35.1]	p = 0.01
Attending (n =5)	13.82 s [9.62; 19.56]	26.27 s [17.72; 41.7]	p <0.01
All combined (n = 15)	18.07 s [11.60; 25.59]	28.16 s [17.62; 52.48]	p <0.01

By recording (Table I.5) the order in which each landmark was identified with a specific device (conventional/novel), we verified that the path taken to visualize the landmarks was consistent for each user group using the two devices (novel and conventional endoscope)verifying that the order of landmark visualization did not influence the results (Z = 0.948 (attendings), 0.923 (fellows), 0.907 (novices)).

All participants operated the novel endoscope successfully despite having no prior experience or formal training outside of the one-minute practice period. The novel endoscope was reliable throughout each trial without video, electric, or mechanical failure. Participants reported both low mental demand and low physical demand (Table I.6).

Five users specifically noted intuitiveness of the novel endoscope (2 novices), ease of use (1 fellow), or easy to learn (1 novice, 1 attending) in their user feedback comments (Table I.7). Three users specifically expressed satisfaction with the novel platforms low weight (1 novice, 1 attending, 1 fellow) and ergonomics (1 fellow) when compared to the conventional endoscope.

I.4.4 Conclusions

The novel upper endoscope (previously defined as DCE) was easy to maneuver, intuitive to use, and successful at visualizing key landmarks in the stomach in a timely manner regardless of users having no prior experience with the novel endoscope. While fellows and attendings had longer mean times with the novel endoscope when compared to the conventional endoscope, their times remained within a clinically acceptable range (difference of approximately 10 seconds). This finding is likely due to the fellows and attendings experience and comfort in using the conventional endoscopeas the mechanism of the novel endoscope is inherently different from a conventional endoscope (i.e. no need for insertion tube torque) or thumb wheel manipulation of Bowden cables.

In the novice group, without any endoscopy experience, there was no such difference, suggesting that unbiased users performed with essentially equal efficiency with both devices. Additionally, both experienced endoscopists and

Table I.5: Order of gastric landmark visualization for participants with each endoscope. The rows correspond to the order in which the landmark was visualized (i.e. firstrow one; secondrow two; etc.). The columns correspond to the anatomic structure that was visualized (body greater curvature (BGC); antrum greater curvature (ACG); body lesser curvature (BLC); antrum lesser curvature (ALC); GE junction (GEJ); fundus (F)).

Novice (Novel Endoscope)					
BGC	*AGC*	*BLC*	*ALC*	*GEJ*	*F*
21	1	0	0	3	0
4	9	0	0	11	1
0	13	6	3	3	0
0	2	16	6	1	0
0	0	2	10	4	9
0	0	1	6	3	15

Novice (Conventional Endoscope)					
BGC	*AGC*	*BLC*	*ALC*	*GEJ*	*F*
22	0	1	0	2	0
2	5	4	1	13	0
0	18	5	0	1	1
1	1	9	11	0	3
0	0	4	10	4	7
0	1	2	3	5	14

Fellow (Novel Endoscope)					
BGC	*AGC*	*BLC*	*ALC*	*GEJ*	*F*
21	0	0	0	4	0
4	7	1	0	12	1
0	10	9	3	1	2
0	6	11	7	0	1
0	2	3	11	2	7
0	0	1	4	6	14

Fellow (Conventional Endoscope)					
BGC	*AGC*	*BLC*	*ALC*	*GEJ*	*F*
21	0	1	0	3	0
0	9	2	1	10	3
3	8	13	0	1	0
1	5	6	8	4	1
0	2	1	11	3	8
0	1	2	5	4	13

Fellow (Novel Endoscope)					
BGC	*AGC*	*BLC*	*ALC*	*GEJ*	*F*
22	0	0	0	3	0
1	11	0	0	12	1
2	7	9	5	1	1
0	6	13	2	1	3
0	1	2	11	5	6
0	0	1	7	3	14

Fellow (Conventional Endoscope)					
BGC	*AGC*	*BLC*	*ALC*	*GEJ*	*F*
21	0	1	0	3	0
1	6	3	1	12	2
2	6	11	3	2	1
0	9	9	2	3	2
1	3	1	11	2	7
0	1	0	8	3	13

Table I.6: The NASA Task Load Index (TLX) subscale scores for the novel endoscope and conventional endoscopy by participant group. All subscales range from 0 (very low) to 100 (very high) with the exception of performance, which ranges from 0 (perfect) to 100 (failure). Median [Q1, Q3].

Subscale	**Novice (n =5)**		**Fellow (n = 5)**		**Attending (n=5)**	
	Novel	Conventional	Novel	Conventional	Novel	Conventional
Mental Demand	32 [7, 62]	41 [23, 66]	45 [9, 51]	3 [1,12]	27 [11, 51]	13 [5,18]
Physical Demand	17 [5,49]	42 [10,82]	20 [14, 47]	10 [2, 29]	13 [10, 41]	12 [5, 20]
Temporal Demand	50 [35,56]	63 [54, 76]	19 [12, 45]	4 [1, 35]	33 [13, 51]	23 [8, 35]
Performance	25 [10, 34]	37 [16, 59]	33 [26, 36]	20 [5,51]	47 [7,59]	17 [7, 33]
Effort	50 [22, 73]	67 [33,80]	25 [9, 55]	20 [6, 36]	34 [20, 58]	7 [5, 13]
Frustration	74 [24, 76]	51 [48, 71]	16 [13, 55]	9 [1, 32]	42 [12, 54]	8 [3, 14]

Table I.7: Representative participant interview comments. Conventional flexible endoscope (CFE); Novel flexible endoscope (NFE).

Participant	n	Comment(s)
Novice	*1*	Retroflexion of CFE helps. Orientation of NFE requires a first use to then be mapped intuitively.
	2	Like the NFE because of lightweight, control. NFE is easier to learn tool. Would be helpful for teaching family doctors, interns.
	3	CFE handle is too big, but has good control (rigid and tip stiffness). NFE easy to control in open space; when in contact with tissue, motion can be hindered.NFE operation felt natural. The body anchoring pad slipped on occasion.
	4	CFE is more rigid than the NFE. NFE felt more intuitive with good image quality.
	5	CFE is frustrating and not intuitive. Retroflexion with the CFE is a two-hand task. The NFE is more intuitive.
Fellow	*1*	No feedback provided
	2	The NFE was easy to use and figure out
	3	The NFE anchoring point sometimes slipped.
	4	The CFE was hard on your back and shoulder. Small fingered people use two hands for certain tasks with the CFE-only one is needed with the NFE. EGD can be performed with mainly with swing motion of the hand holding the scope and no torque using CFE. NFE use and ergonomics line up well with this operation method. The NFE is light weight.
	5	Low rigidity of the NFE body.
Attendings	*1*	There was limited stiffness of the NFE body and therefore less ability to torque it.
	2	Unable to torque the NFE easily.
	3	The NFE had good response at the tip with small angulation to bend.
	4	I'm very use to the CFE. There was a small learning curve with the NFE. The NFE is less heavy.
	5	No feedback provided.

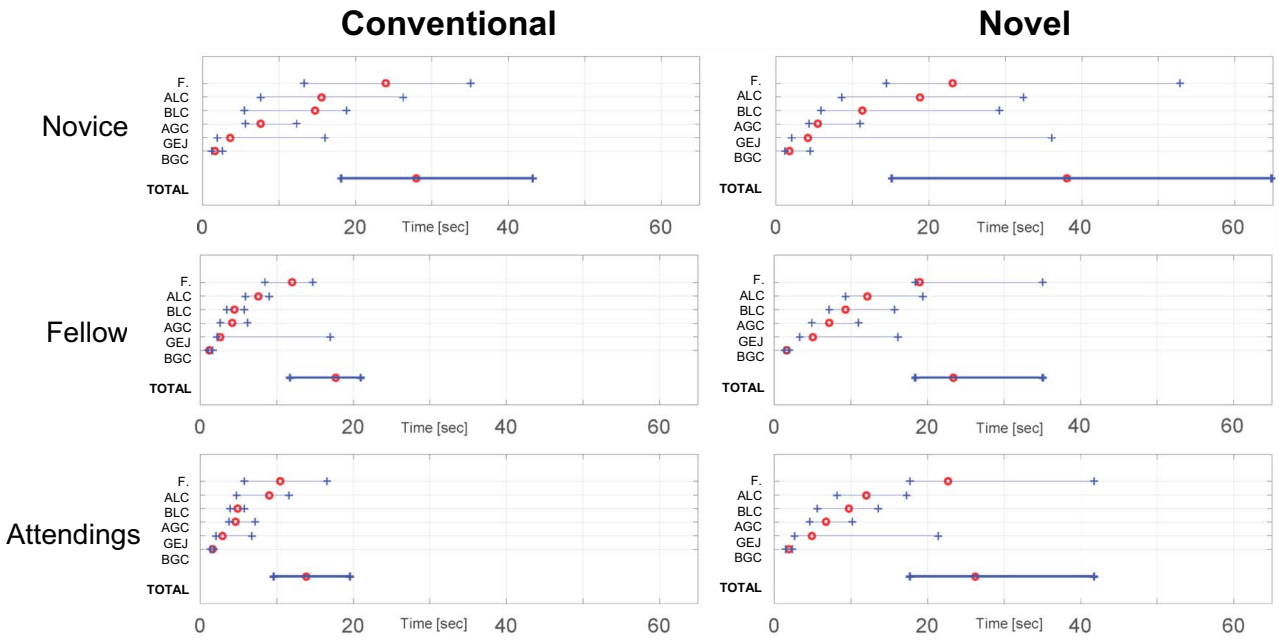

Figure I.20: Trial results by endoscope type (conventional; novel) and user (novice; fellow; attending). Total time and landmark specific identification times are displayed (median = red circle; Q1Q3 = blue line; F = fundus; ALC = antrum lesser curvature; BLC = body lesser curvature; AGC = antrum greater curvature; BGC = body greater curvature; GEJ = gastroesophageal junction).

novices performed well with the novel endoscope, suggesting a short learning curve (supporting the intuitiveness of the novel platform.) This portends well to potential efficacy in clinical scenarios for diagnostic upper endoscopy given our intended demographic of non-specialized users (i.e. non-traditional endoscopists: emergency department providers, ICU physicians, primary care providers, etc.). Users of the novel platform may not require extensive technical training in traditional endoscopy in order to maneuver the novel endoscope, and can instead focus their attention on cognitive skill (i.e. recognition of normal or abnormal findings to support triage decisions).

All participants in the study found the novel endoscope easy to use and intuitive with low mental and physical demand. Novices had reduced temporal demand and effort with the novel endoscope. While attendings and fellows favored the conventional endoscope, novices favored the novel endoscope. This is likely explained by the extensive experience with conventional endoscopy in the fellow and attending groups, who attempted to drive the novel endoscope as if it were a conventional endoscope. Novices, who lacked any experience with either endoscope, preferred the novel endoscope. Regardless of endoscopy experience all user were able to complete the task with the novel endoscope in an efficient manner and were pleased with the novel devices ergonomics, low-weight, and ease of manipulation. This would suggest that the intuitive drive mechanism is robust, effective, and functions well for the task at hand (especially for those without any specialized conventional endoscopy training).

Our results indicate promise of potential efficacy in clinical use. This is especially significant given that the novel endoscope is low-cost (less than $35 in materials; lower if produced on a large scale), intuitive to drive without prior experience, and without need for bulky equipment or device reprocessing. Point-of-care management decisions can be made in non-traditional settings (primary care provider office, inpatient medical or surgical ward) at the initial encounter with a topical anesthetic agent. Similar to other tools such as central line kits, providers would have the potential to take the novel device off-the-shelf, open the package, and perform their exam to triage the patient to conventional endoscopy with intervention (therapeutic upper endoscopy) or another care plan. Adverse events may potentially be reduced as patients can avoid conventional endoscopy with moderate or deep sedation. The risk/benefit ratio may be more advantageous if upper endoscopy were purely a therapeutic procedure.

Examples of this shift in work flow could include a primary care provider seeing a patient in clinic with long-standing GERD or GERD non-responsive to acid suppression medications, progressive dysphagia, odynophagia, or suspicion of peptic ulcer or gastrointestinal etiology for anemia. In this case, a primary care provider could perform rapid bedside diagnostic examination of the patients UGI tract. Identification of any suspicious finding(s) (i.e. presumed Barretts esophagus, esophageal stenosis, candida esophagitis, neoplasm, varices, peptic ulcer) could then be sent for an expedited and directed interventional upper endoscopy performed in the traditional setting.

Another example would be screening for esophageal and gastric varices in an outpatient hepatology clinic for point-of-care diagnosis. As patients with cirrhosis are at increased risk for sedation-related adverse events, avoidance of conventional upper endoscopy, unless necessary to perform esophageal band ligation of varies, would be optimal [5]. With this information obtained in the office, the hepatologist could discuss and decide on potential treatment options with his or her patients without delay (i.e. beta-blocker, schedule for therapeutic upper endoscopy for band ligation, or further discussion regarding transjugular intrahepatic portosystemic shunt (TIPS), sclerotherapy (especially if gastric varices are visualized), and/or transplant.)

In the hospital setting (emergency department, inpatient ward, or ICU), having immediate bedside diagnostic information, as in the case of suspected gastrointestinal bleeding, would allow for prompt and accurate triaging of the patient (i.e. need for gastroenterology consultation versus pulmonary, or interventional radiology, admit or discharge from the ED, expedited inpatient travel case, transfer to an ICU). Suspected foreign bodies in the ED would be able to be confirmed immediately, leading to expeditious gastroenterology consultation for management. Cardiologists may be able to evaluate the esophagus prior to transesophageal echocardiography (TEE), thereby avoiding unnecessary consultation to gastroenterology for diagnostic upper endoscopy prior to TEE.

A potential limitation of our study is the small number of participants from a single institution and single division

(Gastroenterology). While we were able to detect a difference between the groups as intended based on the main outcome measure and power calculation, future studies will include an increased breath of participants from multiple specialties (pulmonologists, emergency medicine providers, primary care providers, surgical), skill levels (PGY trainees in those specialties, mid-level providers, and attendings) and from multiple centers with a formal learning curve assessment.

Another potential limitation was the practice period with the conventional endoscope and the novel endoscope. In order to avoid potentially jeopardizing or influencing the assessment of ease of use, the time frame of one minute was selected. Our team felt that if the practice period was longer, any difference between the platforms that may exist may not be able to be detected. Additionally, given the intended users of the novel platform (primary care providers, ICU providers, emergency department providers), we aimed to demonstrate that use of the novel endoscope was intuitive with a short learning curve that required no more than one minute of time to comprehend. The path taken to visualize the landmarks had the potential to significantly affect the resultsas if one order or path for visualizing the landmarks was inherently quicker than another, the outcome would be more reflective of the path choice taken and less of a measure of the device itself. From careful review of the landmark visualization order for each trial for each device, there was no significant difference for all users with each device. This was also supported by our calculated Z variable.

We used a human stomach phantom with LED markings of key anatomic landmarks. This model was chosen based on its accurate anatomy, as it was created from a human patients CT scan, and has ease of implementation in the outpatient clinic setting (i.e. no need to travel to an animal lab or other facility to perform the trials). As the model could be brought into the outpatient clinic, the set-up and arrangement of the trial was in alignment with the intended location for future clinical use. In addition, the model allowed for confounding factors such as food, debris, mucous, and drying out of ex-vivo tissue to be avoided—thus ensuring that all participants saw the same stomach under the same conditions. The LED markings also ensured that all landmarks remained in constant position for all trials for all users; again eliminating the variability between trials and potentially confounding the results.

Finally, the tip of the novel endoscope is currently 13.5 mm diameter (due to the use of off-the-shelf bellows) which is at the maximum reasonable size for a patient to ingest. As a result, we are in the process of reducing the endoscopic tip dimension to less than 8 mm diameter for enhanced patient comfort, ease of oral intubation, and facilitation of potential duodenal inspection. In conclusion, all users were pleased with the novel endoscope. The intuitiveness and key features of the platform have the potential to allow for rapid, low-cost, diagnostic assessment of the UGI tract in non-endoscopy units or non-ICU based settings to facilitate patient management decisions,

minimize equipment encumbrance, and avoid cross-contamination. This could facilitate patient care, reduce risk from diagnostic procedures by possible avoidance, expedited therapeutic procedures, and improve allocation of endoscopy resources.

Planning for first-in-human trials is currently underway.

Chapter II

Magnetic actuation

II.1 Magnetic actuation for minimally invasive therapy

II.1.1 LESS and NOTES

Surgical techniques and technologies have progressed significantly over the past decades with the aim of minimizing trauma to the patients. Apart from resulting in less pain and faster recovery, the reduction of trauma also minimizes the number and severity of incisions, wound size, and blood loss, hence, reducing the potential of surgical complications. This has been demonstrated through the trend of the technical and technological development of the surgical procedure: from open surgery to laparoscopic or minimally invasive surgery (MIS) [72], laparoendoscopic single site (LESS) [73, 74] and Natural Orifice Transluminal Endoscopic Surgery (NOTES) [75].

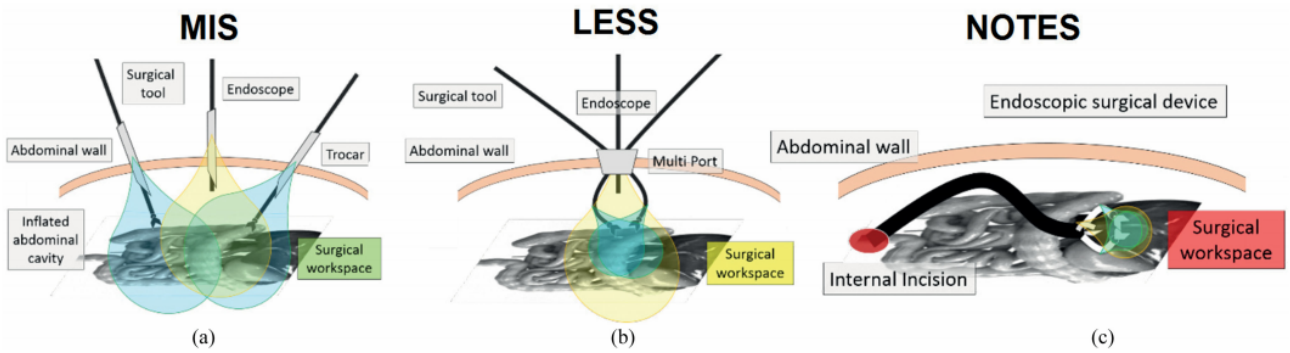

Figure II.1: Schematic representation of the abdominal surgery techniques. (a) MIS scheme; each surgical tool requires a single port (trocar). (b) LESS scheme; mirrored surgical tool are used to fit a 23-cm multiport. (c) Transcolonic NOTES scheme; endoscopic surgical tool reaches the abdominal cavity though an internal incision.

The concept of decreasing surgical trauma via MIS [76, 77] as shown in Figure II.1 (a)], gained popularity throughout the field of abdominal surgery since the 1990s, moving forward from the open surgical procedure. While MIS does not have the large workspace for surgeons to freely access different quadrants of the abdomen, it allows much smaller incisions, thus, reducing the surgical trauma suffered by the patients. Furthermore, using relatively small incisions ranging from 5 to 12 mm [78], this approach leads to fewer wound complications, less postoperative pain, shorter recovery period, better cosmetics, and earlier return to employment and daily activities, hence, greater

patient satisfaction [79–81]. More technical advantages of laparoscopy include lower likelihood of infections and blood loss, improving the preservation of normal immune function, thus, lower morbidity rate [80, 82–84].

The persistent aim in minimizing the invasiveness of surgical procedures stimulated further reduction in surgical trauma by introducing the LESS approach, as illustrated in Figure II.1 (b), with improvements in the aspects of cosmetics and recovery rate [85–87]. LESS aims to eliminate the need of multiple surgical incisions, utilizing only one incision typically through the umbilicus [88, 89], for the insertion of laparoscopic surgical tools [90, 91]. Currently, LESS devices (e.g., SILS port, Triport) are widely available, with a plastic disk of 2 or 3 cm connected to a flange for multiple laparoscopic tools to be inserted through the umbilicus [92, 93]. In order to provide correct triangulation (ability to replicate surgeons head and shoulder relative position in a surgical scenario) curved tools are used which require a mirrored used of them. The surgeon hence operated with the right hand the left surgical tool and with the left hand the right one. This non-intuitive approach limited implementation of complex LESS procedure.

Toward achieving the goal of a completely scarless surgery, NOTES has been proposed [94–97]. The NOTES procedures (see Figure II.1 (c)) gain access to the abdominal cavity via various transluminal access (e.g., transgastric, transvaginal, or transcolonic). Endoscopic-like surgical instruments are used to maneuver into the abdomen through an incision made in the stomach wall, uterus, or colon to access the abdomen. Due to the cumbersome procedural setup and manipulation with current available surgical instruments [98, 99] as well as the lack of cases to evaluate the possibility of infection [100, 101], NOTES remains largely experimental.

In all these approaches, it should be noted that the maneuverability of surgical instruments is constrained by the access port, which is created by surgical incision resulting in limited the access to the abdominal's quadrants. All these surgical methods were conventionally performed manually by surgeons with the use of rigid laparoscopic tools or endoscopic instruments, where limitations (such as human hand tremor, fatigue, inconvenient tools manipulation, and limited vision of the surgical environment) also added to the difficulties.

II.1.1.1 Robotic LESS and NOTES and the incision-less magnetic approach

The introduction of robotic surgical systems alleviated some of the shortcomings associated with the manual operation of the surgical instruments. Robotic MIS surgery, for example, is currently performed in over 4000 hospitals all over the world using commercial robot commercialized by Intuitive Surgical®[102–106]. The latest device released on the market for robotic MIS is the Da Vinci Xi®platform [107], shown in Figure II.2. This

surgical robot has the capability to reach all the abdominal quadrants using six or seven degrees-of-freedom (DOFs) tools thanks to its cable-driven mechanism, EndoWrist®.

Figure II.2: DaVinci Xi platform. Left: the surgical robot with four robotic arm which allow access to all the four abdominal quadrants. Right: The surgical console with 3D vision used as user interface.

In terms of robotic LESS applications, Intuitive Surgical has announced in the past months, the Da Vinci Sp®, Figure II.3(a). The Sp®platform consists of a single cannula that allows the deployment of three snake-like robotic arms and a stereoscopic vision head into the abdominal cavity. In contrast to the previous version, the DaVinci Single Site, the Da Vinci Sp offers more DOFs per surgical instrument, improving triangulation, tools congestion avoidance and multiport dislodgement, Figure II.3(a).

Commercially available robotic platforms for NOTES are on the rise [108]. These platform need to overcome complicated trajectory and the need for highly maneuverable and miniaturized robotic manipulators with the capability of endoscopic instruments. The main technical challenges arise from the connection with long body devices that could deprive the instrument of the rigidity required by surgical tasks. A snake-like surgical endoscopic robot, the Flex ®Robotic System (Medrobotics, Raynham, MA) [109], Figure II.3(b), that has just recently obtained FDA clearance for a wide variety of applications both in the NOTES and LESS scenario. Another promising robotic

platform is represented by the IREP [110] which is being translated by Titan Medical (Toronto, Canada) under the trademarked name of SPORT. The platform consist of two highly dexterous continuum robotic arms that are deployed with a 3D vision steerable system able to provide enhance triangulation.

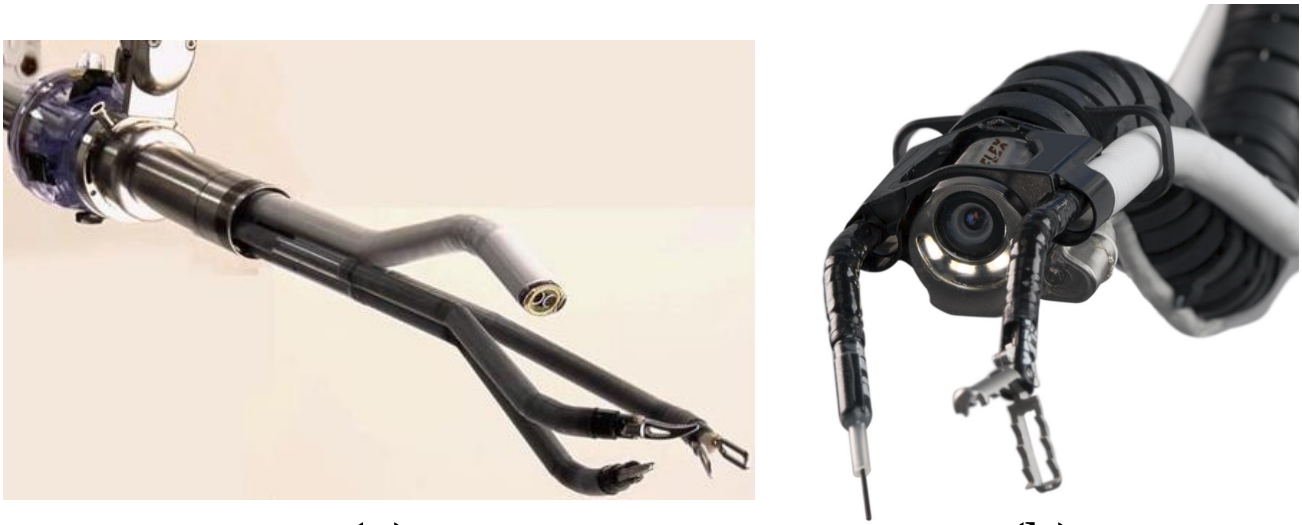

(a) (b)

Figure II.3: (a): Da Vinci Sp platform; (b): Flex Robotic System.

Robotic assistance in MIS, thus far, has extended the capabilities of surgeons via improved precision, dexterity, and computer assistance. The translation of this improvements to the LESS and NOTES is under development by many research group working on the applications. Such surgical approaches impose strict requirements on the design of surgical tools in terms of miniaturization, dexterity, and collision avoidance between surgical tools. Dexterity, which is related to the number of DOFs available by a surgical instrument, decreases from open surgery to MIS, LESS, and NOTES. The same trend is true for triangulation, which decreases along with invasiveness decrease. Less trauma is hence directly related to less workspace and ability to perform complex surgical tasks.

A promising approach that can improve both triangulation and dexterity for surgical instruments leverages the magnetic field interactions of two magnetic sources, located on opposite sides of the abdominal wall. The magnetic sources located on the outside of the abdominal wall is referred to as the external unit and the magnetic source located inside the body is defined internal unit. The magnetic interactions of these sources allow the transmission of torques and forces across the abdominal wall (i.e. physical barriers), and hence, transfer mechanical power from an external magnetic component to a driven one embedded into the surgical tool, which is operating inside the human

body.

The use of magnets in abdominal surgery was first reported by the successful utilization of magnetic systems almost 65 years ago in neurosurgery and cardiology in guiding catheter tips through vessels. The very first magnetic guidance of intravascular catheter was experimentally evaluated in 1949 and published in 1951 by Tillander et al. [111]. The device consisted of a catheter with an articulated steel tip that was steered by a magnetic field generated by a large electromagnet placed beneath a nonmagnetic surgical table. The advancement in technology and the possibility to regulate magnetic fields led to the translation to clinical use, such as Stereotaxis [112, 113], and Magnetecs [114], with the Stereotaxis obtaining FDA approval for atrial flutter treatment in 2010. In recent years, more magnetic-based medical devices received increasing attention, such as the capsule endoscopes (CE) for diagnosis and treatment of the gastrointestinal (GI) tract [115, 116], with various designs exploiting magnetic-based navigation in colonoscopy [117–125], gastroscopy [126–129], tissue biopsy [122], controllable drug delivery [130], and tumor detection [131, 132]. Since then, the use of magnetic systems to deploy, place, and drive independent surgical units intra-abdominally across the abdominal wall has tremendously intrigued researchers. This created an innovative class of externally actuated surgical instruments, which can potentially improve triangulation, tool repositioning, and lower surgical invasiveness.

II.1.2 Review of magnetic surgical devices

The Magnetically Anchoring and Guidance Systems (MAGSs), introduced by Cadeddu and his team in 2007 [133], are surgical tools that benefit from magnetic anchoring between an external permanent magnet (PM) and an internal PM embedded in the internal surgical device. The anchoring serves to guide and reposition the surgical device through manipulation from the outside of the body. The attraction force acting on the internal PM anchors the internal device onto the inside of the abdominal wall. If the external PM is displaced along the surface of the abdominal wall, the magnetic misalignment generates a net force that will act on the internal magnet in the same direction as the displacement, resulting in the internal device undergoing the same displacement. By having the magnetic poles of each magnet in parallel to each other, as shown in Figure II.4(a), the translation and angular displacement can be achieved, resulting in three DOFs of motion, i.e., translation along x and y and rotation about z (the yaw DOF).

II.1.2.1 MAGS with manual guidance

MAGSs were investigated for their ability to perform simple surgical tasks [134], to manipulate a surgical camera [133], surgicalretractors [133], and surgical cauterizer [135]. Different cameras have been proposed by the same authors, where the latest version had Ethicon Endo Surgery involved in its development and was tested in clinical trials [133]. The device consists of an illumination and vision system embedded in a wired capsule that contains a PM. An external magnetic handle is hand operated and gives the surgeon the ability to change the field of view of the camera by manually operating the external PM onto the inflated abdominal cavity. Swain et al. [136] studied the possibility to obtain a stadium view with a miniaturized (15-mm diameter and 30-mm length) camera and illumination systems attached to the abdominal wall. Trials highlighted the benefits of having a mobile camera hanging from the abdominal wall compared to the use of conventional endoscopes which suffer from tunnel vision, i.e., misperception of the surgical workspace for surgeons.

Surgical MAGS retractors were also designed with manipulation capability. Two external PM anchors are arranged such that its relative distance can be varied [134], resulting in the actuation of a device functional unit through simple mechanism (see Figure II.4(b)). A fan-shaped end effector has been successfully used to retract liver portions in a porcine model. Further development on magnetic-based retractor was made by Dominquez et al. [137]

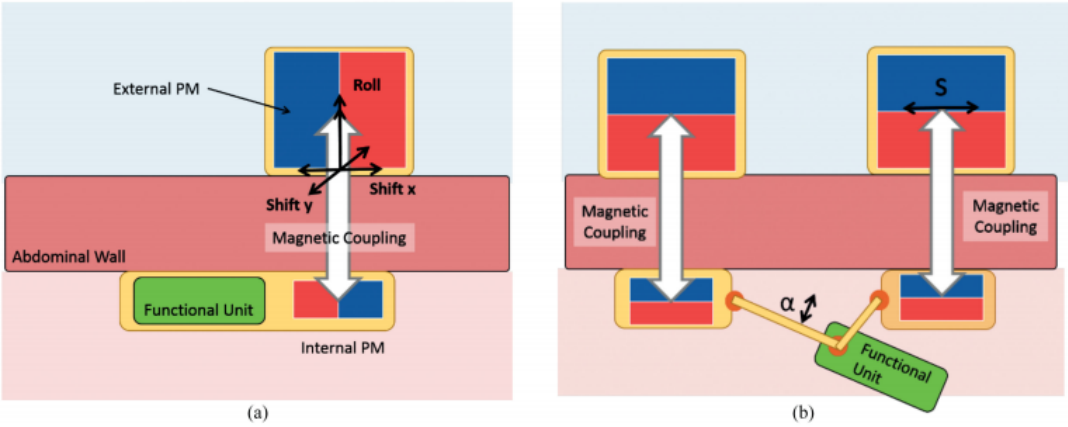

Figure II.4: Illustration of MAGS. (a) MAGS principle of operation. (b) MAGS magnetically actuated by magnetic translation.

and Cho et al. [138], who developed a simpler but functional surgical retractor used in actual abdominal surgeries. Dominguez et al. proposed a surgical grasper directly attached to a PM, while Cho et al. tested a magnet-fixed endoscopic clip. The clip was manipulated by the surgeons using conventional surgical tools. Once attached to the

point of interest, the clip was retracted by the magnetic attraction of the external PM.

From the in vivo experiments [135], [139], the potential of MAGS was validated as a technology that emphasizes the aspects of self-anchoring capability, instrument guidance within the abdominal cavity, and thus, decreased invasiveness. However, without the capability to manipulate objects, only relatively simple surgical tasks have been demonstrated with these instruments so far.

At this point of the development, it was desired to realize instruments that can perform more articulated surgical tasks within the abdominal cavity that would use the MAGS approach. Some amount of mechanical movements have been shown successful with the use of additional magnetic coupling for motion and actuation, however, they were found to be less dexterous and nonrepeatable [134] when hand operated. A more reliable way to control these system was necessary to overcome the limitation that non-linear force and torque transmission between magnetic sources. For more accurate instrument manipulation, the concept of the simple magnetic attraction has to be further exploit to adapt to more complex surgical tasks and motions.

II.1.2.2 MAGS with conventional on board actuation

The idea of incorporating onboard actuation units onto MAGS surgical devices grew out of the need to enhance the manipulation capability of the instruments by decoupling the actuation for manipulation from the anchoring tasks. In this case, the MAGS instruments are further enhanced with onboard actuators (e.g., miniaturized electrical motors) to drive a surgical instrument with higher number of DOFs mounted on the internal unit, for tasks requiring more dexterous manipulation within abdominal cavity (see Figure II.5).

A magnetically anchored and actuated device was first reported in [134] in the form of a three DOFs robotic cauterizer. The surgical cauterizer, 158-mm long, was pneumatically actuated and embedded PMs at the instrument base for anchoring. The pneumatic actuation did not guarantee a smooth operation of the device in vivo, but was able to generate sufficient force to elevate tissue and perform incisions on it. The performance of the device in terms of available force at the end effector and attraction forces at the instrument base was not quantified by the authors.

Vision (camera) systems in surgical instrumentation do not generally require much mechanical power, defined as the product of force and velocity or torque and speed, as no tissue manipulation is required. However, a precise motion in different directions is required. In 2009, a camera system with controllable orientation (pan and tilt) and zoom for MIS surgery was proposed [140]. The device consisted of a MAGS enhanced with conventional motors. Two DC electrical motors connected with miniaturized gears provided the actuation for the two orientation DOFs,

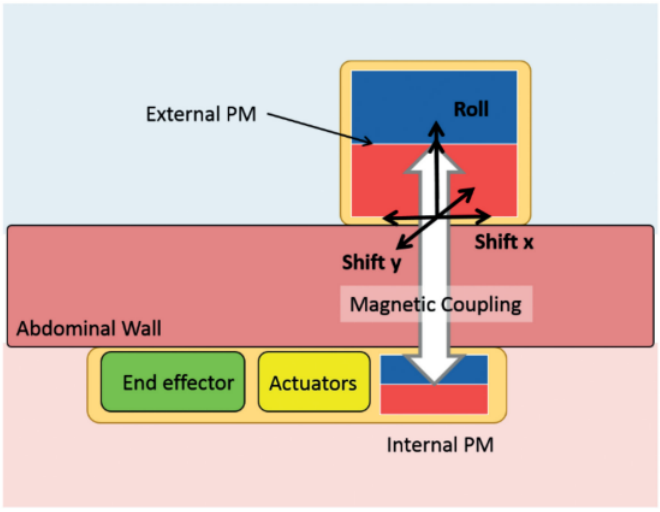

Figure II.5: Operation principle of MAGS with onboard conventional actuation.

while a third motor was used to linearly actuate the camera head, thus, resulting in zoom feature. The device, 9 mm in diameter, was designed without an anchoring solution and in vivo trials were performed by suturing the device onto the abdominal wall. The study, however, highlighted the potential use of magnetic links as a way to reposition and dock the device.

Another camera system, developed in 2012 by Terry et al. [141], is an example of a magnetically anchored system with the conventional actuation for the camera. The device designed for LESS surgery takes advantage of the larger port size (larger than that for MIS approaches) to embed the actuation and gearing systems for the camera motion on board the internal device. Three DC motors were used to provide the actuation to the two rotational DOFs (pan and tilt) and the translation DOF to change the camera relative position to the entry port, and thus, enhance triangulation. *In–vivo* testing had shown an improvement in surgeon tasks completion due to the reduced instrument congestion compared to the multiport approach.

To magnetically solve the retraction task, a magnetic retraction device for NOTES was proposed by Oleynikov et al. [103] and consists of a MAGS platform that embeds two PMs and an electrical motor that bundle or unbundle a wired surgical clip. No description was given of the performance of the retraction system but the authors reported that limited simple maneuvers were achieved.

Tortora et al. [142] developed a surgical retractor that consists of a retracting arm with two DOFs connected to a magnetic frame for anchoring purposes. The device utilizes one DC motor to change the angular position of the retracting arm while a second motor is used to operate the end-effector gripper. While sufficient grasping force is achieved at the end effector (5.3 N), the retracting force generated by the motor at the end effector is insufficient

for surgical practice (1.53 N). The torque available at the end effector, in this case, was increased using mechanical gain mechanism for the purpose of tissue retraction. In [142], the performance of the whole platform (magnetically anchored frame with four surgical insturments attached to and with fixed distance relative to each other) was also evaluated in a mock up simulator. The surgical instruments used in the study included a four DOFs robotic cauterizer, a four DOFs robotic manipulators, a two DOFs camera and a two DOFs surgical retractor. The main benefits of connecting different instruments to the magnetic frame are that:

1. the anchoring frame can embed bigger PMs and support larger load which is shared among the instrument avoiding the anchoring of each;

2. the fixed position of the instruments to each other, improves triangulation, avoids instrument reciprocal interference and provides a known relative location between different instruments facilitating operation.

However, the force available at the four DOF robotic tools tip, based on the same modular components, was not sufficient for further investigation in surgical practice (0.65 N).

In parallel, another three-link miniature surgical robot for NOTES was tested during *in vivo* trials by Lehman et al. [143]. The robot consists of a central body with stereoscopic vision and PMs for the device anchoring. Attached to it, two arms with three DOFs, each attached and actuated by DC electric motors. The experimental validation demonstrated the possibility of combining magnets with traditional actuators for miniature robotic platform for surgery but the dexterity was found to be lower than using the conventional platform (conventional MIS with nonmagnetic based approach). To overcome the dexterity limitation encountered by this study, the same group developed a similar device with four DOFs per arm but without magnetic anchoring [144]. The final dimension of the device could not allow transgastric deployment of the device; as a 20-cm opening on the abdominal wall was required. This platform is currently being developed for clinical used by Virtual Incision Corporation (Sioux Falls, SD, USA) [145].

Though the attempts to incorporate actuation capability in MAGS surgical devices using conventional motors for more dexterous manipulation are proven to be feasible for small payloads, the motors with sizes small enough to fit through the incision do not generally provide enough torque and payload capabilities for the surgical instrument manipulation. Nevertheless, the promising advantages of magnetic coupling were demonstrated in guiding and anchoring of surgical instruments, with now more complex robotic features, albeit limited in power. Surgical devices can be driven without direct connections between the internal unit and the external actuation. As such, surgical devices with embedded PMs can be manipulated across the physical barrier of the abdominal wall through the

appropriate manipulation of the magnetic linkages.

II.1.2.3 Robotic control of magnetic actuation

This type of devices take advantage of magnetic field to develop a generation of surgical devices with improved dexterity, reliable operation, and more powerful actuation. Mechanical power can be transmitted through a magnetic linkage. The magnetic linkage can in fact be used statically to generate attractive forces for anchoring and guidance or dynamically to produce forces/torque in the internal device, as shown in Figure II.6. The resulting internal device is tetherless, and potentially with no electronics on board.

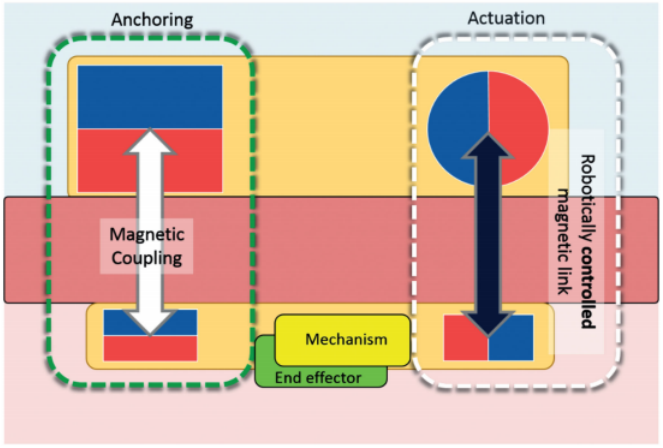

Figure II.6: Illustration of MAGS with robotic actuation.

Various magnetic actuation solutions have been investigated for the cases where the absence of rigid link between the surgical tool and the actuation mechanism can improve the outcome for the patients. In the following, different magnetic links for actuation purposes are reviewed.

- *Position Control of PM*: Using robotic control of the position and orientation of a PM, it is possible to regulate the amount of force and torque transmitted in a more reliable and repeatable manner than that performed manually. A medical field where this approach is well investigated is CE [146–148]. Challenges remain in the field in the effective localization method for the location of the capsule relative to a known reference coordinate system required to close the control loop.

- *PMs With Shielding Material*: Brewer et al. [149] investigated the possibility of modulating the magnetic field by interposing magnetic shielding material between the external PM and the PM on board the internal

device. By controlling the shield position, and thus, interaction mitigation of the magnetic field, it is possible to have force control over the internal device containing an onboard PM. Moreover, an interesting result was reported for possible force regulation strategy: the amount of force transmitted to the device becomes linearly dependent on the shielding position.

- *Electromagnetic Coils*: Coil is another magnetic field generator that has been used by Kummer et al. [150] to actuate and control the position of a miniaturized swimming robot for eye surgery. The magnetic field of a coil can be modulated as a function of the current running through the coil. Moreover, using multiple coils, it is possible to shape the magnetic field in determined areas.

- *Servo Control of Rotating Magnets*: Diametrically magnetized cylindrical PMs can act like mechanical spur gears. The number of the magnetic poles is analogous to the number of teeth of a gear, while allowing contactless torque and speed transmission. Due to this feature, the magnetic coupling is referred as magnetic gear [151]. A motor connected to such magnet can transmit power to another PM across a physical barrier to another magnet. This concept, introduced as Local Magnetic Actuation (LMA) for actuation of surgical devices, leads to interesting applications in the design of surgical devices that are addressed in the following subsection.

II.1.2.4 Conclusion

The advances in surgical instruments have played a significant role in the reduction of surgical trauma on patients. The evolution of surgical applications to the current popular approaches of MIS, LESS and NOTES integrated with the use of magnetic actuation emphasizes the benefits of magnetic systems in the field of abdominal surgery. The transmission of actuation forces and torques across the abdominal wall by means of magnetic coupling between the external magnetic actuator and the internal surgical device embedded with magnets, enables the surgical devices to be deployed intra-abdominally without a rigid link connection to the outside. This provides the freedom for the placement of the internal device within all quadrants of the abdominal cavity without compromising manipulation dexterity, triangulation and actuation forces.

The resulting surgical instruments, residing completely within the abdominal cavity during the operation, need to be designed to cater for the requisite of the surgical task and environment. With advancement in sensing and localisation of multiple DOFs magnetic interaction, effective and dexterous magnetic surgical platform could greatly contribute to the abdominal surgical procedures. The concept of magnetic based techniques in robotic surgery

therefore demonstrates great potentials for surgical innovations that could replace conventional abdominal surgery, elevating the surgical robotics field to the next technological level.

II.1.3 Local magnetic actuation (LMA)

II.1.3.1 Closed loop control of LMA

In [152], the authors introduced the concept of local magnetic actuation (LMA), where mechanical power is transferred across the abdominal wall by magnetic coupling, to drive a DOF of a laparoscopic robot. Each LMA-based device, as shown in Figure II.6 of MAGS with robotic actuation, is composed of at least one anchoring unit, plus an actuation unit per independent DOF. The anchoring unit is composed of an external and an internal permanent magnet, and its function is to support the instrument during surgery. The actuation unit is composed of an External Driving Magnet (EDM) and an Internal Driven Magnet (IDM). The EDM is connected to a motor and can be actuated independently, causing the actuation of the respective IDM, coupled across the abdominal wall (Figure II.7). The IDM is used to actuate, through a mechanism, one DOF of the laparoscopic robot.

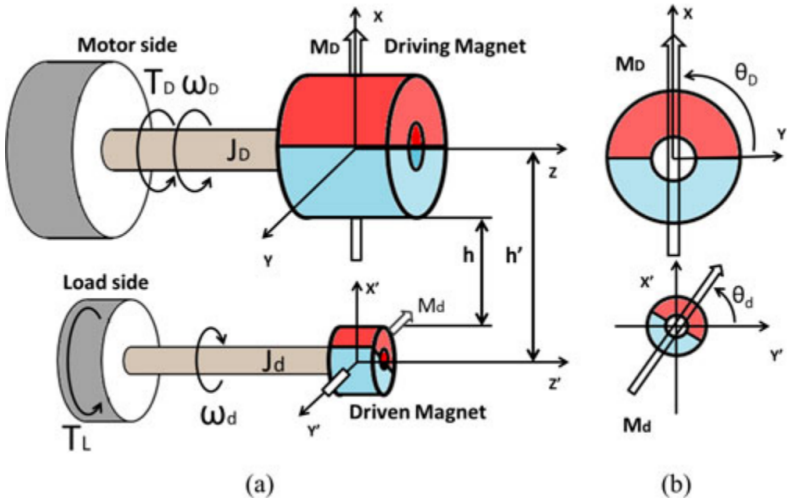

Figure II.7: (a) Schematic overview of the LMA actuation unit; (b) lateral cross section of the magnetic couple.

Considering that the diameter of laparoscopic instruments is constrained by the inner lumen of the surgical port (typically 12 mm), the LMA approach break mechanical continuity of surgical tool by having large and powerful motors, placed outside the body of the patient.

II.1.3.2 Dynamic modeling and loop closure

The closed loop control of LMA was described by Di Natali et al. [11] and part of that study is here summarized as it has been reproduced to control the laparoscopic retractor described in section II.2, and the subcutaneously implantable pump described in section II.4.

As represented in Figure II.8, the closed-loop control diagram for a single LMA actuation unit is composed: (A) the magnetic spur gear coupling; (B) the actuator rotating the EDM, (C) the sensors measuring the feedback parameters, (D) and the controller driving the actuator.

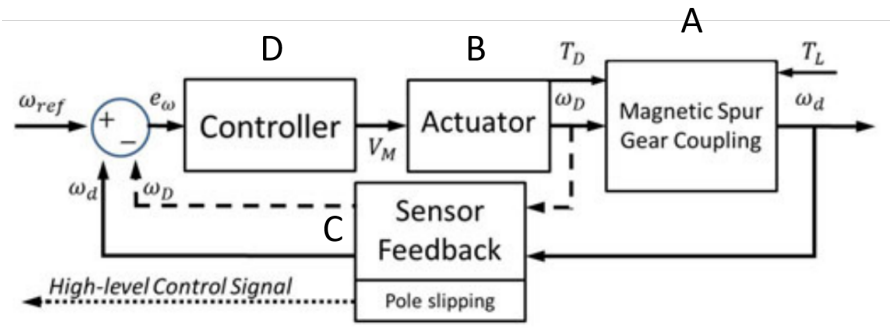

Figure II.8: Block diagram for the closed-loop control of an LMA actuation unit.

Since the proposed LMA actuation strategy is intended to replace an onboard high speed/low torque actuator, the control strategy relies on closing the loop on the angular velocity at the load. As a feedback parameter, the use of either the driving (ω_D) or the driven magnet angular velocity (ω_d) can be used. This value is compared with the desired velocity ω_{ref}, and the error e_ω is fed to the controller that generates the appropriate voltage input V_M to the actuator. The external actuator imposes a torque T_D to the magnetic gear system. The mechanical power is transferred to the driven magnet via magnetic coupling to overcome the load torque T_L, which is seen as a disturbance to the system. As single-dipole magnets are used, the speed ratio between the driving and the driven magnets equals one.

The sensor feedback block measures in real time ω_D and ω_d and detects if the system has entered the pole–slipping regime. This regime consists of loss of control due to torque overload [153], or excessive driving magnet acceleration that induces inertial reaction forces on the IDM [154]. A warning signal can be transmitted to a high level controller in case of pole slipping. As suggested in [153], in case the pole slipping occurs due to excessive driving magnet acceleration, the coupling can be reengaged by forcing ω_D at zero for a short period before being

reset to the original speed command input. On the contrary if pole slipping is induced by overload other solution need to be investigated.

A - Dynamic model magnetic spur gear coupling

A schematic diagram of the LMA actuation unit is represented in FigureII.7. The magnetic couple is composed of two cylindrical permanent magnets diametrically magnetized, having magnetization M_D and M_d for the EDM and the IDM, respectively. While the two magnets have a single dipole each, the general case where the two magnets are different in diameter and length is analyzed.

An important assumption of our model is that the two magnets are lying on two parallel axes (i.e., z and z'), spaced by a separation distance h'. Note that h' is defined as the distance between the two axes and h as the separation between the outer surfaces of the two magnets, as represented in FigureII.7(a). Referring either to h or h' is equivalent, as the difference in their values is constant. Additionally, abdominal tissue thickness is also assumed to not influence the magnetic coupling.

The equivalent inertia at the driving and at the driven magnet side, are defined as J_D and J_d respectively, while θ_D and θ_d describe the angular coordinates of M_D and M_d as represented in Figure II.7. The angular displacement of the magnetic couple is denoted with $\Delta\theta = \pi - (|\theta_D| + |\theta_d|)$. As represented in Figure II.7(a), the directions of rotation for the two magnets are opposite (i.e., a counterclockwise rotation of the EDM induces a clockwise rotation of the IDM).

The magnetic spur gear pair can be analytically described for different h by modifying the equivalent model for a two-inertia mechanical system [155]. In conventional two-inertia servo-drive systems, the interconnecting drive shaft has a linear torsional stiffness K [Nm/rad] that stays constant within the operating range. Therefore, the torque T_C transmitted by the prime mover to the load is a linear function of the angular displacement at the drive shaft. In the LMA case, as introduced in [156], the torque transmitted across a radial magnetic coupling is not constant with $\Delta\theta$ and can be described by a nonlinear trigonometric function

$$T_C(\Delta\theta) = T_G sin(\Delta\theta) \tag{II.1}$$

where T_G is the maximum gear torque that can be transmitted over the magnetic coupling. The value of T_G depends on the volume and magnetization strength of the magnets and on their separation distance h. In case the driving and the driven magnets differ in terms of volume and/or magnetization, the cross-coupling due to the magnetic field

becomes asymmetrical, and two separate nonlinear torque transfer functions must be considered. These are:

$$T_C^{Dd} = T_G^{Dd}(h)sin(\Delta\theta) \tag{II.2}$$

$$T_C^{dD} = T_G^{dD}(h)sin(\Delta\theta) \tag{II.3}$$

where (II.2) refers to the torque transferred from the EDM to the IDM, while (II.3) refers to the torque transferred in the opposite direction.

The numerical values of T_G^{Dd} and T_G^{dD} at different h can be obtained by the static (due to the magneto–static nature of the problem) finite element analysis (FEA) where the EDM and IDM are angularly offset to each other by $\Delta\theta = \pi/2$. $T_G^{Dd}(h)$ and $T_G^{dD}(h)$ can be calculated and approximated by exponential fits.

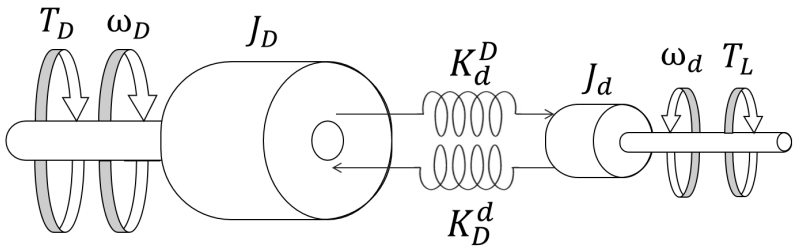

Figure II.9: Equivalent model of a magnetic spur gear pair with asymmetrical magnets.

Referring to the equivalent model represented in Figure II.9, the dynamic behavior of the LMA actuation unit can be described by

$$J_D\dot{\omega}_D = T_D - T_C^{dD}(\Delta\theta, h) \tag{II.4}$$

$$J_d\dot{\omega}_d = T_C^{Dd}(\Delta\theta, h) - T_L \tag{II.5}$$

The trigonometric expressions of T_C^{dD} and T_C^{Dd} can be linearized about $\Delta\theta = 0$ in the range $|\Delta\theta| < \pi/2$, assuming

$$T_C^{Dd}(\Delta\theta, h) \simeq K^{Dd}(h)\Delta\theta = \frac{2}{\pi}\tilde{T}_G^{Dd}(h)\Delta\theta \tag{II.6}$$

$$T_C^{dD}(\Delta\theta, h) \simeq K^{dD}(h)\Delta\theta = \frac{2}{\pi}\tilde{T}_G^{dD}(h)\Delta\theta \tag{II.7}$$

where $\tilde{T}_G^{Dd}(h)$ and $\tilde{T}_G^{dD}(h)$ are the exponential fits for $T_G^{Dd}(h)$ and $T_G^{dD}(h)$, respectively. The transmittable torque is maximized when $|\Delta\theta| = \pi/2$, beyond this angular displacement, the magnetic coupling enters a pole-slipping

regime [153, 157], resulting in a consequential loss of control.

The block diagram representing the open-loop system, shown in Figure II.10, can be derived by combining (II.5,II.4,II.7, II.6). In no-load conditions, the transfer functions relating the driving torque (T_D) to driving, and

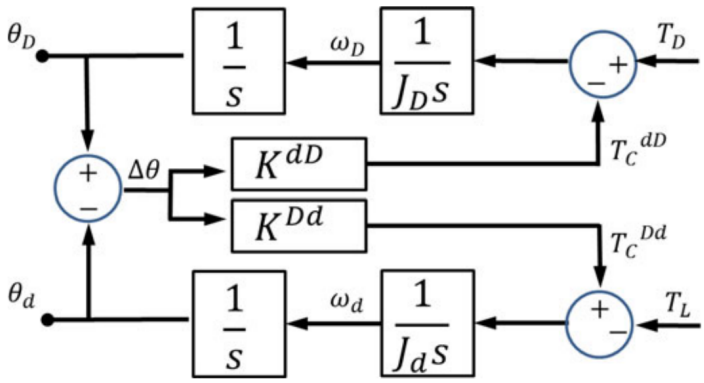

Figure II.10: Block diagram of the open-loop magnetic gear system.

driven angular velocities (ω_D, ω_d) are given by

$$\frac{\omega_D}{T_D} = \frac{s^2 + \frac{K^{Dd}}{J_d}}{J_D s(s^2 + \frac{K^{Dd}J_D + K^{dD}J_d}{J_D J_d})} = \frac{s^2 + {\omega_a}^2}{J_D s(s^2 + {\omega_0}^2)} \tag{II.8}$$

$$\frac{\omega_d}{T_D} = \frac{K^{Dd}}{J_D J_d s} \frac{1}{s^2 + \frac{K^{Dd}J_D + K^{dD}J_d}{J_D J_d}} = \frac{K^{Dd}}{J_d J_D s(s^2 + {\omega_0}^2)} \tag{II.9}$$

where the antiresonant ω_a and the resonant ω_0 frequencies are, respectively, expressed as by

$$\omega_a = \sqrt{\frac{K^{Dd}}{Jd}} \tag{II.10}$$

$$\omega_0 = \sqrt{\frac{K^{Dd}J_D + K^{dD}J_d}{J_D J_d}} \tag{II.11}$$

B - Dynamic model of actuator

A DC motor with current monitoring is used to drive the EDM in a first LMA implementation. The motor dynamic model, schematically represented in Figure II.11, considers

$$V_M = K_M \omega_D + R_{tot} i_M + L\dot{i_M} \tag{II.12}$$

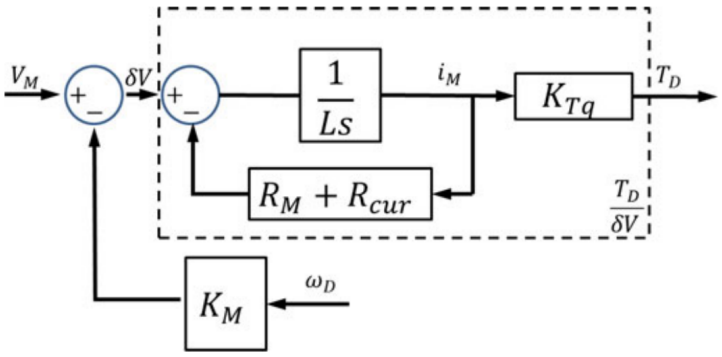

Figure II.11: Dynamic model of DC motor with current monitoring

where V_M is the voltage applied to the motor, K_M is the electromotive force constant scaled by the gear ratio of the motor gearbox, i_M is the current, and L is the motor inductance. The term R_{tot} includes both the motor and the current monitor resistances, R_M and R_{cur} respectively.

The motor torque T_D, fed to the magnetic gear system, is derived by monitoring the motor current as

$$T_D = K_{Tq} i_M \tag{II.13}$$

where K_{Tq} is the motor torque constant.

Defining δV as $\delta V = V_M - K_M \omega_D$, the transfer function relating the motor torque T_D to δV in the Laplace domain is

$$\frac{T_D}{\delta V} = \frac{K_{Tq}}{L(R_{tot}/L + s)} \tag{II.14}$$

C - Sensor feedback

Magnetic field sensors (MFS) were used to investigate both motor-side and load-side sensing strategies. The motor-side sensor is placed next to the driving magnet, whereas the load-side sensor is placed close to the driven magnet.

The block diagram in Figure II.11 shows how the signals acquired by the two MFS are used to derive EDM and IDM angular positions θ_D and θ_d, angular velocities ω_D and ω_d, angular displacement of the drive train $\Delta\theta$, and its time derivative $\Delta\omega$. Referring to Figure II.7, the component along x of the magnetic field generated by the EDM M_D is acquired by the motor-side MFS, while the load-side MFS acquires the component along x' of the magnetic field

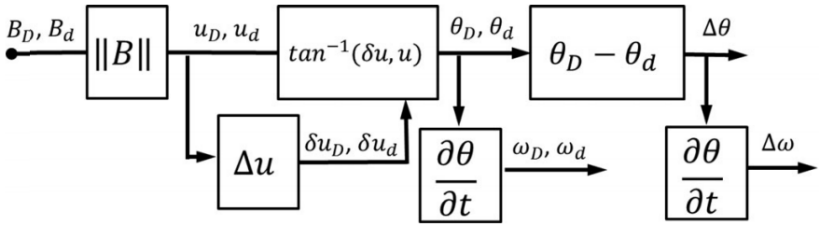

Figure II.12: Angular position (θ_D and θ_d), angular speed (ω_D and ω_d), angular displacement of the drive train ($\Delta\theta$), and its time derivative ($\Delta\omega$) are obtained through direct measurement of the magnetic field (M_D and M_d) generated by the driving and the driven magnets along the vertical direction.

generated by the IDM, M_d . As the two magnets spin, M_D and M_d can be described by two cosine functions. The magnetic field values are normalized, obtaining u_D or u_d, and the angular derivatives δu_D and δu_d are calculated. The inverse of the tangent function is applied to $(u_D, \delta u_D)$ and to $(u_d, \delta u_d)$ to derive θ_D and θ_d, respectively. Angular velocities ω_D and ω_d are then obtained by the time derivative of θ_D and θ_d, respectively.

D - Close loop strategies

To develop intracavitary surgical tool electronic free, i.e. sensor may be used only outside of the patients. Here the close loop control strategy that relies only on magnetic field sensor placed on the external permanent magnetis presented. The controller is designed to endure controllability within a range of intermagnetic separation distances h from 2 to 7 cm.

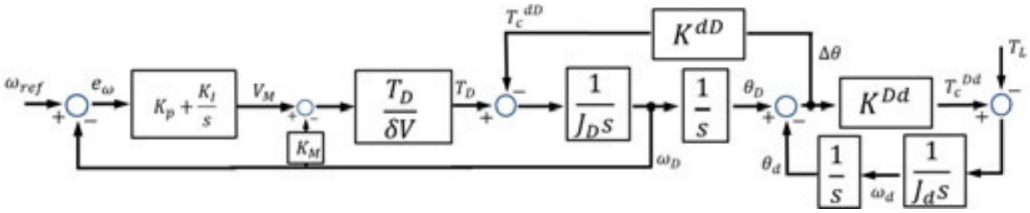

Figure II.13: Motor-side speed control system with PI controller.

When implementing this closed-loop control strategy, the driven part of the actuator may be seen as a disturbance. In this approach, similar to [153, 155], the effect of coupling in the control loop is considered. A standard proportional-integral (PI) controller fed with the motor-side angular velocity ω_D is adopted. The block diagram of the closed-loop system is shown in Figure II.13. In this Figure, K_p is the proportional feedback coefficient, while K_I

is the integral feedback coefficient. The closed-loop transfer function from the reference input to the motor speed is given by

$$\frac{\omega_D}{\omega_{ref}} = \frac{A}{B};\quad A = \frac{(K_I + K_p s)}{s}\frac{\frac{T_D}{\delta V}\frac{s^2+{\omega_a}^2}{J_D s(s^2+{\omega_0}^2)}}{1+\frac{T_D}{\delta V}\frac{s^2+{\omega_a}^2}{J_D s(s^2+{\omega_0}^2)}K_M};\quad B = 1+\frac{(K_I + K_p s)}{s}\frac{\frac{T_D}{\delta V}\frac{s^2+{\omega_a}^2}{J_D s(s^2+{\omega_0}^2)}}{1+\frac{T_D}{\delta V}\frac{s^2+{\omega_a}^2}{J_D s(s^2+{\omega_0}^2)}K_M} \tag{II.15}$$

II.1.3.3 Model validation and experimental assessment

Experimental platform

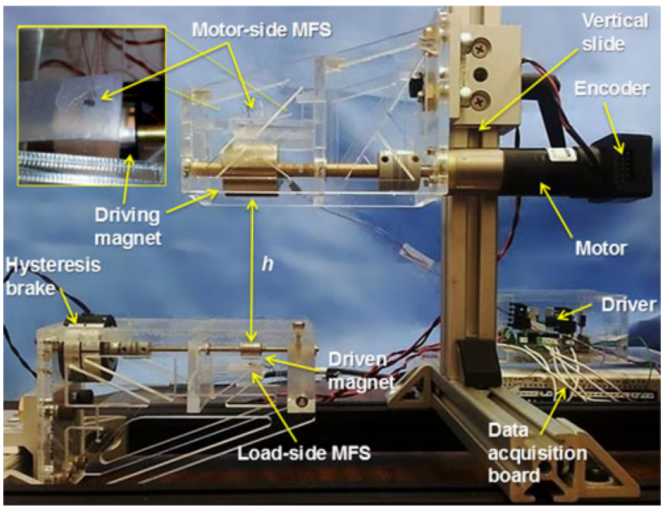

Figure II.14: Picture of the experimental platform. The upper left inset shows the placement of the MFS next to the EMD magnet.

The experimental platform designed to validate the LMA control is represented in Figure II.14. A DC motor was used to spin the EDM, whereas the driven magnet was connected to a hysteresis brake. The motor-side assembly was mounted on a vertical slide that allowed adjustment of the intermagnetic distance h.

The dc motor ($2342-024CR$, Faulhaber, Germany) embeds a 1:3.71 planetary gearhead, and can provide a maximum torque of 60 mNm at a maximum speed of 1900 RPM. A two-channel optical encoder ($HEDS5500$, Avago Technologies, USA) with 96 counts per revolution was connected to the motor and provided the reference for assessing the feedback strategy.

The EDM ($K\&J$ Magnetics, Inc., Pennsylvania, USA) is made of NdFeB and has a cylindrical shape (25.4 mm in both diameter and length) with diametrical magnetization (N42 grade, 1.32 T in magnetic remanence). The

IDM has the same features, but smaller dimensions (9.5 mm in both diameter and length). The diameter of the IDM was selected to fit a laparoscopic device that can enter the abdominal cavity through a 12-mm surgical port. Given the selected pair of magnets, T_G^{Dd} and T_G^{dD} for h ranging from 2 to 7 cm were estimated by FEA (COMSOL Multiphysics, USA). Two two-term exponential models were used to fit the FEA results, obtaining

$$\tilde{T}_G^{dD}(h) = 222e^{-169h} + 63e^{-51h}[mNm] \tag{II.16}$$

$$T_G^{Dd}(h) = 78e^{-105h} + 12e^{-31h}[mNm] \tag{II.17}$$

where h has the unit of meters. The fitting functions were obtained with the Curve Fitting Toolbox (MATLAB, Mathworks, USA), by setting the confidence level at 98%.

The hysteresis brake (H3, Placid Industries, USA) was used to impose on the IDM a controllable T_L . One MFS (CYP15A, ChenYang Technologies, Germany) was placed next to each the EDM and the IDM for real time monitoring of their angular displacement via the algorithm previously described.

The motor-side and the load-side inertias of the experimental platform resulted in $J_D = 8.9 \times 10^6 Kgm^2$ and $J_d = 0.46 \times 10^6 Kgm^2$, respectively.

A data acquisition board (DAQ USB-6211, National Instruments, USA) was used to collect the data from the MFS at 500 Hz and to control both the motor and the hysteresis brake via a custom driver. Regarding the operation of the motor, the current drained is monitored across a 10Ω buffered resistor R_{cur}. The hysteresis brake was also controlled in voltage, while the drained current was monitored via a second buffered resistor. The user interface, developed in C++, allowed the user to set ω_{ref} up to 1900 RPM and T_L from 0.5 to 25 mNm.

Dynamic model validation

The first step of validation focused on assessing the sensor feedback strategy, as this was used for all the experiments. In particular, ω_D was compared between the encoder measurement with the value estimated by implementing the algorithm represented by Figure II.12. This test was performed for ω_D = [500, 700, 900, 1100, 1300, 1500] RPM showing an average error of $7.28 \pm 2.82 RPM$. We can reasonably assume a similar uncertainty in reconstructing ω_d and $\Delta\omega$.

The next step consisted of validating the dynamic model of the magnetic gear coupling for different separation distances h, angular velocities ω_D and ω_d, and applied load torques T_L. A single experiment consisted of increasing T_L, while driving the external magnet at a constant speed ω_D and maintaining a fixed intermagnetic distance h.

As soon as the system entered in the pole-slipping regime, this was detected and the experiment was ended. The intermagnetic distance h was varied from 2 to 7 cm in steps increments of 1 cm, while ω_D was increased from 500 to 1500 RPM in steps increments of 200 RPM. The closed-loop control was adopted to guarantee a constant ω_D, as T_L increased. Once a trial was started, the platform increased the voltage driving the hysteresis brake in 0.15 V increments every 0.2 s, resulting in an exponential increase of T_L over time. The event of pole slipping was detected by monitoring θ_d as measured by the sensor-side MFS.

For each experiment, the data recorded for θ_D, θ_d, and T_D were used together with platform-specific parameters (i.e., J_D, J_d, $\tilde{T}_G^{Dd}, \tilde{T}_G^{dD}$) to estimate T_L. The dynamic model for T_L was derived by combining (II.4) and (II.5) and integrating over time, thus obtaining

$$T_L(t) = J_d \Delta\theta(t)\left(\frac{1}{\Delta t^2} + \frac{2}{\pi}\frac{\tilde{T}_G^{dD}}{J_D} + \frac{2}{\pi}\frac{\tilde{T}_G^{Dd}}{J_d}\right) - \frac{J_d}{J_D}T_D(t). \tag{II.18}$$

The reference value for T_L was obtained by measuring the current drained by the hysteresis brake and deriving the torque applied to the driven magnet from its calibration curve. A typical plot for a single experiment is represented in Figure II.15 where the following testing parameters were used: $h = 4cm$, $\omega_D = 1000RPM$.

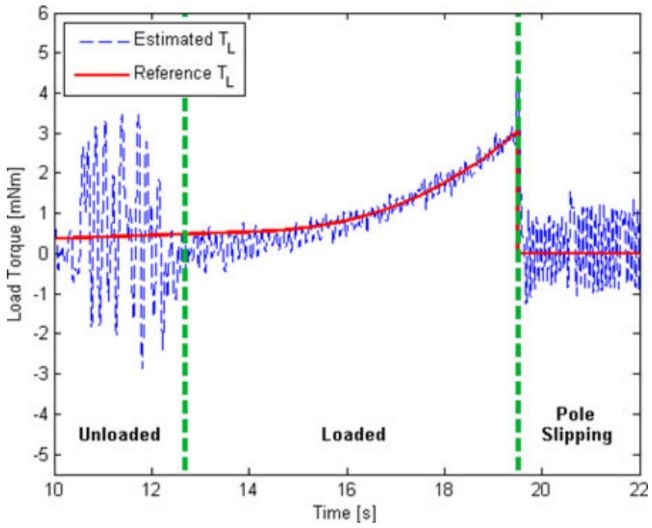

Figure II.15: Dynamic model validation: comparison between the estimated and the reference load torque for $h = 4cm$ and $\omega_D = 1000RPM$. The unloaded, loaded, and pole-slipping regimes are highlighted by the dashed vertical lines.

Here, three different regimes can be observed. When in unloaded conditions, angular oscillations at the driven

magnet were induced by the low inertia, combined with the nonlinear elastic coupling of the magnetic link. In this regime, reconstruction of T_L by the model was noisy. As T_L increased, the amplitude of oscillations decreased significantly, and the model allowed for a reliable real-time estimation of the load torque. As expected, the system entered the pole-slipping regime as T_L overcame the maximum value of torque that can be transmitted over the magnetic coupling at the specified distance h.

Five experiments were repeated for each combination of h and ω_D, and the estimation errors were averaged. The mean relative errors in estimating T_L at different velocities and intermagnetic distances are reported in Table II.1 Over the entire range of distances and velocities tested, the mean relative error was 7.12.3%, while the mean

Table II.1: Mean relative error in T_L estimation at different velocities and intermagnetic distances within the loaded regime

	$\omega_D[RPM]$					
h	500	700	900	1100	1300	1500
2 cm	9.4%	14.7%	5.7%	8.5%	7.9%	8.8%
3 cm	13.8%	8.1%	9.4%	6.4%	8.4%	3.1%
4 cm	9.6%	12.1%	10.9%	8.4%	8.3%	8.2%
5 cm	9.2%	13.4%	5.8%	7.6%	6.7%	7.9%
6 cm	8.7%	3.7%	4.0%	3.9%	4.1%	3.8%
7 cm	5.7%	3.1%	3.4%	3.8%	4.0%	5.5%

absolute error was 0.180.06mNm. All of these values are related to the loaded regime of operation.

Closed loop validation

The proportional and integral coefficients for the motor-side closed-loop control were determined via the PID Tuning function of the Control System Toolbox (MATLAB, MathWorks, USA), obtaining $K_p = 52.42 \times 10^3 Vs/rad$ and $K_I = 5.90V/rad$. A comparison between simulated and experimental step response is reported in Figure II.16. The reported experiment was performed with $\omega_{ref} = 1000RPM$ at $h = 4cm$ in unloaded conditions, and both ω_D and ω_d were recorded. The step response the closed-loop control in Figure II.16, the measured ω_D and ω_d presented an overshoot of 11.2% and 11.6%, respectively. These results were comparable with the overshoot obtained in the simulated response. Concerning the steady state, ω_D presented an average value of $998 \pm 23RPM$, while the average ω_d was $1032 \pm 32RPM$.

Load rejection and performance evaluation

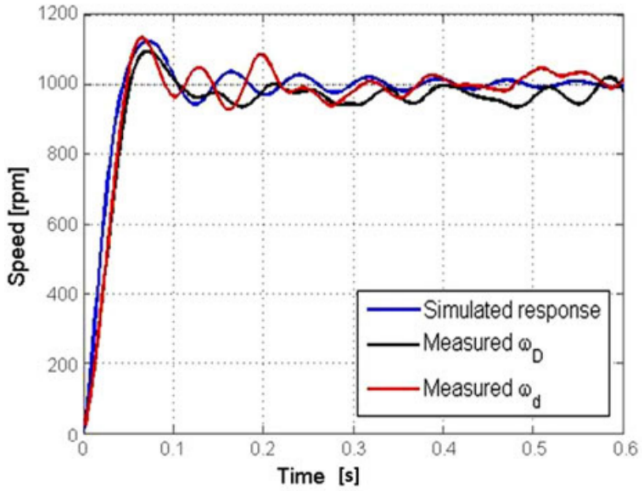

Figure II.16: Simulated and experimental step response at $h = 4cm$ for motorside closed-loop control. Both the measured ω_D and ω_d are reported in the figure.

The presence of a load torque applied at the gear train induces variations in the parameters of the system, as it affects the equivalent inertia at the driven shaft. In particular, system characteristics such as the resonant and antiresonant frequencies are both influenced by variations in J_d. Load rejection experiments were hence carried out to verify the ability of the system to maintain coupling as sudden increase in the load torque may occur. The test were conducted for $h = 4cm$, and the results are represented in Figure II.17.

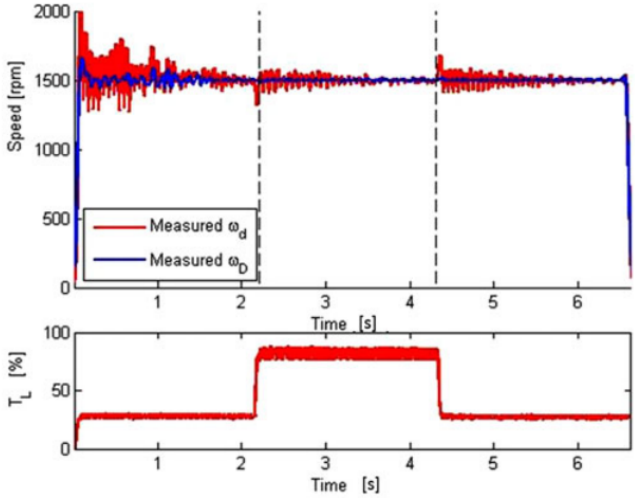

Figure II.17: Load rejection responses. The profile of T_L, moving from 28% of $\tilde{T}_G^{Dd}(h)$ to 85% of $\tilde{T}_G^{Dd}(h)$ and back to its initial value, is represented below the speed plot. Experiments were performed at $h = 4cm$ setting $\omega_{ref} = 1500RPM$. Each plot shows the measured values for both ω_d and ω_D and the trend of the applied load torque.

The reference speed ω_{ref} was set to 1500 RPM, while T_L was initially set to 28% of $\tilde{T}_G^{Dd}(h)$, then increased up to 85% of $\tilde{T}_G^{Dd}(h)$ for about 2.5s before resetting it to the initial value. While the load was at the 85% of $\tilde{T}_G^{Dd}(h)$, the average error and the ripple for ω_d were 6 ± 31 RPM. The implemented strategy allowed rejection of the effect of a load variation without pole slipping.

A final test was performed to evaluate the mechanical power that can be transmitted by an LMA actuation unit at different intermagnetic distances and further validate the FEA estimation of $\tilde{T}_G^{Dd}(h)$. The maximum torque at the load T_L^{MAX} before entering the pole-slipping regime was experimentally measured for ω_{ref} ranging from 600 to 1700RPM at different separation distances (i.e., $h = [2,3,4,5,6,7]cm$). Each trial was repeated ten times, and the results are reported in Figure II.18.

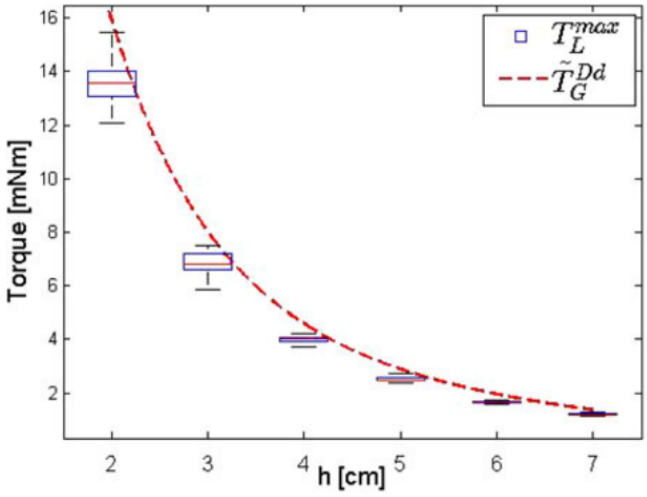

Figure II.18: Maximum torque at the load before entering the pole-slipping regime as a function of the intermagnetic distance. Theoretical value $\tilde{T}_G^{Dd}(h)$ and experimental data T_L^{max}.

With the proposed dynamic modeling and control strategy, we are able to transfer an average of 86.2% of the theoretical value of maximum torque. This deviation is due to the adoption of a linear model for T_C^{Dd} and T_C^{dD} in (II.7) and (II.6). For large angular displacements, which are expected as the load torque brings the system toward the pole-slipping regime, a linear model is far from being accurate and needs to be replaced by a nonlinear equivalent. From Figure II.18, it is also interesting to observe that the standard deviation in T_L^{max} is larger at smaller distances. This may be explained by considering other magnetic effects that are present in the system, but have not been included in the dynamic model, such as the vertical attraction force between the driving and the driven magnets that varies as the magnets spin. As previously mentioned, an LMA actuation unit can be used instead of an onboard

Table II.2: Off-the-shelf DC micro motors comparable with the size of the IDM.

Model and Make	*Diameter*	*Length*	*Max Speed*	*Stall Torque*
Namiki SBL04	4 mm	13.8 mm	7,000 RPM	0.13 mNm
Faulhaber 1016	10 mm	16 mm	18,400 RPM	0.87 mNm
Maxon DCX10L	10 mm	25 mm	12,000 RPM	5.42 mNm
Precision NC110	12 mm	12.5 mm	10,000 RPM	0.50 mNm
Faulhaber 1224	12 mm	24 mm	13,800 RPM	3.62 mNm

EM motor for driving a DOF of a laparoscopic robot. Thanks to a speed ratio equals one, the maximum speed that can be achieved at the driven shaft with the LMA approach corresponds to the maximum speed of the external EM motor. As the external motor is not as constrained in size as a motor to be embedded on board, a faster actuator can be adopted.

As represented in Figure II.18, we can consider the stall torque to be constant as the speed increases. Considering that the driven magnet used in this study was 9.5 mm in both diameter and length, we can conclude that the LMA approach can provide a volumetric power density that is above any of the DC micro motors commercially available, listed in table II.2 at any of the intermagnetic distances investigated.

II.1.3.4 Conclusions

It is possible to control a parallel-axis radial coupling with asymmetrical single-dipole magnets within a range of intermagnetic separation distances compatible with the abdominal thickness in humans. This particular kind of magnetic coupling, referred as LMA actuation unit, can be used in designing robotic surgical instruments to transfer mechanical power from outside the body of a patient to a laparoscopic instrument within. Given the constraints in diameter and volume for a surgical instrument, the proposed approach allows for transferring a larger amount of mechanical power than what is possible to achieve by embedding actuators on board.

The proposed solution for the servo control of an LMA actuation unit takes advantage of a dynamic model of the coupling, adapted from a two-inertia servo-drive system, and a sensing strategy based on Hall effect MFSs placed next to the driving and the driven magnets. In this dissertation a closed-loop strategy based on MFS placement only on the motor side has been presented. This uses the angular velocity of the driving magnet as the feedback parameter and has the advantage of relying only on sensors placed on the motor-side of the coupling, thus outside the patients body. From the experimental results, it is possible to conclude that the dynamic model we developed presented a relative error below 7.5% in estimating the load torque from the system parameters. Concerning closed-loop control, effective regulation of the load speed was achieved with a relative error below 2% of the desired steady-state value.

While this study should serve as the background for the servo control of LMA-based DOFs in laparoscopic robots, a number of challenges still remain for future research.

The first direction of future work is improving the robustness of the control. A nonlinear approach must be adopted to increase the amount of transmitted torque closer to its theoretical limit. Predictive control, suggested in [154] for coaxial magnetic gears, can be a viable solution. To reduce the oscillations in ω_d further, a digital notch-filter compensator, as suggested in [158], can be adopted. In addition, the model needs to be extended to a situation in which the two magnets spin on axes that are not fixed, nor parallel, as analyzed in [121]. Horizontal and vertical vibrations must be considered, as they will be present during laparoscopic surgery. Vertical attraction force between the driving and the driven magnets must be included in the model.

If the surgical robot needs more than one DOF, a number of LMA actuation modules will have to interact within the same confined space. Magnetic cross-coupling among LMA anchoring and actuation units may become an issue in this case. As the magnetic force and torque, respectively, decrease with the inverse of the fourth and third power of the inter-magnetic distance, this challenge can be addressed by properly spacing the magnets on board the surgical instrument. Shielding with ferromagnetic or diamagnetic material can also be considered to address this problem. The model of the system would then be extended to include cross-coupling and to provide a tool for designing appropriate shielding between modules. This limitations have been addressed in [12].

Furthermore,the system can enter in the pole-slipping regime as a consequence of torque overload. As suggested in [153], the coupling can be reengaged by stopping the motor rotation for a short period and then resetting the input command. However, if the load is still above the maximum torque that can be transmitted, this strategy will be ineffective. A potential solution to this problem consists of controlling the vertical position of the external driving magnet so that the intermagnetic distance can be reduced if a larger torque is required at the load. A different approach may be to replace the driving unit with a set of coils that can generate a rotating magnetic field at the driven magnet. In this case, commutation control can be implemented to prevent the pole-slipping regime and maximize the transferred torque at any given time. This limitation has been tackled by our Australian collaborators in [159].

II.2 Laparoscopic retractor based on LMA

The closed loop control strategy developed for the Local Magnetic Actuation allows control of the actuation of LMA based surgical devices. As previously shown, the LMA approach guarantees a higher mechanical power available on board of the device in comparison to traditional actuation (e.g. DC micro motors).

In the surgical practice different are the task that the surgeons have to accomplish. The tools mush hance satisfy certain specification in terms of number of DOFs, available force at the tip of the instrument and speed. Table II.3 a summary of this specification for surgical-assist device is shown.

Table II.3: Desired DOF, force, and speed at the end–effector of different surgical-assist devices.

Surgical-Assist Device	DOF	Force [N]	Speed [deg/sec]	References
Tissue Retractor	1	6	N/A	[160–162]
Surgical Camera	2	0.2	18	[163, 164]
Surgical Manipulator	6	5	360	[165–167]

The task that requires the higher amount of forces is hence retraction. The LMA method is hence exploited to design a laparoscopic surgical retractor.

II.2.1 Principle of operation and design

The design of an LMA-based laparoscopic instrument entails the development of both the external controller and the surgical tool. The former embeds External Anchoring Magnet (EAM) and External Driving Magnet (EDM), while the latter contains Internal Anchoring Magnet (IAM) and Internal Driven Magnet (IDM). The main design specications for the two parts of the system can be derived from clinical considerations summarized in Table II.4. To fulfill the design specification outlined in Table II.4 the developed LMA–based tissue retractor is schematically presented in Figure II.19 and referred to as LapR-LMA. 1

While the anchoring unit is mainly responsible for gross positioning and for supporting both the device and the retracted tissue, the actuation unit is designed to transmit mechanical power from the external DC motor to the mechanism inside the LapR-LMA. The spinning motion of the Internal Driven Magnet (IDM) is fed to a custom mechanical train, which has been designed to maximize the lifting force at the grasper and to fit the size constraints. In particular, the IDM is connected to a three-stage planetary gearhead (PG), which rotates a power screw (PS) actuating an offset crank mechanism (OCM). The OCM controls the angular position of a retracting lever.

In order to assess the proposed design, we connected a crocodile grasper to the lever via an inextensible wire. As proposed by Padilla et al. [161], the surgeon can clamp the grasper on the target tissue with standard laparoscopic forceps.

The design process of the LapR-LMA can be divided in *design of the magnetic components* – to quantify mag-

Table II.4: Clinical specification use to derive design specification for the LMA surgical retractor.

Clinical Specification	Description	References
Incision Port	Laparoscopic surgery is usually performed by placing three to four trocars across theabdominal wall. The trocar with the largest inner diameter is usually dedicated to the laparoscope (i.e., 13mm inner diameter for the Versaport V2, Covidien, Manseld, MA). Assuming the use of such port for insertion, we can consider 13mm as the maximum outer diameter for an LMA-based instrument. The limitation in diameter affects the design of all the components inside the surgical tool, including the internal magnets.	[122]
Abdominal Thickness	Magnetic field strength decreases exponentially with the increase in the distance between the magnets outside the body of the patient and those inside. Therefore, abdominal thickness plays a fundamental role in the selection of the magnets particularly the external ones as the ones embedded in the instrument are already constrained by the access port diameter. A value ranging from 20 mm to 40 mm upon insufflation can be assumed for abdominal tissue thickness to include overweight patients (body mass index up to 30kg/m2).	[168]
Safety	Rare-earth permanent magnets can generate strong attraction forces, posing the risk of damaging the tissue in between the external and the internal magnets. A pressure of 46.7 kPa was reported to be well tolerated in a porcine model. This value can hence be assumes as safety threshold not to be exceeded during the operation of the LMA-based instrument.	[169]
Sterlization	To permit reprocessing, a reusable surgical instrument should be able to withstand the high temperature commonly used for autoclave sterilization (i.e., 132 C). This disables the possibility of using electronics on board and requires the selection of special-grade permanent magnets	N/A
Internal Workspace	Laparoscopic procedures are performed after pneumoperitoneum is induces. As a general guideline for how long an insertable instrument should be, a distance of 275 mm was reported as the maximum between the abdominal wall and the point of intervention. This provides an indication about the workspacethat the instrument should be able to reach, as well as a limitation on the instrument length.	[170]
External Workspace	The external controller must be compact and easy to use for the surgeon,enabling the internal device gross positioning by magnetic guidance. Once the desired positioning is achieved, the controller should be locked in place while the LMA actuation unit is running.	N/A
Ease of Use	In order to maximize the potential for future adoption, the surgical instrument must be easy to introduce in the abdominal cavity and the external controller must be intuitive to operate.Once the feasibility of the proposed approach is demonstrated, the input from surgeons becomes crucial in improving the integration is the OR.	N/A
DOF	See Table II.3	[]
Force	See Table II.3	[]
Interaction with Tissue	If the tissue to be retracted is not going to be resected, the surgical tool must be gentle in interacting with it. Suction cups or fan-shaped levers can beadopted in this case. On the other hand, traumatic graspers (e.g., crocodile jaws) are a viable solutionif the surgeon plans to remove the retracted tissue at the end of the procedure (e.g., cholecystectomy).	[133, 161, 171]

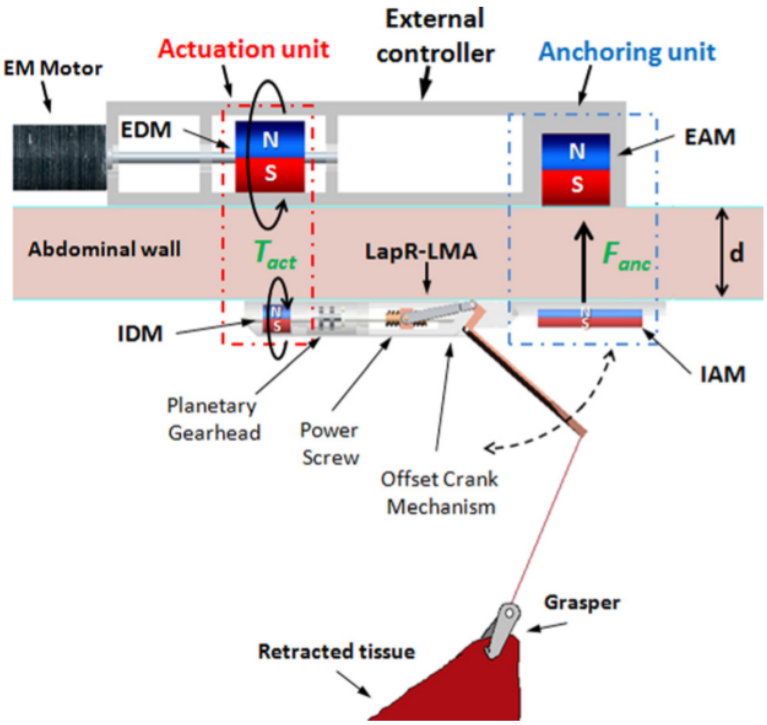

Figure II.19: Schematic representation of the LapR-LMA and the external controller components

netic forces and torques available on board of the device –, and *mechanical train design* – to evaluate efficiencyof each component and predict the overall device's performance.

In modeling and designing both the anchoring and the actuation units, magnetic torques and forces were estimated via finite element analysis (FEA) (Comsol Multiphysics 4.3b, Sweden) as presented in Section II.1.3.2. In particular, FEA simulations were based on the theories and the methods used in the analysis of steady currents, permanent magnets, and magnetic circuits [172]. In estimating the different contributions of the magnetic units, we assumed that the anchoring and the actuation units were spaced far enough to neglect cross-talking effects.

Mechanical components were designed in Creo (PTC, Needham, MA) and the each component performance or transfer function, estimated either via dedicated bench trial or via kinematic modeling in Matlab (Matlab and Simulink, Natick, MA).

II.2.1.1 Anchoring unit design

The LapR-LMA must have a cylindrical shape to enter a surgical port. Therefore, the space available for the IAM has a round cross section. This would suggest using a cylindrical magnet. However, as reported by Agashe and Arnold [173], square-section permanent magnets exert a stronger coupling than cylindrical magnets. Therefore, a

38mm long permanent magnet, with a cross section of 6.35mm in side, was selected to fit inside the LapR-LMA. The permanent magnet was made out of neodymiumironboron (NdFeB) with magnetization N52 oriented as in Figure II.19. A cubic NdFeB magnet with a side of 25.4mm and N52 magnetization (1.48T magnetic remanence) was selected as EAM to achieve an adequate attraction force, F_{anc}, on the IAM within the intermagnetic separation range investigated in this work. Given the two selected anchoring magnets, F_{anc} was estimated via FEA simulation using a mesh with more than 3,500,000 elements, and by varying the intermagnetic separation distance d from 2cm to 6cm in 0.1cm increments. As presented in Figure II.20, the data fit (R^2 >0.94) a two term exponential.

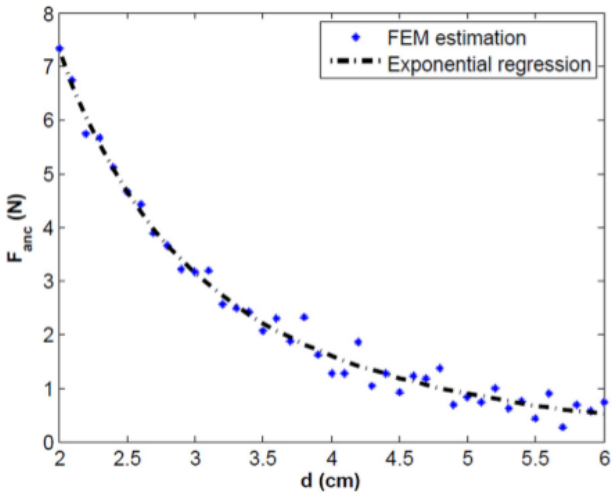

Figure II.20: FEA simulation and two term exponential fit for the magnetic attraction force at increasing intermagnetic separation distance.

II.2.1.2 Actuation unit design

The actuation unit is the same as the one previously discusses (Section II.1.3.2).

In this study, a vertical attraction force between EDM and IDM was also estimated. This force, referred to as F_{act}, contributes to supporting the retracted tissue by working in synergy with F_{anc}. As presented in Figure II.21(c), F_{act} has been analyzed assuming constant $\Delta\theta = 0$ and it can be formulated as a trigonometric function of purely the rotation angle θ_D (or equivalently θ_d), thus obtaining

$$Fact(\theta_D) = \frac{F_v + F_h}{2} + \frac{F_v + F_h}{2} cos(2\theta_D) \tag{II.19}$$

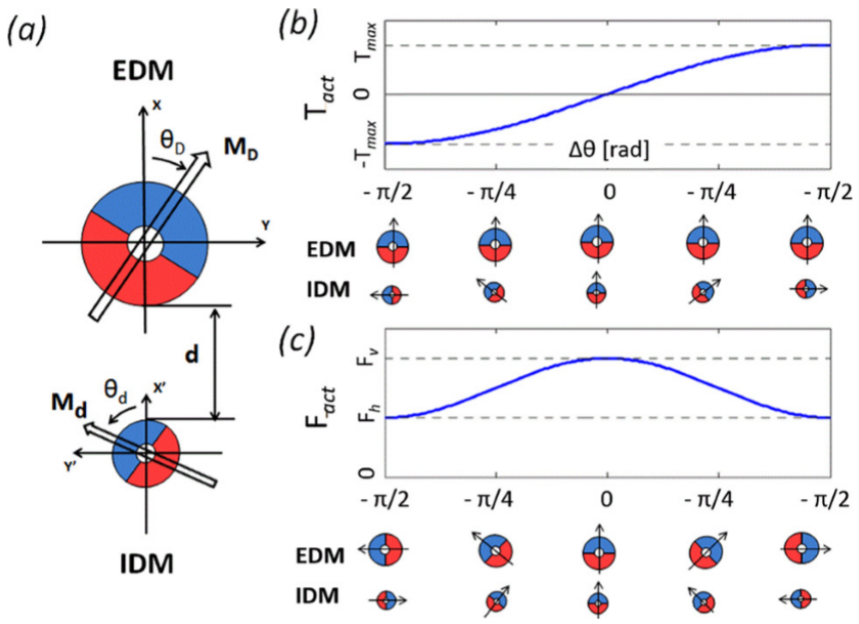

Figure II.21: (a) Schematic cross section of the EDM and IDM composing the actuation unit. (b) Torque transferred from the EDM to the IDM as a function of the angular displacement between EDM and IDM. The cross section view of the actuation unit is reported below the plot. (c) Vertical attraction force generated by the actuation unit as the magnets rotate. This plot assumes $\Delta\theta = 0$. The cross section view of the actuation unit is reported below the plot.

where F_v and F_h are the maximum and minimum values of F_{act}, corresponding to the vertical and the horizontal arrangements of the actuation magnets. As T_{max}, also F_v and F_h depend on the volume and magnetization strength of both the EDM and the IDM, and on their separation distance d.

Given the two selected magnets, a set of FEA simulations are used to calculate T_{max}, F_v, and F_h as functions of d. In estimating F_v and F_h, we assumed $\Delta\theta = 0$. In the FEA simulations, we used a mesh with more than 3,500,000 elements and we varied d from 2cm to 6cm in 0.2cm increments. Simulation results and exponential regressions tting the data are reported in Figure II.22(a) for T_max and in Figure II.22(b) for F_v and F_h.

II.2.1.3 Planetary gear head (PG) design

The first module of the mechanical train consists of a PG with three stages having a 1:64 gear ratio (GR_{pg}) used to decrease the output speed while increasing output torque. The annular ring (A in Figure II.23(a)) and the entire PG is 11mm in outer diameter and 17mm in length. For each stage, the load is transferred from the sun to the annular ring via the planets. The more the planets, the lower is the local stress at the interface between each planet and the annular ring. Therefore, to optimize the load the system can carry, we maximized the number of planets by using four of them for each stage. Suns (S in Figure II.23(a)) and planets (P in Figure II.23(a)) were designed with 10

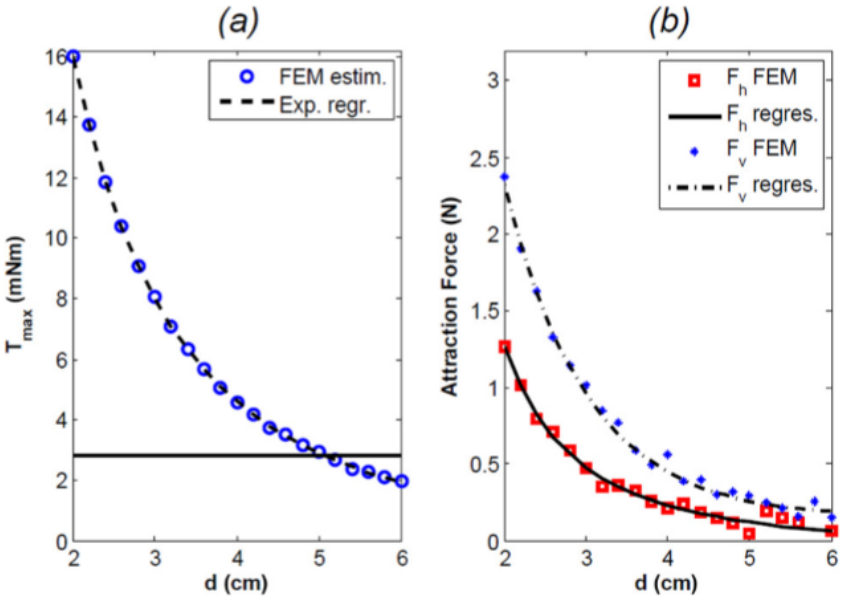

Figure II.22: (a) T_{max} and its exponential regression at different separation distances, the solid horizontal line represents the average nominal torque for commercially available EM motors that would t a volume similar to the IDM. (b) F_v and F_h and their exponential regressions at different separation distances, assuming $\Delta\theta = 0$.

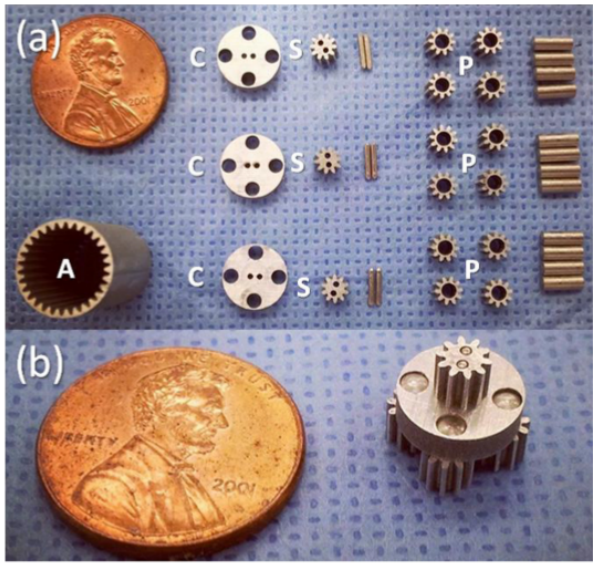

Figure II.23: (a) Three-stage PG components fabricated by electrical discharge machining. (b) One of the three stages assembled.

involute prole teeth, 0.32 module, 22.5° pressure angle, 3.2mm pitch diameter, and 3.125mm thickness. The parts were fabricated in Aluminum 6061-T6 (tensile strengthyield 276MPa; tensile strength ultimate 310MPa; relative magnetic permeability 1.004) by electrical discharge machining.

Stainless steel pins with a diameter of 0.8mm were used to mate the suns and the carriers (C in Figure II.23(a)), while 2mm diameter pins were adopted to assemble the planets. The single components of the three-stage PG are presented in Figure II.23(a), while an assembled stage is shown in Figure II.23(b).

The PG efciency was characterized via a custom-made bench test where a DC motor (2342S-024CR, Faulhaber, Germany) was connected to the PG input sun. A two-channel optical encoder (HEDS 5500, Avago Technologies, San Jose, CA) with 96 counts per revolution was connected to the EM motor to measure the input angular velocity, $\omega_i n$. The PG output carrier was connected to a hysteresis brake (H3, Placid Industries, Lake Placid, NY). The brake was controlled in current by a PC-based workstation to increase the output torque, τ_{out}, during the trial.

The torque applied by the DC motor to the PG input (τ_{in}) was measured by monitoring the current drained by the EM motor on a buffer resistor. Similarly, the torque generated at the PG output (τ_{out}) was derived by monitoring the current drained by the hysteresis brake. The output velocity, ω_{out}, was measured by connecting a diametrically magnetized permanent magnet to the output shaft and measuring the rotation of the magnetic field via a stationary Hall effect sensor (CY-P15A, ChenYang Technologies, Finsing, Germany).

The PG efficiency, dened as

$$\nu_{pg} = \frac{\tau_{out}\omega_{out}}{\tau_{in}\omega_{in}} \times 100\% \tag{II.20}$$

was derived from the experiments by using a constant ω_{in} at 1700 RPM, while τ_{out} was increased from 0 mNm to 80 mNm within a time period of 15s. This trial was repeated three times and the average efficiency resulted in $61.25 \pm 3.16\%$.

Concerning loadability, the PG working range was estimated from the safe tooth load via the Lewis equation as

$$W = \frac{SFY}{D_p} \tag{II.21}$$

where W [N] is the safe tooth load, S is the maximum bending stress of the material, F is the face width of the gear, D_p is the diametric pitch, and Y is the Lewis form factor. Considering a pitch radius of 1.6mm and a four-planet arrangement, a PG safe output torque (T_{safe}) of 134.96 mNm was estimated.

II.2.1.4 Power screw (PS) design

A PS with a single thread was designed to mate with a 7mm nut. The PS has a pitch diameter d_m of 4.8mm, a length of 25mm, a pitch P of 0.2725mm/rad, a thread angle θ of 30°, and a lead angle α of 18.3°. The nut has a thickness of 6mm and its motion is used to actuate the OCM. Connection between the PS and the OCM was achieved via 2mm pins placed in the nut sides.

The PS parts were fabricated in brass (tensile strength-yield 310MPa; tensile strength-ultimate 476MPa; magnetic permeability 1.05).

The torque τ_r that must be applied to the PS for achieving a force F_{nut} can be estimated via the following equation:

$$\tau_r = \frac{d_m F_{nut}}{2} tan(\alpha + \phi) + \frac{d_{mc}\mu_c W}{2} \quad = \frac{W}{\beta ps} \tag{II.22}$$

where d_{mc} represents the mean collar diameter, μ_s the static friction coefficient between screw and nut, μ_c the static friction coefficient at the collar surface, ϕ is the friction angle which is obtained as $tan^{-1}(\mu_s/cos(\theta))$, and β_{ps} is the conversion factor [N/mNm] that convert input torque to output force. The collar friction was assumed negligible since we used low friction Delrin bearings. With the designed geometrical parameters and the static friction coefficient of dry brass to brass (i.e., μ_s = 0.1 [174]), β_{ps} resulted in 0.91N/mNm.

The PS efciency η_{ps} was assessed with a weight lifting test. The same DC motor used to evaluate performance of the PG was rigidly connected to the PS. A weight ranging from 0.45kg to 4.53kg in 0.45kg increments was applied to the nut, and the torque τ_{mot} required by the EM motor to lift the weight was measured by monitoring the supply current. For each weight, three trials were performed and the average efciency η_{ps} was calculated assuming no loss in the nut velocity (i.e., the nut velocity V_{nut} was estimated from the motor speed ω_{mot} via the pitch P of the PS) by using the following equation:

$$\eta_{ps} = \frac{F_{nut} V_{nut}}{\tau_{mot}\omega_{mot}} \times 100\% = \frac{F_{nut} P}{\tau_{mot}} \times 100\% \tag{II.23}$$

The efficiency η_{ps} resulted $69.85 \pm 5.44\%$.

II.2.1.5 Offset crank mechanism (OCM) design

The final component of the mechanical train is the OCM operating the retracting lever. The OCM link dimensions, the initial conguration, and the required motion range were identied to achieve a total angular displacement of $\pi/2$ at the crank angle γ. Via quasi-static analysis, assuming a slow motion of the nut and negligible inertia of the

links, we defined the OCM mechanical transmission factor Γ $[mNm/N]$ as the ratio between the crank mechanism output torque, τ_{cran} in Figure II.24(a), and the related input force acting on the slider, F_{nut}. Considering the schematic

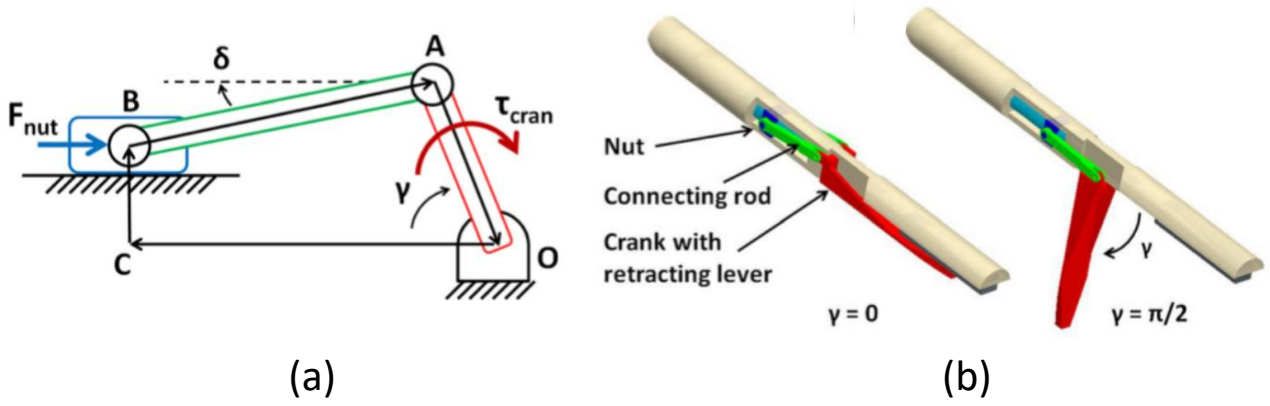

Figure II.24: (a): Schematic representation of the OCM. The slider is placed with an offset ($\overline{BC}$) with respect to the hinge point of the crank (O). Thanks to the connecting rod ($\overline{AB}$), the nut linear motion is converted in a crank angular displacement γ; (b) Perspective rendering of the assembled LapR-LMA in the closed (γ = 0) conguration and in the open ($\gamma = \pi/2$) conguration.

diagram in Figure II.24(a), we can express Γ as a function of γ using loop closure equation to obtain:

$$\Gamma(\gamma) = \frac{\tau_{cran}}{F_{nut}} = \overline{AO}sin(\gamma) + \overline{AO}cos(\gamma)tg(\delta) \tag{II.24}$$

where the angle γ is defined zero for the initial conguration –retracting lever closed (Figure II.24(b))- and $\pi/2$ when the retracting lever is fully open (Figure II.24(b)).

Considering that $\overline{OC}$ –the nut horizontal displacement- is the input parameter of the 1-DOF OCM system, the angle δ can be expressed as a function of γ by solving the following system of equations in $\overline{OC}$:

$$\gamma = \frac{2tan^{-1}(-2\overline{AB}\,\overline{BC} - \sqrt{(-2\overline{OC}\,\overline{AB})^2 + (2\overline{AB}\,\overline{BC})^2 - (\overline{OC}^2 + \overline{BC}^2 + \overline{AB}^2 - \overline{AO}^2)^2)}}{-2\overline{OC}\,\overline{BA} - \overline{OC}^2 - \overline{BC}^2 - \overline{AB}^2 + \overline{AO}^2} \tag{II.25}$$

$$\delta = \frac{2tan^{-1}(-2\overline{AO}\,\overline{BC} - \sqrt{(-2\overline{OC}\,\overline{AO})^2 + (2\overline{AO}\,\overline{BC})^2 - (\overline{OC}^2 + \overline{BC}^2 + \overline{AO}^2 - \overline{AB}^2)^2)}}{-2\overline{OC}\,\overline{AO} - \overline{OC}^2 - \overline{BC}^2 - \overline{AO}^2 + \overline{AB}^2} \tag{II.26}$$

The length of the two links (i.e., $\overline{AB}$ = 25mm, $\overline{AO}$ = 9.43mm) and the offset of the slider with respect to the hinge point (i.e., $\overline{BC}$ = 4mm) provides a $\pi/2$ angular displacement in γ for a 12.7mm motion of the slider. The mechanical transmission factor Γ as the lever angle γ varies -obtained via iterative computation by assuming negligible inertia

and a quasistatic regime- is presented in Figure II.25, together with its third order polynomial regression ($R^2 = 0.99$).

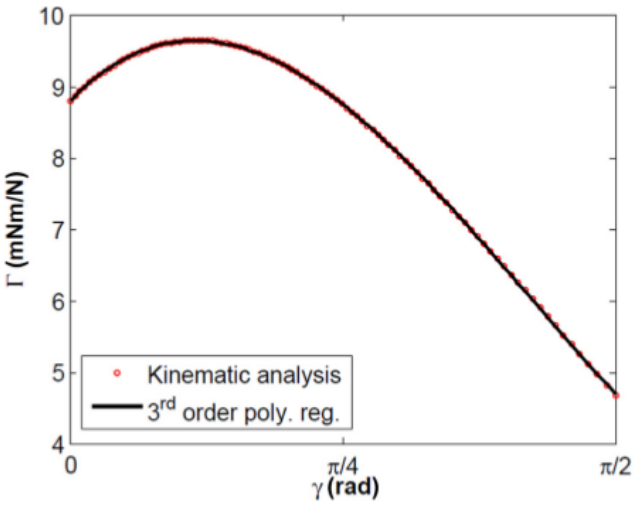

Figure II.25: Mechanical transmission factor Γ (mNm/N) of the OCM and its polynomial regression as a function of the lever angle γ (rad). A maximum value of 9.63 mNm/N is obtained for $\gamma = 2\pi/17$, while a $4.67 mNm/N$ minimum occurs for the fully open conguration (i.e., $\gamma = \pi/2$).

The OCM parts were fabricated in aluminum 6061-T1 (tensile strengthyield 55MPa; tensile strengthultimate 120MPa; magnetic permeability 1.004) via traditional machining. Stainless steel pins of 1mm and 1.5mm diameter were used for mating the parts.

II.2.1.6 Additional components and external controller

The LapR-LMA body, designed to embed the described components, was fabricated by rapid prototyping (Objet 30 pro, Stratasys, Rehovot, Israel) in Vero White+plastic. The outer diameter was set to 12.5mm to prevent mechanical failure. The device body was fabricated in two halves to facilitate the assembly of the internal components. The mechanical train alignment was guaranteed by delrin planar bearings that offer low friction and high wear resistance.

Two connecting rods were used to couple the OCM with the PS, thus balancing the nut motion and splitting the transmitted force to lower the internal stresses among mating components. The retracting lever, designed to mate with the two connecting rods, rotates about a hinge point in the device body. The retracting lever length (RL) is 58.5mm and enables a total vertical tissue displacement of the same length for the full span of γ. Buttresses in the lever design prevent it from bending.

In the current version of the LapR-LMA, the OCM and the PS are exposed to verify their motion during the trials. In the future, they can be encapsulated within the outer shell of the device.

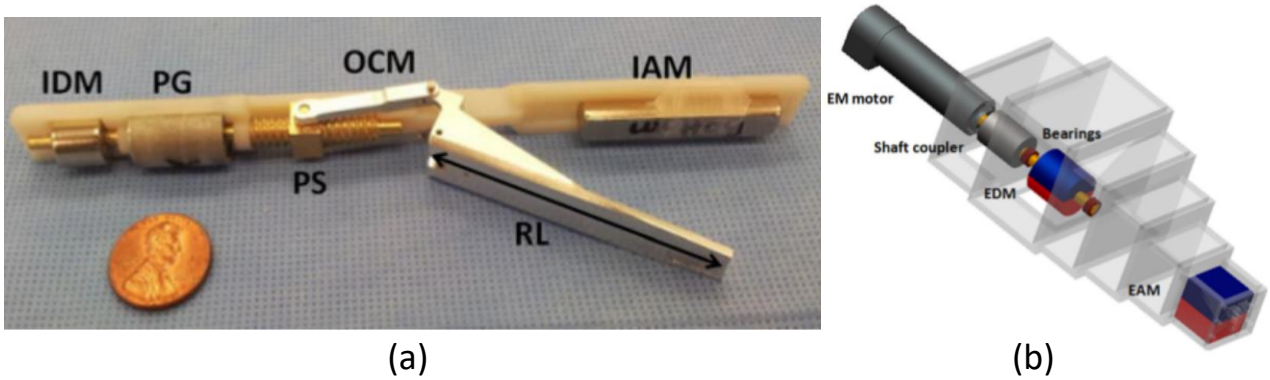

Figure II.26: (a) The LapR-LMA prototype, where half of the outer shell was removed to shows the internal components. (b) Perspective rendering of the external controller.

As presented in Figure II.26(a), the mechanical train components are arranged around a thick extrusion in the core of the device. This feature guarantees structural resistance for the LapR-LMA. The fabricated prototype, presented in Figure II.26(a), is 154mm long, 12.5mm in diameter, and weights 39.16g.

The external controller was designed to host the EDM, the EAM and the DC motor in a plastic handle. A shape with five cavitieswhere the operator can insert his/her fingers was obtained by laser-cutting and assembling Plexiglas sheets.

As presented in Figure II.26(b), the EDM was rigidly connected to the EM motor via a shaft coupler. Bearings were used to support the shaft. Spacing between the EDM and the EAM mirrored the positioning of the IDM and the IAM inside the LapR-LMA. A two-state switch was connected to the motor controller to change the direction of rotation for the EDM. This enabled switching between lifting up and lowering down the tissue connected to the grasper. An adjustable clutch arm –not shown in Figure II.26(b)– can be connected to the controller to hold it in place during the surgical procedure.

II.2.2 Experimental assessment

With the LapR–LMA components designed, characterized and assembled, is possible to develop model aimed to predict the allowable weight that the device is predicted to securely support and retract.

II.2.2.1 Performance estimation modeling

A first mathematical model aimed to provide an estimation of the tissue lifting performance of the device from the torque that can be transmitted over the magnetic coupling and the efficiencies of the single submodules. This model can also be used to predict the angular displacement $\Delta\theta$ corresponding to the weight at the gripper.

Assuming no power losses due to internal friction, the weight W_L (g) that can be lifted up as the rotation of the EDM is activated can be predicted as follows:

$$W_L < \begin{cases} \frac{10^3}{9.81}\frac{(T_{act} G R_{pg} \eta_{pg} \beta_{ps} \eta_{ps})}{RL}\Gamma(\gamma), & \text{if } T_{act} < \frac{T_{safe}}{G R_{pg} \eta pg} 0. \\ \frac{10^3}{9.81}\frac{(T_{safe} \beta_{ps} \eta_{ps})}{RL}\Gamma(\gamma), & \text{if } T_{act} > \frac{T_{safe}}{G R_{pg} \eta pg} 0. \end{cases} \tag{II.27}$$

As represented by dashed blue lines in Figure II.27, W_L is constant with d, as long as T_{act} exceeds the safe tooth-loading regime of the PG (Eq.(II.21)). In this working regime the overall efficiency of the mechanical train is

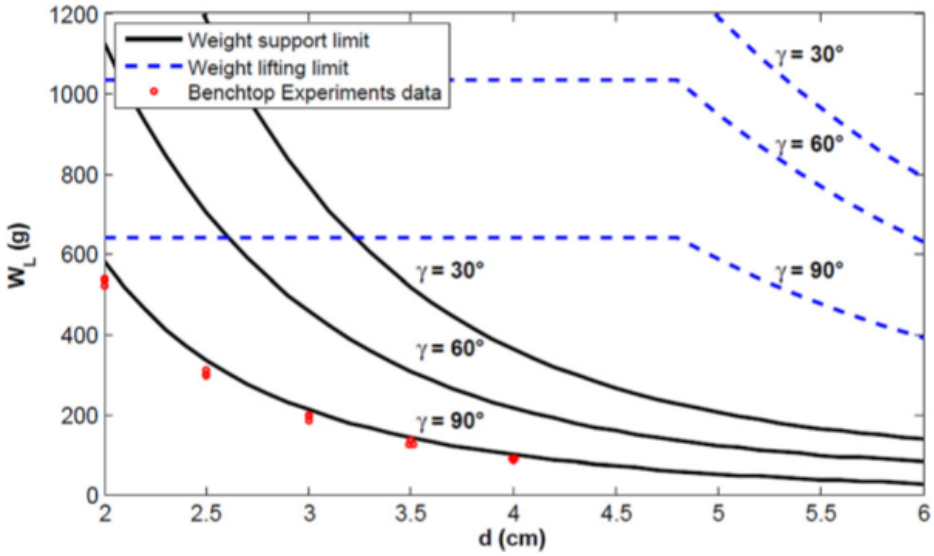

Figure II.27: Maximum weight that can be lifted by operating the LapR-LMA (dashed line), and maximum weight that can be statically supported by the LapR-LMA (solid line). Both weight limitations are plotted as functions of the intermagnetic distance and the opening angle of the retracting lever. The measurements obtained during benchtop experiments are presented as single data points.

42.78%. In most of this region, the angular displacement $\Delta\theta$ stays below $\pi/18$ (i.e., 10°), therefore we can assume $\Delta\theta_{max} = \pi/18$.

It is also worth mentioning that W_L and the mechanical train efficiency increase as γ goes from $\pi/2$ to zero

thanks to the OCM contribution presented in Figure II.25. This is an advantage in doing controlled retraction, as the portion the tissue (and its weight) increases as this is being lifted.

The second model we developed was a free body diagram of the LapR-LMA. This can be used to predict how much weight can be statically supported by the magnetic attraction force provided by both the anchoring unit and the actuation unit.

To predict the weight that can be statically supported by the LapR-LMA at different d and γ, we studied the free-body diagram of the device that is presented in Figure II.28.

The model considers F_{anc} as described, the weight force acting on the LapR-LMA, denoted with F_{lap}, and the force F_W required to lift the weight W_L at the gripper. The model also considers F_{act} as previously described (II.19), but scaled for $\Delta\theta_{max} = \pi/18$. In case of $|\Delta\theta| < \pi/18$, we estimated via FEA simulation a variation of F_h and F_v below 2.7% of the values reported in Figure II.21(b).

In our structural model, the device body was assumed as a beam in which the magnetic forces, acting on the IAM and the IDM, are responsible for anchoring the LapR-LMA against the abdominal wall (here assumed as a rigid constraint). The force F_w was assumed to act downward on a point whose position depends on the angular coordinate of the lever γ. As presented in Figure II.28(a), the LapR-LMA is designed so that F_w is always applied to a position in between the points of application of F_{anc} and F_{act} (B and D in Figure II.28(b)), thus improving the stability during controlled retraction.

Since F_{anc} is larger than F_{act} for any d, anchoring failure would most likely occur with the LapR-LMA pivoting about the edge next to the IAM (i.e., point A in Figure 12(b)). In particular, the worst-case scenario occurs for $\gamma = \pi/2$, as F_w is applied at the lever hinge point (i.e., C in Figure II.28(b)) and its moment arm around A is maximized. The condition for a stable anchoring can then be expressed by considering the rotational equilibrium in A, as

$$F_w < \frac{F_{anc}AB + F_{act}AD - F_{lap}AX}{AC} \tag{II.28}$$

where F_{lap} is the force required to lift the LapR-LMA and X is the position of the LapR-LMA center of mass.

This stability condition is plotted with solid black lines in Figure II.27, showing the maximum weight W_L that can be statically supported by the LapR-LMA as a function of d and γ. Also in this case, the performance improves as γ goes from $\pi/2$ to 0, since the point of application of F_w moves closer to the pivoting point (i.e., A in Figure II.28(b)).

By plotting together the tissue lifting and the tissue support models, as in Figure II.27, we can derive the operative

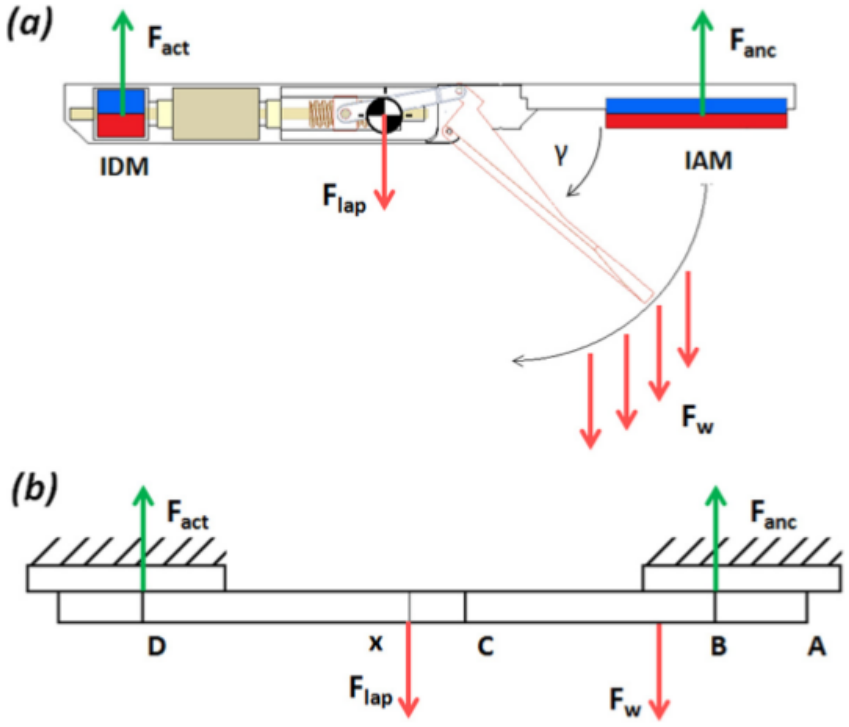

Figure II.28: Structural model used to predict the weight that the LapR-LMA can statically support. (a) Cross section of the LapRLMA with the points of application of the different forces. (b) Free body diagram of the LapR-LMA. A is the extremity of the device at the side of the IAM, B is the point of application of F_{anc}, C is the point where the hinge of the lever is located, D is the point of application of F_{act}, X is the LapR-LMA center of mass.

range for the LapR-LMA as the area below the minimum value of W_L that can be supported and lifted at the same time. Considering the geometrical features of the LapR-LMA and the values of the anchoring forces within the operative range, the pressure exerted by the device on the abdominal wall always stays below 30.7kPa, thus satisfying the clinical requirement on safety in the previous section II.2.1.

To validate the proposed performance modeling and demonstrate the feasibility of this approach, a three-tier validation approach was used. First, a benchtop experiment was performed to verify the weight that the device can controllably lift and hold at different intermagnetic separation distances. Then, an ex vivo experiment, using freshly excised porcine tissues, was performed to investigate the feasibility of using the LapR-LMA for liver retraction. Finally, the same procedure was performed laparoscopically in a porcine model to assess the usability and the safety of the device.

II.2.2.2 Benchtop experiments

The main goal of the benchtop experiment was to conrm the operative range of the LapR-LMA as previously estimated. As presented in Figure II.29, the external controller was afxed to a vertical adjustable slider and coupled with the LapR-LMA through a rigid plastic surface. The weight was connected to the lever –starting at $\gamma = \pi/2$– via an inextensible wire. Then, the external EM motor was activated with a step command at a speed of 1700rpm. The direction of rotation was reversed when γ reached zero, and the lever was moved back to its starting position. The maximum value of weight that was successfully lifted up and lowered down was recorded for each trial. This test was performed three times for each intermagnetic distance ranging from 2cm to 4cm, with 0.5cm increments

The trial performed at $d = 2cm$ lifting a weight of $500g$ is presented in Figure II.29.

The benchtop experiment confirmed that the designed mechanism is not backdrivable, as the lever was able to maintain its position for $\gamma = 0$.

II.2.2.3 Ex-vivo trials

A common procedure (cholecystectomy) requires retraction of the liver to achieve gallbladder exposure for removal. Liver retraction was hence simulated with the same setup used for the benchtop experiments using a freshly excised porcine liver with a weight of 672gr. The liver was placed 15cm away from the plastic surface. A crocodile grasper - connected to the LapR-LMA lever via an inextensible wire- was secured to a lobe of the liver. Retraction was performed starting from $\gamma = \pi/2$ for $d = 2cm$ (Figure II.30(a)) and $d = 4cm$ (Figure II.30(b)). The

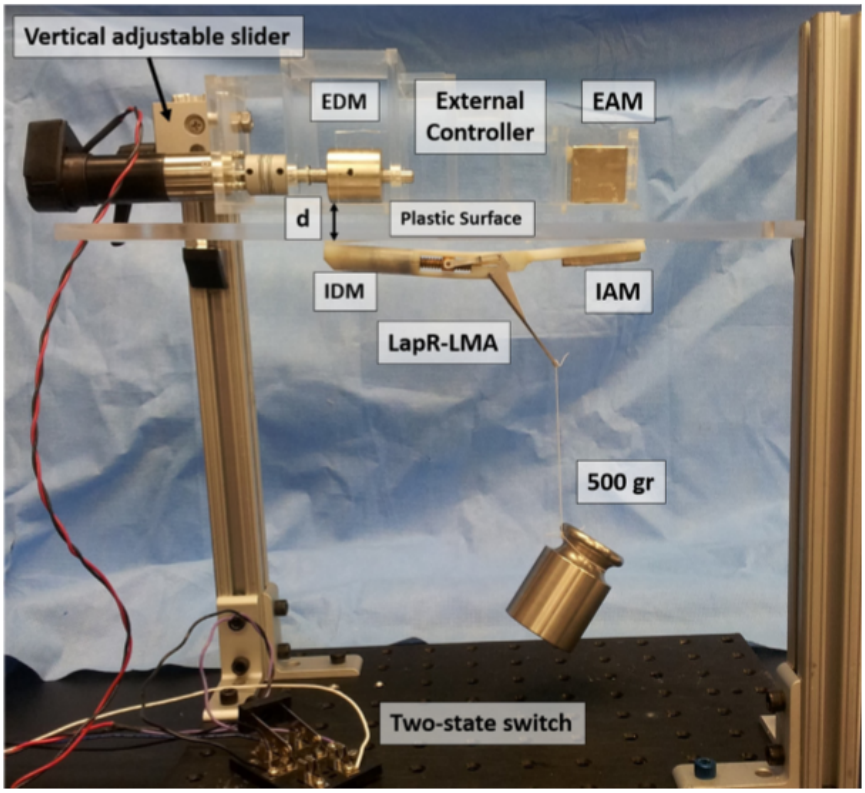

Figure II.29: Experimental setup during the benchtop experiments.

DC motor was driven at 1700rpm. Three trials were performed for each distance, and the liver was always lifted up and lowered down successfully. From the frames in Figure II.30, it is possible to appreciate how the portion of suspended tissue increases during retraction.

II.2.2.4 In-vivo trials

The primary goal of the in vivo trials was to qualitatively assess the functionality, the usability, and the safety of the LapR-LMA on an anesthetized porcine model. In particular, having a compliant tissue in between the external controller and the LapR-LMA allows the retractor to vibrate in the vertical direction under the effect of the varying F_{act}. This vertical wobbling may affect the lifting and the anchoring capacity, whereas the magnetic pinching may pose a safety risk to the tissue in between the external controller and the LapR-LMA.

The surgical procedure was performed at Vanderbilt University, with the assistance and collaboration of a specially trained medical team (IACUC Approval No. M/2014/163), in accordance with all ethical considerations and the regulations related to animal experiments. A 55-kg female Yorkshire swine was used for this study. After intravenous sedation, minimally invasive access was gained by one 5-mm trocar (5 Versaport Plus, Covidien, Norwalk,

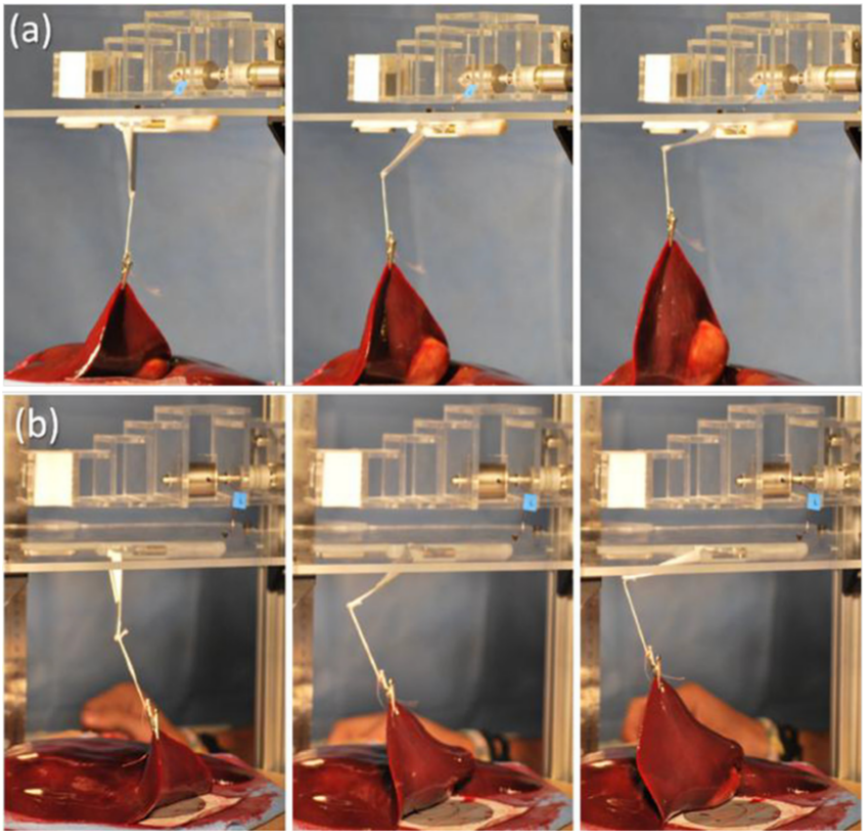

Figure II.30: Ex vivo liver retraction using the LapR–LMA. In the sequence presented in (a), the intermagnetic distance is 2cm, while in the sequence in (b) is 4cm.

CT) and one 12-mm trocars (5-12Versaport Plus, Covidien, Norwalk, CT). The LapR-LMA was introduced in the abdominal cavity and coupled with the external controller. An abdominal thickness of 2cm was measured by the surgeon at the insertion point, before the placement of the port. Then, a pneumoperitoneum was achieved with carbon dioxide gas.

Under endoscopic vision, the external controller was manually operated to drag the LapR–LMA next to the liver. The surgeon used a standard laparoscopic grasper to attach the crocodile jaws to one lobe of the liver. Retraction was then activated by rotating the driving magnet until the tissues below the liver were exposed, as shown in Figure II.31.

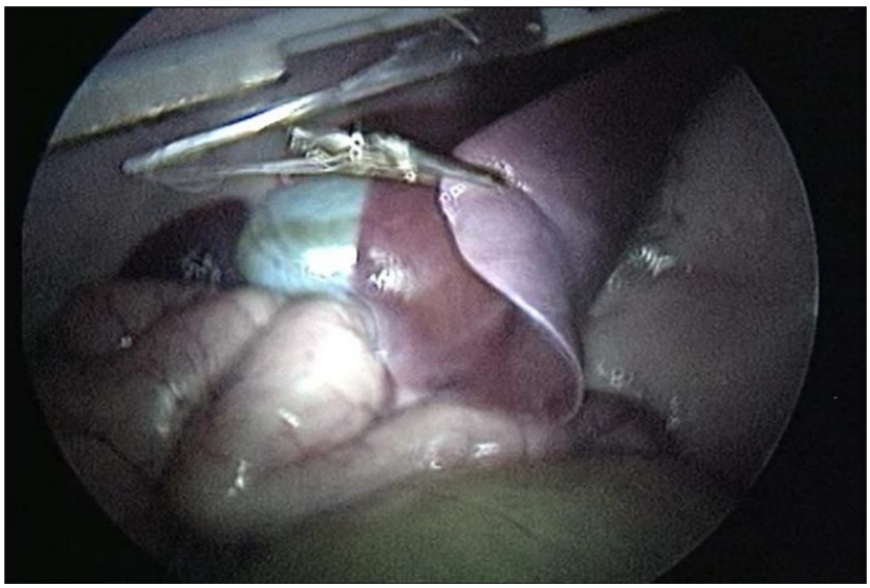

Figure II.31: LapR–LMA performing liver retraction during *in–vivo* trials.

This procedure was repeated five times, always changing the position of the LapR-LMA and the point at which the liver was grasped. The animal was sacriced at the end of the procedure. The region of abdominal tissue at which the LapR-LMA was anchored during retraction was then explanted and examined by an expert pathologist, reporting no sign of tissue damage due to magnetic pinching.

While the retraction was always successful and the LapR-LMA never lost the magnetic coupling with the external controller, the length of the device sometimes hampered the mobility inside the abdominal cavity. This limited the positioning of the LapR-LMA by only a few degrees off the sagittal plane of the animal. Placing the LapR-LMA along the transverse direction was not possible. This limited the reachable workspace and the possible approaching

angles to the tissue to be retracted.

II.2.3 Conclusions

Given the constraints in diameter and volume of a MIS instrument, the proposed design enables the transfer of a larger amount of mechanical power than what is possible to achieve by embedding typical electromechanical actuators on board. At the same time, due to magnetic coupling, triangulation is enhanced and invasiveness is reduced.

The LapR-LMA is 12.5mm in diameter and can be introduced laparoscopically. If the abdominal wall thickness is about 2cm, the LapR-LMA is able to retract more than ten times its own weight. Bench trials demonstrated that the designed mechanism is not backdrivable and guarantees accurate and controllable motion of the retraction lever in both directions. The mechanism is able to cover the full range of motion in about 20s. While the motion is slower if compared with manual operation of a laparoscopic retractor, the surgeon has the ability to adjust precisely the degree of retraction achieved by the LapR-LMA. Should a shorter time be required, the motor in the external controller can be replaced with a faster one.

In situations of overload, failure occurs in anchoring rather than actuation. If the anchoring failure occurs, the LapR-LMA needs to be recoupled with the external controller by the surgeon during the procedure. However, no failure was observed during the liver retraction experiment that was performed on a porcine model presenting an abdominal tissue thickness of 2cm.

While this study showed promising results, a number of challenges remain for future research. The closer the anchoring and the actuation units, the stronger the cross-coupling between them, thus, a better understanding will be crucial for designing a shorter version of the LapR-LMA. Reducing the length of the device would improve maneuverability and provide better access to the surgical target, as observed during the in vivo trials. The control strategy presented in [12] can hence be extended and generalized to a static anchoring unit to overcome such limitation.

This more in depth investigation can also be used to design LMA-based surgical robot with multiple DOFs.

II.3 Laparoscopic camera based on OMA

Local Magnetic Actuation has the potential to be used as an actuation method for robotic surgical platform with multiple degrees of freedom. The LMA method, however entails the use of two separate magnetic couples: one for actuation and one for anchoring. As a consequence the device size resulted too big for correct placement not

facilitating its use. Challenges still remain in terms of miniaturization, and mitigation of cross coupling effect for implementation of multi DOF platforms.

Another fundamental surgical device used in MIS is the surgical camera. The imaging device, from a robotic stand point (see Table II.3), does not require high actuation forces as interaction with the tissue is absent and it should be oriented precisely to favor visibility of the surgical workspace without limiting surgeons action. In fact, controlling camera orientation in a precise and smooth manner is necessary to provide the operator with a stable view of the area of interest [136].

Magnetic cameras that aimed to reduce the number of incisions in MIS or provide better workspace in the LESS approach, have been investigated, this concept is summarized in Figure II.32. The limitations of these past work are commonly to be found in the encumbering dimension of the device, and specifically include restricted tilt range [134, 175], the use of complex and bulky electromagnetic drivers [176], or the need for on board DC motors [140, 141].

To overcome the limitations that the devices proposed thus far have, and offer a compact low-cost laparoscope alternative solution, a novel magnetic approach that combines actuation and anchoring in one singe magnetic couple is developed for the actuation of a surgical capsule camera. This magnetic approach is defined as Orthogonal Magnetic Arrangement (OMA) and relies on smart placement of permanent magnets on board of the device. OMA allows for the pan and tilt of a magnetically anchored device with a mechanical auto–flip that compensates for dipole-dipole singularity. This arrangement, consisting of two internal permanent magnets (IPMs) and an external permanent magnet (EPM) coupled with a motor, has been developed and evaluated as the core component of a magnetic camera for MIS and LESS surgeries, though the concept is scalable and can be applied to address other clinical needs. The proposed magnetic camera (MC) is 5.5 mm in diameter and has 4 DOFs: robotic actuation of pan and tilt of the camera, as well as the ability to passively reposition the device along the abdominal wall. As the camera is tilted through 180°, the mechanical auto-ip is convenient since no software for correcting/flipping the image is necessary. The small form factor of the MC is ideal for laparoscopic procedures where space is constrained, such as MIS, LESS, NOTES in humans and in particular in pediatric patients [177, 178].

II.3.1 Principle of operation

Typically, magnetic instruments for laparoscopic surgery consist of an exterior body that embeds an EPM and an intra-abdominal device that embeds IPM(s) [134, 141, 163, 175, 179, 180]. Referring to Figure II.33(a), magnetic

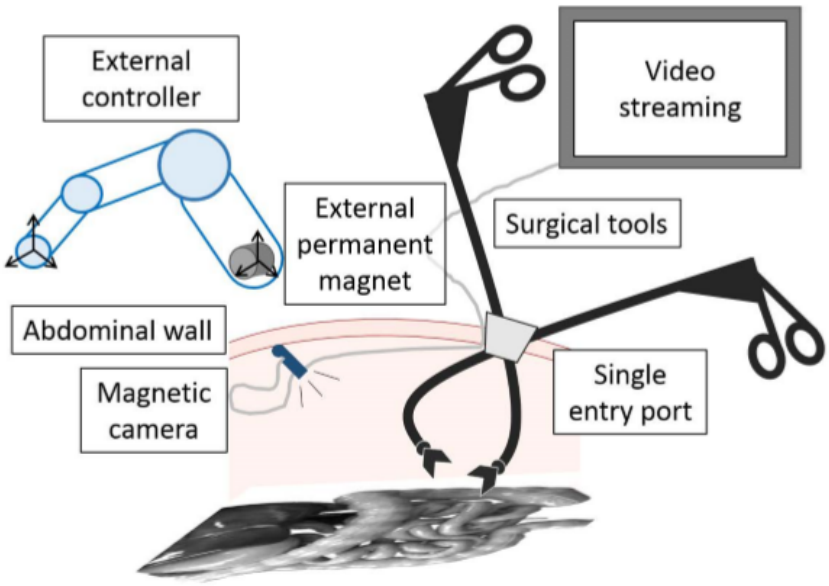

Figure II.32: A magnetic camera in a LESS surgical procedure. Once deployed inside the abdominal cavity, the camera can be optimally positioned to improve triangulation for the surgeon. The wiring required for power and communication can be placed on the side of the entry port, thus not requiring a dedicated access port for the camera.

coupling provides two gross translational DOF and a rotational DOF (pan) that are enabled via control position and orientation of the EPM: changing X_{EPM}, Y_{EPM} and Γ results in a corresponding variation in X_{IPMs}, Y_{IPMs} and γ.

In addition, the magnet arrangement that we propose -the OMA– provides a tilt DOF that can be controlled in a hemispherical workspace (i.e., range $0° - 180°$) when combine with pan γ DOF, with no need for flipping the image as the camera crosses the $\alpha = 90°$ position. The OMA consists of a cylindrical EPM with diametrical magnetization (indicated as $M1$ in Figure II.33(b)) and two IPMs: a spherical permanent magnet ($M2$ in Figure II.33(b)) that functions as the center of rotation of tilt, and a cylindrical and diametrically magnetized permanent magnet ($M3$ in Figure II.33(b)) that is placed in proximity of the first. Axial rotation of the EPM by an angle β results in a change in $M1$ orientation that, in turn, induces a tilt angle α of the internal device. This DOF can be achieved with the use of a single spherical IPM, though the symmetry of the magnetic field causes a singularity in the magnetic link when α reached $90°$. This symmetry results in infinite possible orientations of the internal device along its main axis. To compensate for such singularity, the additional IPM in the OMA is positioned so that its magnetization $M3$ is orthogonal to $M2$ and thus defines a unique orientation (tilting plane) of the device throughout the tilt range, while simultaneously generating additional attraction forces and torques used to control the device. This magnetic arrangement places the singularity plane outside of the working range of the device. The auto–flip feature resulting from this specific magnet arrangement allows the MC to always maintain an intuitive

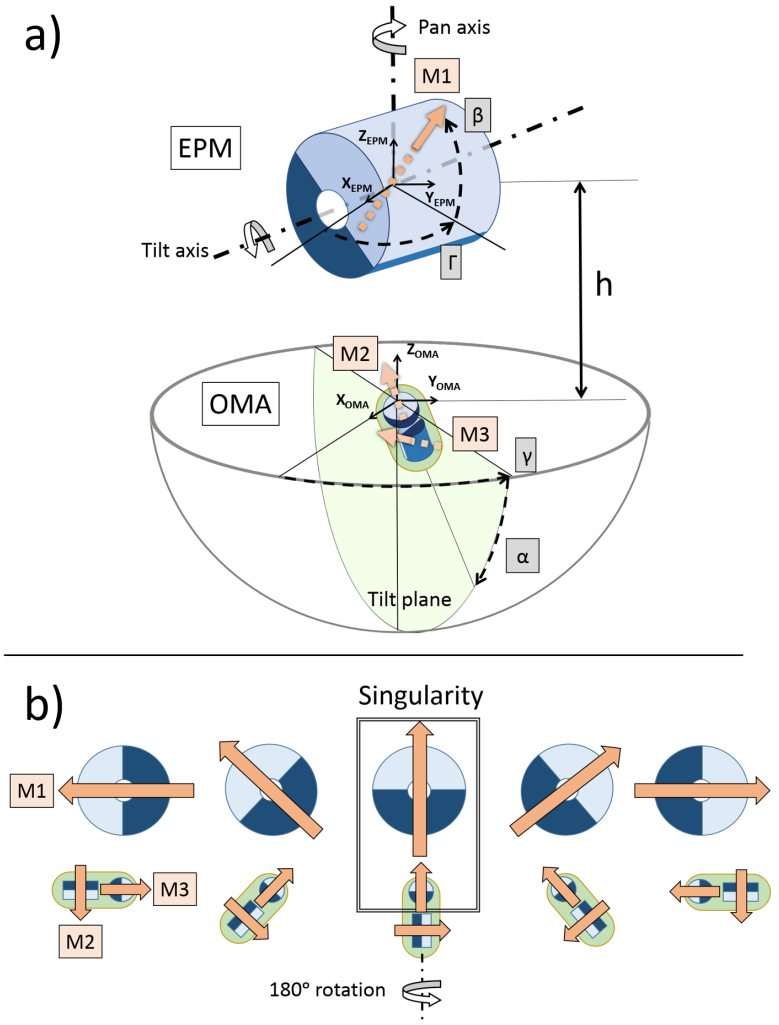

Figure II.33: (a) Schematic view of the EPM and IPMs with their reference frames. (b) Sequence along the tilt plane highlighting the auto-ip of the IPMs for $\alpha = 90^{circ}$.

image orientation, thus avoiding the additional computational burden of software correction.

II.3.2 No-slip tilt model

In this study, focus is given on modeling the tilting motion of the OMA as this is the main innovative feature of the proposed magnet arrangement. A static force and torque model as well as FEA simulations were utilized to quantify the tilt and establish a relationship between the β tilt angle of the EPM and α tilt angle of the capsule, hence of the IPMs. These models are later experimentally validated.

A 2D free body diagram was used to develop a static model along the tilt plane represented in Figure II.33(a). Owing to low velocities, inertial terms can be neglected.

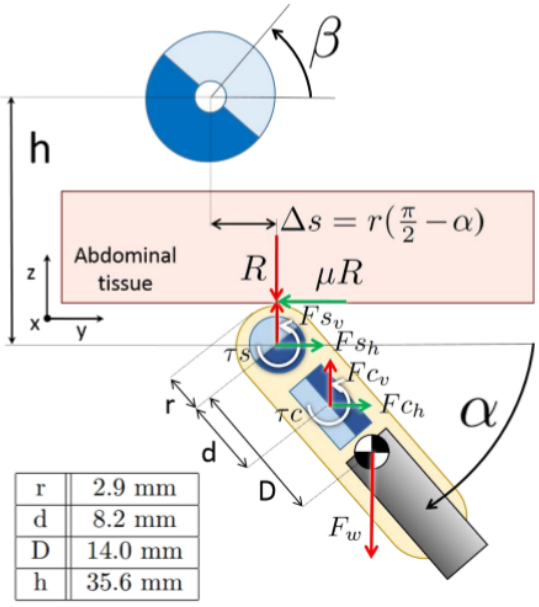

Figure II.34: Free body diagram and values of the main geometrical parameters of the magnetic camera based on the OMA.

Referring to Figure II.34, the forces and torque induced by the EPM on the spherical IPM are F_{s_v}, F_{s_h}, and τ_s, while those induced on the cylindrical IPM are F_{c_v}, F_{c_v}, and τ_c. The weight force, F_w, is the only applied external force and may be generalized for any payload. The use of highly compliant and lightweight electrical wiring allows for neglecting imposed constraint forces. Reaction force R is present due to contact with abdominal tissue. By consequence, a friction force μ_R acts along the y axis. The distance between the center of mass and the center of the spherical IPM is dened as D, the distance between centers of the two IPMs is dened as d, while r identifies the

radius of the spherical tilting end of the device. The axes of rotation of the EPM and spherical IPM are separated by a constant distance h along z, and Δs along y. The following equations of static equilibrium result from the applied forces:

$$\sum F_y : F_{s_h}(\beta,\alpha) + F_{c_h}(\beta,\alpha) = \mu R \tag{II.29}$$

$$\sum F_z : F_{s_v}(\beta,\alpha) + F_{c_v}(\beta,\alpha) = R \tag{II.30}$$

$$\begin{aligned}\sum M_z :& \tau_s(\beta,\alpha) + \tau_c(\beta,\alpha) - F_w(\beta,\alpha)Dcos(\alpha) \\ &+ F_{c_v}(\beta,\alpha)dcos(\alpha) + F_{c_h}(\beta,\alpha)dsin(\alpha) + \mu Rr = 0\end{aligned} \tag{II.31}$$

In order to develop a model that approximates the device behavior in a surgical scenario, tissue interaction and relative lateral displacement between EPM and IPMs must be considered. Local tissue deformation and normal force owing to magnetic attraction acting normal to the abdominal wall (F_{c_v}, F_{s_v}) suggest that the surface be better approximated as innitely rough ($\mu = \infty$). A no-slip condition, due to assumed pure rotational motion of the OMA, defines a displacement of the center of rotation as $\Delta s = r(\frac{\pi}{2}\alpha)$, where r represents the radius of the rotation.

A **no-slip tilt model** accounts for the innite friction approximation where Δs is a function of α and thus has an effect on induced forces and torques. Equations (II.29) are combined to take friction forces into account and thus result in:

$$\begin{aligned}\tau_s(\beta,\alpha) + \tau_c(\beta,\alpha) - F_w(\beta,\alpha)Dcos(\alpha) + F_{c_v}(\beta,\alpha)dcos(\alpha) \\ + F_{c_h}(\beta,\alpha)dsin(\alpha) + (F_{s_h}(\beta,\alpha) + F_{c_h}(\beta,\alpha))r = 0\end{aligned} \tag{II.32}$$

All magnetic forces and torques are dependent on both the positions (h and Δs) and tilt angles (α and β) of the EPM and IPMs. However because of the no–slip assumption, given a certain α we can determine Δs and parameterize it into the simulation. The intermagnetic distance h instead was kept constat to 35.6 mm. The forces and torques that the EDM induced on each IDM were computed via FEA simulation (Comsol Multiphysics, Sweden) individually and superimposed, following the linearity of Maxwells magneto-static equations ($\nabla \cdot B = 0$; $\nabla \times B = \frac{J}{c^2 \varepsilon_0}$, where J represent a steady current density, c the speed of light, and ε_0 the dielectric permittivity of vacuum) [181]. This assumption holds in absence of ferromagnetic materials beyond the accounted permanent magnets. The interaction between IPMs can be neglected owing to their constrained nature. The simulations were made by varying the tilt angle α in a range of 0^{circ} to 90° with an incremental step of 9°. Owing to symmetry of the OMA, only half of the 180° tilt span needs to be modeled. Simultaneously, β was varied in the range α to $\alpha - 60^\circ$ with an incremental step

of 6°. By mapping forces and torques over the aforementioned span of α and β and utilizing equation (II.32), it is always possible to unequivocally determine β given α.

II.3.3 Design and fabrication

An abdominal tissue thickness upon insufation ranging from 2*cm* to 4*cm* was considered when selecting the magnets for the MC and the external controller.

1) Magnetic Camera: The MC was designed to be inserted through a 5.5 mm trocar incision .The vision system is a 3.9*mm* diameter miniature endoscopic camera with embedded light source and 320*x*240 pixels resolution (AD-3915, Shenzhen Aidevision Technology, China).

The OMA IPMs consist of a 4.1 mm diameter spherical magnet (1.32T) and a 3.155 mm diameter and 6.35 mm long cylindrical magnet (1.32T) with diametrical magnetization (K&J Magnetics, Inc, PA, USA). The capsule body was 3D printed in Vero White material (Objet Pro30, Stratasys, Israel). Electrical wires with high exibility and low weight (Calmont, California, USA) were used to power and communicate with the camera. A Pebax 00-35 (Apollo Medical Extrusion, UT, USA) catheter (6 French gauge) with a wall thickness of 0.003 was used to embed the electrical wires. Heat-shrink tubing was utilized to ensure reliable electrical connections and to secure the camera orientation once calibrated. Finally, a thin plastic coating (EcoFlex 00-50, SmoothOn, PA, USA) was adopted to waterproof the device. This coating increases MC surface friction, which also enforces the no-slip assumption adopted during modeling. The MC prototype results 5.5 mm in diameter, 35 mm long, and weighs 2.32 g. A picture of the MC highlighting its main components is represented in Figure II.35(a).

2) External Robotic Controller: To precisely control the two rotational DOF of the EPM (25.4 mm OD, 6.35 mm ID, 25.4 mm TH, 1.32 T, also from K&J Magnetics, Inc, PA, USA), two stepper motors (28BYJ-48, Kiatronics, New Zealand) with holding torque of 15 mNm and step resolution of 0.35*deg* were adopted. To drive the motors, stepper drivers (ULN2003, Amazon,com) were controlled with a joystick embedding a dedicated microcontroller (MSP430, Texas Instrument, TX, USA). In order to avoid magnetic interference, non magnetic bearings (Igus, RI, USA) and other materials were used. The motors were placed at least 5*cm* away from the EPM in order to minimize their interaction with the magnetic eld. Pulley transmission was adopted to actuate the tilt angle β of the EPM. The resolution in controlling β, thus the tilt angle of the MC, can be adjusted by varying the radii of the two pulleys. The external controller, represented in Figure II.35(b), was designed to allow an easy integration with a robotic manipulator or a mechanical arm as support.

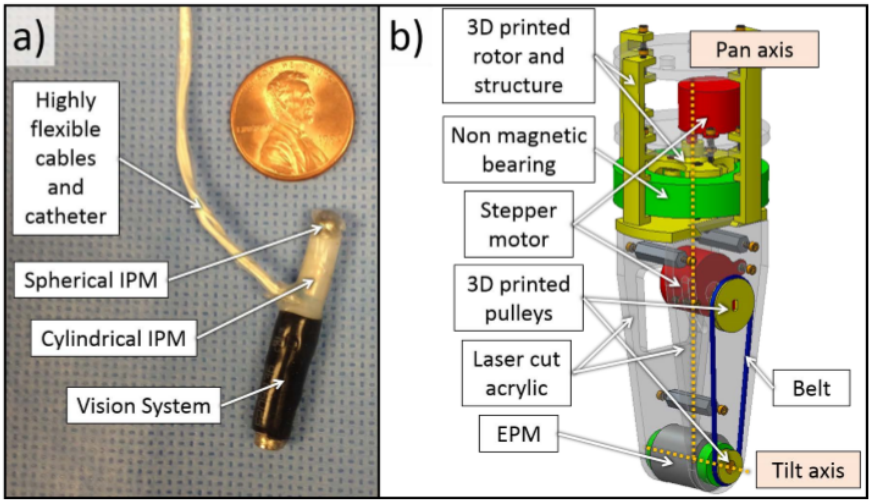

Figure II.35: (a) Magnetic camera prototype. (b) Graphic rendering of the external robotic controller.

II.3.4 Experimental validation

The rolling translation of the OMA resulting from a change in α was experimentally investigated. The external robotic controller, equipped with an accelerometer was placed 2 cm (h' in Figure II.36) away from an MC phantom. An acrylic sheet was used as a physical barrier. The MC phantom was equipped with a custom printed circuit board (PCB) mounting an accelerometer and a gyroscope in a single chip (LY3200ALHTR, ST Microelectronics, Switzerland) as seen in Figure II.36. The mass of the MC phantom was 2.25 g, thus very close to the MC prototype previously described.

The EPM was rotated at a constant speed of $11^\circ/s$ through the entire workspace. Three data sets, each consisting of five consecutive full α range spans, were collected. Experimental data are plotted in Figure II.37, together with the no-slip tilt model, equation (II.32). From the results, we can observe that the data match the predicted model with relative mean squared (RMS) error of $9.95\% \pm 4.16\%$. This may be due to imperfect orthogonality between the $M2$ and $M3$ magnetization vectors as well as a violation of the no-slip condition (slipping occurs) in the auto-flip region. Nevertheless, it is interesting to note that the relationship may be linearized in the β range of 6° and 55°. As expected, workspace symmetry can be seen about $\beta = 90^\circ$. The mid-region of the graph, the auto-flip region, corresponds to a β range between 55° to 125°.

The auto–flip was investigated by recording the angular velocity ω around the longitudinal axis of the MC phantom (see Figure II.36) using the same experimental setup. For this trial, the EPM was rotated with an angular velocity of $52.5^\circ/s$ so that the IPMs underwent an auto-flip, then direction was changed and this sequence repeated. The angular position β of the EPM is shown in Figure II.38 as a function of time. The MC phantom was then

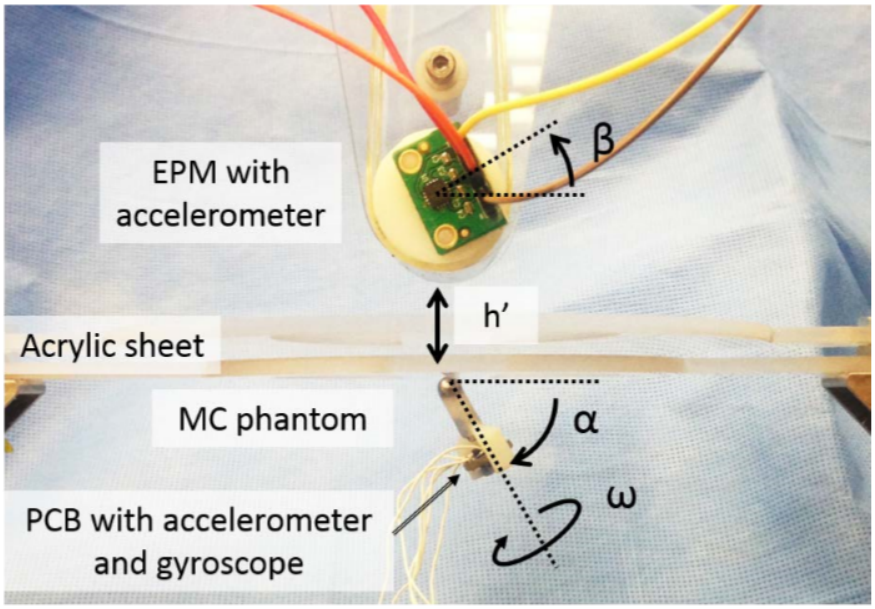

Figure II.36: Experimental setup used to validate the no-slip tilt model and to characterize the auto-flipping of the MC.

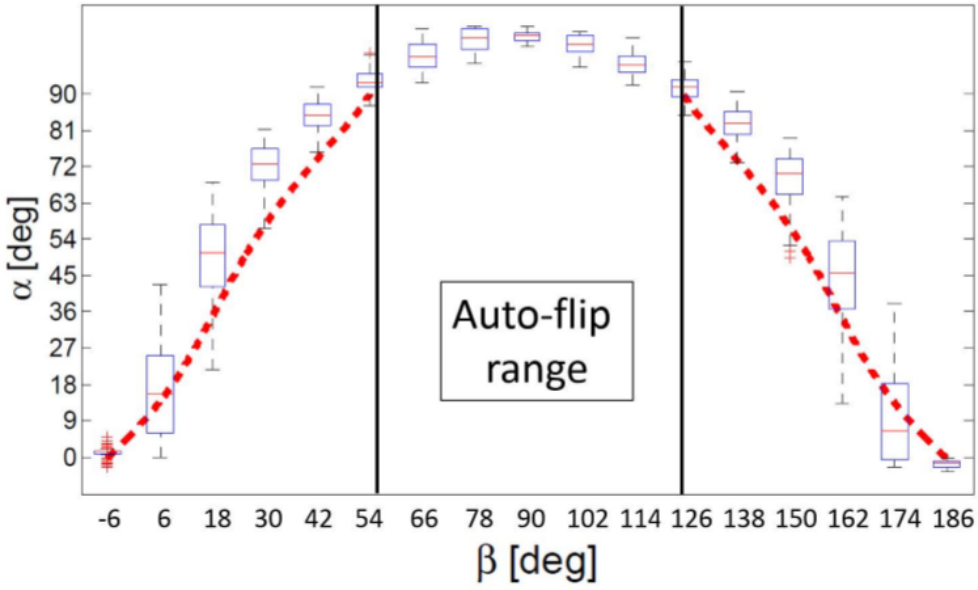

Figure II.37: Relationship between the input tilt angle β at the EPM and the MC tilt angle α from the experiments (box-plot) as compared to the theoretical model (dashed line). The region from 55° to 125° is where auto-ipping occurs.

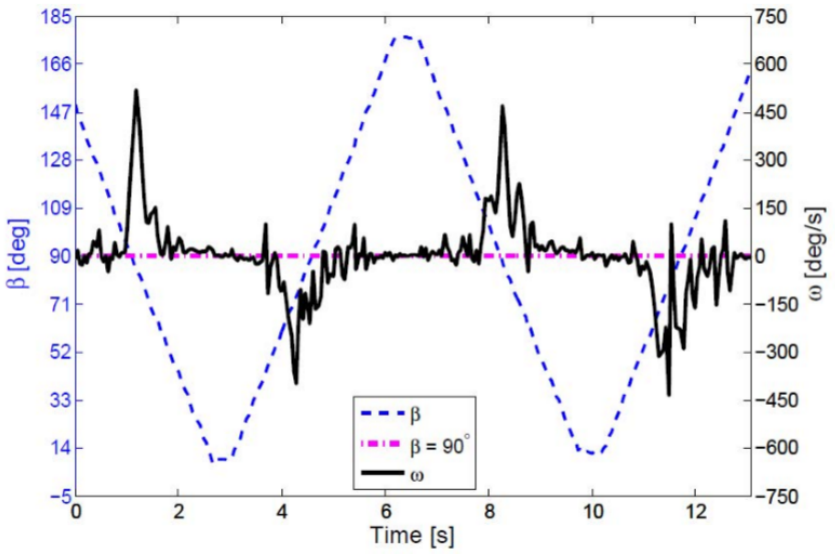

Figure II.38: Experimental characterization of the auto-flip. As the EPM tilt angle β (blue dashed line) crosses 90° (pink dashed line), auto-flipping of the MC occurs. The angular velocity ω around the longitudinal axis of the MC phantom is plotted as a black solid line.

moving through the auto-flip region (β range between 55° to 125°). On the plot in Figure II.38 is also represented the angular velocity of the MC along its main axis, ω, as recorded by the gyroscope. The auto-flip is repeatable and depends on the direction of rotation of the EPM. When the EPM is rotated clockwise, the MC rotation occurs in the positive direction of the gyroscope axis, while, when the EPM is rotated counterclockwise, ω assumes a negative value. This guarantees that the wires will not tangle if multiple auto-flips are executed. These results are further supported in Figure II.37, where the no-slip tilt model applies everywhere except the 55° to 125° range. Though the autoflip is difcult to model, explicit knowledge of this range can allow for implementation of control in the linearized span, while implementing a quicker flip sequence in the auto-flip range.

The functionality of the MC prototype was assessed by using the external robotic controller with a pulley transmission ratio of 1 and an acrylic sheet as in Figure II.36. The motion resolution for the MC was 0.5 in tilt and 0.35 in pan (same resolution as the stepper motor). With the same setup, we also investigated the effect of increasing the intermagnetic distance h' above $2cm$. The full range of tilt motion was reliably observed for $h' < 41mm$, while magnetic connection with the MC was lost for $h' > 51mm$.

II.3.5 Ex-vivo trials

To qualitatively assess the functionality of the device in a MIS clinical scenario, the MC was tested in a cadaver trial. A fresh tissue canine cadaver (25-kg female Beagle) was utilized to mimic a small workspace as seen in pe-

diatric patients. The surgical procedure was performed at Vanderbilt University Medical Center with the assistance and collaboration of a specially trained medical team, in accordance with all ethical considerations and the regulations related to animal experiments. Two incisions were made in the abdomen, the first of about 15 mm, placed in the lower quadrant along the anterior axillary line, and the second of 5 mm, just inferior to the sub-costal margin, for introducing the MC. The abdominal thickness was measured at the insertion point as 1 cm. Then, a 12-mm laparoscopic port was placed in the lower incision, and a pneumoperitoneum was achieved with carbon dioxide gas.

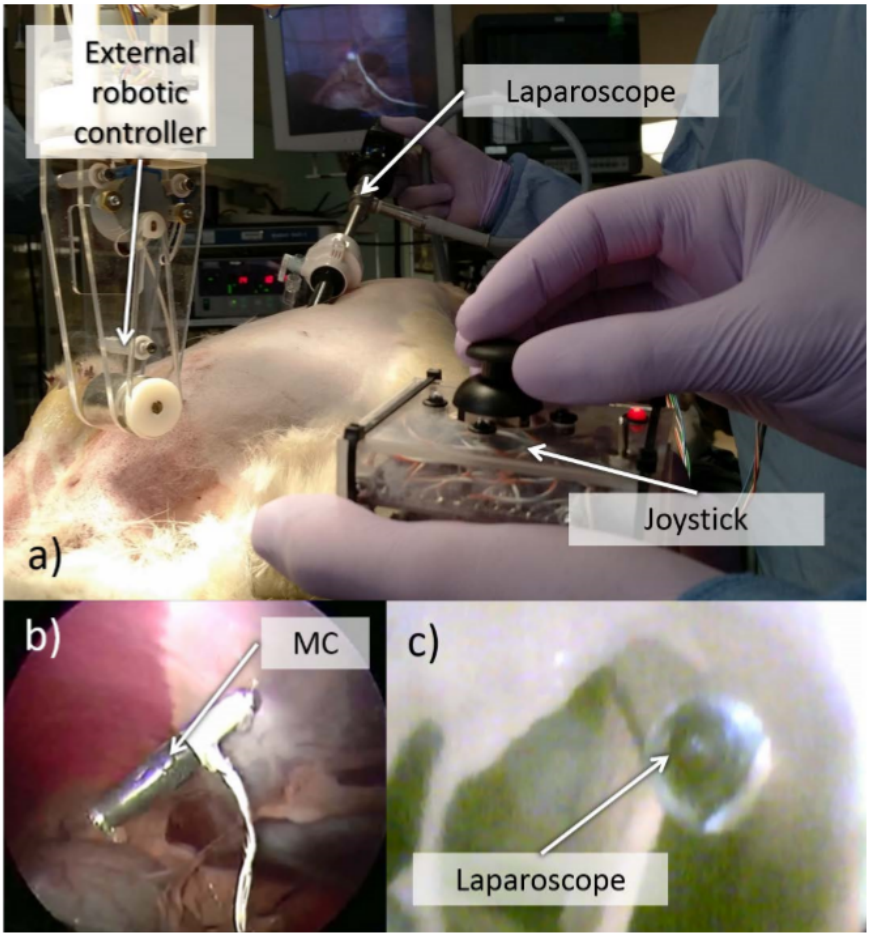

Figure II.39: (a) Photograph of the operative setup during the cadaver trial. (b) Laparoscopic view of the MC. (c) View of the laparoscope from the MC.

The MC was introduced through the upper incision along with 20 cm of cable and anchored to the intra-abdominal wall using the external robotic controller placed close to the skin, as represented in Figure II.39(a). Once anchored, the camera was shifted along the abdomen and placed to focus on the liver area. We evaluated the

full pan and tilt range by operating the EPM with the joystick. A standard laparoscopic camera (frame rate $30fps$, field of view 85°) introduced through the 12-mm port was used to visualize the MC while tilting and to record the image stream.

To simulate accidental magnetic decoupling, the EPM was displaced vertically to allow the MC to fall in the abdomen. Magnetic coupling was easily reengaged once the external robotic controller was brought back to its original position. A fallen camera may become dirty, though it may be cleaned via laparoscopic grasper and gauze within the cavity.

Static frames of the MC as observed by the laparoscope and of the laparoscope as visualized by the MC are represented in Figure II.39(b) and Figure II.39(c), respectively. During the cadaver trials, the MC qualitatively confirmed

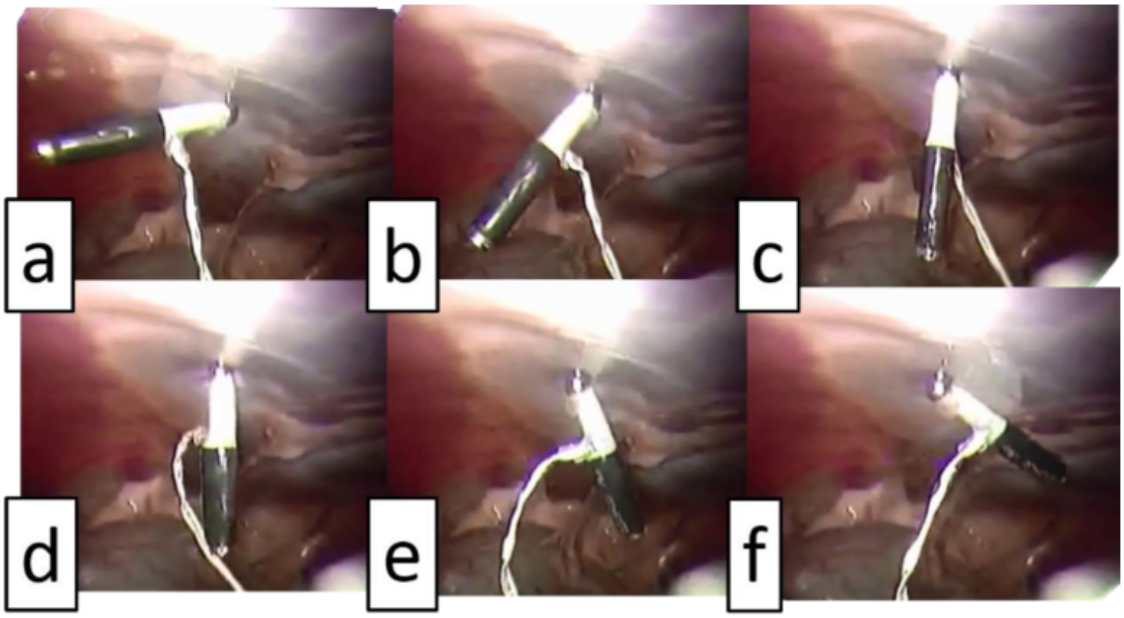

Figure II.40: Snapshots of the tilt angle control during the ex vivo trial. (a)(b): Linear and controllable range before the auto-ip regime [$6^\circ < \beta < 55^\circ$] (c)(d): auto-flip regime [$55^\circ < \beta < 125^\circ$]. (e)(f): Linear and controllable range after the auto-ip regime [$125^\circ < \beta < 186^\circ$].

the same range of motion and resolution observed during bench-top trials, Figure II.40. Magnetic coupling was always reliable and camera image was stable whenever the external controller was not activated. No significant image vibrations, potentially caused by laparoscope motion and by pressure regulation, were observed during operation of the MC. Image quality of the vision module integrated in the MC was below the standard for laparoscopy.

II.3.6 Conclusions

OMA was introduced for the first time as alternative simultaneous magnetic actuation and anchoring solution to the LMA. This solution has been modeled, validated, and utilized in an MC prototype. A unique feature of the device is the auto-flip at the bottom of its hemispherical workspace that provides a controlled and repeatable rotation of the device about its own axis. An immediate use for this unique feature is to prevent the need for flipping the image as the MC crosses the vertical plane. To improve usability, sensors can be placed on the external controller to measure the magnetic moment M1 of the EPM allowing for real-time monitoring of pan and tilt of the MC. It may benet the user to be alerted via software of the pan and tilt angles during operation as well as whether the MC is in, or is approaching, the auto-flip region.

Although this work targets an imaging application, the OMA can be utilized in other scenarios, such as automatic suturing, where translation and rotation are both required.

Successful fresh-tissue cadaver trials were conducted on the MC using a canine model. Ease of device placement and operator viewing via joystick suggest that, if the image quality is improved, the MC has application for laparoscopic procedures where space is constrained, such as MIS in pediatric patients.

The OMA solution, from a fabrication point of view is extremely low–cost. Two miniaturized permanent magnets and a plastic case used for the imaging device can be considered disposable if they are used to augment wireless endoscopic capsule systems already available in the market which can be reused (e.g. Pillcam). This magnetic implementation, comes with a compact external controller that contains only one permanent magnet. This favourites device integration in the OR by using a supporting arm such as the ones already in use [182] or by substituting an imaging robotic arm in a surgical robotic platforms.

II.4 Subcutaneously implantable pump for the treatment of refractory ascites

II.4.1 Clinical need

Ascites is a chronic condition in which accumulation of fluids occurs in the abdominal cavity. This liquid formation is due to portal venous hypertension, which causes body fluids to collect in the abdomen from the liver. The main cause for ascites is liver cirrhosis (80-85% of the cases) [183].

The preferred treatment for ascites is a low-sodium diet and administration of diuretics. However in 10% of the cases, ascites develops in refractory ascites (RA) for which conventional treatments are ineffective, and it has significant high morbidity [184].It has been estimated that by 2020, 100,000 patients will develop RA between the

United States and Europe [185].

Treatment options to RA are large volume paracentesis (LVP) [186] or transjugular portosystemic shunt (TIPS) [187]. LVP consists of draining the excess fluid through a needle inserted in the abdominal cavity. LVP larger than 5 liters are followed by the administration of albumin to decrease post-paracentesis circulatory disfunction [188]. This approach can only be performed at the hospital–lowering the patient's quality of life and increasing cost of care due to the recurrent drugs administration [189]. TIPS is instead an invasive surgical procedure in which a shunt between portal and suprahepatic veins is formed. This relaxes the portal vein hypertension but with complications such as worsening encephalopathy [190].

There is hence an urgent need to develop an alternative solution for the treatment of RA.

Recently, an implantable automated low-flow pump, trademarked with the name of alfapump® (Sequana Medical AG, Zurich, CH), received CE approval, and its efficacy is currently under clinical investigation. The device consists of a pumping element and two separate catheters which transfers the accumulated liquid from the abdominal cavity to the bladder for elimination via urination [191]. The implantable pump monitors the pressure inside the abdominal cavity and autonomously drains small quantities of liquid every 15-30 minutes. The pumping mechanism is a gear pump, and it is powered via wireless rechargeable battery. The amount of liquid drained is pre-programmed, and the device is charged using a rechargeable external controller. The alfapump®, embeds a brushless motor, gear mechanism, and electrical board with recharging coil. Due to its large form factor, it has encountered a variety of complications during implantation (e.g. pump pocket infection, pump malfunctioning, macroscopic haematuria). A pilot study with 56 patients conducted in 2017 [192], reported a significant decrease in the number or LVP for the patients treated with alfapump®, but it also reported 23 pump-related reinterventions required during follow up, and pump explantation in 48% of the patients due to serious adverse events.

A subcutaneous pump can be seen as a single degree of freedom mechanism that lays underneath a thin (< 5 mm) layer of skin. This represents an ideal clinical scenario for exploitation of the LMA approach.

In this study, the development and evaluation of an LMA-based is presented, subcutaneous pump, Figure II.41. The device is composed of: a Catheter-like Implantable Pump (CIP), and a Magnetic External Controller (MEC) that actuates and monitors the correct functioning of the CIP.

Both CIP and MEC have low fabrication costs. The wireless transmission of mechanical power across physical barriers offered by the LMA approach, enables the CIP to be composed by passive components only (power supply, DC motor and electronics are embedded in the MEC only), obtaining a catheter-like shape, which can take advantage of traditional interventional implantation methods (e.g. Tenckhoff catheter placement [193]).

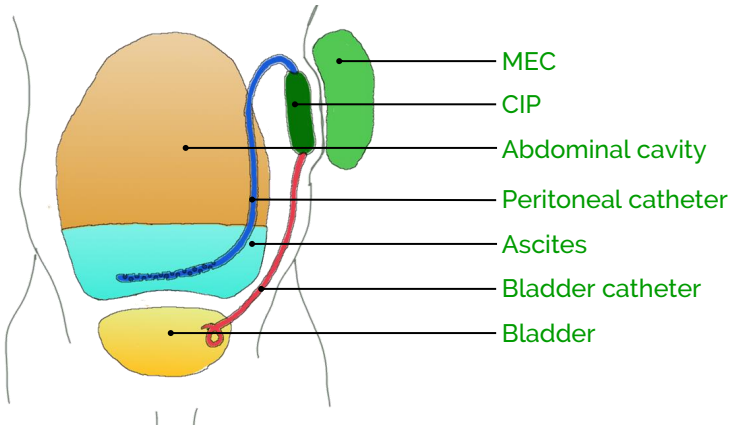

Figure II.41: Schematic representation of the LMA based pump. The LMA pump collects ascitic liquid from the abdominal cavity and delivers it to the bladder for expulsion via urination.

II.4.2 Principle of operation

In the presented LMA implementation, the rotation of the IDM, is converted into linear motion to move a syringe plunger in a reciprocating positive displacement pump design. This is achieved by augmenting the IDM with a threaded section which converts IDM rotation in linear motion about a fixed nut, Figure II.42(a). As the IDM is spun in one direction and the other, a syringe plunger, connected to one side of the IDM, converts the bidirectional linear motion into pressurization, depressurization of an internal chamber.

Two check valves (one opens for negative pressure ratings, one for positive) ensure unidirectional flow and avoid any unwanted reflux from the bladder to the abdominal cavity. From a study conducted on bladder outlet obstruction [194], an obstructed bladder is identified when the bladder internal pressure surpasses 40 cmH_2O. Hence, the selected check valve must have low cracking (opening) pressure to offer low resistance to the device's generated flow, while being an effective seal to abnormal bladder pressures. To maintain a catheter shape of the pump, the internal chamber is embedded into a concentric outer case.

II.4.2.1 LMA actuation unit dipole model

The EDM and IDM of the LMA actuation unit are two diametrically magnetized magnets free to rotate about their parallel axes. Each magnet orientation in space is defined by the reference frame ($\{\Omega\}$ and $\{\Sigma\}$ for EDM and IDM, respectively) located in the center of mass of each magnet. The distance between EDM and IDM reference

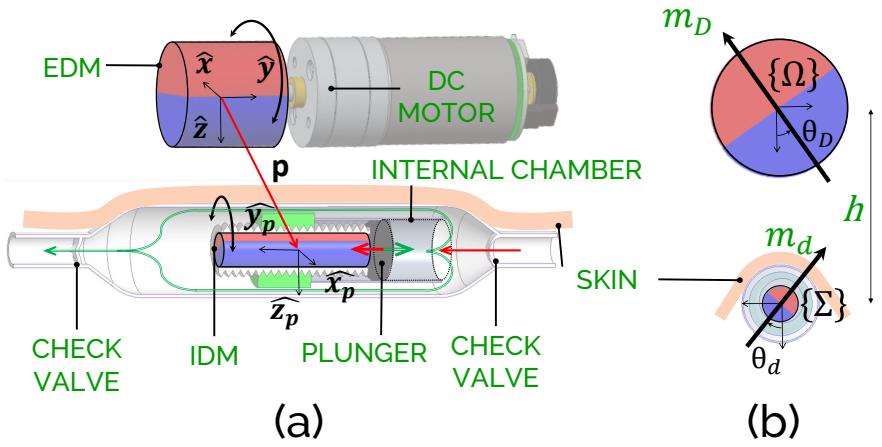

Figure II.42: (a) Schematic representation of the principle of operation of the LMA based pump; (b) Cross sectional view of EDM and IDM to show their magnetization vectors ($\boldsymbol{m_D}$ and $\boldsymbol{m_d}$) and angular displacements (θ_D and θ_d).

frames, is a three dimensional separation vector $\mathbf{p} \in \mathbb{R}^{3\times 1}$, Figure II.42(b).

$$\begin{aligned} \{\Omega\} &= [\hat{\mathbf{x}},\ \hat{\mathbf{y}},\ \hat{\mathbf{z}}] \quad \{\Omega\} \in \mathbb{R}^{3\times 3} \\ \{\Sigma\} &= [\hat{\mathbf{x}}_\mathbf{p},\ \hat{\mathbf{y}}_\mathbf{p},\ \hat{\mathbf{z}}_\mathbf{p}] \quad \{\Sigma\} \in \mathbb{R}^{3\times 3} \end{aligned} \tag{II.33}$$

Each magnet diametrical magnetization vector ($\mathbf{m_D}$ and $\mathbf{m_d}$ for the EDM and IDM, respectively) is described by an angular coordinate (θ_D and θ_d for EDM and IDM, respectively) defined on the plane ($\hat{\mathbf{x}}\hat{\mathbf{z}}$ and $\hat{\mathbf{x}}_\mathbf{p}\hat{\mathbf{z}}_\mathbf{p}$ for EDM and IDM, respectively) perpendicular to magnet's rotational axis. As a reminder to the reader, the torque transmittable (T_{LMA}) across the magnetic link, when the magnets relative position to each other is fixed, depends in a non-linear fashion to the angular displacement $\Delta\theta$:

$$T_{LMA}(\Delta\theta) \triangleq T_{MAX}\sin(\Delta\theta) \tag{II.34}$$

where T_{MAX} is a maximum transmittable torque over the magnetic couple and occurs when $\Delta\theta = {}^{pi}/_{2}$. The value of T_{MAX} is a function of the magnetization vectors (i.e. $\mathbf{m_D}$ and $\mathbf{m_d}$) and on the separation distance vector ($\mathbf{p}$).

When the torque transmitted by the EDM to the IDM (T_{LMA}) is higher than the torque acting as a load on the IDM, the coupling is established and both magnets rotate with the same average angular velocity (i.e. $\dot{\theta}_d = \dot{\theta}_D$). However, if the load acting on the IDM surpasses the maximum transmittable torque (T_{MAX}), the magnetic coupling is lost ($\dot{\theta}_d$ averages 0), and the IDM unit enters in a so-called pole slippage regime [157].

In the proposed clinical scenario, an overload of the IDM might be the result of a clogged portion of the catheter (e.g. tissue ingrown or catheter kinking). This can be overcome with proper catheter material and design, nev-

ertheless, the ability to detect pole slippage (as detailed later in Section II.4.3.4) can be used to warn the user of malfunctioning.

In previous LMA investigations [7, 11], alignment assumptions were used to estimate T_{MAX}. The value was calculated via Finite Element Analysis (FEA) varying solely the intermagnetic separation distance (h) along the EDM's $\hat{\mathbf{z}}$ axis, such as $\mathbf{p} = [0, 0, h]^T$.

In this study, however, the separation vector $\mathbf{p}$ must consider a varying intermagnetic distance h (to generalize for various skin thicknesses, hence include different patients), and a varying controllable displacement l along the rotation axis $\hat{\mathbf{y}}$ (to include IDM resultant linear motion).

Hence, to expand the understanding of LMA actuation unit, we calculated the maximum transmittable torque (T_{MAX}) along two directions such as $T_{MAX} = T_{MAX}(\mathbf{m_D}, \mathbf{m_d}, \mathbf{p})$, where $\mathbf{p} = [0, l, h]^T$.

The problem of estimating torques (and forces) between permanent magnets can be solved using either (1) FEA as proposed by [7, 9] or (2) with analytical dipole-dipole modeling for magnetic field approximation such as in [195]. The FEA method achieves good results in calculating the magnetic field expression in proximity of the magnet by including the magnet's shape in its formulation, but it is computationally expensive. The dipole-dipole model, on the contrary, is easier to compute, achieves equivalent results to FEA in far-field calculation, but, due to magnet's shape generalization, lacks in precision for close-field (in proximity of the magnetic source) quantification. In this study, for quick selection of permanent magnets and subsequent estimation of forces and torques of the coupling, the latter approach was adopted. We hence calculated T_{MAX} using the expression

$$T_{MAX}(\mathbf{m_D}, \mathbf{m_d}, \mathbf{p}) = \frac{\mu_0 \|\mathbf{m_d}\| \|\mathbf{m_d}\|}{4\pi \|\mathbf{p}\|^3} \mathbf{m_d} \times D(\mathbf{p}) \mathbf{m_D} \tag{II.35}$$

where μ_0 is the vacuum permeability, and $D = 3\mathbf{p}\mathbf{p}^T - \mathbf{I}$, with $\mathbf{I} \in \mathbb{R}^{3\times3}$ being the identity matrix.

Among the commercially available Neodymium magnets, $RX04X0DIA$ and $D4X0DIA$ (K&J Magnetics Inc., Pipersville, PA, USA) were selected as EDM and IDM, respectively. The selection was based on the assumption that the chosen magnets were able to transmit to the IDM an amount of torque larger then what conventional micro motor can provide. This ties with the final aim of avoiding pole slippage and maintain a stable coupling during pumping action. The limits for h were chosen assuming a thin cutaneous layer of a few millimeter with the addition of a variable fat tissue while l was limited to the IDM axial size.

T_{MAX} was estimated using Matlab (Mathworks, Natick, MA) varying $h \in [5mm, 25mm]$ and $l \in [0, 25mm]$. Only a positive l displacement was analyzed due to symmetry in the magnetic field. Figure II.43 shows a contour map of

the T_{MAX} as a function of the considered workspace.

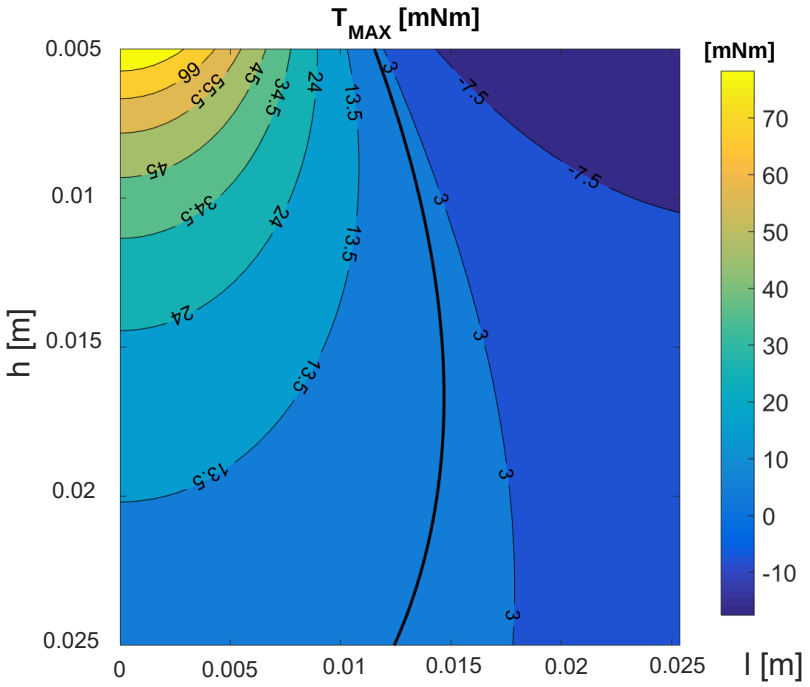

Figure II.43: Contour plot of T_{MAX} for varying h and l. The black thick line identifies the stall torque (5.42 mNm) for a commercially available DC micro motor comparable in size to the IDM.

In Figure II.43, the thick black line identifies the contour line for T_{MAX} = 5.42 mNm. This value is the stall torque of a commercially available DC micro motor (DCX10L, Maxon Motor, Sachseln, Switzerland) with comparable size to the IDM.

The selected coupling can hence transmit to the IDM an amount of torque larger than what can be achieved by a DC micro motor within a separation distance h range suitable for subcutaneous implantation, while offering a lateral displacement l of $\pm$ 11.4 mm.

II.4.2.2 Off-board sensing

To correctly operate an LMA device, once within the body, two challenges arise:

1. IDM alignment over the EDM.
2. pole slippage – malfunctioning – detection.

In Subsection II.1.3.1, the closed loop control problem of LMA was addressed using magnetic field sensors

(MFSs) to measure EDM and IDM magnetization vectors angular displacement to estimate the respective angular velocities ($\dot{\theta}_D$ and $\dot{\theta}_d$). The EDM and IDM were assumed aligned, and the MFS used to estimate $\dot{\theta}_d$ was located in close proximity of the IDM, requiring electronics on board of an LMA device.

In [12], the LMA control problem was augmented by introducing the use of an observer to verify the correct functioning of the magnetic link (i.e. identify pole-slipping). The prediction problem was casted using feedback from the EDM side only (i.e. control input: ΔV, DC motor torque: τ_D, and EDM angular velocity: $\dot{\theta}_D$).

The IDM alignment over the EDM (problem 1. above), was tackled using MFSs embedded in the MEC only – outside the body. The MFS arrangement, the algorithm used for localization and the methods used to validate a localization routine is presented with details in Section II.4.4.1.

The ability to instead solve for: 2) pole slippage detection, has been addressed in [12], hence it is not here discussed.

II.4.3 Design consideration and fabrication

The alfapump®'s main advantage compared to LVP is the daily removal of small quantities of ascitic liquid. The alfapump® autonomously removes a preprogrammed amount of liquid during the day and deactivates at nights for patients comfort. A preliminary clinical trial of the alfapump® performed on 10 patients revealed a median pumped volume of 1 liter per day [196].

A study on the performance of LVP has shown that on average, an LVP session lasts 97 minutes, removes 8.7 liters with a pumping rate of 1 liter every 6 minutes [197]. Patients affected by RA require an LVP every 8-10 days. The ability to remove large quantity of fluid in a short period of time comes with the disadvantage of administering albumin to prevent postparacentesis circulatory dysfunction due to alteration of system hemodynamics [198].

With the presented device, the patient self administers a pumping session to follow treatment plan or whenever he/she has a discomfort sensation (bloating) – hence avoiding recurrent hospital visits for treatment.

The main input parameter used to design the system is the pumping flow rate. Assuming a daily volume of 1 liter to be removed, a reasonable self administer session of 15-20 minutes, identifies a target flow rate of 3-4 L/h.

II.4.3.1 CIP – Catheter-like implantable pump

The main advantages of the CIP, when compared to alfapump® are: 1) its catheter-like shape that simplifies the implantation procedures, and 2) a simpler low-cost design with no electronics on board.

The CIP can be manufactured as a single-piece catheter device with three functional parts: a peritoneal catheter (CIP_a), a bladder catheter (CIP_b) and a cylindrical pump (CIP_c) connected with CIP_a and CIP_b on either sides, Figure II.44(a).

Both CIP_a and CIP_b are dual lumen 10 Fr catheter. One lumen is dedicated to a 0.035" diameter guide-wire, while the other lumen displaces fluids via a series of distally placed holes (suction for CIP_a, ejection for CIP_b). The guide-wire lumen's access (Figure II.44(b)) is located in proximity of the pump portion (CIP_c). A tapered distal end of the catheters facilitates catheter deployment through soft tissue under guide-wire guidance.

These features have the potential to allow interventionist (e.g. interventional radiologist, interventional urologists) to implant the CIP_c thought the fat subcutaneous layer (tunneling), while CIP_a and CIP_b to be routed via ultra-sounds/guide-wire guidance to the target area. This implantation method builds on existing and established techniques, avoiding complex and costly surgical procedures. If catheter's ends require anchoring with the surrounding tissue for correct function, Dacron cuffs – included in the distal portions of CIP_a and CIP_b – can be internally sutured via minimally invasive (laparoscopic) approach.

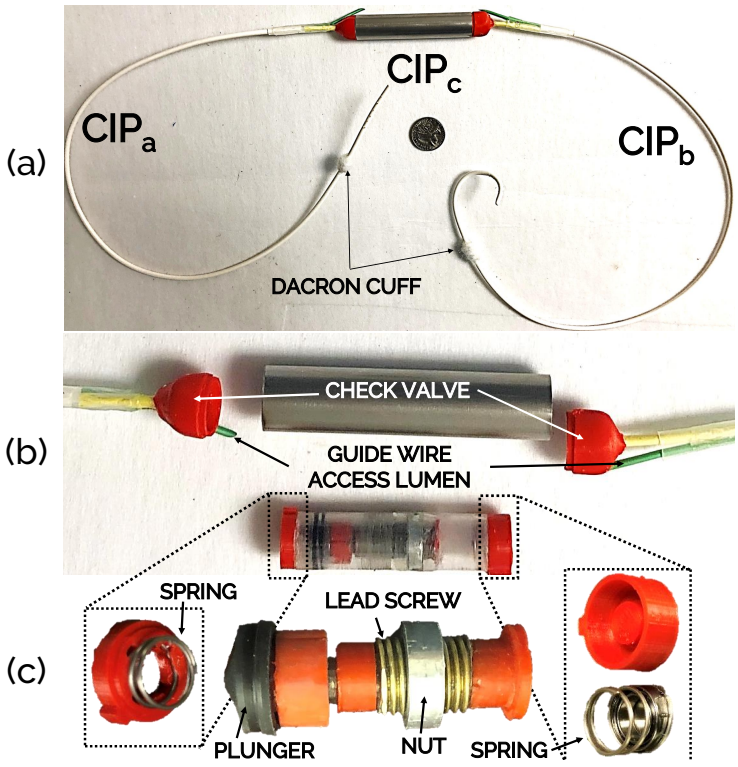

Figure II.44: (a) Assembled CIP next to a quarter dollar; (b) CIP_c before assembly; (c) Assembled pumping element.

The CIP_c is instead composed of a 70 mm long stainless steel case (16 mm outside diameter) used as concentric chamber of the embedded pumping element. On both ends of the steel case, a 3D printed part embeds a check valve (80500 - Qosina Corp. Edgewood NY) which is connected to the infusion lumen of either CIP_a and CIP_c, Figure II.44(b).

The pumping element is a reciprocating positive displacement pump, which has a linear relationship between output flow rate and input IDM resulting linear velocity. It consists of an IDM (6.35 mm in diameter, 25.4 mm long) with a threaded central section (brass lead screw with pitch p = 1.06 mm). One side the IDM is glued to a ball bearing that mates with a 3D printed plunger hold; the other side instead is glued to a flat, 3D printed part, Figure II.44(c). An aluminum nut is aligned over the thread during assembly, and glued to two plastic cylinders (D = 12.07 mm internal diameter). Two 3D printed parts sit on either ends of the plastic cylinders II.44(c). On the plunger side, the mount holds a spring while allowing fluid to pass; on the flat end side, a watertight mount holds a spring via ball bearing.

The ball bearings included on both ends remove rotational motion of the IDM's extremity to obtain a pure translational motion, hence minimizing friction. Similarly, the use of springs facilitates inversion of IDM rotational motion. This design is fail-safe (piston travel is limited by the length of the threaded portion) and does not require an IDM known initial position with respect to the nut. If the IDM is spun so that the threaded section surpasses the fixed nut, the pumping element spins free until rotation is inverted – hence autonomously removing any initial position bias.

To minimize friction of moving components, a biocompatible PTFE-based lubricant was used (TriboSys®, Miller-Stephenson Corp., Danbury, Connecticut, USA). All the components were glued using medical grade UV-curing glue (4307 Loctite, Düsseldorf, Germany).

II.4.3.2 Estimated $\dot{\theta}_d$ for desired flow-rate

A target flow rate of 3 L/h converts to 0.83 ml/s. The designed pump is able, during one pumping cycle, to remove a cyclic volume V of:

$$V_{cyc} = \pi(D/2)^2(Np) \tag{II.36}$$

where N is the number of revolutions and p is the pitch of the lead screw. With N = 10, and given the above mentioned pitch p, the cyclic volume is estimated as V_{cyc} = 1.21 ml.

To meet the required flow-rate, the cyclic period T, during which the pump advances and retracts, is T = 1.45

s. During half cycle, the pump is pumping water, while on the other cycle half, liquid is collected. Keeping the assumption of N = 10 rotations, and assuming a step-wise constant velocity of the IDM ($\dot{\theta}_d$), leads to estimating:

$$\dot{\bar{\theta}}_d = \frac{N}{T/2}, \quad \dot{\bar{\theta}}_d = 827.58\, RPM. \tag{II.37}$$

This value is theoretical and serves as feasibility check as well as quick estimate for the designer to match hardware needs with application's requirements. In practice, motor and control scheme performances affect the profile of $\dot{\theta}_d$.

II.4.3.3 MEC – Magnetic external controller

To locate, actuate and monitor the implanted CIP, a MEC was fabricated. Figure II.45(a) shows an exploded schematic view of the MEC. A plastic (3D printed) case Ⓐ (dimensions: 2.1" H x 2.4" W x 5.5" L) embeds a series of electrical and mechanical components. Four layers (1/2" x 1/2" x 0.004") of steel (ASTM A109) sheets Ⓑ are used to shield two magnetic field sensors Ⓒ (A1326, Allegro MicroSystems, Worcester, MA, USA) located in proximity of the EDM Ⓓ. A DC motor with encoder Ⓔ (#3237. Pololu Corp., Las Vegas, NV, USA) is controlled via and H-bridge motor driver Ⓕ (#1212; Pololu). A coupler Ⓖ connects the motor shaft to the EDM one which terminates with a bronze sleeve bearing Ⓗ to minimize friction. Embedded in the top cover part of the case, three push buttons Ⓘ, a Light Emitting Diode, and OLED Screen Ⓙ (#931, Adafruit Industries, New York City, NY, USA) are used as user interface.

The electronic components are all connected to an embedded micro controller Ⓚ (ATmega32U4, Microchip Technology, Chandler, AZ). The MEC is powered operating an ON/OFF switch Ⓛ included in the case, after connecting the MEC with a 12V power supply via a 2.1 mm DC barrel-jack Ⓜ. Currently, the MEC is hand held, but to enhance ease of use, straps, similar to the support belt for the recording device of a capsule endoscope (Pillcam, Medtronic, Minneapolis, MN, USA), can be added.

As visible from the MEC assembled view in Figure II.45(b) the MEC has a concave bottom surface. This feature, as further discussed in more details in Section I.3.4, ensures proper alignment of EDM and IDM axis of rotation.

II.4.3.4 Controlling $\dot{\theta}_D$

In Section II.1.3.1, closed loop control of the EDM angular velocity $\dot{\theta}_D$ was achieved via PI controller, while a custom controller was developed to achieve closed loop control of the IDM angular velocity $\dot{\theta}_d$. A higher level

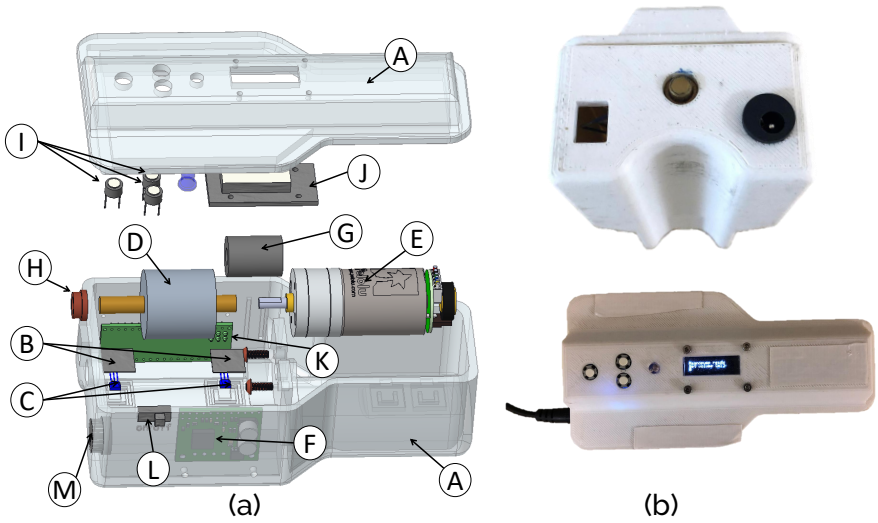

Figure II.45: (a): Exploded view of the magnetic external controller (MEC); (b) fabricated MEC, front and top view.

controller was anticipated to monitor pole slippage condition.

Thus, to control the CIP we assumed stable coupling of the IDM with the EDM, and used a PI controller for speed control of the EDM. The K_p and K_i parameters were firstly estimated using the method described in [11], and then manually tuned to compensate from unknown frictions and interactions with added shielding.

To achieve linear oscillating motion of the pump's piston, we switched the sign of $\dot{\theta}_{des}$ based on the combined conditions of: 1) the norm of angular position θ_D (integrated from $\dot{\theta}_D$) is lower that half of the required number of turn N (Section II.4.3.2); and 2) the angular velocity $\dot{\theta}_D$ and the angular displacement θ_D were of the same sign. This is a double threshold implementation, which ensures stability of the control loop. Figure II.46 shows a schematic of the control scheme used to actuate the EDM in the MEC.

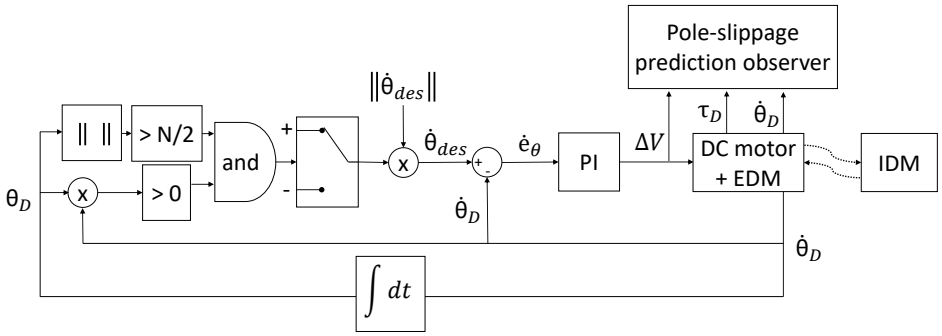

Figure II.46: Pumping control scheme based on $\dot{\theta}_D$ feedback measured from the DC motor encoder. The torque experienced by the DC motor (τ_D), along with the angular velocity $\dot{\theta}_D$, and with the control parameter (ΔV) can be used for prediction of pole slippage – malfunctioning.

In Figure II.46 a pole-slippage prediction observer block in included. As detailed in [12], the state space formulation of the LMA is considered a Multiple Input Multiple Output (MIMO) linear system with the DC motor's controlling voltage (ΔV) as measurable input, and the torque (τ_D) and speed (ω_D) of the DC motor as measurable part of the state vector. Pole slipping prediction is established by using *Kalman state observer* to estimate the velocity of the IDM ω_d.

II.4.3.5 Costs

The standard of care for the treatment of RA is LVP plus administration of albumin. This procedure is generally performed every 8-10 days and lasts 6-8 h. It was estimated that RA treatment via LVP has a cumulative costs of about 4500 USD per patient on a monthly basis [199, 200].

TIPS comes as alternative surgical solution. TIPS does lower the rate of ascites, but does not improve survival rates and worsen the encelophalopathy. Moreover, the overall costs of TIPS including follow ups and revisions is more then double compare to LVP, in US [201].

Alfapump® aims to decrease the treatment costs for RA by improving life quality (higher survival) and decreased hospital visits (no recurrent costs). A recent single-center experience, comparing alfapump® to LVP, showed a significant decrease of necessary LVP between two control study groups. Due to its high cost (28,800 USD) and high complication rates related to device malfunctioning, the device's cost compensation was achieved after 6 months post-implantation. At that time, the survival rate was however low (60%) [200], putting in doubt the system's cost benefit.

An alternative approach for the management of RA, recommended by the NHS of the United Kingdom, is the use of a Tunneled Periteoneal Catheter (TPC). Implantation of such devices comes with an upfront surgical cost, but allows patients to drain ascitic fluids on their own, at home. A cost analysis between TPC and LVP conducted in the US, demonstrated that TPC becomes more cost effective than LVP after less than 3 months (83 days) [202].

The presented LMA device, similarly to TPC, requires minimally invasive surgery for the placement of the catheter-like pump, and allows patients to remove ascitic fluids on their own at home. In contrast to TPC though, the risk of infections is minimized – the device does not leave open wounds on the patient's body. To obtain similar cost effectiveness, as the one shown by [202], the LMA device needs to be low in cost.

Table II.5 summarizes prototyping (PR), and estimated mass production (MP) cost of goods for the proposed device. MP costs were estimated by discussing the design of the LMA pump with a medical device manufacturer

(Medical Murray, North Barrington, IL, USA).

Table II.5: Prototyping (PR) and estimated mass production (MP) cost of goods of the LMA based magnetic subcutaneous pump.

Component	*PR Cost[UDS]*	*MP Cost[UDS]*
CIP		
IDM	2.18	2.00
Plastic parts	2.15	1.00
Threaded shaft	1.34	1.00
Check valves	1.36	0.80
Catheters	4.05	1.50
Dual chamber case	1.56	1.00
TOTAL	**12.63**	**7.30**
MEC		
Plastic part	9.17	2.00
DC motor with encoder	34.95	30.00
Motor driver	17.95	8.00
Shaft coupler and shaft	24.96	20.00
Magnetic field sensors	3.78	3.50
Micro controller	3.33	2.00
Other electronic components	46.35	10.00
EDM	22.77	20.00
TOTAL	**163.26**	**95.50**

II.4.4 Experimental validation

II.4.4.1 IDM alignment over the EDM

The thin layer of skin under which the pump is placed, allows for gross localization of the implanted pump portion (CIP_c) of the device. The use of the concave bottom surface of the MEC (Figure II.45(b)) in direct mechanical coupling with the skin protrusion indicating the CIP_c, simplifies the alignment problem to a single degree of freedom in translation along the EDM axis of rotation. Hence, proper alignment is defined when the separation distance **p** is minimal along the EDM's $\hat{\mathbf{y}}$ axis.

An algorithm based on MFSs feedback was developed. Figure II.47 shows a cross sectional view of the $\hat{\mathbf{y}}\hat{\mathbf{z}}$ plane of the MEC after implantation, and describes MFS placements.

Two MFSs had been strategically embedded in the MEC such as MFSs' centers, related to the reference frame of the EDM ($\{\Omega\}$), are located at [mm]:

- MFS1: $x = 0$; $y = 20$; $z = 12.7$;
- MFS2: $x = 0$; $y = -20$; $z = 12.7$.

The MFS sensing area is perpendicular and off-centered from the rotational plane of the EDM magnetization vector, preventing saturation from EDM magnetic field, and enabling sensing of the IDM super imposed magnetic field. The position along the **y** axis for both sensors was defined by minimizing the distance from the EDM while centering the sensors to the shield.

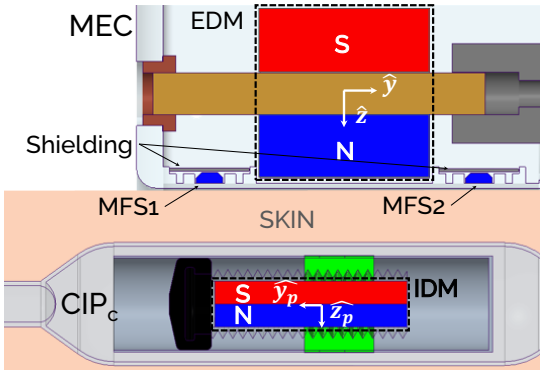

Figure II.47: Schematic cross sectional view of the EDM $\hat{\mathbf{y}}\hat{\mathbf{z}}$ plane. MFS position and shielding is shown.

The alignment routine consists in rotating the EDM at low speed for a more then a full rotation ("shake mode"). This allows the IDM to align its magnetic poles with the MFSs. By continuously monitoring both MFSs readings while manually translating the MEC over the gross location of the CIP, the intensity of local maxima/minima varies and this information is used in a custom function which combines sensors readings and determines alignment between EDM and IDM.

A series of experiments was carried out to validate this algorithm.

Experimental set up

A miniature vise clamp mounted on a x-y stage (MicroLux X-Y Table Attachment, MICRO MARX, Berkeley Heights, NJ, USA) secured a 3D printed part embedding nut and threaded IDM used in CIP. An acrylic sheet was used to lock the MEC and simulate a separation distance h between EDM and IDM rotational axis of 28.7 mm (simulated skin thickness of 6 mm), Figure II.48(a). The 3D printed part holding the IDM and the acrylic sheet holding the MEC are not in contact with one another.

While the EDM was in "shake mode" ($\dot{\theta}_{des}$ = 250 RPM, N = 1.5, using control scheme shown in Figure II.46) the IDM was moved about the centered EDM, manually using the x-y stage. An increment of 0.1" was used to cover an area of interest of 1.6" along the EDM $\hat{\mathbf{y}}$ axis and 1" along the EDM $\hat{\mathbf{x}}$ axis, Figure II.48(b). In total, 187 readings for each sensor were acquired and filled in pre-compiled matrices.

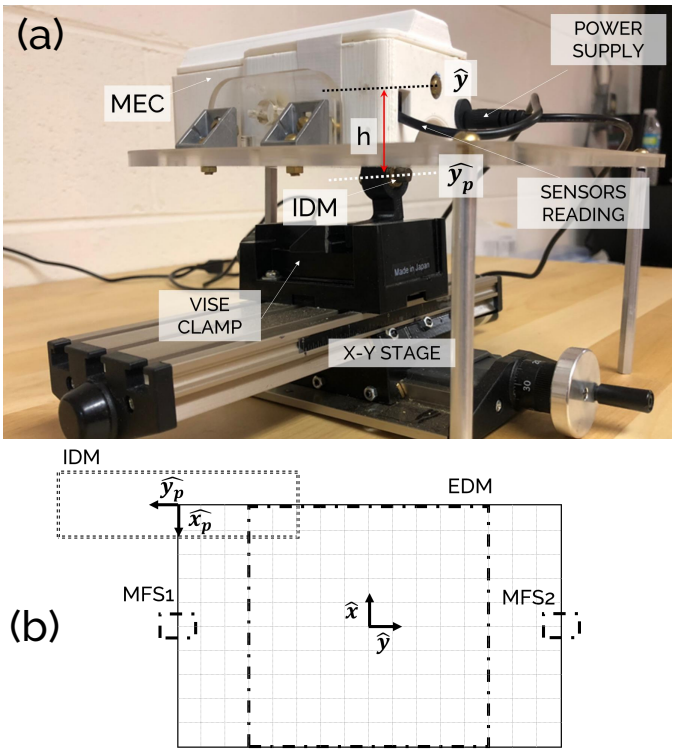

Figure II.48: (a): Experimental set up used to validate algorithm for IDM/EDM alignment; (b) Schematic representation of the area of interest used for IDM/EDM alignment testing.

The experiment was carried out with and without the presence of shielding over the MFSs to demonstrate the contribution of shielding in increasing sensor sensitivity to the IDM's magnetic field.

In both scenarios (MFS with and without shielding), the sensor readings were biased using the EDM magnetic contribution measured without the presence of the IDM.

Sensor fusion results

Figure II.49 shows the polynomial regression plots from MFSs readings. On the left hand side, the sensors regression plots (MFS1 top, MFS2 bottom) when shielding was employed is shown; while, the right hand side shows the equivalent results for the non-shielded case.

As visible from the plots, the minimum obtained over the MFSs location represents the proximity of the South pole of the IDM. The algorithm was developed to monitor for local maxima, and as the EDM aligned its North pole to the MFSs, the IDM contrariwise aligned its South pole to the MFSs.

By comparing the lowest reading occurring at the MFSs location, the use of shielding provided an increase in sensitivity of +45% for MFS1, and +14% for MFS2. This difference in performance may be attributed to imprecise sensor position and orientation, and imperfect depositions of the four layer composing the shield.

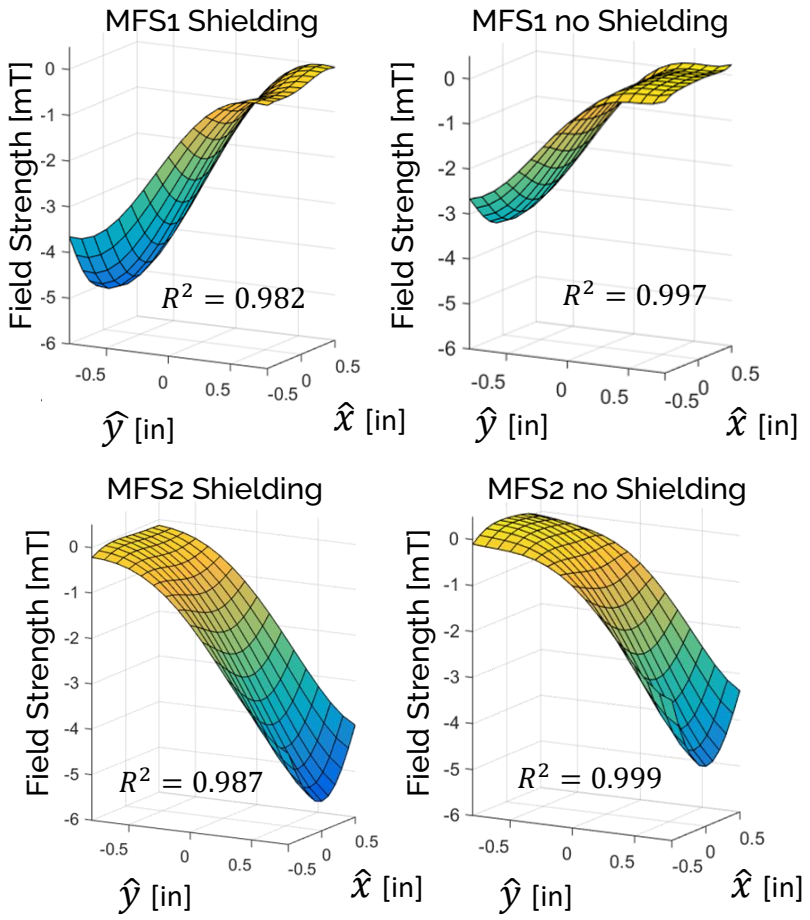

Figure II.49: Regression curves of sensors (MFS1 and MFS2) readings with and without shielding while the IDM scanned the defined area of interest. Coefficient of determination R^2 value is shown in each plot.

A custom function $f(MFS1, MFS2)$ that fuses both sensors local maxima reading was defined to determine alignment.

$$f(MFS1, MFS2) = -(MFS1 - MFS2)^2 \tag{II.38}$$

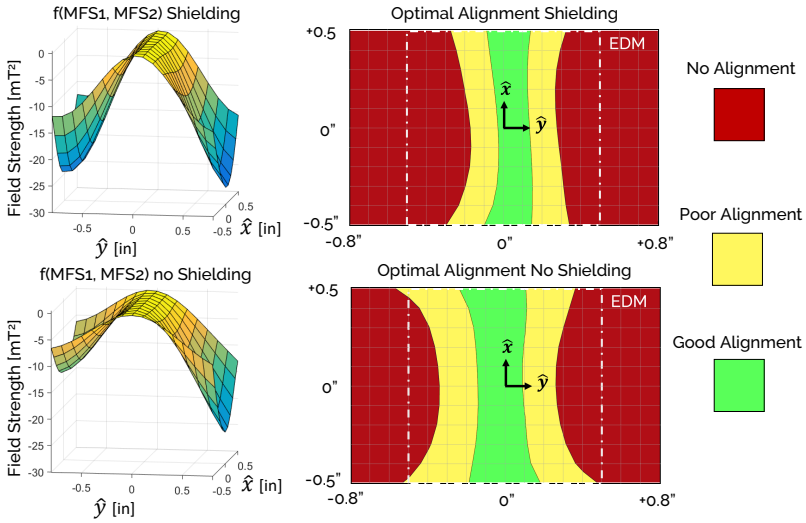

Figure II.50: Left: Custom functions $f(MFS1, MFS2)$; Right: optimal alignment colormaps which is used to inform the user when proper alignment is established.

On the left hand side of Figure II.50, the values of $f(MFS1, MFS2)$ over the tested area of interest are shown; on right hand side, instead, optimal alignment 2D colormap of $f(MFS1, MFS2)$ is shown. The optimal alignment map was determined by setting constant thresholds. These threshold can be tuned based on MFS resolution, and estimation of separation distance h during implantation. By converting this results in color signal for the LED embedded in the MEC, the correct/incorrect IDM/EDM alignment is intuitively shown to the user.

With a simulated skin thickness of 6 mm, the selected thresholds provided in case of shielding: a green area 3.8 mm wide in the center, and a yellow region 11.4 mm wide; while when no shielding was adopted: the green area resulted 5.6 mm wide, and the yellow region 15.5 mm.

Interestingly the IDM translation along the EDM $\hat{\mathbf{x}}$ axis was not significantly sensed by the MFSs. Hence, this algorithm tied with the assumption of mechanical coupling between the MEC concave surface and the implanted CIP, providing a precise way to optimally couple the LMA based device.

II.4.4.2 Pumping validation

Experimental set up

Pumping efficacy of the LMA subcutaneous pump was validated with a series of experiments that simulated the device's implantation. A 6 mm thick silicone layer (Sorta Clear 40A, Smooth-On inc. Macungie, PA, USA) was secured in a dedicated bench set up over the CIP, Figure II.51. The flexible physical barrier between MEC and CIP was used to simulate implantation of the CIP under a compliant layer of skin such that the concave surface of the MEC could to fit with the protuberance created by the CIP itself. The peritoneal catheter (CIP_a) was submerged in a simulated abdominal cavity (2 liter flask), which contained liquid to replicate the presence of ascites. The bladder catheter (CIP_b) was instead connected to a simulated empty bladder (2 liter flask) through air tight rubber stopper.

The instantaneous flow rate generated by the pump, was measured using a dry flow sensor (HAFBLF0150C4AX5, Honeywell International Inc, Morris Plains, NJ, USA). The flow sensors was secured to the rubber stopper of the flask via rubber tubing. As liquid was delivered into the flask by the CIP_c, air was flowing out of the flask through the rubber tube connected to the flow sensor. A dedicated micro controller (ATmega32U4) was used to acquire flow sensor data and output them over serial port to a CPU for data collection.

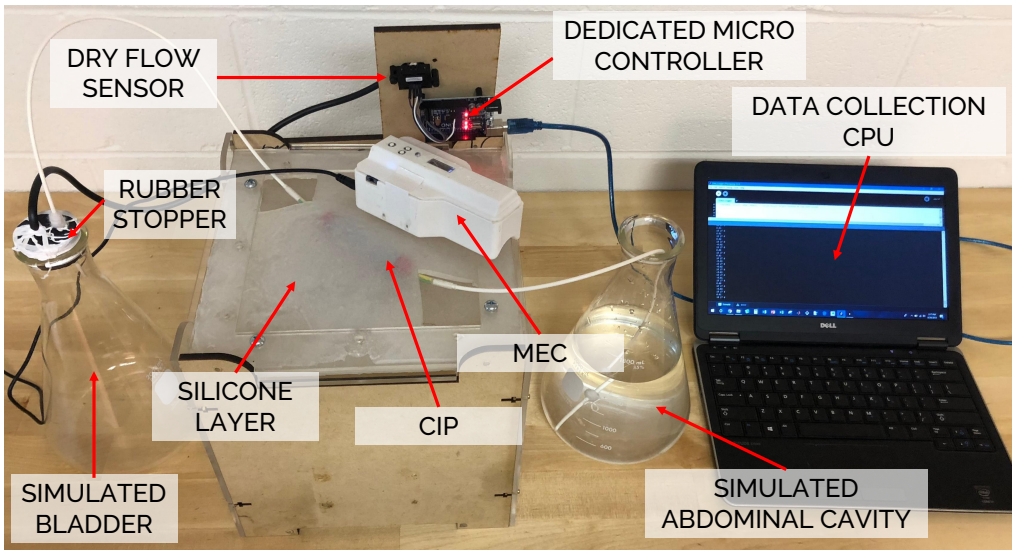

Figure II.51: Experimental bench test used to validate and quantify pumping efficacy.

The experiment consisted of setting the pumping volume first, achieving proper alignment of the MEC over the CIP (following the alignment algorithm discussed in Section II.4.4.1) then, and holding manually the MEC in place, while the pumping routine was running. Given the reciprocate positive displacement nature of the pump, the desired

amount of volume was divided by the theoretical cyclic pumping volume V_{cyc} (Section II.4.3.2) to determine the number of cycles necessary to pump the desired amount.

It was shown that ascitic fluid has a viscosity (μ) ranging between 0.86±0.12 cP and 1.22 ± 0.25 cP depending on patients' serum-ascites albumin gradient [203]. To validate the pumping efficacy in extreme condition water (1 cP) and a mixed solution of water and antifreeze concentrate (Camco Manufacturing Inc, Greensboro, NC, USA) were used as simulated ascitic fluid. Using a Zahn cup [204] #3 the mixed solution was estimated having a viscosity of 5.5 cP.

40 ml of both fluids were pumped three times each. To ultimately test robustness of the system toward animal trials, we tested removal of 750 ml, 1000 ml, and 1750 ml using water (1 cP).

The main outcomes of the trials were: total pumping time (t_{tot}), average cyclic time (T), pumping duty cycle (DC), pumped cyclic volume (V_{cyc}), and total pumped volume (V_{tot}).

For all the experiments, a desired $\dot{\theta}_D$ of 1500 RPM and N = 10 were used in the control scheme, Figure II.46.

Results

The top plot of Figure II.52 shows the flow rate profile for the removal (Trial #1) of 40 ml of water (1 cP). The middle plot of Figure II.52 shows instead the flow rate profile for the removal (Trial #4) of 40 ml of the mixed solution (5.5 cP). The bottom plots represent instead the average (± standard deviation) pumping cycle profile of both previously shown trials.

Table II.6 summarizes instead the numerical findings of all the trials. In all the occurrences, pump functioning was reliable, and once coupling engaged, it never experienced malfunctioning - pole slippage.

The main advantage of designing a positive displacement reciprocal pump is highlighted by the fact that various viscosities (μ) – various loading/unloading condition of the pump – do not significantly influence the pump effectiveness. The 5.5 cP fluid took longer for removal due to a higher torque that the magnetic link had to overcome, hence resulting in a slower average pumping speed.

While the 40 ml trials validated the pump efficacy under different loading conditions, the larger volume tests proved the effectiveness of the design, while validating the desired user need of removing a daily amount of 1 liter within 15-20 min.

It must be noted that the flow rate tended over time. This can be explained with decreased performance of DC motor which overheated because of the intermittent change of direction of rotation. This issue can be solved by slowing down the motor, which, however, will also slow down the resultant flow rate. Additionally one could design

a specific EDM actuation system with two motors and a brake, so that each motor is responsible for one direction of rotation while the brake dissipates the kinetic energy of the EDM.

Nevertheless the results shown hold promises for future acute *in-vivo* animal trials.

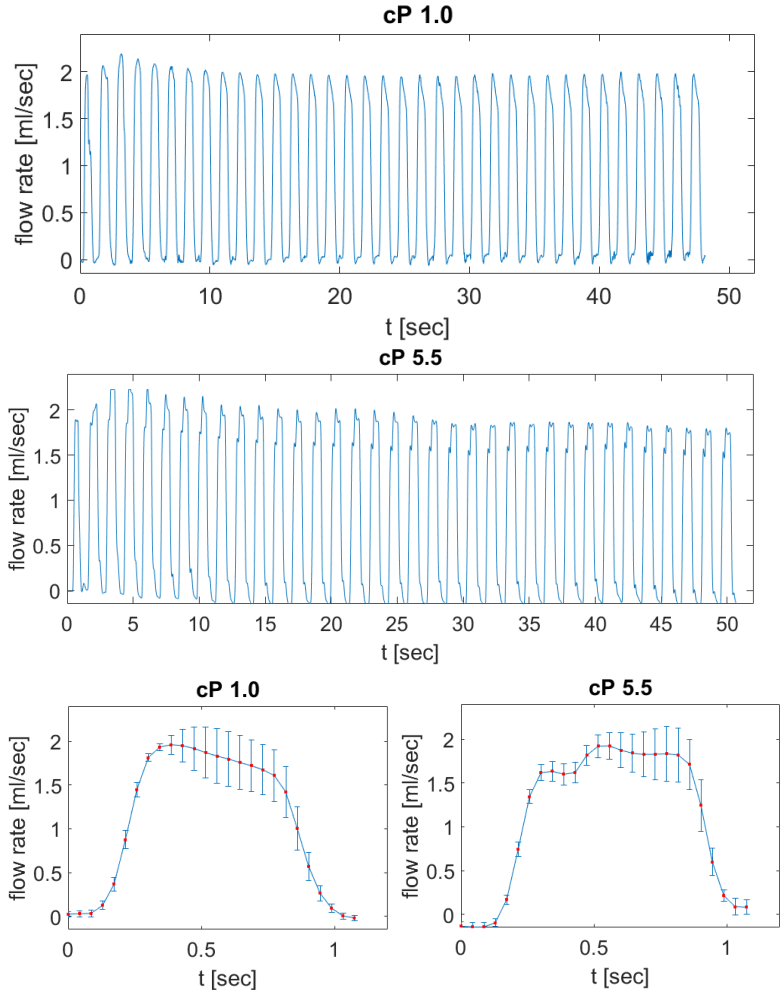

Figure II.52: Top: Recorder flow rate when pumping 40 ml of water; Middle: recorded flow rate when pumping 40 ml of mixed water and antifreeze concentrate; Bottom: cyclic pumping profiles (mean $\pm$ standard deviation) of the top and middle plot.

II.4.5 In-vivo *trials*

The primary goal of the in-vivo trial was to qualitatively assess the functionality of the pump and define a surgical procedure protocol for the implantation of the device on an anesthetized porcine model.

For the purpose of this study both CIP and MEC were modified. The CIP was assembled with shorter (30 cm

Table II.6: Summarized experimental results: liquid viscosity (μ), total pumping time (t_{tot}), average cyclic time (T), pumping duty cycle (DC), pumped cyclic volume (V_{cyc}), total pumped volume (V_{tot}), and desired volume (V_{des}).

Trial #	μ	t_{tot}	**T**	**DC**	V_{cyc}	V_{tot}	V_{des}
1	1cP	46.54 s	1.36 ± 0.06 s	42.98 ± 3.72 %	1.18 ± 0.11 ml	41.60 ml	40 ml
2	1cP	46.52 s	1.35 ± 0.06 s	45.61 ± 4.90 %	1.22 ± 0.13 ml	42.93 ml	40 ml
3	1cP	47.41 s	1.38 ± 0.05 s	44.78 ± 6.54 %	1.20 ± 0.15 ml	43.14 ml	40 ml
4	5.5cP	51.08 s	1.49 ± 0.06 s	48.85 ± 5.29 %	1.24 ± 0.12 ml	43.29 ml	40 ml
5	5.5cP	49.80 s	1.45 ± 0.06 s	48.85 ± 5.29 %	1.24 ± 0.10 ml	43.14 ml	40 ml
6	5.5cP	52.69 s	1.54 ± 0.11 s	48.21 ± 4.89 %	1.24 ± 0.12 ml	42.98 ml	40 ml
7	1cP	12 min 36.67 s	1.22 ± 0.02 s	43.25 ± 1.91 %	1.15 ± 0.05 ml	756.67 ml	750 ml
8	1cP	16 min 25.76 s	1.21 ± 0.02 s	43.01 ± 1.93 %	1.12 ± 0.06 ml	985.76 ml	1000 ml
9	1cP	28 min 10.10 s	1.20 ± 0.02 s	42.91 ± 1.85 %	1.10 ± 0.06 ml	1690.10 ml	1750 ml

long) catbheter catheter ends (CIP_a, and CIP_b) to fit the animal anatomy. A 14 Fr silicone catheter was used for CIP_a while an 8 Fr silicone catheter was used for CIP_b. The MEC was instead assembled without the shielded MFS used for MEC over the CIP optimal placement. This was done for two main reasons: 1) to avoid preliminary optimal placement routine allowing simplified and direct pump actuation during the trial; 2) validate the pumping efficacy assuming that optimal placement could be achieved by visually identifying the pumping section (CIP_c) of the implant upon subcutaneous implantation.

The surgical procedure was performed at Vanderbilt University, with the assistance and collaboration of a specially trained medical team (Procotol number M1800159), in accordance with all ethical consideration and the regulation related to animal experiments. A 42-kg female Yorkshire swine was used for the study. After intravenous sedation and urinary catheter placement, a 10 cm lower midline incision was made to provide access to the apex of the urinary bladder and to the intra abdominal space for placement of inflow and outflow leads (CIP_a and CIP_b, respectively). Successively, two full thickness 3 cm skin incisions were made at the level of the umbilicus, one 8 cm to the left of the abdominal midline and one 8 cm to the right of the abdominal midline. Subcutaneous dissection was performed at each site and a subcutaneous tunnel was made from left to right across midline.

The CIP_b was carefully drawn into the subcutaneous tunnel using a 30 cm sponge forces such that the CIP_c final position was centered in the subcutaneous tunnel. The pump was then actuated to verify its functioning. Two full thickness puncture wounds were performed intra abdominally at the site of each side incisions. CIP_a and CIP_b were then pulled through the puncture wounds and positioned in the lower abdominal cavity. A urinary bladder ostomy was performed with a 14 Gauge needle in the apex of the bladder, the CIP_c was advanced through the ostomy and secured with two purse-string suture placed in the bladder wall. CIP_b was instead positioned freely in the lower left abdominal quadrant, Figure II.53. Two 14 Gauge 5 cm long intracath flexible needles were percutaneously placed in

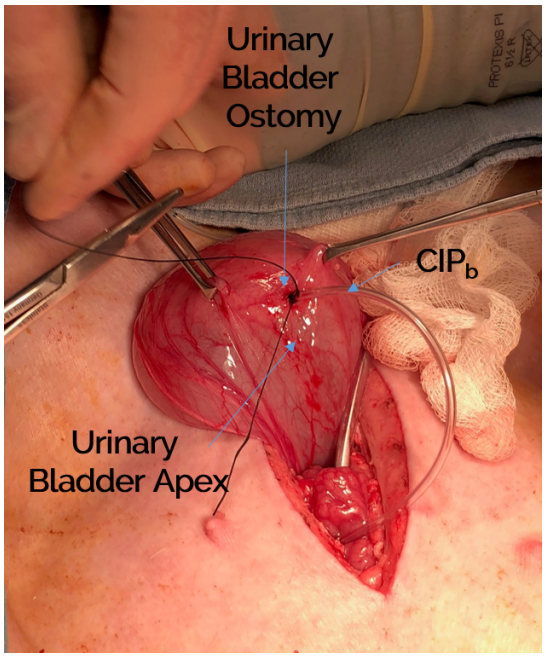

Figure II.53: Bladder catheter CIP_b placement in the urinary bladder ostomy.

the upper right and left quadrants of the abdomen to permit fluid (saline solution at body temperature) administration in the abdomen. All incisions were double sewn to prevent leakages, Figure II.54. The urinary bladder was emptied

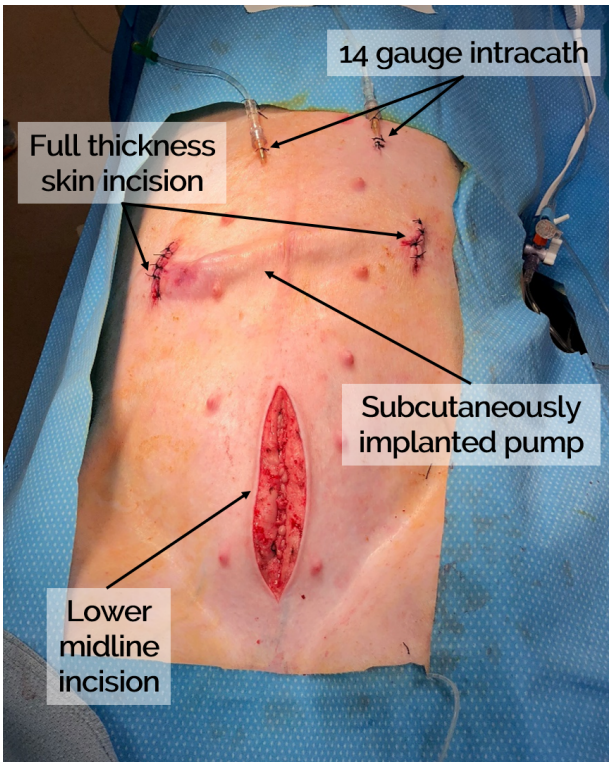

Figure II.54: Subcutaneous placement of the pump.

via urinary catheter using syringes. In 30 minutes, 3 liters of warmed saline were infused in the abdominal space to simulate ascites.

Before actuating the pump the urine production was estimated by emptying the bladder again after the 30 infusion minutes. 8 ml of urine were measured. Following the pump was actuated for 10 minutes placing a 2 mm surgical towel over the incision to simulate a clothes wearing patient and possible increase in separation distance between CIP and MEC. Given the pump setting, and pumping time, 600 ml were expected to collect in the bladder. One the pump was deactivated, the urinary bladder was emptied measuring 250 ml, Figure II.55.

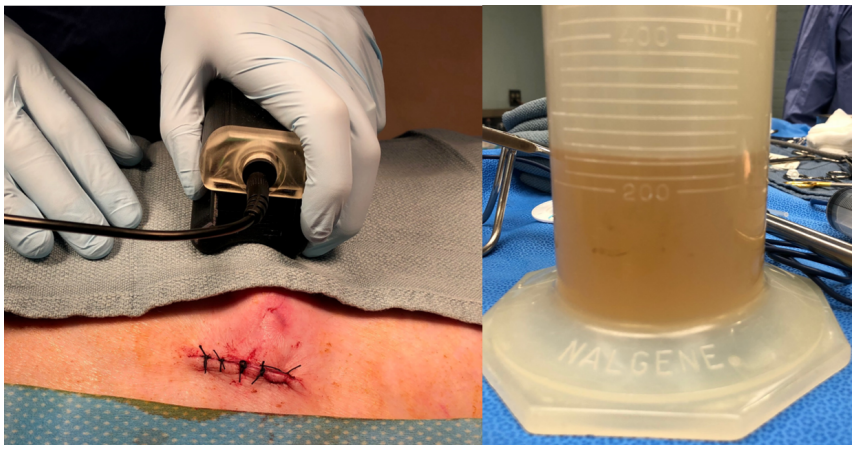

Figure II.55: Left: modified MEC placed over a 2 mm thick fabric actuating the pump; Right: bladder content after 10 minutes actuation.

Then the same procedure was then repeated 3 times. The bladder content measured 8 ml, 6 ml, and 5 ml in order.

The lower incision was opened to observe CIP_a and CIP_b placement after draining the infused abdominal cavity. CIP_a presented some particulate material in a couple of orifices. After the bladder ostomy was enlarged to show the CIP_b, it was visually confirmed that the end of it was securely placed in the bladder and free of particulate material. The two surgical punctures sites were also opened and the CIP_a was visually kinked in the space created to access the abdominal cavity. By returning it to a straight position and actuating the pump, the pump functioning resumed to normal.

Hence the impaired measurement and observed in urinary bladder fluid delivery was caused by a restriction of the inflow catheter, CIP_a. At what time the restriction occurred could not be determined but it most likely occurred during the first successful run of the trials.

The trial hence validated: 1) safe placement of the device in the subcutaneous space via a tunnel approach; 2)

ability to locate the pumping portion of the device (CIP_c) for optimal MEC positioning; 3) ability of the proposed reciprocating positive displacement design to pump accumulated fluid from the abdominal cavity to the bladder.

Improvement on the design will include: kinking resistant catheters, and different CIP_a and CIP_b tip solution to prevent particulate material migration as well as tissue ingrown.

II.4.6 Conclusions

This device represents an example of how the LMA concept can be used to tackle different clinical scenario than minimally invasive surgery.

The reciprocating positive displacement design is able not only to drain fluids with comparable viscosity of ascitic fluids (μ = 1 cP) but also with higher viscosity (μ = 5.5 cP).

The pump's efficacy has been validated for a fixed, clinically relevant, separation distance (6 mm). Though, the response of the system to a variation in skin thickness can be predicted by the understanding of the LMA approached described in in Section II.1.3.1. By testing the system at 6 mm, we inherently validated the device's efficacy for thinner skin layers. The resulted increase in transmittable torque allows the IDM to overcome the same loading condition. Alternatively, the MEC can be lifted up by means of flexible pads to maintain the verified distance of 6 mm. By testing the system with a much more viscous fluid, we not only validated the functionality of the device with a fluid that has more resistance to flow, but also varied the loading and unloading condition at the piston level. This results in an increased torque requirement at the IDM level, which the system was able to provide. Hence we also proved the ability of the system to pump ascetic fluids, having a viscosity reported in Section II.4.4.2, for both thinner and thicker skin layers.

Pump functioning during experimental bench top trials was reliable and effective. An optimal alignment algorithm enables correct alignment between EDM and IDM based on externally placed MFSs. The algorithm localizes the location of the center of the IDM within a $\pm$ 1.9 mm range. This feature ensures optimal placement of the MEC, and minimizes loss of magnetic coupling.

Limitations of our study are: 1) the need of FEA simulations for optimal estimation of magnetic forces and torques of the magnetic coupling; 2) upon implantation, the need of a calibration process to determine correct thresholds for proper IDM alignment over the EDM; 3) ability to detect malfunction (IDM pole slipping) [12], but inability to determine the causes (e.g. tissue ingrow, catheter clogging due to absence of ascetic fluid, catheter kinking); 4) possible subcutaneous pinching and discomfort generated by the attraction forces acting on the IDM

when coupled with the EDM; 5) need for a long term solution to overcome motor overheating.

As demonstrated by the *in-vivo* animal trial, the device can be easily implanted using established surgical techniques (i.e. tunneling of the device in the subcutaneous space, exhaust catheter placement in the urinary bladder's apex). The device's functioning was validated but the kinking of the intake catheter limited the amount of clinical data that were collected.

It has been estimated that 100,000 new cases of RA will develop across US and Europe by 2020. Current solutions are either too invasive and expensive (TIPS and alfapump®), or lower patients' quality of life with high recurrent cost (LVP). A magnetically actuated pump that can be intuitively actuated to follow clinician's treatment plan or during a discomfort sensation (bloating), and with estimated mass production cost of good below 8 USD, has the potential to be a revolutionary introduction for the treatment of RA.

Conclusion and future directions

In summary, this dissertation proposed a series of endoscopic and magnetically actuated lifesaving devices. This body of work was driven by the need for developing medical devices that expand patient access to diagnostic procedures, and to treat pathological conditions using a minimally invasive approach.

The endoscopic platforms for the diagnosis of the upper gastrointestinal tract presented in chapter I, were conceived as supplemental endoscopic tools to conventional flexible endoscopy for diagnostic procedure, leaving the use of conventional endoscopes for therapeutic interventions. In addition, these devices could be used for triage in emergency situations, and to implement cost effective UGI tract screening programs around the world. These devices, in both robotic and manual implementation, could be disposed of given the low fabrication cost, hence removing any risk of cross contamination between patients. The modeling approach adopted for the robotic version of the device showed the ability to drastically improve the bending angle error, opening promising venues for closed loop control toward the implementation of autonomous tasks such as lesion detections as well as screening of anatomical landmarks. The manual version of the novel endoscope is extremely intuitive thanks to a direct user-to-task mapping achieved via direct mechanical coupling between a novel user interface (multi-backbones continuum joystick) and a pneumatically actuated endoscopic tip. The cadaveric trial demonstrated the ability to perform diagnostic procedures in clinically acceptable time. Moreover the results from an approved user study, demonstrated that medical providers without any specialized training were able to detect all the gastric key landmarks of a UGI tract simulator using the novel device, and preferred the novel device to a conventional flexible endoscope. Remarkable appreciation was given by the users to the device's intuitiveness, lightweight design, portability (no need of an endoscopic tower), and ability to stream the camera view via Wi-Fi network on any smart device.

To effectively translate these innovative solutions into clinical use and further improve the device capabilities, future studies are mandatory to overcome some of the limitations that the device currently faces. First the rubber bellows, currently off-the-shelf components, used to form the articulating tip of both the robotic and manual endoscopic instrument, need to be substituted by custom bellows to achieve a smaller overall tip diameter and increase the tip bending motion. This is expected to simplify even further the device's use, and remove the need for anesthesia. Suggested approaches to this problem are the use of blow molding techniques to manufacture miniaturized custom bellows, as well as designing a single flexible articulation that embeds three expandable chambers arranged in parallel fashion. This is a design problem that requires continuum robot kinematic modeling for the description and validation of the achievable range of motion. An actuation system similar to the one proposed in the robotic

implementation of the device should be used for validation. With such a robotic platform, more advanced models can be developed to further decrease the tip's bending errors, and to quantify non-linearity of the tip's motion to aid the design of a compensating mechanism for manual actuation (e.g. camshafts for the generation of non-linear piston displacement). The proposed modeling techniques and translation into a design problem is there for researchers in the field of soft robotics to take inspiration from and expand on for adaptation to other similar designs/systems. Additional approved user studies that include larger user populations with a wider spectrum of specialization and expertise in medicine will have to be carried out to strengthen the assumption that the technical skills required by the proposed device are much lower, compared to conventional flexible endoscopes.

In parallel, robotic control of magnetic actuation demonstrated in chapter II, hold promises toward the development of the next technological set of medical devices for laparoscopy, and other therapeutic applications. The proposed laparoscopic retractor and camera demonstrated the efficacious use of permanent magnets to perform surgical tasks without the need of dedicated incisions, hence improving access to the surgical workspace for the surgeons. More in detail, the retractor based on local magnetic actuation was able to retract up to ten times its own weight, hence overcoming the main limitation in using conventional micro motors to actuate intracavitary surgical devices. The miniaturized laparoscopic camera was instead developed exploiting a compact magnetic coupling based on smart placement of permanent magnets, and achieved a hemispherical workspace with an auto-flip feature (rotation of 180° along the device's main axis) at the bottom of it. The local magnetic actuation unit was then further exploited and described to develop an implantable pump for the treatment of refractory ascites. The device, composed by a fully implantable catheter-like pump, and an external magnetic controller, was able to reliably remove accumulated fluids without the need of electronics on board of the implantable pump. Mechanical power was in fact transferred over the magnetic coupling from the external magnetic controller. All of these devices were tested in a series of bench and *in-vivo* trials demonstrating the effectiveness and potential of the medical devices that exploit robotic control of magnetic actuation.

Nevertheless, new challenges arose from the developments of these technologies and will require future research efforts. Since the foundation for the exploitation of local magnetic actuation was set by the preliminary closed loop control validation and the subsequent independent control of multiple local magnetic actuation units with cross coupling compensation, the next research challenges are related to the development and fabrication of surgical devices with multiple DOFs all actuated via independently controlled local magnetic actuation units. This requires a deep understanding of the control problem of multiple LMA actuation units, and the use of this knowledge as groundwork for conceptualizing and further assessing feasible designs. In addition, the magnetic modeling strategies

presented in this body of work (i.e. dipole-dipole model, and FEA analysis) and by other researchers, can be used to propose, exploit, and compose magnetic couplings with unique features and control algorithms tailored to specific surgical tasks/applications. Although magnetic actuation methods might seem radical and complex to integrate in the operating room for a skeptical person, recently more attention is being paid to medical technologies that exploit magnetism in medicine. An example of it is provided by Levita Magnetics (San Francisco, CA, USA). This start up proposes a magnetically coupled retraction system for MIS, and is undergoing preliminary human trials.

Finally, the goal in developing simpler yet effective robotic and robotically inspired solutions presented in this dissertation is to help patients, providers and health care systems with the aim of simplifying and decreasing invasiveness and increase patients' access to lifesaving devices. This work sets out to improve the standard of care for diagnosis and treatment of diseases that affect millions of people. Through the combination of engineering and medicine, we have the opportunity to positively affect the future of health care for everyone.

REFERENCES

[1] N. Garbin, L. Wang, J. Chandler, K. Obstein, N. Simaan, and P. Valdastri, "Dual-continuum design approach for intuitive and low-cost upper gastrointestinal endoscopy." *IEEE Transactions on Biomedical Engineering*, vol. in press.

[2] N. Garbin, A. Mamunes, D. Sohn, R. Hawkins, P. Valdastri, and K. Obstein, "Evaluation of a novel low-cost disposable upper endoscope for assessment of the upper gastrointestinal tract." *Endoscopy International Open*, under revision.

[3] N. Garbin, L. Wang, J. H. Chandler, K. L. Obstein, N. Simaan, and P. Valdastri, "A disposable continuum endoscope using piston-driven parallel bellow actuator," in *Proceedings of the International Symposium on Medical Robotics (ISMR 2018)*. IEEE, 2018.

[4] N. Garbin, A. Stilli, A. Shiva, J. Fras, P. Slawinski, K. Obstein, K. Althoefer, H. Wurdemann, and P. Valdastri, "Toward a low-cost soft robotic manipulator based on fluid-actuated bellows for gastric cancer screening," in *10th Hamlyn Symposium on Medical Robotics*. Hamlyn Center, 2017, pp. 53–54.

[5] N. Garbin, S. Sarker, D. C. Sohn, P. R. Slawinski, P. Valdastri, and K. L. Obstein, "Su1180 evaluation of a novel disposable upper endoscope for unsedated bedside (non-endoscopy unit based) assessment of the upper gastrointestinal (ugi) tract," *Gastrointestinal Endoscopy*, vol. 85, no. 5, p. AB304, 2017.

[6] N. Garbin, W. Long, S. Dennis, O. Keith, S. Nabil, and P. Valdastri, "An intuitive a disposable endoscope with intrinsic pneumatic actuation," in *29th Conference of the International Society for Medical Innovation and Technology*. SMIT, 2017, pp. 27–28.

[7] N. Garbin, C. Di Natali, J. Buzzi, E. De Momi, and P. Valdastri, "Laparoscopic tissue retractor based on local magnetic actuation," *Journal of Medical Devices*, vol. 9, no. 1, p. 011005, 2015.

[8] N. Garbin, P. Doyle, B. Smith, J. G. Taylorm, M. H. Khan, Q. Khalil, and P. Valdastri, "Miniature pump for treatment of refractory ascites based on local magnetic actuation," *Journal of Medical Devices*, vol. *in press*, 2018.

[9] N. Garbin, P. R. Slawinski, G. Aiello, C. Karraz, and P. Valdastri, "Laparoscopic camera based on an orthogonal magnet arrangement," *IEEE Robotics and Automation Letters*, vol. 1, no. 2, pp. 924–929, 2016.

[10] F. Leong, N. Garbin, C. Di Natali, A. Mohammadi, D. Thiruchelvam, D. Oetomo, and P. Valdastri, "Magnetic surgical instruments for robotic abdominal surgery," *IEEE reviews in biomedical engineering*, vol. 9, pp. 66–78, 2016.

[11] C. Di Natali, J. Buzzi, N. Garbin, M. Beccani, and P. Valdastri, "Closed-loop control of local magnetic actuation for robotic surgical instruments," *IEEE Transactions on Robotics*, vol. 31, no. 1, pp. 143–156, 2015.

[12] B. Scaglioni, N. Fornarelli, N. Garbin, A. Menciassi, and P. Valdastri, "Independent control of multiple degrees of freedom local magnetic actuators with magnetic cross-coupling compensation," *IEEE Robotics and Automation Letters*, vol. 3, no. 4, pp. 3622–3629, 2018.

[13] A. F. Peery, E. S. Dellon, J. Lund, S. D. Crockett, C. E. McGowan, W. J. Bulsiewicz, L. M. Gangarosa, M. T. Thiny, K. Stizenberg, D. R. Morgan *et al.*, "Burden of gastrointestinal disease in the united states: 2012 update," *Gastroenterology*, vol. 143, no. 5, pp. 1179–1187, 2012.

[14] MedlinePlus. (2018, Jul) Egd - esophagogastroduodenoscopy. [Online]. Available: https://medlineplus.gov/ency/article/003888.htm

[15] E. Rozeboom, J. Ruiter, M. Franken, and I. Broeders, "Intuitive user interfaces increase efficiency in endoscope tip control," *Surgical Endoscopy*, vol. 28, no. 9, pp. 2600–2605, 2014.

[16] J. Kovaleva, F. T. Peters, H. C. Van Der Mei, and J. E. Degener, "Transmission of infection by flexible gastrointestinal endoscopy and bronchoscopy," *Clinical Microbiology Reviews*, vol. 26, no. 2, pp. 231–254, 2013.

[17] P. Murray, "Preventable tragedies: Superbugs and how ineffective monitoring of medical device safety fails patients," *United States: United States Senate Health, Education, Labor and Pensions Committee*, 2016.

[18] C. L. Ofstead, M. R. Quick, J. E. Eiland, and S. J. Adams, "A glimpse at the true cost of reprocessing endoscopes," *International Association of Healthcare Central Service Material Management*, 2017.

[19] M. Broe, M. Barry, S. Patchett, and A. Hill, "Evaluating the clinical efficacy and cost effectiveness of direct access endoscopy," *The Surgeon*, vol. 11, no. 6, pp. 304–308, 2013.

[20] J. G. Lee, S. Turnipseed, P. S. Romano, H. Vigil, R. Azari, N. Melnikoff, R. Hsu, D. Kirk, P. Sokolove, and J. W. Leung, "Endoscopy-based triage significantly reduces hospitalization rates and costs of treating upper gi bleeding: a randomized controlled trial," *Gastrointestinal endoscopy*, vol. 50, no. 6, pp. 755–761, 1999.

[21] J. Ferlay, I. Soerjomataram, R. Dikshit, S. Eser, C. Mathers, M. Rebelo, D. M. Parkin, D. Forman, and F. Bray, "Cancer incidence and mortality worldwide: sources, methods and major patterns in globocan 2012," *International Journal of Cancer*, vol. 136, no. 5, pp. E359–E386, 2015.

[22] W. Chen, R. Zheng, P. D. Baade, S. Zhang, H. Zeng, F. Bray, A. Jemal, X. Q. Yu, and J. He, "Cancer statistics in china, 2015," *CA: a Cancer Journal for Clinicians*, vol. 66, no. 2, pp. 115–132, 2016.

[23] T. Rösch, A. Adler, H. Pohl, E. Wettschureck, M. Koch, B. Wiedenmann, and N. Hoepffner, "A motor-driven

single-use colonoscope controlled with a hand-held device: a feasibility study in volunteers," *Gastrointestinal Endoscopy*, vol. 67, no. 7, pp. 1139–1146, 2008.

[24] Z. Liao, X. Hou, E.-Q. Lin-Hu, J.-Q. Sheng, Z.-Z. Ge, B. Jiang, X.-H. Hou, J.-Y. Liu, Z. Li, Q.-Y. Huang *et al.*, "Accuracy of magnetically controlled capsule endoscopy, compared with conventional gastroscopy, in detection of gastric diseases," *Clinical Gastroenterology and Hepatology*, vol. 14, no. 9, pp. 1266–1273, 2016.

[25] F. Campisano, F. Gramuglia, I. R. Dawson, C. T. Lyne, M. L. Izmaylov, S. Misra, E. De Momi, D. R. Morgan, K. L. Obstein, and P. Valdastri, "Gastric cancer screening in low-income countries: System design, fabrication, and analysis for an ultralow-cost endoscopy procedure," *IEEE Robotics & Automation Magazine*, vol. 24, no. 2, pp. 73–81, 2017.

[26] H. H. Hopkins and N. S. Kapany, "A flexible fibrescope, using static scanning," *Nature*, vol. 173, no. 4392, p. 39, 1954.

[27] E. D. Rozeboom, R. Reilink, M. P. Schwartz, P. Fockens, and I. A. Broeders, "Evaluation of the tip-bending response in clinically used endoscopes," *Endoscopy international open*, vol. 4, no. 4, p. E466, 2016.

[28] J. Wehrmeyer, J. Barthel, J. Roth, and T. Saifuddin, "Colonoscope flexural rigidity measurement," *Medical and Biological Engineering and Computing*, vol. 36, no. 4, pp. 475–479, 1998.

[29] G. M. Eisen, T. H. Baron, J. A. Dominitz, D. O. Faigel, J. L. Goldstein, J. F. Johanson, J. S. Mallery, H. M. Raddawi, J. J. Vargo II, J. P. Waring *et al.*, "Complications of upper gi endoscopy," *Gastrointestinal endoscopy*, vol. 55, no. 7, pp. 784–793, 2002.

[30] L. Trevisani, V. Cifalà, S. Sartori, G. Gilli, G. Matarese, and V. Abbasciano, "Unsedated ultrathin upper endoscopy is better than conventional endoscopy in routine outpatient gastroenterology practice: a randomized trial," *World Journal of Gastroenterology: WJG*, vol. 13, no. 6, pp. 906–911, 2007.

[31] R. T. Garcia, J. P. Cello, M. H. Nguyen, S. J. Rogers, A. Rodas, H. N. Trinh, N. H. Stollman, G. Schlueck, and K. R. McQuaid, "Unsedated ultrathin egd is well accepted when compared with conventional sedated egd: a multicenter randomized trial," *Gastroenterology*, vol. 125, no. 6, pp. 1606–1612, 2003.

[32] J. M. Inadomi, C. L. Gunnarsson, J. A. Rizzo, and H. Fang, "Projected increased growth rate of anesthesia professional–delivered sedation for colonoscopy and egd in the united states: 2009 to 2015," *Gastrointestinal Endoscopy*, vol. 72, no. 3, pp. 580–586, 2010.

[33] M. Ferrua and R. Singh, "Modeling the fluid dynamics in a human stomach to gain insight of food digestion," *Journal of food science*, vol. 75, no. 7, pp. R151–R162, 2010.

[34] G. Harvin, "Review of musculoskeletal injuries and prevention in the endoscopy practitioner," *Journal of Clinical Gastroenterology*, vol. 48, no. 7, pp. 590–594, 2014.

[35] O. W. Cass, M. L. Freeman, C. J. Peine, R. T. Zera, and G. R. Onstad, "Objective evaluation of endoscopy skills during training," *Annals of Internal Medicine*, vol. 118, no. 1, pp. 40–44, 1993.

[36] J. Burgner-Kahrs, D. C. Rucker, and H. Choset, "Continuum robots for medical applications: A survey," *IEEE Transactions on Robotics*, vol. 31, no. 6, pp. 1261–1280, 2015.

[37] A. Orekhov, C. Abah, and N. Simaan, "Snake-like robots for minimally invasive, single-port, and intraluminal surgeries," in *The Enciclopedia of Medical Robotics*. World Scientific, 2018, ch. 8, pp. 203–243.

[38] P. Sears and P. Dupont, "A steerable needle technology using curved concentric tubes," in *Intelligent Robots and Systems, 2006 IEEE/RSJ International Conference on*. IEEE, 2006, pp. 2850–2856.

[39] R. J. Webster, A. M. Okamura, and N. J. Cowan, "Toward active cannulas: Miniature snake-like surgical robots," in *Intelligent Robots and Systems, 2006 IEEE/RSJ International Conference on*. IEEE, 2006, pp. 2857–2863.

[40] N. Simaan, "Snake-like units using flexible backbones and actuation redundancy for enhanced miniaturization," in *Robotics and Automation, 2005 IEEE/ICRA International Conference on*. IEEE, 2005, pp. 3012–3017.

[41] R. E. Goldman, A. Bajo, L. S. MacLachlan, R. Pickens, S. D. Herrell, and N. Simaan, "Design and performance evaluation of a minimally invasive telerobotic platform for transurethral surveillance and intervention," *IEEE Transactions on Biomedical Engineering*, vol. 60, no. 4, pp. 918–925, 2013.

[42] N. Simaan, K. Xu, W. Wei, A. Kapoor, P. Kazanzides, R. Taylor, and P. Flint, "Design and integration of a telerobotic system for minimally invasive surgery of the throat," *The International Journal of Robotics Research*, vol. 28, no. 9, pp. 1134–1153, 2009.

[43] N. Simaan, A. Bajo, A. Reiter, L. Wang, P. Allen, and D. Fowler, "Lessons learned using the insertable robotic effector platform (irep) for single port access surgery," *Journal of Robotic Surgery*, vol. 7, no. 3, pp. 235–240, 2013.

[44] J. H. Kaouk, G.-P. Haber, R. Autorino, S. Crouzet, A. Ouzzane, V. Flamand, and A. Villers, "A novel robotic system for single-port urologic surgery: first clinical investigation," *European Urology*, vol. 66, no. 6, pp. 1033–1043, 2014.

[45] K. Xu, J. Zhao, and M. Fu, "Development of the sjtu unfoldable robotic system (surs) for single port laparoscopy," *IEEE/ASME Transactions on Mechatronics*, vol. 20, no. 5, pp. 2133–2145, 2015.

[46] P. Dario, M. C. Carrozza, M. Marcacci, S. D'Attanasio, B. Magnami, O. Tonet, and G. Megali, "A novel mechatronic tool for computer-assisted arthroscopy," *IEEE Transactions on Information Technology in Biomedicine*, vol. 4, no. 1, pp. 15–29, 2000.

[47] R. E. Goldman, A. Bajo, and N. Simaan, "Compliant motion control for multisegment continuum robots with actuation force sensing," *IEEE Transactions on Robotics*, vol. 30, no. 4, pp. 890–902, 2014.

[48] M. Cianchetti, C. Laschi, A. Menciassi, and P. Dario, "Biomedical applications of soft robotics," *Nature Reviews Materials*, vol. 3, p. 143153, 2018.

[49] R. V. Martinez, J. L. Branch, C. R. Fish, L. Jin, R. F. Shepherd, R. M. Nunes, Z. Suo, and G. M. Whitesides, "Robotic tentacles with three-dimensional mobility based on flexible elastomers," *Advanced Materials*, vol. 25, no. 2, pp. 205–212, 2013.

[50] M. Cianchetti, T. Ranzani, G. Gerboni, T. Nanayakkara, K. Althoefer, P. Dasgupta, and A. Menciassi, "Soft robotics technologies to address shortcomings in today's minimally invasive surgery: the stiff-flop approach," *Soft Robotics*, vol. 1, no. 2, pp. 122–131, 2014.

[51] H. Abidi, G. Gerboni, M. Brancadoro, J. Fras, A. Diodato, M. Cianchetti, H. Wurdemann, K. Althoefer, and A. Menciassi, "Highly dexterous 2-module soft robot for intra-organ navigation in minimally invasive surgery," *The International Journal of Medical Robotics and Computer Assisted Surgery*, vol. 14, no. 1, p. e1875, 2018.

[52] Y. Bailly and Y. Amirat, "Modeling and control of a hybrid continuum active catheter for aortic aneurysm treatment," in *Robotics and Automation, 2005 IEEE/ICRA International Conference on*. IEEE, 2005, pp. 924–929.

[53] D. O'Brien and D. M. Lane, "3d force control system design for a hydraulic parallel bellows continuum actuator," in *Robotics and Automation, 2001 IEEE/ICRA International Conference on*, vol. 3. IEEE, 2001, pp. 2375–2380.

[54] T. Gagarina and P. Joli, "Modeling and experimental analysis of a new bellow type actuators for active catheter end-effector," in *Robot and Human Interactive Communication, 2001 10th IEEE International Workshop on*. IEEE, 2001, pp. 612–617.

[55] V. Falkenhahn, A. Hildebrandt, R. Neumann, and O. Sawodny, "Dynamic control of the bionic handling assistant," *IEEE/ASME Transactions on Mechatronics*, vol. 22, no. 1, pp. 6–17, 2017.

[56] T. Mahl, A. Hildebrandt, and O. Sawodny, "A variable curvature continuum kinematics for kinematic control of the bionic handling assistant," *IEEE Transactions on Robotics*, vol. 30, no. 4, pp. 935–949, 2014.

[57] M. Sfakiotakis, D. Laue, and B. C. Davies, "An experimental undulating-fin device using the parallel bellows actuator," in *Robotics and Automation, 2001. Proceedings 2001 ICRA. IEEE International Conference on*, vol. 3. IEEE, 2001, pp. 2356–2362.

[58] M. Cianchetti, T. Ranzani, G. Gerboni, I. De Falco, C. Laschi, and A. Menciassi, "Stiff-flop surgical manipulator: mechanical design and experimental characterization of the single module," in *2013 IEEE/RSJ International Conference on Intelligent Robots and Systems*. IEEE, 2013, pp. 3576–3581.

[59] A. Stilli, H. A. Wurdemann, and K. Althoefer, "Shrinkable, stiffness-controllable soft manipulator based on a bio-inspired antagonistic actuation principle," in *Intelligent Robots and Systems (IROS 2014), 2014 IEEE/RSJ International Conference on*. IEEE, 2014, pp. 2476–2481.

[60] A. Shiva, A. Stilli, Y. Noh, A. Faragasso, I. De Falco, G. Gerboni, M. Cianchetti, A. Menciassi, K. Althoefer, and H. A. Wurdemann, "Tendon-based stiffening for a pneumatically actuated soft manipulator," *IEEE Robotics and Automation Letters*, vol. 1, no. 2, pp. 632–637, 2016.

[61] J. Fraś, J. Czarnowski, M. Maciaś, J. Główka, M. Cianchetti, and A. Menciassi, "New stiff-flop module construction idea for improved actuation and sensing," in *Robotics and Automation (ICRA), 2015 IEEE International Conference on*. IEEE, 2015, pp. 2901–2906.

[62] L. Wang and N. Simaan, "Investigation of error propagation in multi-backbone continuum robots," in *Advances in Robot Kinematics*. Springer, 2014, pp. 385–394.

[63] B. A. Jones and I. D. Walker, "Kinematics for multisection continuum robots," *IEEE Transactions on Robotics*, vol. 22, no. 1, pp. 43–55, 2006.

[64] K. Xu and N. Simaan, "Actuation compensation for flexible surgical snake-like robots with redundant remote actuation," in *Robotics and Automation, 2006 IEEE/ICRA International Conference on*. IEEE, 2006, pp. 4148–4154.

[65] R. Roy, L. Wang, and N. Simaan, "Modeling and estimation of friction, extension, and coupling effects in multisegment continuum robots," *IEEE/ASME Transactions on Mechatronics*, vol. 22, no. 2, pp. 909–920, 2017.

[66] D. Compare, A. Rocco, and G. Nardone, "Screening for and surveillance of gastric cancer," *World Journal of Gastroenterology: WJG*, vol. 20, no. 38, p. 13681, 2014.

[67] C. Medical. (2018, May) Single-use self-propelled colonoscope. [Online]. Available: https://consis-medical.com/

[68] K. Oliver-Butler, Z. H. Epps, and D. C. Rucker, "Concentric agonist-antagonist robots for minimally invasive

surgeries," in *Medical Imaging 2017: Image-Guided Procedures, Robotic Interventions, and Modeling*, vol. 10135. International Society for Optics and Photonics, 2017, pp. 10 135 111–8.

[69] D. W. Schölvinck, H. T. Künzli, C. Kestens, P. D. Siersema, F. P. Vleggaar, M. I. Canto, H. Cosby, J. A. Abrams, C. J. Lightdale, E. Tejeda-Ramirez *et al.*, "Treatment of barrett's esophagus with a novel focal cryoablation device: a safety and feasibility study," *Endoscopy*, vol. 47, no. 12, pp. 1106–1112, 2015.

[70] S. G. Hart and L. E. Staveland, "Results of empirical and theoretical research," *Ergonomics: Skill, Displays, Controls, and Mental Workload*, vol. 2, p. 408, 2005.

[71] P. A. Harris, R. Taylor, R. Thielke, J. Payne, N. Gonzalez, and J. G. Conde, "Research electronic data capture (redcap)a metadata-driven methodology and workflow process for providing translational research informatics support," *Journal of biomedical informatics*, vol. 42, no. 2, pp. 377–381, 2009.

[72] A. G. Harrell and B. T. Heniford, "Minimally invasive abdominal surgery: lux et veritas past, present, and future," *The American journal of surgery*, vol. 190, no. 2, pp. 239–243, 2005.

[73] M. M. Lirici, "Single site laparoscopic surgery: an intermediate step toward no (visible) scar surgery or the next gold standard in minimally invasive surgery?" 2012.

[74] J. R. Romanelli and D. B. Earle, "Single-port laparoscopic surgery: an overview," *Surgical endoscopy*, vol. 23, no. 7, pp. 1419–1427, 2009.

[75] A. D. Strickland, M. G. Norwood, F. Behnia-Willison, S. A. Olakkengil, and P. J. Hewett, "Transvaginal natural orifice translumenal endoscopic surgery (notes): a survey of womens views on a new technique," *Surgical endoscopy*, vol. 24, no. 10, pp. 2424–2431, 2010.

[76] A. Johnson, "Laparoscopic surgery," *The Lancet*, vol. 349, no. 9052, pp. 631–635, 1997.

[77] S. J. Spaner and G. L. Warnock, "A brief history of endoscopy, laparoscopy, and laparoscopic surgery," *Journal of Laparoendoscopic & Advanced Surgical Techniques*, vol. 7, no. 6, pp. 369–373, 1997.

[78] D. McKay and G. Blake, "Optimum incision length for port insertion in laparoscopic surgery," *The Annals of The Royal College of Surgeons of England*, vol. 88, no. 1, pp. 78–78, 2006.

[79] A. M. Lacy, J. C. García-Valdecasas, S. Delgado, A. Castells, P. Taurá, J. M. Piqué, and J. Visa, "Laparoscopy-assisted colectomy versus open colectomy for treatment of non-metastatic colon cancer: a randomised trial," *The Lancet*, vol. 359, no. 9325, pp. 2224–2229, 2002.

[80] K. L. Leung, P. B. Lai, R. L. Ho, W. C. Meng, R. Y. Yiu, J. F. Lee, and W. Y. Lau, "Systemic cytokine response after laparoscopic-assisted resection of rectosigmoid carcinoma: a prospective randomized trial," *Annals of surgery*, vol. 231, no. 4, p. 506, 2000.

[81] M. Carbajo, J. M. Del Olmo, J. Blanco, C. De la Cuesta, M. Toledano, F. Martin, C. Vaquero, and L. Inglada, "Laparoscopic treatment vs open surgery in the solution of major incisional and abdominal wall hernias with mesh," *Surgical endoscopy*, vol. 13, no. 3, pp. 250–252, 1999.

[82] J. E. Varela, S. E. Wilson, and N. T. Nguyen, "Laparoscopic surgery significantly reduces surgical-site infections compared with open surgery," *Surgical endoscopy*, vol. 24, no. 2, pp. 270–276, 2010.

[83] C. Sietses, R. Beelen, S. Meijer, and M. Cuesta, "Immunological consequences of laparoscopic surgery, speculations on the cause and clinical implications," *Langenbeck's archives of surgery*, vol. 384, no. 3, pp. 250–258, 1999.

[84] W. Schwenk, C. Jacobi, U. Mansmann, B. Böhm, and J. Müller, "Inflammatory response after laparoscopic and conventional colorectal resections–results of a prospective randomized trial," *Langenbeck's archives of surgery*, vol. 385, no. 1, pp. 2–9, 2000.

[85] O. Aziz, V. Constantinides, P. P. Tekkis, T. Athanasiou, S. Purkayastha, P. Paraskeva, A. W. Darzi, and A. G. Heriot, "Laparoscopic versus open surgery for rectal cancer: a meta-analysis," *Annals of surgical oncology*, vol. 13, no. 3, pp. 413–424, 2006.

[86] E. C. Tsimoyiannis, K. E. Tsimogiannis, G. Pappas-Gogos, C. Farantos, N. Benetatos, P. Mavridou, and A. Manataki, "Different pain scores in single transumbilical incision laparoscopic cholecystectomy versus classic laparoscopic cholecystectomy: a randomized controlled trial," *Surgical endoscopy*, vol. 24, no. 8, pp. 1842–1848, 2010.

[87] S. Khandelwal, A. S. Wright, E. Figueredo, C. A. Pellegrini, and B. K. Oelschlager, "Single-incision laparoscopy: training, techniques, and safe introduction to clinical practice," *Journal of Laparoendoscopic & Advanced Surgical Techniques*, vol. 21, no. 8, pp. 687–693, 2011.

[88] B. D. Ciprian and R. Daniela, "Appendectomy single incision laparoscopic surgery (sils)-our early experience," *Colectiv Stiin Ific Si de Recenzie*, vol. 8, no. 4, pp. 25–29, 2013.

[89] W.-H. Shin and D.-S. Kwon, "Surgical robot system for single-port surgery with novel joint mechanism," *IEEE Transactions on Biomedical Engineering*, vol. 60, no. 4, pp. 937–944, 2013.

[90] R. Tacchino, F. Greco, and D. Matera, "Single-incision laparoscopic cholecystectomy: surgery without a visible scar," *Surgical endoscopy*, vol. 23, no. 4, pp. 896–899, 2009.

[91] M. A. Cuesta, F. Berends, and A. A. Veenhof, "The invisible cholecystectomy: a transumbilical laparoscopic operation without a scar," *Surgical endoscopy*, vol. 22, no. 5, pp. 1211–1213, 2008.

[92] J. R. Romanelli, T. B. Roshek, D. C. Lynn, and D. B. Earle, "Single-port laparoscopic cholecystectomy: initial

experience," *Surgical endoscopy*, vol. 24, no. 6, pp. 1374–1379, 2010.

[93] S. Agrawal, A. Shaw, and Y. Soon, "Single-port laparoscopic totally extraperitoneal inguinal hernia repair with the triport system: initial experience," *Surgical endoscopy*, vol. 24, no. 4, pp. 952–956, 2010.

[94] D. E. Bowman, "Asge/sages working group on natural orifice translumenal endoscopic surgery," *Gastrointestinal Endoscopy*, vol. 63, no. 2, pp. 199–203, 2006.

[95] A. Cuschieri, "The spectrum of laparoscopic surgery," *World journal of surgery*, vol. 16, no. 6, pp. 1089–1097, 1992.

[96] Y. Song, Y. Kim, C. S. Shin, and D. Hong, "Natural orifice translumenal endoscopic surgery: Current status and future technical development," *International Journal of Precision Engineering and Manufacturing*, vol. 14, no. 5, pp. 859–867, 2013.

[97] J. P. Pearl and J. L. Ponsky, "Natural orifice translumenal endoscopic surgery: a critical review," *Journal of Gastrointestinal Surgery*, vol. 12, no. 7, pp. 1293–1300, 2008.

[98] S. C. Jayasingh, "Comparison of advantages and disadvantages between sils and notes," *World Journal of Laparoscopic Surgery*, vol. 4, no. 1, pp. 67–72, 2011.

[99] S. S. Kommu, A. Chakravarti, C. J. Luscombe, A. Golash, M. M. Desai, J. H. Kaouk, I. S. Gill, J. A. Cadeddu, and A. Rané, "Laparoendoscopic single-site surgery (less) and notes; standardised platforms in nomenclature," *BJU international*, vol. 103, no. 5, pp. 701–702, 2009.

[100] D. W. Rattner, R. Hawes, S. Schwaitzberg, M. Kochman, and L. Swanstrom, "The second sages/asge white paper on natural orifice transluminal endoscopic surgery: 5 years of progress," *Surgical endoscopy*, vol. 25, no. 8, pp. 2441–2448, 2011.

[101] S. Schwaitzberg, "Identifying and overcoming the potential barriers to the adoption of natural orifice transluminal endoscopic surgery," *Asian Journal of Endoscopic Surgery*, vol. 3, no. 2, pp. 53–59, 2010.

[102] N. T. Nguyen, M. W. Hinojosa, D. Finley, M. Stevens, and M. Paya, "Application of robotics in general surgery: initial experience," *The American Surgeon*, vol. 70, no. 10, p. 914, 2004.

[103] D. Oleynikov, "Robotic surgery," *Surgical Clinics*, vol. 88, no. 5, pp. 1121–1130, 2008.

[104] P. Dario, E. Guglielmelli, B. Allotta, and M. C. Carrozza, "Robotics for medical applications," *IEEE Robotics & Automation Magazine*, vol. 3, no. 3, pp. 44–56, 1996.

[105] E. S. Park, J. W. Shum, T. G. Bui, R. B. Bell, and E. J. Dierks, "Robotic surgery: a new approach to tumors of the tongue base, oropharynx, and hypopharynx," *Oral and Maxillofacial Surgery Clinics*, vol. 25, no. 1, pp. 49–59, 2013.

[106] S. Atallah, M. Albert, S. Larach *et al.*, "Robotic transanal minimally invasive surgery in a cadaveric model," *Techniques in coloproctology*, vol. 15, no. 4, pp. 461–464, 2011.

[107] "Da vinci xi.intuitive surgical," *Available: http://www.intuitivesurgical.com/*, 2018.

[108] J. Zhao, B. Feng, M.-H. Zheng, and K. Xu, "Surgical robots for spl and notes: a review," *Minimally Invasive Therapy & Allied Technologies*, vol. 24, no. 1, pp. 8–17, 2015.

[109] "Medrobotics," *Available: http://medrobotics.com//*, 2018.

[110] K. Xu, R. E. Goldman, J. Ding, P. K. Allen, D. L. Fowler, and N. Simaan, "System design of an insertable robotic effector platform for single port access (spa) surgery," in *Intelligent Robots and Systems, 2009. IROS 2009. IEEE/RSJ International Conference on*. IEEE, 2009, pp. 5546–5552.

[111] H. Tillander, "Selective angiography with a catheter guided by a magnet," *IEEE Transactions on Magnetics*, vol. 6, no. 2, pp. 355–358, 1970.

[112] Stereotaxis. (2018) Stereotaxis. [Online]. Available: Available:http://ir.stereotaxis.com/phoenix.zhtml?c=179896&p=irol-newsArticle&ID=1373918

[113] D. G. Latcu, P. Ricard, N. Zarqane, K. Yaici, J.-P. Rinaldi, A. Maluski, and N. Saoudi, "Robotic magnetic navigation for ablation of human arrhythmias: initial experience," *Archives of cardiovascular diseases*, vol. 102, no. 5, pp. 419–425, 2009.

[114] "Magnetecs," *Available: http://www.magnetecs.com/*, 2015.

[115] M.-H. Meng, T. Mei, J. Pu, C. Hu, X. Wang, and Y. Chan, "Wireless robotic capsule endoscopy: State-of-the-art and challenges," in *Intelligent Control and Automation, 2004. WCICA 2004. Fifth World Congress on*, vol. 6. IEEE, 2004, pp. 5561–555a.

[116] K. T. Gottlieb, S. Banerjee, B. A. Barth, Y. M. Bhat, S. S. Chauhan, V. Konda, J. T. Maple, F. Murad, P. Pfau, D. Pleskow *et al.*, "Magnets in the gi tract," *Gastrointestinal Endoscopy*, vol. 78, no. 4, pp. 561–567, 2013.

[117] M. Sendoh, K. Ishiyama, and K.-I. Arai, "Fabrication of magnetic actuator for use in a capsule endoscope," *IEEE Transactions on Magnetics*, vol. 39, no. 5, pp. 3232–3234, 2003.

[118] W. Zhang, Y. Chen, and P. Huang, "Study on the system of a capsule endoscope driven by an outer rotational magnetic field," in *Mechatronic and Embedded Systems and Applications, Proceedings of the 2nd IEEE/ASME International Conference on*. IEEE, 2006, pp. 1–5.

[119] X. Wang and M. Q.-H. Meng, "Guided magnetic actuator for active capsule endoscope," in *Nano/Micro Engineered and Molecular Systems, 2007. NEMS'07. 2nd IEEE International Conference on*. IEEE, 2007, pp. 1153–1158.

[120] F. Carpi, S. Galbiati, and A. Carpi, "Controlled navigation of endoscopic capsules: Concept and preliminary experimental investigations," *IEEE Transactions on Biomedical Engineering*, vol. 54, no. 11, pp. 2028–2036, 2007.

[121] A. W. Mahoney and J. J. Abbott, "Generating rotating magnetic fields with a single permanent magnet for propulsion of untethered magnetic devices in a lumen," *IEEE Transactions on Robotics*, vol. 30, no. 2, pp. 411–420, 2014.

[122] M. Simi, G. Gerboni, A. Menciassi, and P. Valdastri, "Magnetic torsion spring mechanism for a wireless biopsy capsule," *Journal of Medical Devices*, vol. 7, no. 4, p. 041009, 2013.

[123] S. Yim and M. Sitti, "Design and analysis of a magnetically actuated and compliant capsule endoscopic robot," in *Robotics and Automation (ICRA), 2011 IEEE International Conference on*. IEEE, 2011, pp. 4810–4815.

[124] ——, "Design and rolling locomotion of a magnetically actuated soft capsule endoscope," *IEEE Transactions on Robotics*, vol. 28, no. 1, pp. 183–194, 2012.

[125] M. Gao, C. Hu, Z. Chen, H. Zhang, and S. Liu, "Design and fabrication of a magnetic propulsion system for self-propelled capsule endoscope," *IEEE Transactions on Biomedical Engineering*, vol. 57, no. 12, pp. 2891–2902, 2010.

[126] J.-F. Rey, H. Ogata, N. Hosoe, K. Ohtsuka, N. Ogata, K. Ikeda, H. Aihara, I. Pangtay, T. Hibi, S. Kudo *et al.*, "Feasibility of stomach exploration with a guided capsule endoscope," *Endoscopy*, vol. 42, no. 07, pp. 541–545, 2010.

[127] J.-F. Rey, H. Ogata, N. Hosoe, K. Ohtsuka, N. Ogata, K. Ikeda, H. Aihara, I. Pangtay, T. Hibi, S.-E. Kudo *et al.*, "Blinded nonrandomized comparative study of gastric examination with a magnetically guided capsule endoscope and standard videoendoscope," *Gastrointestinal endoscopy*, vol. 75, no. 2, pp. 373–381, 2012.

[128] P. Swain, A. Toor, F. Volke, J. Keller, J. Gerber, E. Rabinovitz, and R. I. Rothstein, "Remote magnetic manipulation of a wireless capsule endoscope in the esophagus and stomach of humans (with videos)," *Gastrointestinal endoscopy*, vol. 71, no. 7, pp. 1290–1293, 2010.

[129] A. W. Mahoney and J. J. Abbott, "Five-degree-of-freedom manipulation of an untethered magnetic device in fluid using a single permanent magnet with application in stomach capsule endoscopy," *The International Journal of Robotics Research*, vol. 35, no. 1-3, pp. 129–147, 2016.

[130] S. Yim and M. Sitti, "Shape-programmable soft capsule robots for semi-implantable drug delivery," *IEEE Transactions on Robotics*, vol. 28, no. 5, pp. 1198–1202, 2012.

[131] M. Beccani, C. Di Natali, M. E. Rentschler, and P. Valdastri, "Wireless tissue palpation: Proof of concept for

a single degree of freedom," in *Robotics and Automation (ICRA), 2013 IEEE International Conference on*. IEEE, 2013, pp. 711–717.

[132] M. Beccani, C. Di Natali, L. J. Sliker, J. A. Schoen, M. E. Rentschler, and P. Valdastri, "Wireless tissue palpation for intraoperative detection of lumps in the soft tissue," *IEEE Transactions on Biomedical Engineering*, vol. 61, no. 2, pp. 353–361, 2014.

[133] S. Park, R. A. Bergs, R. Eberhart, L. Baker, R. Fernandez, and J. A. Cadeddu, "Trocar-less instrumentation for laparoscopy: magnetic positioning of intra-abdominal camera and retractor," *Annals of Surgery*, vol. 245, no. 3, p. 379, 2007.

[134] J. Cadeddu, R. Fernandez, M. Desai, R. Bergs, C. Tracy, S.-J. Tang, P. Rao, M. Desai, and D. Scott, "Novel magnetically guided intra-abdominal camera to facilitate laparoendoscopic single-site surgery: initial human experience," *Surgical endoscopy*, vol. 23, no. 8, pp. 1894–1899, 2009.

[135] I. S. Zeltser, R. Bergs, R. Fernandez, L. Baker, R. Eberhart, and J. A. Cadeddu, "Single trocar laparoscopic nephrectomy using magnetic anchoring and guidance system in the porcine model," *The Journal of urology*, vol. 178, no. 1, pp. 288–291, 2007.

[136] P. Swain, R. Austin, K. Bally, and R. Trusty, "Development and testing of a tethered, independent camera for notes and single-site laparoscopic procedures," *Surgical endoscopy*, vol. 24, no. 8, pp. 2013–2021, 2010.

[137] G. Dominguez, L. Durand, J. De Rosa, E. Danguise, C. Arozamena, and P. A. Ferraina, "Retraction and triangulation with neodymium magnetic forceps for single-port laparoscopic cholecystectomy," *Surgical endoscopy*, vol. 23, no. 7, pp. 1660–1666, 2009.

[138] Y. B. Cho, C.-M. Park, H.-K. Chun, L. J. Yi, J. H. Park, S. H. Yun, H. C. Kim, and W. Y. Lee, "Transvaginal endoscopic cholecystectomy using a simple magnetic traction system," *Minimally Invasive Therapy & Allied Technologies*, vol. 20, no. 3, pp. 174–178, 2011.

[139] S. L. Best and J. A. Cadeddu, "Development of magnetic anchoring and guidance systems for minimally invasive surgery," *Indian journal of urology: IJU: journal of the Urological Society of India*, vol. 26, no. 3, p. 418, 2010.

[140] T. Hu, P. K. Allen, N. J. Hogle, and D. L. Fowler, "Insertable surgical imaging device with pan, tilt, zoom, and lighting," *The International Journal of Robotics Research*, vol. 28, no. 10, pp. 1373–1386, 2009.

[141] B. S. Terry, Z. C. Mills, J. A. Schoen, and M. E. Rentschler, "Single-port-access surgery with a novel magnet camera system," *IEEE transactions on biomedical engineering*, vol. 59, no. 4, pp. 1187–1193, 2012.

[142] G. Tortora, M. Salerno, T. Ranzani, S. Tognarelli, P. Dario, and A. Menciassi, "A modular magnetic platform

for natural orifice transluminal endoscopic surgery," in *Engineering in Medicine and Biology Society (EMBC), 2013 35th Annual International Conference of the IEEE*. IEEE, 2013, pp. 6265–6268.

[143] A. C. Lehman, J. Dumpert, N. A. Wood, L. Redden, A. Q. Visty, S. Farritor, B. Varnell, and D. Oleynikov, "Natural orifice cholecystectomy using a miniature robot," *Surgical endoscopy*, vol. 23, no. 2, pp. 260–266, 2009.

[144] A. C. Lehman, N. A. Wood, S. Farritor, M. R. Goede, and D. Oleynikov, "Dexterous miniature robot for advanced minimally invasive surgery," *Surgical endoscopy*, vol. 25, no. 1, pp. 119–123, 2011.

[145] V. I. Corp.Stereotaxis. (2018) Virtual incision. [Online]. Available: Available:https://www.virtualincision.com/

[146] A. Arezzo, A. Menciassi, P. Valdastri, G. Ciuti, G. Lucarini, M. Salerno, C. Di Natali, M. Verra, P. Dario, and M. Morino, "Experimental assessment of a novel robotically-driven endoscopic capsule compared to traditional colonoscopy," *Digestive and Liver Disease*, vol. 45, no. 8, pp. 657–662, 2013.

[147] G. Ciuti, R. Donlin, P. Valdastri, A. Arezzo, A. Menciassi, M. Morino, and P. Dario, "Robotic versus manual control in magnetic steering of an endoscopic capsule," *Endoscopy*, vol. 42, no. 02, pp. 148–152, 2010.

[148] G. Ciuti, P. Valdastri, A. Menciassi, and P. Dario, "Robotic magnetic steering and locomotion of capsule endoscope for diagnostic and surgical endoluminal procedures," *Robotica*, vol. 28, no. 2, pp. 199–207, 2010.

[149] R. D. Brewer, K. E. Loewke, E. F. Duval, and J. K. Salisbury, "Force control of a permanent magnet for minimally-invasive procedures," in *Biomedical Robotics and Biomechatronics, 2008. BioRob 2008. 2nd IEEE RAS & EMBS International Conference on*. IEEE, 2008, pp. 580–586.

[150] M. P. Kummer, J. J. Abbott, B. E. Kratochvil, R. Borer, A. Sengul, and B. J. Nelson, "Octomag: An electromagnetic system for 5-dof wireless micromanipulation," *IEEE Transactions on Robotics*, vol. 26, no. 6, pp. 1006–1017, 2010.

[151] K. Ikuta, S. Makita, and S. Arimoto, "Non-contact magnetic gear for micro transmission mechanism," in *Micro Electro Mechanical Systems, 1991, MEMS'91, Proceedings. An Investigation of Micro Structures, Sensors, Actuators, Machines and Robots. IEEE*. IEEE, 1991, pp. 125–130.

[152] C. Di Natali, T. Ranzani, M. Simi, A. Menciassi, and P. Valdastri, "Trans-abdominal active magnetic linkage for robotic surgery: Concept definition and model assessment," in *Robotics and Automation (ICRA), 2012 IEEE International Conference on*. IEEE, 2012, pp. 695–700.

[153] R. Montague, C. Bingham, and K. Atallah, "Servo control of magnetic gears," *IEEE/Asme Transactions on Mechatronics*, vol. 17, no. 2, pp. 269–278, 2012.

[154] R. Montague and C. Bingham, "Nonlinear control of magnetically-geared drive-trains," *International Journal of Automation and Computing*, vol. 10, no. 4, pp. 319–326, 2013.

[155] G. Zhang, "Speed control of two-inertia system by pi/pid control," *IEEE Transactions on industrial electronics*, vol. 47, no. 3, pp. 603–609, 2000.

[156] E. Furlani, "A two-dimensional analysis for the coupling of magnetic gears," *IEEE Transactions on Magnetics*, vol. 33, no. 3, pp. 2317–2321, 1997.

[157] R. G. Montague, C. Bingham, and K. Atallah, "Magnetic gear pole-slip prevention using explicit model predictive control," *IEEE/ASME Transactions on Mechatronics*, vol. 18, no. 5, pp. 1535–1543, 2013.

[158] S. N. Vukosavic and M. R. Stojic, "Suppression of torsional oscillations in a high-performance speed servo drive," *IEEE Transactions on Industrial Electronics*, vol. 45, no. 1, pp. 108–117, 1998.

[159] A. Mohammadi, D. Samsonas, F. Leong, Y. Tan, D. Thiruchelvam, P. Valdastri, and D. Oetomo, "Modeling and control of local electromagnetic actuation for robotic-assisted surgical devices," *IEEE/ASME Transactions on Mechatronics*, vol. 22, no. 6, pp. 2449–2460, 2017.

[160] M. Cadeddu, M. Boyd, P. Swain *et al.*, "Retraction force measurement during transgastric and transvaginal notes," *Gastrointestinal Endoscopy*, vol. 67, no. 5, p. AB119, 2008.

[161] B. E. Padilla, G. Dominguez, C. Millan, and M. Martinez-Ferro, "The use of magnets with single-site umbilical laparoscopic surgery," in *Seminars in pediatric surgery*, vol. 20, no. 4. Elsevier, 2011, pp. 224–231.

[162] M. Ryou and C. Thompson, "Magnetic retraction in natural-orifice transluminal endoscopic surgery (notes): addressing the problem of traction and countertraction," *Endoscopy*, vol. 41, no. 02, pp. 143–148, 2009.

[163] M. Simi, G. Sardi, P. Valdastri, A. Menciassi, and P. Dario, "Magnetic levitation camera robot for endoscopic surgery," in *Robotics and Automation (ICRA), 2011 IEEE International Conference on*. IEEE, 2011, pp. 5279–5284.

[164] M. Simi, N. Tolou, P. Valdastri, J. Herder, A. Menciassi, and P. Dario, "Modeling of a compliant joint in a magnetic levitation system for an endoscopic camera," *Mechanical Sciences*, vol. 3, no. 1, pp. 5–14, 2012.

[165] G.-P. Haber, M. A. White, R. Autorino, P. F. Escobar, M. D. Kroh, S. Chalikonda, R. Khanna, S. Forest, B. Yang, F. Altunrende *et al.*, "Novel robotic da vinci instruments for laparoendoscopic single-site surgery," *Urology*, vol. 76, no. 6, pp. 1279–1282, 2010.

[166] M. Piccigallo, U. Scarfogliero, C. Quaglia, G. Petroni, P. Valdastri, A. Menciassi, and P. Dario, "Design of a novel bimanual robotic system for single-port laparoscopy," *IEEE/ASME Transactions On Mechatronics*, vol. 15, no. 6, pp. 871–878, 2010.

[167] C. Richards, J. Rosen, B. Hannaford, C. Pellegrini, and M. Sinanan, "Skills evaluation in minimally invasive surgery using force/torque signatures," *Surgical endoscopy*, vol. 14, no. 9, pp. 791–798, 2000.

[168] S. L. Best, R. Bergs, M. Gedeon, J. Paramo, R. Fernandez, J. A. Cadeddu, and D. J. Scott, "Maximizing coupling strength of magnetically anchored surgical instruments: how thick can we go?" *Surgical endoscopy*, vol. 25, no. 1, pp. 153–159, 2011.

[169] S. L. Best, W. Kabbani, D. J. Scott, R. Bergs, H. Beardsley, R. Fernandez, L. B. Mashaud, and J. A. Cadeddu, "Magnetic anchoring and guidance system instrumentation for laparo-endoscopic single-site surgery/natural orifice transluminal endoscopic surgery: lack of histologic damage after prolonged magnetic coupling across the abdominal wall," *Urology*, vol. 77, no. 1, pp. 243–247, 2011.

[170] P. Berkelman and J. Ma, "A compact, modular, teleoperated robotic minimally invasive surgery system," in *Biomedical Robotics and Biomechatronics, 2006. BioRob 2006. The First IEEE/RAS-EMBS International Conference on*. IEEE, 2006, pp. 702–707.

[171] P. Gan, "A novel liver retractor for reduced or single-port laparoscopic surgery," *Surgical endoscopy*, vol. 28, no. 1, pp. 331–335, 2014.

[172] E. P. Furlani, *Permanent magnet and electromechanical devices: materials, analysis, and applications*. Academic press, 2001.

[173] J. S. Agashe and D. P. Arnold, "A study of scaling and geometry effects on the forces between cuboidal and cylindrical magnets using analytical force solutions," *Journal of Physics D: Applied Physics*, vol. 41, no. 10, p. 105001, 2008.

[174] M. Chowdhury, D. Nuruzzaman, A. Mia, and M. Rahaman, "Friction coefficient of different material pairs under different normal loads and sliding velocities," *Tribology in Industry*, vol. 34, no. 1, pp. 18–23, 2012.

[175] M. Simi, R. Pickens, A. Menciassi, S. D. Herrell, and P. Valdastri, "Fine tilt tuning of a laparoscopic camera by local magnetic actuation: two-port nephrectomy experience on human cadavers," *Surgical innovation*, vol. 20, no. 4, pp. 385–394, 2013.

[176] X. Liu, G. J. Mancini, and J. Tan, "Design of a unified active locomotion mechanism for a capsule-shaped laparoscopic camera system," in *Robotics and Automation (ICRA), 2014 IEEE International Conference on*. IEEE, 2014, pp. 2449–2456.

[177] T. Blinman and T. Ponsky, "Pediatric minimally invasive surgery: laparoscopy and thoracoscopy in infants and children," *Pediatrics*, vol. 130, no. 3, pp. 539–549, 2012.

[178] N. E. Bruns, O. S. Soldes, and T. A. Ponsky, "Robotic surgery may not make the cut in pediatrics," *Frontiers*

in pediatrics, vol. 3, p. 10, 2015.

[179] J. D. Raman, D. J. Scott, and J. A. Cadeddu, "Role of magnetic anchors during laparoendoscopic single site surgery and notes," *Journal of endourology*, vol. 23, no. 5, pp. 781–786, 2009.

[180] S. R. Platt, J. A. Hawks, and M. E. Rentschler, "Vision and task assistance using modular wireless in vivo surgical robots," *IEEE Transactions on Biomedical Engineering*, vol. 56, no. 6, pp. 1700–1710, 2009.

[181] R. P. Feynman, "Feynman lectures on physics. volume 2: Mainly electromagnetism and matter," *Reading, Ma.: Addison-Wesley, 1964, edited by Feynman, Richard P.; Leighton, Robert B.; Sands, Matthew*, 1964.

[182] K. C. Zorn, O. N. Gofrit, G. P. Zagaja, and A. L. Shalhav, "Use of the endoholder device during robotic-assisted laparoscopic radical prostatectomy: the poor man's fourth arm equivalent," *Journal of endourology*, vol. 22, no. 2, pp. 385–388, 2008.

[183] B. Appenrodt, "Differential diagnosis of ascites," *Ascites, Hyponatremia and Hepatorenal Syndrome: Progress in Treatment*, vol. 28, pp. 1–10, 2011.

[184] P. Ginès, A. Cárdenas, V. Arroyo, and J. Rodés, "Management of cirrhosis and ascites," *New England Journal of Medicine*, vol. 350, no. 16, pp. 1646–1654, 2004.

[185] G. L. Davis, M. J. Alter, H. El-Serag, T. Poynard, and L. W. Jennings, "Aging of hepatitis c virus (hcv)-infected persons in the united states: a multiple cohort model of hcv prevalence and disease progression," *Gastroenterology*, vol. 138, no. 2, pp. 513–521, 2010.

[186] K. S. Habeeb and J. L. Herrera, "Management of ascites: paracentesis as a guide," *Postgraduate medicine*, vol. 101, no. 1, pp. 191–200, 1997.

[187] A. Ochs, M. Rössle, K. Haag, K.-H. Hauenstein, P. Deibert, V. Siegerstetter, M. Huonker, M. Langer, and H. E. Blum, "The transjugular intrahepatic portosystemic stent–shunt procedure for refractory ascites," *New England Journal of Medicine*, vol. 332, no. 18, pp. 1192–1197, 1995.

[188] J. Sola-Vera, J. Miñana, E. Ricart, M. Planella, B. González, X. Torras, J. Rodríguez, J. Such, S. Pascual, G. Soriano *et al.*, "Randomized trial comparing albumin and saline in the prevention of paracentesis-induced circulatory dysfunction in cirrhotic patients with ascites," *Hepatology*, vol. 37, no. 5, pp. 1147–1153, 2003.

[189] K. Fagan, E. Y. Zhao, L. Horsfall, B. J. Ruffin, M. S. Kruger, S. McPhail, P. O'Rourke, E. Ballard, K. Irvine, and E. Powell, "Burden of decompensated cirrhosis and ascites on hospital services in a tertiary care facility: time for change?" *Internal medicine journal*, vol. 44, no. 9, pp. 865–872, 2014.

[190] K. A. Somberg, J. L. Riegler, J. M. LaBerge, M. M. Doherty-Simor, P. Bachetti, J. P. Roberts, and J. R. Lake, "Hepatic encephalopathy after transjugular intrahepatic portosystemic shunts: incidence and risk factors."

American Journal of Gastroenterology, vol. 90, no. 4, pp. 549–555, 1995.

[191] G. Stirnimann, V. Banz, F. Storni, and A. De Gottardi, "Automated low-flow ascites pump for the treatment of cirrhotic patients with refractory ascites," *Therapeutic advances in gastroenterology*, vol. 10, no. 2, pp. 283–292, 2017.

[192] G. Stirnimann, T. Berg, L. Spahr, S. Zeuzem, S. McPherson, F. Lammert, F. Storni, V. Banz, J. Babatz, V. Vargas *et al.*, "Treatment of refractory ascites with an automated low-flow ascites pump in patients with cirrhosis," *Alimentary pharmacology & therapeutics*, vol. 46, no. 10, pp. 981–991, 2017.

[193] E. C. Tsimoyiannis, P. Siakas, G. Glantzounis, C. Toli, G. Sferopoulos, M. Pappas, and A. Manataki, "Laparoscopic placement of the tenckhoff catheter for peritoneal dialysis," *Surgical Laparoscopy Endoscopy & Percutaneous Techniques*, vol. 10, no. 4, pp. 218–221, 2000.

[194] V. W. Nitti, "Pressure flow urodynamic studies: the gold standard for diagnosing bladder outlet obstruction," *Reviews in urology*, vol. 7, no. Suppl 6, p. S14, 2005.

[195] A. Z. Taddese, P. R. Slawinski, M. Pirotta, E. De Momi, K. L. Obstein, and P. Valdastri, "Enhanced real-time pose estimation for closed-loop robotic manipulation of magnetically actuated capsule endoscopes," *International Journal of Robotics Research*, vol. 37, no. 8, pp. 890–911, 2018.

[196] P. Bellot, M.-W. Welker, G. Soriano, M. von Schaewen, B. Appenrodt, R. Wiest, S. Whittaker, R. Tzonev, S. Handshiev, C. Verslype *et al.*, "Automated low flow pump system for the treatment of refractory ascites: a multi-center safety and efficacy study," *Journal of hepatology*, vol. 58, no. 5, pp. 922–927, 2013.

[197] C. M. Grabau, S. F. Crago, L. K. Hoff, J. A. Simon, C. A. Melton, B. J. Ott, and P. S. Kamath, "Performance standards for therapeutic abdominal paracentesis," *Hepatology*, vol. 40, no. 2, pp. 484–488, 2004.

[198] M. Bernardi, P. Caraceni, R. J. Navickis, and M. M. Wilkes, "Albumin infusion in patients undergoing large-volume paracentesis: a meta-analysis of randomized trials," *Hepatology*, vol. 55, no. 4, pp. 1172–1181, 2012.

[199] V. Harding, E. Fenu, H. Medani, R. Shaboodien, S. Ngan, H. Li, R. Burt, N. Diamantis, M. Tuthill, S. Blagden *et al.*, "Safety, cost-effectiveness and feasibility of daycase paracentesis in the management of malignant ascites with a focus on ovarian cancer," *British journal of cancer*, vol. 107, no. 6, p. 925, 2012.

[200] M. Thomas, G. Sauter, A. Gerbes, M. Stangl, T. Schiergens, M. Angele, J. Werner, and M. Guba, "Automated low flow pump system for the treatment of refractory ascites: a single-center experience," *Langenbeck's archives of surgery*, vol. 400, no. 8, pp. 979–983, 2015.

[201] P. Ginès, J. Uriz, B. Calahorra, G. Garcia-Tsao, P. S. Kamath, L. R. Del Arbol, R. Planas, J. Bosch, V. Arroyo, J. Rodés *et al.*, "Transjugular intrahepatic portosystemic shunting versus paracentesis plus albumin for

refractory ascites in cirrhosis," *Gastroenterology*, vol. 123, no. 6, pp. 1839–1847, 2002.

[202] K. A. Bohn and C. E. Ray Jr, "Repeat large-volume paracentesis versus tunneled peritoneal catheter placement for malignant ascites: a cost-minimization study," *American Journal of Roentgenology*, vol. 205, no. 5, pp. 1126–1134, 2015.

[203] H. S. Gokturk, M. Demir, N. A. Ozturk, G. K. Unler, S. Kulaksizoglu, I. Kozanoglu, E. Serin, and U. Yilmaz, "The role of ascitic fluid viscosity in the differential diagnosis of ascites," *Canadian Journal of Gastroenterology and Hepatology*, vol. 24, no. 4, pp. 255–259, 2010.

[204] E. A. Zahn, "Viscosity cup," Dec. 27 1938, uS Patent 2,141,329.